ISSN 2221-7754

МІНІСТЕРСТВО ОСВІТИ І НАУКИ УКРАЇНИ

ВІСНИК

ХАРКІВСЬКОГО НАЦІОНАЛЬНОГО УНІВЕРСИТЕТУ

імені В.Н. Каразіна

№ 1040

серія: фізична

«Ядра, частинки, поля»

Заснована у 1998 р.

Випуск **1** /57/

The Journal of Kharkiv National University

№ 1040

physical series

«Nuclei, Particles, Fields»

Issue **1** /57/

Харків

2013

DESCRIPTION AND PURPOSE OF THE JOURNAL

The Journal of Kharkov National University (Physical series "Nuclei, Particles, Fields") is a journal covering elementary particles physics, nuclear physics, plasma physics and technologies, solid state physics and radiation physics. The Journal publishes research articles, short communications, review articles and scientific book reviews.
Issues per year – 4.

Editorial office address
High Technology Institute
V.N. Karazin Kharkiv National University
Kurchatov av., 31, office 402, Kharkiv, 61108, Ukraine
Phone: +38-057-335-18-33
E-mail: visnyk.npf@univer.kharkov.ua
Web-page: http://www-nuclear.univer.kharkov.ua

ПРОФІЛЬ ЖУРНАЛУ ТА МЕТА ВИДАННЯ

"Вісник Харківського національного університету" (серія: фізична «Ядра, частинки, поля») є збірником наукових праць з фізики елементарних частинок, ядерної фізики, фізики плазми та плазмових технологій, фізики твердого тіла та радіаційної фізики. Збірник публікує наукові статті, короткі повідомлення, оглядові статті та рецензії на наукові видання.
Періодичність випуску збірника – 4 рази на рік.

Затверджено до друку рішенням Вченої ради Харківського національного університету імені В.Н. Каразіна (протокол № 1 від 25 січня 2013 р.)

Адреса редакції
Інститут високих технологій
Харківський національний університет імені В.Н. Каразіна
пр. Курчатова, 31, кімната 402, м. Харків, 61108, Україна
Телефон: +380-57-335-18-33
E-mail: visnyk.npf@univer.kharkov.ua
Web-сторінка: http://www-nuclear.univer.kharkov.ua

Статті пройшли внутрішнє і зовнішнє рецензування.
Свідоцтво про державну реєстрацію КВ № 11825-696 ПР від 4.10.2006.

CONTENTS

Reviews

Articles

ЗМІСТ

Огляди

Статті

The articles are based on materials presented at the International Conference "Problems of modern physics", Kharkov, Ukraine, October 25-26, 2012, dedicated to the 50th anniversary of the Physics and Engineering Department, V.N. Karazin Kharkiv National University.

Статті ґрунтуються на матеріалах, представлених на Міжнародній конференції «Проблеми сучасної фізики», Харків, Україна, 25-26 жовтня 2012 р., присвяченої 50-річчю заснування фізико-технічного факультету Харківського національного університету імені В.Н. Каразіна.

UDC 532.5

PATTERN FORMATION IN CONVECTIVE MEDIA

I.V. Gushchin, A.V. Kirichok, V.M. Kuklin
V.N. Karazin Kharkov National University
61022, Kharkov, Svobody sq. 4, Ukraine
E-mail: kuklinvm1@rambler.ru
Received 4 December 2012, accepted 20 January 2013

The several models of convection in a thin layer of liquid (gas) with poorly heat conducting boundaries are considered. These models demonstrate a rich dynamics of pattern formation and structural phase transitions. The primary analysis of pattern formation in such a system is performed with using of the well-studied Swift-Hohenberg model. The more advanced Proctor-Sivashinsky model is examined in order to study the second-order structural phase transitions both between patterns with translational invariance and between structures with broken translational invariance but keeping a long-range order. The spatial spectrum of arising structures and visual estimation of the number of defects are analyzed. The relation between the density of defects and the spectral characteristics of the structure is found. We also discuss the effect of noise on the formation of structural defects. It is shown that within the framework of the Proctor-Sivashinsky model with additional term, taking into account the inertial effects, the large-scale vortex structures arise as a result of the secondary modulation instability.
KEY WORDS: Rayleigh-Bénard convection, mathematical modeling, dissipative structures, structural phase transitions, structural defects

ФОРМИРОВАНИЕ СТРУКТУР В КОНВЕКТИВНЫХ СРЕДАХ
И.В. Гущин, А.В. Киричок, В.М. Куклин
Харьковский Национальный университет имени В.Н. Каразина
61022, г. Харьков, пл. Свободы 4, Украина
Рассмотрено несколько моделей конвекции в тонком слое жидкости (газа) в условиях слабой теплопроводности на его границах. Эти модели демонстрируют разнообразную динамику формирования пространственных структур и структурно-фазовых переходов между ними. Первоначальный анализ формирования ячеек в таких системах был представлен при использовании модели Свифта-Хоенберга. Более развитая и корректная модель Проктора-Сивашинского исследована для нескольких фазовых переходов между структурами с трансляционной инвариантностью и структурами с нарушенной трансляционной инвариантностью, но с сохраненным дальним порядком. Изучается связь между пространственным спектром структур и количеством дефектов. Найдено соотношение между плотностью дефектов и спектральными характеристиками структуры. Обсуждается эффект влияние шума на развитие фазовых переходов. Показано, что обобщенная модель Проктора-Сивашинского, учитывающая инерциальные эффекты, способна описывать формирование крупномасштабных вихревых структур, как результат вторичной модуляционной неустойчивости.
КЛЮЧЕВЫЕ СЛОВА: конвекция Релея-Бенара, математическое моделирование, диссипативные структуры, структурно-фазовые переходы, структурные дефекты

ФОРМУВАННЯ СТРУКТУР У КОНВЕКТИВНИХ СЕРЕДОВИЩАХ
І.В. Гущин, О.В. Киричок, В.М. Куклін
Харківський національний університет імені В.Н. Каразіна
61022, м. Харків, пл. Свободи, 4, Україна.
Розглянуто декілька моделей конвекції у тонкому шарі рідини (газу) в умовах слабкої теплопровідності на його межах. Ці моделі демонструють різнобарвну динаміку формування просторових структур та структурово - фазових переходів між ними. Попередній аналіз формування чарунок в таких системах було розроблено при використанні моделі Свіфта-Хоенберга. Більш розвинута та коректна модель Проктора-Сівашинського вивчена для декількох фазових переходів між структурами з трансляційною інваріантністю та структурами, які мали порушену трансляційну інваріантність, та дальній порядок. Вивчається зв'язок між просторовим спектром та кількістю дефектів. Знайдено відношення між густиной дефектів та характеристиками просторового спектру. Розглянуто ефект впливу шуму на розвиток фазових переходів. Показано, що більш загальна модель Проктора-Сівашинського, яка враховує інерціальні ефекти, дозволяє розглядати формування крупно масштабних вихорів, я к результат вторинної модуляційної нестійкості.
КЛЮЧОВІ СЛОВА: конвекція Релея-Бенара, математичне моделювання, дисипативні структури, структурно-фазові переходи, структурні дефекти

CONTENTS

1. INTRODUCTION

Considering the various processes in continuous media, we need to take into account the dynamics of perturbations with not only different spatial and temporal scales but also different spatial orientation [1-12]. The last one is responsible in the common geometric sense for symmetry of the spatial structures, which possess not only short-range but also a long-range order [13-17].

The nonlinearity of the medium manifests itself in certain mechanisms of interaction between these perturbations. Different approaches to description of such interactions in nonequilibrium media are presented in [18-25]. The processes involving a large number of perturbations of all scales and orientation are often called multi-wave or multimode, in the case of wave media or periodic systems.

1.1. The problems of description of structure formation processes

Currently, the problem of most interest is the elucidation of the nature of spatial structures appearance, the search for physically transparent mechanisms of these processes, and then the formulation of adequate (which have a clear physical background) mathematical models for description of these phenomena.

Considering the behavior of multimode or multiwave spatial structures formation processes, we can see the appearance of their specific features, such as a change in dynamics of the instability (i.e. delay or even suppression [26]) during the formation of unstable nonlinear structures. The number of degrees of freedom plays the significant role, such as the number of spectrum modes (which leads to appearance of a small parameter $\eta \propto 1/N$ inversely proportional to the number of spectrum modes N). The existence of a dense spectrum of perturbations can form long-lived quasi-stable nonlinear states and can delay the development of transient processes and structural phase transitions between these states [27, 28].

The issues of structural transformations, structural second-order phase transitions, resulting in the changes of the symmetry and some characteristic scales of spatial structures always be of great interest to researchers and developers of technologies.

In particular, one of the main problems of radiative study of materials is the problem of occurrence of a complex system of defects and phase transformations caused by irradiation. The authors of [29-32] drew attention to the collective character of the macro-scale processes in such materials. The formation of spatio-temporal dislocation inhomogeneities, dislocation channels, the moving Chernov-Luders lines, the dynamic self-wave structures (the Danilov-Zuev relaxation waves, the phase transformation front in the dislocation-vacancy ensemble etc.) may be caused namely by macroscopic processes. The self-organization of structural transformation under the action of external factors demonstrates the nonlocal properties caused most likely by the large scale instabilities. Note that in some cases the experimental and calculated data also point to the fact that local defects and disorders may be a result of imperfection in a large scale packing, occurring in particular when the system selects the characteristic scaling with broken geometric orientation on the structural elements.

Developed phenomenological approaches which allows to describe the dynamics of macroscopic characteristics

with acceptable degree of accuracy but nevertheless qualitatively (see, e.g. [33,34]) could not adequately represent the microscopic description of the processes. The statistical models, which use the probabilistic characteristics of the process of interaction between the individual elements (particles of dust, fragments-crystallites, etc.) of the medium [35-37] allowed to estimate the time to process equilibrium only qualitatively. The dynamics of non-stationary processes could not be always identified under such consideration. In order to calculate the stable states, the collection of techniques is commonly used known as renormalization procedure. This procedure allows reduction of the large number of interactions (diagrams) to an integral or a small number of interactions. However, some assumption and simplifications should be used at this for classic (see the so-called, S-theory [22, 38-39]) as well as for quantum systems [40-42].

With the development of the computing power the direct methods of simulation became more popular such as descriptions of structurization dynamics on microscopic level, the use of computing procedures for detailed description of structural transformations [43-44]. However, the weak point of such direct computational methods is a necessity to use a very large number of interacting elements with a set of short-range and long-range interactions between them. Besides, the temporal and spatial horizons of interaction are often not fully specified. This leads to the large number of the dynamic equations, and the accounting of interactions increases the dimension of the task.

It is therefore understandable the wish of researchers to find such mathematical models of structurization based on simple physically transparent principles which would be able to select the most essential types of interaction, i.e. select the dominant symmetries of the system and to simplify the model for its practical use in simulation modeling. The models of spatial structure formation were considered by many researches, which main ideas can be found in monographs [45-48]. However, of main interest, as it was pointed in [49], are the dynamical models, which could be described by differential equations in partial derivatives, the mathematical apparatus of the analysis of which is well developed. The special attention should be attended to the models that are capable to describe the imperfect quasi-periodic systems, quasi-crystals (that is characterized by a long-range order and symmetry inadmissible in a classical crystallography [50,51]).

In the opinion of the authors [49], the rational procedure of design of new materials should start with “selection or construction of basic nonlinear models relevant to phenomena of different physical or other origins and, moreover, design of key experiments for verification of *a priori* hypotheses that these models are universal”. Developing the simulation models, it is useful to bring changes into the well-known universal equations and generalize their representations. Even H. Poincaré noted that “equations must teach us, primarily, what we can and what we should change in them”. For specific implementation of these tasks, it is useful to apply the approximate methods based on small parameters, and to use actively the numerical modeling for investigation not only the particular solutions, but mainly in order to discover the nature of the considered phenomena itself, for a formulation of constructive prompts to experimentalists and technologists.

1.2. Choice of models and research methods

Often quite sufficient effective method of the description of quasiperiodic structures is the expansion of perturbations in terms of the orthogonal spatial eigenmodes interacting with each other. All spatial patterns arising in this system will be a result of the linear interference of these modes and under the action of non-equilibrium (pumping) the interference may be considered as stimulated [52]. The nonlinearity of the medium manifests itself in slow evolution of these eigenmodes due to interaction between themselves and with the pumping. The summation over the spectrum of the eigenmodes with appropriate weight gives a possibility to study the process of formation of spatial structures and the diverse forms of spatial derangements (structure imperfections or defects) and even cardinal structure rearrangement (structural-phase transformations). In particular, it was observed a periodic track of defects [53] when considering the periodic spatial perturbations with the spectrum consisting of a small number of modes (for instance, see [54]). The quasi-crystalline spatial structure in turn is often appears due to presence of several incommensurate harmonicas in the spatial spectrum or in non-one-dimensional case due to existence of harmonicas, angles between wave vectors of which are rather random or they correspond to the irrational values (for instance, see, [55]). This fact brings up an association with the Landau – Hopf model of turbulence, that represents a development of a disorder via an excitation of a large number of freedom degrees [56,57] (that is, quasiperiodic "winding" on the multidimensional torus [58]).

The quadratic nonlinearity together with a certain choice of initial conditions often brings into existence the propagating fronts. It is possible when the perturbations lie within a sufficiently broad annular spectrum zone of some radius in $\vec{k}$-space (the reverse character scale). The existence of minima in the perturbation spectrum intermodal potential makes possible the formation of stable or metastable structures. The narrower the annular the more sharp the spatial structure that demonstrates a long-range order. By the way, the small width of the spectrum of growing spatial modes provides a long-range order even in the absence of minima of the interaction potential in real space, at least on a scale inversely proportional to the spectrum width. The selection of initial conditions can provide a formation of a spatial structure firstly in some bounded space and its further expansion over the periphery of this area. For description of these phenomena that were found at first in numerical simulation of models similar to the Swift – Hohenberg model [59] (for example see also, [60]) there are enough methods of the standard analysis of the equations of mathematical physics. But using of other methods and approaches seems to be also useful.

So, in particular, the imperfect structures can be characterized by various structural and scaling parameters, for example by Lyapunov, Hausdorff or fractal dimension [61]. Generally speaking, any signal which is generated by a real source or simulative dynamic system has a finite set of objects with finite dimension. At the same time, the signals generated by fluctuations in the systems with very large number of constituting elements, can be characterized by a very high dimension (in this sense the dimension of the idealized white noise is infinite). The dimension of the structure is capable to change in time during its evolution [49], and only the approaching to the attractor allows to see the long-living scales and configuration state of the system. It must be kept in mind however that dimensions and scales in different spaces (including phase spaces) where the dynamic system is considered can be different. Therefore it is rationally to discuss the real space only where the structure (a straight or curved line, a plane or surface, a three-dimensional formation) is implemented. As for slowly evolving structures, the observer can face a necessity of studying of the intermediate quasiperiodic metastable states, which in most cases can be similar to quasicrystals or other structures with similar properties [50,51].

Until recently, in models based of the differential and integration-differential equations, the main attention was paid to structurally phase transitions of the first order which result in formation of the regular structures from previously amorphous state [49]. The authors [27] have drawn attention to a possibility of structural-phase transitions of second order (structural transformations) in such models, as was proved afterwards in [28].

1.3. The Proctor-Sivashinsky model for description of pattern formation in a thin layer of liquid or gas

The Proctor-Sivashinsky model is found to be very attractive [62,63] for studying the processes of pattern formation in systems which possess a preferred characteristic spatial scale of interaction between quasi-particles or elements of future structure. This model was developed for description of the convection in a thin layer of liquid with poorly conducting heat boundaries. Authors of [64] have found the stationary solutions with a small number of the spatial modes one of which (convective cells) was steady and the second one (convective rolls) turned out to be unstable. A special future of the model is that it forces a preferred spatial scale of interaction, leaving for the system's evolution an opportunity to select the symmetry. It was found the type of symmetry and hence the characteristics of the structure are determined by the minima of the potential of interaction between modes with equal absolute wavenumber value. Modifying the structure of intermodal coupling potential within the framework of the generalized Proctor-Sivashinsky model, it is possible to change the symmetry of steady solutions [64] with changing the number of the potential minima. Below, we show that changing the amplitude of the minima also effects on the dynamics of structure and phase transformations in this system. The authors of [64] restricted themselves by studying of stationary states and the analysis of their linear stability (i.e. stability to small perturbations) and didn't consider the dynamics of structural transitions. Therefore, they didn't discuss a possibility to change a value of a minimum of interactional potential.

The Proctor-Sivashinsky model allows further development and a short time later the generalized Proctor-Sivashinsky-Pismen model [65] was formulated which includes the inertial effects and consider the poloidal vortices inside a thin layer. This model, as was shown by further researches, allows to describe correctly a process of transformation of the energy of toroidal Proctor-Sivashinsky vortices (which forms the periodic structure) into the energy of large-scale poloidal vortex motion [66, 67]. This phenomenon of the "hydrodynamic dynamo" is may be responsible for formation of large-scale vortices in convective layers, in particular in the atmosphere of planets. However even in the Proctor-Sivashinsky model not all processes and the phenomena were studied.

The detailed analysis of instability leading to formation of the quasi-stationary structure – convective rolls will be presented below. The model [27] with use of the multimode description allowed to find out that at first the quasi-stable long-living state (the curved quasi-one-dimensional convective rolls) arises. And later after a lapse of time (which is considerably greater than the reverse linear increment of the process), the system transforms to the stable state (square convective cells). The detailed treatment of the Proctor – Sivashinsky model [28,68] presented below have shown that this structural transition demonstrates all the characteristics of second order phase transition (the continuity of the sum of squared mode amplitudes over the spectrum $I = \sum_j a_j^2 \equiv \sum_{k_j} |\, a_{k_j} \,|^2$ or that the same, the continuity of density of this value and discontinuity of its time derivative $\partial I / \partial t$). The important problem discussed in this paper is the determination of level of imperfection of originating regular structures and also the searching for a correlation between integral spectral characteristics and a fraction of defective cells in the originating structure. The deficiency of structures appears, in particular, in the intermediate, transient regimes and is caused by stimulated (due to non-equilibrium) interference of growing modes [52]. In the case of the external influence, the noise is able to support the number of weak spatial modes which were suppressed before and which interference with dominating modes is also capable to provide the interference pattern corresponding to the imperfect spatial lattice. The understanding of processes which lead to violations of spatial periodicity of structures, would allow estimating the level of structures imperfection by their spatial spectrum that can be quite possible measured experimentally. Especially, it should be clarified the influence of external noise on stability of states and structural-phase transitions.

It has been just the existence of the preferred scale (the distances between the regular spatial perturbations) and a possibility of selection of the required steady symmetry (the regular spatial configuration) motivate the interest to this physical model, especially for description of processes in solid state physics where the characteristic distance between elements of spatial structures (atoms, molecules) in their condensed state is almost invariable. This model, as it turned

out, is capable to describe not only the nature of pattern formation including with local spatial defects, but also simulate the dynamics of second order phase transitions in a two-dimensional case.

It is also shown below that the intermediate states with broken short-range order, but saving a long-range order can be a result of structural-phase transitions (second order phase transitions) and demonstrate the same formation dynamics, as the regular spatial structures.

Of some interest is the evolution of the secondary modulation instability of the convective cells, which results in formation of a self-similar structure - the convective cells of various scales [27], and also in generation of large-scale poloidal vortices [66, 67]. This phenomenon, which was previously investigated for irregular models (see detailed review [25]), come about from modulation instability of the regular convective structure of finite amplitude, as was predicted earlier by S.S. Moiseev.

The objective in this work is to understand the mechanisms of formation of spatial convection structures. The dynamics and nature of structural phase transitions between structures of different topology are considered in details. We study the development of secondary instability, which leads to generation of large-scale patterns, known as the hydrodynamic dynamo effect. Besides the regular periodic structures, we also analyze the imperfect patterns i.e. the structures with implemented spatial defects.

2. RAYLEIGH-BENARD CONVECTION

2.1. Main equations

Thermal convection in a thin horizontal layer of fluid heated from below can be represented by equations of hydrodynamics and thermal conduction in the Boussinesq approximation [69]

$$\mathrm{Pr}^{-1}\left(\frac{\partial \vec{u}}{\partial t}+(\vec{u}\nabla)\vec{u}\right)=-\frac{\nabla p}{p}+\Theta\vec{z}+\nabla^2 u \tag{2.1}$$

$$\left\{\frac{\partial}{\partial t}+(\vec{u}\nabla)\right\}\Theta=Ra(\vec{z}\vec{u})+\nabla^2\Theta \tag{2.2}$$

$$\nabla\vec{u}=0 \tag{2.3}$$

with the boundary conditions, for example, at the solid boundary $u_z=\partial u_z/\partial z=0$. Here $\vec{z}$ is the unit vector directed against the gravity force, $\vec{u}$ is the velocity vector, p and Θ are the pressure and the temperature deviation from equilibrium (varies linearly) correspondingly, g is the gravity acceleration.

Consider the derivation of the Proctor-Sivashinsky equation, which describes the convection in a thin liquid layer with a weakly conductive heat the walls, following to [63]. Here the value of Prandtl number $\mathrm{Pr}=\nu/\chi$ is taken to be infinity. Due to buoyancy convection in a liquid or a gas (at the appropriate scales of processes) can be represented by the following equations for the dimensionless temperature θ and stream function ψ [63].

$$\frac{\partial\theta}{\partial t}+\frac{\partial\psi}{\partial y}\frac{\partial\theta}{\partial x}-\frac{\partial\psi}{\partial x}\frac{\partial\theta}{\partial y}+\frac{\partial\psi}{\partial x}=\nabla^2\theta \tag{2.4}$$

$$Ra\frac{\partial\theta}{\partial x}=\nabla^4\psi \tag{2.5}$$

The range of the spatial parameters

$$-\infty<x<\infty,\ \ 0<y<1. \tag{2.6}$$

For a layer between two planes boundary conditions take the form

$$\psi|_{y=0}=0,\ \ \frac{\partial\psi}{\partial y}|_{y=0}\equiv\psi_y|_{y=0}=0,\ \ \frac{\partial\theta}{\partial y}|_{y=0}-b\theta|_{y=0}\equiv\theta_y|_{y=0}-b\theta|_{y=0}=0, \tag{2.7}$$

$$\psi|_{y=1}=0,\ \ \frac{\partial\psi}{\partial y}|_{y=1}\equiv\psi_y|_{y=1}=0,\ \ \frac{\partial\theta}{\partial y}|_{y=1}+b\theta|_{y=1}\equiv\theta_y|_{y=1}+b\theta|_{y=1}=0, \tag{2.8}$$

where θ is the dimensionless temperature in terms of the difference between fixed temperature of the bottom plane T_d and the upper surface T_u in the absence of convection; ψ is the dimensionless velocity in units of the thermal diffusivity χ (is equal to the coefficient of thermal conductivity λ, divided by the density of ρ and thermal conductivity C_p) of fluid; coordinates in terms of the layer thickness d, time interval d^2/χ, the Prandtl number $\mathrm{Pr}=\nu/\chi$ is one of the criteria of similarity; the Rayleigh number $\mathrm{Ra}=\sigma g(T_d-T_u)d^3/\nu\chi$ – the number that

determines the behavior of the fluid under the action of a temperature gradient (convection currents arise when this parameter exceeds the threshold value [70]); b is the dimensionless coefficient characterizing the heat transfer between the fluid and the boundary, here it is taken equal to the Bio number $\mathrm{Bi} = \alpha l/\lambda$ – the similarity coefficient for stationary heat exchange between hot or cold body and the environment that is the same on the lower and upper boundaries of the layer; where ν is the kinematic viscosity (dynamic viscosity of the kinematic, multiplied by the density), σ here is the coefficient of thermal expansion of the liquid, α is the coefficient of heat transfer from the surface to the environment, λ is the thermal conductivity, l is the characteristic distance.

The convection flows arise when the Rayleigh number Ra_c exceeds some threshold value

$$Ra = Ra_c(1+\varepsilon), \tag{2.9}$$

where we assume

$$\varepsilon << 1 \tag{2.10}$$

We assume also the small heat loss through the walls, that is

$$b = \varepsilon^2 \cdot \beta, \tag{2.11}$$

and use the following traditional [63] scaling for spatial and temporal variables

$$\xi = x\sqrt{\varepsilon}, \tag{2.12}$$

$$\eta = y, \tag{2.13}$$

$$\tau = \varepsilon^2 t. \tag{2.14}$$

2.2. Selection of scaling

The choice of scaling (2.12) - (2.14) is based on the analysis of satisfying the boundary conditions of the linear problem (2.4) - (2.8) and can be argued as follows. Let seek the solution in the form

$$\theta = h(y)\cdot\exp\{\Omega t + iKx\} \tag{2.15}$$

$$\psi_x = v(y)\cdot\exp\{\Omega t + iKx\} \tag{2.16}$$

Now, the boundary value problem for these functions takes the form

$$\Omega h = h_{yy} + K^2 h - v = 0, \tag{2.17}$$

$$v_{yyyy} + 2K^2 v_{yy} + K^4 v - Ra\cdot K^2 h = 0, \tag{2.18}$$

$$h_y|_{y=0} = bh|_{y=0}, \quad v_y|_{y=0} = v|_{y=0} = 0, \tag{2.19}$$

$$h_y|_{y=1} = -bh|_{y=1}, \quad v_y|_{y=1} = v|_{y=1} = 0. \tag{2.20}$$

In order to find the dependence $\Omega = \Omega(K)$ we use the Bubnov–Galerkin method, for which propose it is necessary to determine the basis functions satisfying the boundary value problem. For example, the authors [63] recommend the using of

$$v(y) = Ay^2(1-y)^2, \tag{2.21}$$

$$h(y) = B(by^2 - by - 1), \tag{2.22}$$

Then we must substitute (2.21) and (2.22) into the left side of (2.17) (2.18). Result of the substitution (discrepancy) must be orthogonal basis functions, that is received two expressions must be multiplied respectively by the functions $(by^2 - by - 1)$ and $y^2(1-y)^2$ and integrate over y from zero to one and put result of integration equal to zero, which gives a system of two equations

$$A\left\{\frac{4}{5} + \frac{4}{105}K^2 + \frac{1}{610}K^4\right\} + B\left\{Ra\cdot K^2\left(\frac{b}{140} + \frac{1}{30}\right)\right\} = 0 \tag{2.23}$$

$$A\left\{\frac{b}{140}+\frac{1}{30}\right\}+B\left\{2b+\frac{b^2}{3}+\left(\Omega+K^2\right)\left(\frac{b^2}{30}+\frac{b}{3}+1\right)\right\}=0 \tag{2.24}$$

At first, we find the stability threshold for steady state, assuming $\Omega=0$ and keeping only the terms proportional to K^2. Then, one obtains for Ra

$$Ra=720+\frac{240}{7}K^2+1440\frac{b}{K^2}. \tag{2.25}$$

In the absence of convection $\mathrm{Ra}_c=720$. For the case of $\Omega\neq 0$, the dispersion equation $\Omega=\Omega(K)$ can be obtained from the requirement on non-triviality of solution of the system (2.23) - (2.24)

$$\Omega=\left(\frac{Ra-Ra_c}{Ra_c}\right)K^2-\frac{1}{21}K^4+2b. \tag{2.26}$$

As $\left(\mathrm{Ra}-\mathrm{Ra}_c\right)/\mathrm{Ra}_c\propto\varepsilon$, $b\propto\varepsilon^2$, the dependences of other variables from ε can be easily restored, e.g. $\Omega\propto\varepsilon^2$, $K\propto\sqrt{\varepsilon}$ that allows to select the desired scaling. Let assume in following that the nonlinear problem has the same scaling.

Note that $\psi\propto\theta\sqrt{\varepsilon}$ as follows from (2.5), and then we assume for convenience

$$\Theta(\xi,\eta,\tau,\varepsilon)=\theta(x,y,t,\varepsilon), \tag{2.27}$$

$$\Psi(\xi,\eta,\tau,\varepsilon)=\sqrt{\varepsilon}\cdot\psi(x,y,t,\varepsilon). \tag{2.28}$$

Now, in the new variables and notation the problem can be written as

$$\varepsilon^2\frac{\partial\Theta}{\partial\tau}+\varepsilon\frac{\partial\Psi}{\partial\eta}\frac{\partial\Theta}{\partial\xi}-\varepsilon\frac{\partial\Psi}{\partial\xi}\frac{\partial\Theta}{\partial\eta}+\varepsilon\frac{\partial\Psi}{\partial\xi}=\varepsilon\frac{\partial^2\Theta}{\partial\xi^2}+\frac{\partial^2\Theta}{\partial\eta^2}, \tag{2.29}$$

$$Ra_c\cdot(1+\varepsilon)\frac{\partial\Theta}{\partial\xi}=\varepsilon^2\frac{\partial^2\Psi}{\partial\xi^2}+2\varepsilon\frac{\partial^2\Psi}{\partial\xi\cdot\partial\eta}+\frac{\partial^2\Psi}{\partial\eta^2}, \tag{2.30}$$

$$\Psi|_{\eta=0}=0,\qquad \frac{\partial\Psi}{\partial\eta}|_{\eta=0}\equiv\Psi_\eta|_{\eta=0}=0,..\frac{\partial\Theta}{\partial\eta}|_{\eta=0}-\varepsilon^2\beta\cdot\Theta|_{\eta=0}\equiv\Theta_\eta|_{\eta=0}-\varepsilon^2\beta\cdot\Theta|_{\eta=0}=0 \tag{2.31}$$

$$\Psi|_{\eta=1}=0,\ \frac{\partial\Psi}{\partial\eta}|_{\eta=1}\equiv\Psi_\eta|_{\eta=1}=0,..\frac{\partial\Theta}{\partial\eta}|_{\eta=1}-\varepsilon^2\beta\cdot\Theta|_{\eta=1}\equiv\Theta_\eta|_{\eta=1}-\varepsilon^2\beta\cdot\Theta|_{\eta=1}=0 \tag{2.32}$$

Let's integrate (2.29), using the identity

$$\Theta_\eta\Psi_\xi-\Theta_\xi\Psi_\eta=\left(\Theta\Psi\right)_{\xi\eta}-\left(\Theta_\eta\Psi\right)_\xi-\left(\Theta\Psi_\xi\right)_\eta \tag{2.33}$$

and the boundary conditions (2.31) and (2.32).

$$\varepsilon\frac{\partial}{\partial\tau}\int_0^1 d\eta\cdot\Theta-\frac{\partial}{\partial\xi}\int_0^1 d\eta\cdot\Theta_\eta\Psi+\frac{\partial}{\partial\xi}\int_0^1 d\eta\cdot\Psi=\frac{\partial^2}{\partial\xi^2}\int_0^1 d\eta\cdot\Theta-\beta\varepsilon\left(\Theta|_{\eta=0}+\Theta|_{\eta=1}\right), \tag{2.34}$$

2.3. The hierarchy of approximations

It is appropriate to seek the solution of (2.29) - (2.32) in the form of series

$$\Psi=\Psi^{(0)}+\varepsilon\cdot\Psi^{(1)}+\varepsilon^2\cdot\Psi^{(2)}+\ldots, \tag{2.35}$$

$$\Theta=\Theta^{(0)}+\varepsilon\cdot\Theta^{(1)}+\varepsilon^2\cdot\Theta^{(2)}+\ldots. \tag{2.36}$$

In the zero-order approximation

$$\Theta_{\eta\eta}{}^{(0)}=0, \tag{2.37}$$

$$\Psi_{\eta\eta\eta\eta}{}^{(0)} = Ra_c \cdot \Theta_{\xi}{}^{(0)}, \tag{2.38}$$

$$\Psi^{(0)}|_{\eta=0} = 0, \ \Psi_{\eta}{}^{(0)}|_{\eta=0} = 0, \ \Theta^{(0)}{}_{\eta}|_{\eta=0} = 0, \tag{2.39}$$

$$\Psi^{(0)}|_{\eta=1} = 0, \ \Psi_{\eta}{}^{(0)}|_{\eta=1} = 0, \ \Theta^{(0)}{}_{\eta}|_{\eta=1} = 0 \tag{2.40}$$

Thus,

$$\Theta^{(0)} = F(\xi,\tau), \tag{2.41}$$

$$\Psi^{(0)} = \frac{1}{24} Ra_c \cdot F_{\xi}\left(\eta^4 - 2\eta^3 + \eta^2\right). \tag{2.42}$$

For the zero-order approximation Eq. (2.34) takes the form

$$-\frac{\partial}{\partial\xi}\int_0^1 d\eta \cdot \Theta^{(0)}{}_{\eta}\Psi^{(0)} + \frac{\partial}{\partial\xi}\int_0^1 d\eta \cdot \Psi^{(0)} = \frac{\partial^2}{\partial\xi^2}\int_0^1 d\eta \cdot \Theta^{(0)}, \tag{2.43}$$

Substituting (2.41) (2.42) to (2.43) we can see that a certain critical value of the Rayleigh number

$$\left(Ra_c - 720\right) \cdot F_{\eta\eta} = 0. \tag{2.44}$$

The next approximation gives following

$$\frac{\partial\Psi^{(0)}}{\partial\eta}\frac{\partial\Theta^{(0)}}{\partial\xi} - \frac{\partial\Psi^{(0)}}{\partial\xi}\frac{\partial\Theta^{(0)}}{\partial\eta} + \frac{\partial\Psi^{(0)}}{\partial\xi} = \frac{\partial^2\Theta^{(0)}}{\partial\xi^2} + \frac{\partial^2\Theta^{(1)}}{\partial\eta^2}, \tag{2.45}$$

$$Ra_c \cdot \frac{\partial\Theta^{(0)}}{\partial\xi} + Ra_c \cdot \frac{\partial\Theta^{(1)}}{\partial\xi} = 2\varepsilon\frac{\partial^4\Psi^{(0)}}{\partial\xi^2 \cdot \partial\eta^2} + \frac{\partial^4\Psi^{(1)}}{\partial\eta^4}, \tag{2.46}$$

$$\Psi^{(1)}|_{\eta=0} = 0, \ \Psi_{\eta}{}^{(1)}|_{\eta=0} = 0, \ \Theta^{(1)}{}_{\eta}|_{\eta=0} = 0, \tag{2.47}$$

$$\Psi^{(1)}|_{\eta=1} = 0, \ \Psi_{\eta}{}^{(1)}|_{\eta=1} = 0, \ \Theta^{(1)}{}_{\eta}|_{\eta=1} = 0, \tag{2.48}$$

Using the zero-order approximation, for the first approximation we obtain expressions

$$\Theta^{(1)} = G(\xi,\eta) + F_{\xi}^2\left(6\eta^5 - 15\eta^4 + 10\eta^3\right) + \frac{1}{2}F_{\xi\xi}\left(2\eta^6 - 6\eta^5 + 5\eta^4 - \eta^2\right), \tag{2.49}$$

$$\begin{aligned}\Psi^{(1)} &= \frac{10}{7}F_{\xi}F_{\xi\xi}\left(2\eta^9 - 9\eta^8 + 12\eta^7 - 20\eta^3 + 15\eta^2\right) + \\ &+ \frac{1}{14}F_{\xi\xi\xi\xi}\left(2\eta^{10} - 9\eta^9 + 15\eta^8 - 42\eta^6 + 84\eta^5 - 70\eta^4 + 20\eta^3 + \eta^2\right) + \\ &+ 30F_{\xi}\left(\eta^4 - 2\eta^3 + \eta^2\right) + 30G_{\xi}\left(\eta^4 - 2\eta^3 + \eta^2\right).\end{aligned} \tag{2.50}$$

Meanwhile, the integral (2.43)

$$\begin{aligned}&\frac{\partial}{\partial\tau}\int_0^1 d\eta \cdot \Theta^{(0)} - \frac{\partial}{\partial\xi}\int_0^1 d\eta \cdot \left(\Theta^{(1)}{}_{\eta}\Psi^{(0)} + \Theta^{(0)}{}_{\eta}\Psi^{(1)}\right) + \frac{\partial}{\partial\xi}\int_0^1 d\eta \cdot \Psi^{(1)} = \\ &= \frac{\partial^2}{\partial\xi^2}\int_0^1 d\eta \cdot \Theta^{(1)} - \beta\left(\Theta^{(0)}|_{\eta=0} + \Theta^{(0)}|_{\eta=1}\right)\end{aligned} \tag{2.51}$$

Substituting the expressions for zero and first approximation, we can find the equation for $F(\xi,\eta)$

$$\frac{\partial F}{\partial\tau} + \frac{17}{462}\frac{\partial^4 F}{\partial\xi^4} + \frac{\partial}{\partial\xi}\left[\left(1 - \frac{10}{7}\left(\frac{\partial F}{\partial\xi}\right)^2\right)\frac{\partial F}{\partial\xi}\right] + 2\beta F = 0 \tag{2.52}$$

which is symmetrical with respect to change the sign F (By the way, the equations (2.1) - (2.5) has symmetry while simultaneously changing the sign y θ, ψ, y). In addition, the equation has not diffusion term $\propto \partial^2 F / \partial \xi^2$.

Table 1.

The correspondence of used variables and their real physical values

Physical quantity	Representation of explicit view
Temperature $T\left(x\sqrt{\varepsilon}, y\right)$	$T_d + \left(T_d - T_u\right)\left(-y + F(x\sqrt{\varepsilon}, y\right)$
Horizontal velocity ψ_y	$60\sqrt{\varepsilon} \cdot F_{x\sqrt{\varepsilon}} \cdot \left(2y^3 - 3y^2 + y\right)$
Vertical velocity $-\psi_x$	$-30\varepsilon \cdot \left(F_{x\sqrt{\varepsilon}}\right)_{x\sqrt{\varepsilon}} \cdot \left(y^4 - 2y^3 + y^2\right)$

where $\xi = x\sqrt{\varepsilon}$, $\eta = y$, $Ra = Ra_c\left(1+\varepsilon\right)$.

2.4. Accounting for temperature dependence of viscosity

Equation (2.4) in this case takes the form

$$Ra\frac{\partial \theta}{\partial x} = \left(\nu\psi_{xx}\right)_{xx} + 2\left(\nu\psi_{xy}\right)_{xy} + \left(\nu\psi_{yy}\right)_{yy}, \tag{2.53}$$

where ν is the temperature-dependent viscosity, normalized, as noted above. Moreover, to simplify the model, we set this dependence is sufficiently weak

$$\nu = 1 + \varepsilon \cdot \mu \cdot \left(0.5 - \eta + \theta\right) \tag{2.54}$$

where the terms $-\eta + \theta$ takes into account the temperature perturbations in the vertical direction and μ is the numerical coefficient of the order of one. Equation (2.52) will undergo some changes

$$\frac{\partial F}{\partial \tau} + \frac{17}{462}\frac{\partial^4 F}{\partial \xi^4} + \frac{\partial}{\partial \xi}\left[\left(1 - \mu F - \frac{10}{7}\left(\frac{\partial F}{\partial \xi}\right)^2\right)\frac{\partial F}{\partial \xi}\right] + 2\beta F = 0 . \tag{2.55}$$

2.5. The Proctor-Sivashinsky equation

Applying the following notation

$$F = \varphi \cdot \sqrt{17/660}\ ,\ \beta = a \cdot \sqrt{231/68}\ ,\ \mu = \gamma \cdot \sqrt{165/17}\ ,\ \xi = \zeta \cdot \sqrt{17/231}\ ,\ \tau = \mathrm{T} \cdot \sqrt{34/231}\ , \tag{2.56}$$

we obtain the Proctor-Sivashinsky equation having regard the temperature dependence of the viscosity in the one-dimensional case

$$\frac{\partial \varphi}{\partial T} + \frac{\partial^4 \varphi}{\partial \zeta^4} + \frac{\partial}{\partial \zeta}\left[\left(2 - \gamma\varphi - \left(\frac{\partial \varphi}{\partial \zeta}\right)^2\right)\frac{\partial \varphi}{\partial \zeta}\right] + a\varphi = 0 . \tag{2.57}$$

It should be noted, that the equation contains the nonlocal quadratic nonlinearity $-\gamma\frac{\partial}{\partial \zeta}\left(\varphi\frac{\partial \varphi}{\partial \zeta}\right)$ due to the dependence of viscosity on temperature with the layer height, and the nonlocal cubic nonlinearity in the form of $\frac{\partial}{\partial \zeta}\left[\left(\frac{\partial \varphi}{\partial \zeta}\right)^2\frac{\partial \varphi}{\partial \zeta}\right]$.

In two-dimensional geometry, Eq. (2.57) takes the form

$$\frac{\partial \varphi}{\partial T} + \nabla^4\varphi + \nabla\left[\left(2 - \gamma\varphi - \left(\nabla\varphi\right)^2\right)\nabla\varphi\right] + a\varphi = 0 , \tag{2.58}$$

where the two-dimensional operator $\nabla\varphi = \vec{i} \cdot \frac{\partial \varphi}{\partial \zeta} + \vec{j} \cdot \frac{\partial \varphi}{\partial \vartheta}$ with unitary orthogonal vectors $\vec{i}$ and $\vec{j}$ oriented in the plane of the medium division (ζ, ϑ).

If the temperature dependence of the viscosity can be neglected $\gamma = 0$, the model, commonly referred as the Proctor-Sivashinsky model, contains just a nonlocal cubic nonlinearity $\nabla\left[(\nabla\varphi)^2 \nabla\varphi\right]$

$$\frac{\partial\varphi}{\partial T} + \nabla^4\varphi + \nabla\left[\left(2 - (\nabla\varphi)^2\right)\nabla\varphi\right] + a\varphi = 0\,. \tag{2.59}$$

This equation can be written as

$$\frac{\partial\varphi}{\partial T} = -\frac{\delta F[\varphi]}{\delta\varphi} \tag{2.60}$$

where $\delta F[\varphi]/\delta\varphi$ is the variation derivative of the functional

$$F[\varphi] = -\int d\zeta \cdot d\vartheta \cdot \left\{(\nabla\varphi)^2 - \frac{1}{4}(\nabla\varphi)^4 - \frac{1}{2}\left(\nabla^2\varphi\right)^2 - \frac{a}{2}\varphi^2\right\} \tag{2.61}$$

Th particular feature of this model is that it describes as the Marangoni convection and convection in a layer with one free boundary [63].

3. ANALYSIS OF THE SIMPLIFIED SWIFT-HOHENBERG MODEL

3.1. Instability regimes

Consider the Proctor-Sivashinsky equation with the temperature dependence of viscosity in one dimension case. Equation (2.58) can be rewritten as

$$\frac{\partial\varphi}{\partial T} + (a-1)\varphi + \left(1 + \frac{\partial^2}{\partial\zeta^2}\right)^2 \varphi - \gamma\frac{\partial}{\partial\zeta}\left(\varphi\frac{\partial\varphi}{\partial\zeta}\right) - \frac{\partial}{\partial\zeta}\left[\left(\frac{\partial\varphi}{\partial\zeta}\right)^2 \frac{\partial\varphi}{\partial\zeta}\right] = 0\,. \tag{3.1}$$

Let assume the dependence of φ on coordinates as $\varphi \propto \exp\{ik_0\zeta\}$ and $k_0 \approx 1$, $e = (1-a)$ since we consider only the weak above-threshold case $|e| << 1$. Indeed, for any deviation from unity of the wave number perturbation amplitude decrease rapidly. The equation (3.1) takes the form

$$\frac{\partial\varphi}{\partial T} = e\varphi - \left(1 + \frac{\partial^2}{\partial\zeta^2}\right)^2 \varphi - 2\gamma\varphi^2 + 3\varphi^3 \tag{3.2}$$

The growth of the instability $\varphi \propto \exp(\mathrm{Im}\,\omega T)$ happens with the growth rate $\mathrm{Im}\,\omega \approx e - (k^2-1)^2$. For $\gamma > 0$ the gas (this corresponds to the gas convection) flows up to the center of the cell, for $\gamma < 0$ (which corresponds to the movement of the liquid) the liquid flows outside and down from the center of the cell.

The perturbations with wave vectors in the vicinity of the unit are unstable, that is,

$$1 - e < |k| < 1 + e \tag{3.3}$$

3.2. Swift-Hohenberg model

Equation (3.2) is called the Swift – Hohenberg equation [59].

The parameter $\gamma < 0$ determines for convection the instability threshold. So when $e < 0$, the subthreshold (subcritical) growth of perturbations is possible only for perturbation amplitudes exceeding the threshold

$$\varphi_{thr} = -\frac{2|\gamma|}{6} + \sqrt{\frac{4\gamma^2}{36} + \frac{|e|}{3}} \tag{3.4}$$

Despite of some unacceptable (from the point of view of strict approach) assumptions, it has been possible to obtain from this equation a number of interesting and relevant effects observed in experiments.

In the one dimension case, (3.2) can be written in gradient form with the Lyapunov potential (free energy functional):

$$F[\varphi] = -\int d\zeta \cdot \left\{-\frac{2|\gamma|}{\sqrt{3}}\varphi^3 + \frac{1}{4}\varphi^4 + \frac{1}{2}\left(1 + \frac{\partial^2}{\partial\xi^2}\right)^2 \varphi^2 - \frac{\varepsilon}{2}\varphi^2\right\}. \tag{3.5}$$

Note that

$$\frac{\partial}{\partial T}F[\varphi]=-\int d\zeta\cdot\frac{\partial}{\partial T}\left\{-\frac{2|\gamma|}{\sqrt{3}}\varphi^3+\frac{1}{4}\varphi^4+\frac{1}{2}(1+\frac{\partial^2}{\partial\xi^2})^2\varphi^2-\frac{\varepsilon}{2}\varphi^2\right\}=-\int d\zeta\left(\frac{\partial\varphi}{\partial T}\right)^2<0, \qquad (3.6)$$

If the free energy functional has no minima, then the front propagation will be observed as, for example, in the equations describing the reaction of burning. In this case, the free energy functional will be continuosly decreasing until the front approaches the boundary of the medium if it is bounded. An alternative possibility is realized when the free energy functional has minima. There may be many such minima. Each minimum corresponds to an equilibium state in time (multistability).

The Swift-Hohenberg equation can be generalized to two-dimensional case in the following way

$$\frac{\partial\varphi}{\partial T}=e\varphi-\left(1+\nabla^2\right)^2\varphi-2\gamma\varphi^2+3\varphi^3, \qquad (3.7)$$

or in the gradient form

$$\frac{\partial\varphi}{\partial T}=-\frac{\delta F[\varphi]}{\delta\varphi}, \qquad (3.8)$$

$$F[\varphi]=-\int d\zeta\cdot\left\{-\frac{2|\gamma|}{\sqrt{3}}\varphi^3+\frac{1}{4}\varphi^4+\frac{1}{2}\left(1+\nabla^2\right)^2\varphi^2-\frac{\varepsilon}{2}\varphi^2\right\}. \qquad (3.9)$$

Position of the functional minima determines the stable or quasistable state. Note that extension on two-dimensional case like that of the Swift-Hohenberg equation is incorrect, and justifies this is only a good qualitative agreement between the simulation results and experimental data. Incorrectness seen in the fact, that basic and well-received equation of convection in this case is a multidimensional the Proctor-Sivashinsky equation, which has a non-local quadratic (occurring only with accounting of the temperature dependence of viscosity) and cubic nonlinearity. The transition to local dependence in this case is not formally justified. However, as noted in the introduction to this paper for simulation this modification of equations is useful, because they retain a number of important physical features of the systems and quite simple to describe.

3.3. Dynamics of spatial structure defects

During the formation of stable or quasi-stable structures occurs the violations of regularity, defects. More often occurs point and one-dimensional defects, and last one correspond to the dislocation in imperfect crystal. The dynamics of these defects has been well studied [71, 72]. The mobility of defects has come to the end when a stable state is reached. As this takes place, the defects are comes to rest or disappear. The force acting on the defects associated with the change in the functional (3.9) in the vicinity of its action.

3.4. Development of instabilities

In the above-threshold regime $e>0$, the perturbations of arbitrarily small amplitude become unstable. The bell-shaped initial perturbation begins expansion from its center (Fig.1). If the functional has a minimum that we can observe the formation of a periodic structure behind the propagating front which can be considered as the structurization front. Similar processes of structure formation is typical for the first-order phase transitions.

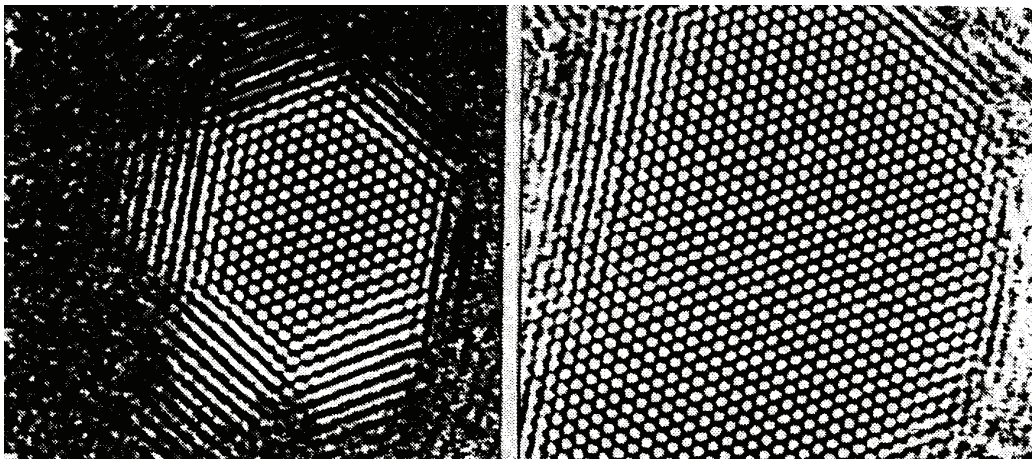

Fig. 1. Experiment. Thermal convection in a thin layer of gaseous CO_2 [73,49]. Growth of hexagonal crystal lattice in the above-threshold mode (figure on the right corresponds to a later time)

In the subthreshold regime $e < 0$ only perturbations of finite amplitude (3.4) grow, which leads either to formation of a localized perturbation region, if the functional has no minimum, or to the formation of structurization region of finite size, if the functional has minima (Fig.2).

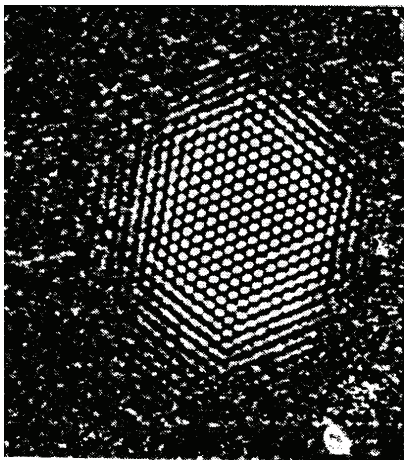

Fig. 2. Experiment. Thermal convection in a thin layer of gaseous CO_2 [73].
Stable localized state in the subthreshold state.

Of particular interest is the growth dynamic of perturbations in the above-threshold regime $e > 0$ for given periodic boundary conditions. In this case, the functional has several minima and it results in arising of expanding areas containing hexagonal cells that simulates Benard-Marangoni convection in a plane layer of liquid heated from below. That is convective rolls (poorly defined metastable structure) quickly decays into hexagonal cells. By the way, the formation of hexagonal structure is caused by existence of fixed scale that requires an equal distance between the maxima and minima of the field correspondingly. In two dimension case, this topology only is possible in an equilateral triangle, set of which generates a hexagon.

It should be noted that results obtained by simulation of the Swift-Hohenberg model and experimental results are demonstrate qualitative agreement despite the fact that after generalization of this model to the two-dimensional case, the non-local nonlinearity in quadratic and cubic term has been replaced by a local one that results in the loss of anisotropy in the cubic nonlinearity. However, these problems were solved in the below discussed Proctor-Sivashinsky model, where the cubic nonlinearity retained the anisotropy.

So, we can conclude that the models of this type demonstrate the behavior, which very close to experimental observations. This is indicative of the physical adequacy of the models, based on the differential and integro-differential equations and their applicability for analysis of a number of physical processes which take place in technical devices.

4. PROCTOR-SIVASHINSKY MODEL TO DESCRIBING INVISCID CONVECTION

4.1. Convection equation including the noise influence

More correct description of convection in a thin layer of liquid or gas with poorly heat conducting boundaries can be carried out within the framework of the Proctor-Sivashinsky model.

As shown below, this model allows detecting the structural-phase transitions which can be identified as second order phase transitions. In addition, if we define the quasi-crystal as a spatial structure with long-range order and broken translational symmetry than one of the metastable states corresponds to this definition. In this case, the structural transitions leading to this state can be also considered as second-order transitions. Namely the analysis of phase structure transitions is being the objective of this work, because the transformation of the spatial structures of all scales (from planetary to microscopic) in the hydro- and gas dynamics is the key problem in the subject area of physical technologies.

Restrict the consideration to the case of the lack of dependence of viscosity on the temperature ($\gamma = 0$). The equation for the temperature field in the horizontal plane (x,y) has the form:

$$\frac{\partial \Phi}{\partial T} = \varepsilon^2 \Phi - \left(1 - \nabla^2\right)^2 \Phi + \frac{1}{3} \nabla \left(\nabla \Phi \left| \Phi \right|^2 \right) + \varepsilon^2 f \,, \tag{4.1}$$

where $\Phi = \theta / \sqrt{3}$, $\varepsilon^2 = e$, f is the random function describing the external noise, and the quantity ε that determines the convection threshold overriding is assumed to be sufficiently small ($0 < \varepsilon < 1$).

We shall search for solution of Eq. (4.1) in the form of series

$$\Phi = \varepsilon \sum_j A_j \exp\left(i \vec{k}_j \vec{r} \right) \tag{4.2}$$

where $|\vec{k}_j|=1$. Substituting $T\varepsilon^2 = t$, we get the mathematical expression of the Proctor-Sivashinsky model for slow amplitudes A_j (with additional term corresponding to the noise):

$$\frac{\partial A_j}{\partial t} = A_j - \sum_{i=1}^{N} V_{ij} \,|\, A_i \,|^2 \; A_j + f \tag{4.3}$$

where the interaction coefficients V_{ij} are defined as follows

$$V_{jj}=1\,, \tag{4.4}$$

$$V_{ij}=(2/3)\left(1-2\left(\vec{k}_i\vec{k}_j\right)^2\right)=(2/3)\left(1+2\cos^2\vartheta\right), \tag{4.5}$$

and ϑ is the angle between vectors $\vec{k}_i$ and $\vec{k}_j$. Here we should note the difference between Eq. (4.3) with interaction potential (4.4)-(4.5) from the two-dimensional Swift-Hohenberg equation, where the cubic nonlinearity has the isotropic but not a vector form which was made from the qualitative considerations.

Expressions (4.1) - (4.5) should be supplemented by the initial values of the amplitudes A_j

$$A_j\,|_{t=0} = A_{j0}\,. \tag{4.6}$$

The instability interval in *k*-space represents a ring with average radius equal to unit and the width is order of relative above-threshold parameter ϵ, i.e. much less than unity. During the development of the instability, the effective growth rate of modes that lies outside of the very small neighborhood near the unit circle will decrease due to the growth of the nonlinear terms and can change sign which will lead to a narrowing of the spectrum to the unit circle in the *k*-space. Since the purpose of further research will be the study of stability of spatial structures with characteristic size of order $2\pi/k \propto 2\pi$ and the important characteristic for visualization of simulation results will be evidence of these structures, so we restrict ourselves by considering some idealized model of the phenomenon, assuming that the oscillation spectrum is already located on the unit circle in the *k*-space.

From the results of preliminary studies [64] it is clear that at least two stationary solutions can exist in the system: the roll structure (Fig. 3a), and the field of square cells (Fig. 3b).

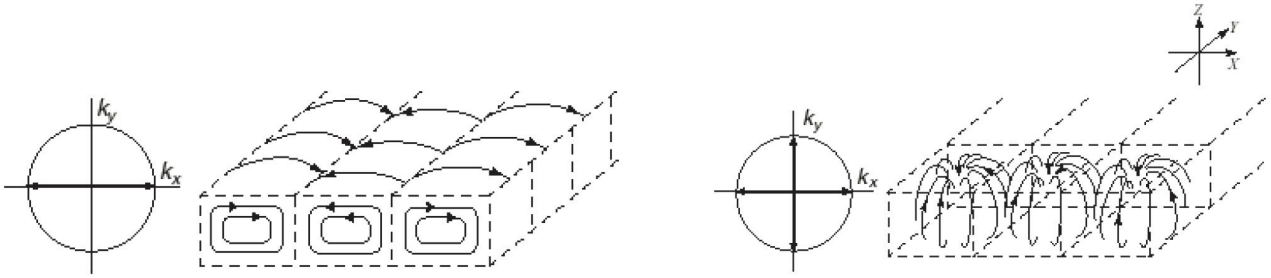

a b

Fig. 3. Convective structures: rolls (a) and square cells (b).

4.2. Linear stability

It follows from Eqs. (4.3)-(4.5) with the initial conditions of the form (4.6) that initial development of the process will be determined by the exponential growth of the spectrum modes with the identical linear growth rate equal to unit in the conventional time scale.

Further growth of unstable modes will slow down due nonlinear terms in Eq.(4.3). The nonlinear growth rate can be written as

$$\left(\mathrm{Im}\,\omega\right)_{NL} = 1-\langle\sum_{i=1}^{N} V_{ij} \,|\, A_i \,|^2\rangle \propto 1-\langle V\rangle\sum_{i=1}^{N} A_i^{\,2}\,, \tag{4.7}$$

and the averaged interaction potential takes the value of

$$\langle V\rangle \propto \frac{4}{3} \tag{4.8}$$

Thus, we can obtain the energy density[1] of perturbation for this «*amorphous state*» at the active stage of the interaction between modes when they are approximately equal in amplitude

$$I = \frac{1}{N}\sum_{i=1}^{N} A_i^2 \approx I_{amor} = \frac{3}{4}. \tag{4.9}$$

4.3. The qualitative Proctor-Sivashinsky model for inviscid convection

We can qualitatively estimate further dynamics of the system. Let introduce the amplitude of the fundamental mode $A_1 = A(\vartheta = 0)$ (assuming it is large enough), as well the intensity of the spectrum near $\vartheta = \pi/2$ in the form of $A_{sp} = \sum_{\vartheta_i \neq \pi/2} A^2(\vartheta_i)$ excluding from this sum the central mode $A_2 = A(\vartheta = \pi/2)$. Thus, we can get from (4.3)-(4.5) the system of equations for these quantities

$$\dot{A}_1^2 = 2A_1^2\left[1 - A_1^2 - \frac{2}{3}A_2^2 - \frac{2}{3}A_{sp}\right], \tag{4.10}$$

$$\dot{A}_2^2 = 2A_2^2\left[1 - \frac{2}{3}A_1^2 - A_2^2 - 2A_{sp}\right] \tag{4.11}$$

$$\dot{A}_{sp} \approx 2A_{sp}\left[1 - \frac{2}{3}A_1^2 - 2A_2^2 - 2A_{sp}\right] \tag{4.12}$$

Dynamics of the spectrum without the central mode $A_2 = A(\vartheta = \pi/2)$ and dynamics of this mode can be described by equations

$$Y' = Y\left(1 - \frac{14}{5}X - Y\right), \quad X' = X\left(1 - X - Y\right), \tag{4.13}$$

where $Y = 14A_{sp}/3$, $X = 5A_2^2/3$, $X' \equiv dX/d\tau$, $\tau = 1.5t$, and for the quantities $I = \frac{1}{N}\sum_j A_j^2$ and $Z = 5A_1^2/3$, is valid relation of $I = \frac{3}{5}\left[X + Z + 5Y/4\right]$ and $Z = \frac{5}{3} - \frac{2}{3}X - \frac{5}{21}Y$, respectively. The result of numerical solution of Eqs.(4.13) is represented in Fig. 4.

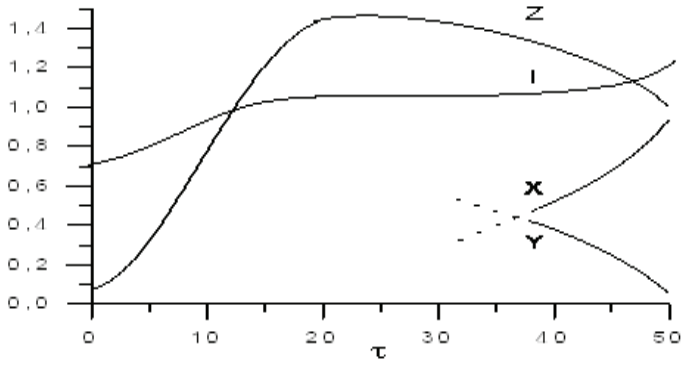

Fig. 4. Dynamics of some parameters during the secondary instability: the spectrum of without the central mode Y, the squared amplitude of the central mode of this spectrum X, squared amplitude of the fundamental mode Z and the integral value $I = \frac{1}{N}\sum_j A_j^2$.

4.4. The mechanism of mode competition

Let us consider the nonlinear growth rate (or damping factor, which depends on the sign of the expression) of each

[1] As $\sum_k |A(k)|^2 = \frac{1}{L}\int_{-L/2}^{L/2} |A(r)|^2\, dr$, where $A(k)$ is the Fourier transform of the function $A(r)$.

mode (obviously $\left(\mathrm{Im}\,\omega\right)_L = 1$)

$$\left(\mathrm{Im}\,\omega\right)_{NL} = 1 - \sum_{i=1}^{N} V_{ij} \mid A_i \mid^2 . \tag{4.14}$$

At the end of the stage of rapid linear growth, the so-called "amorphous" state is established when the nonlinear growth rates become much less than unity, and the process slows down essentially. One of the modes begins to grow due to fluctuation, while suppressing the other modes which nonlinear growth rates become negative. As a result of this competition only one mode from the initial spectrum survives. Then, it turns out that this state is also unstable, that leads to the growth of side spectrum in vicinity of $\vartheta = \pi/2$. This results in the competition among the side modes, which develops in the same scenario and only one leader mode $A_2 = A(\vartheta = \pi/2)$ survives. The fundamental mode $A_1 = A(\vartheta = 0)$ slightly reduces its amplitude, and the mode $A_2 = A(\vartheta = \pi/2)$ increases its amplitude until they align. Each state has different intensity values and has a different topology.

4.5. Accounting of the external noise

In the case of a sufficiently high level of noise, both additive ($f \neq 0$) and multiplicative (a random component proportional to ε^2 in the first term in r.h.s of Eq.(4.1)), the level of modes amplitudes may be rather large from the start of the process. The initial conditions may also provide the starting system state can be considered as highly irregularity “amorphous”, i.e. the perturbation amplitudes are large enough and randomly different from each other. This state can be maintained in the future by random noise. It is important to find out in what noise levels it is possible the "amorphous" state, characterized by a large number of spatial modes can exist for a long time.

Apparently, the very intensive noise is able to keep the system from the formation of convective structures, however, preliminary estimates suggest that the noise of lesser intensity cannot prevent the successive transition to metastable (rolls) and stable (square cells) states. When the noise intensity falls down, the transition from a metastable to stable state can slow down and the system stays (“freezes”) for a long time in the metastable state.

5. RESULTS OF NUMERICAL MODELING

5.1. The mathematical Proctor-Sivashinsky model for inviscid convection

The basic Proctor-Sivashinsky model (4.3)–(4.5) can be represented by the equation

$$\frac{\partial A_j}{\partial t} = A_j - \sum_{i=1}^{N} V_{ij} \mid A_i \mid^2 A_j + f , \tag{5.1}$$

where the coefficients are defined as following

$$V_{jj} = 1 , \tag{5.2}$$

$$V_{ij} = (2/3)\left(1 - 2\left(\vec{k}_i \vec{k}_j\right)^2\right) = (2/3)\left(1 + 2\cos^2\vartheta\right), \tag{5.3}$$

where ϑ is the angle between vectors $\vec{k}_i$ and $\vec{k}_j$. Expressions (2.8) - (2.9) should be supplemented by the amplitudes initial values of the spectrum

$$A_j \mid_{t=0} = A_{j0} . \tag{5.4}$$

The width of the instability interval in *k*-space is the unit circle with a radius $\mid \vec{k}_i \mid = 1$. Let initial values of $\vartheta_s(t=0)$ are distributed uniformly from zero to 2π for each mode and interval should be divided by *N* (this is the number of modes). Then, if we impose zero boundary conditions, the spatial dependence of each of *n*-th mode will be

$$A_{n,m} Sin\left(2\pi n x\right) Sin\left(2\pi m y\right), \tag{5.5}$$

where *n, m* (they can be represented as $n = N\cos\vartheta_s$, $m = N\cos\vartheta_s$) are integers and $N^2 = n^2 + m^2$. In the calculations, in general, it is sufficient to sum over *n*, as *m* determined from $m^2 = N^2 - n^2$. Obviously

$$n \leq N , \quad m = \sqrt{N^2 - n^2} \geq 0 . \tag{5.6}$$

That is, in this case (5.5) can be written as

$$A_{n,\sqrt{N^2-n^2}}\sin(2\pi nx)\sin\left(2\pi y\sqrt{N^2-n^2}\right)=A_n\cdot\sin(2\pi nx)\sin\left(2\pi y\sqrt{N^2-n^2}\right), \quad (5.7)$$

5.2. Structural-phase transitions

Development of perturbations in the system, as shown by the numerical analysis of Eq.(5.1) will be as follows [4,6]. Starting from initial fluctuations, the modes over a wide range of ϑ begin grow. The value of the quadratic form of the spectrum $I=\frac{1}{N}\sum_j A_j^2$ can be estimated by equating the r.h.s of Eq. (5.1) to zero and to obtain in result a value close to 0.75. It was shown in [4, 7] that when the number of modes is sufficiently large and calculation proceeds with high precision the system delayed the development while remaining in a dynamic equilibrium. For further development - "crystallization", one of the modes must get a portion of the energy which excesses some threshold value. That is, in these case, it is necessary a certain level of noise (fluctuations). This can be achieved either at finite noise level $f\neq 0$ or by decreasing the accuracy of calculations that is the same as noted in [68]. Similar cases, when the noise can trigger or accelerate instability are reviewed in the book [26].

Researches of this process have found the following dynamics of integral characteristics with time (Fig.5, 6).

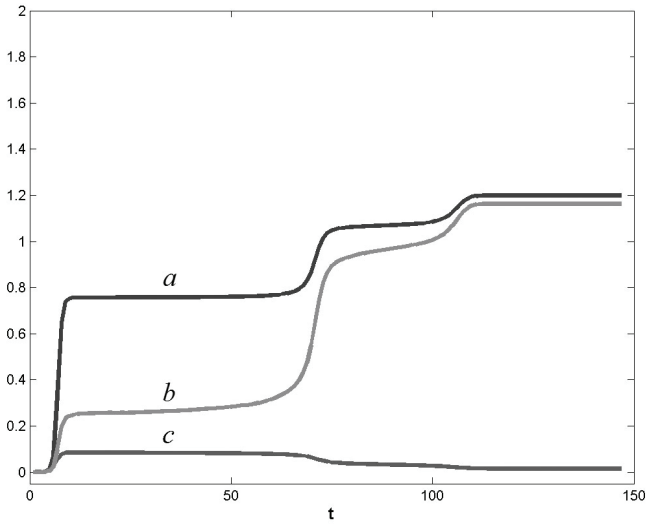

Fig. 5. Time dependence of the integral characteristics of the process.
a) $\frac{1}{N}\sum_i A_i^2$, b) $\frac{1}{N}\sqrt{\sum_i (A_i-\bar{A})^2}=\sigma$, c) $\frac{1}{N}\sum_i A_i=A_{av}$.

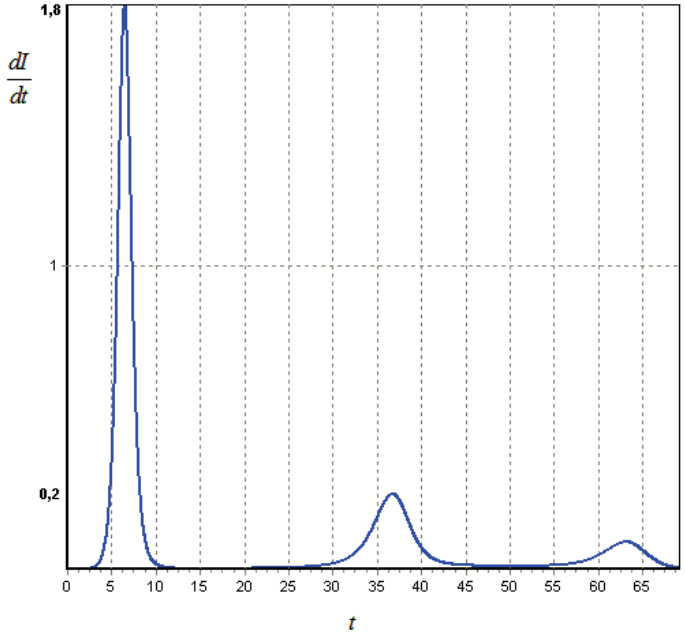

Fig. 6. The evolution of the derivative dI/dt of the integral quadratic form $I=\sum_j a_j^2$.

Exact after the first peak of the derivative, the metastable structure – a system of convective rolls is formed, and up to the moment when the second burst have appeared with value of $I \approx 1$ it has remain unchanged. The next burst of $\partial I / \partial t$ indicates the emergence of a secondary metastable structure with a new value of $I \approx 1.07$. After the second burst of the quadratic form derivative a stable structure of squared convective cells is started to build up (Fig. 7). Such behavior proves the existence of structural-phase transitions in the system.

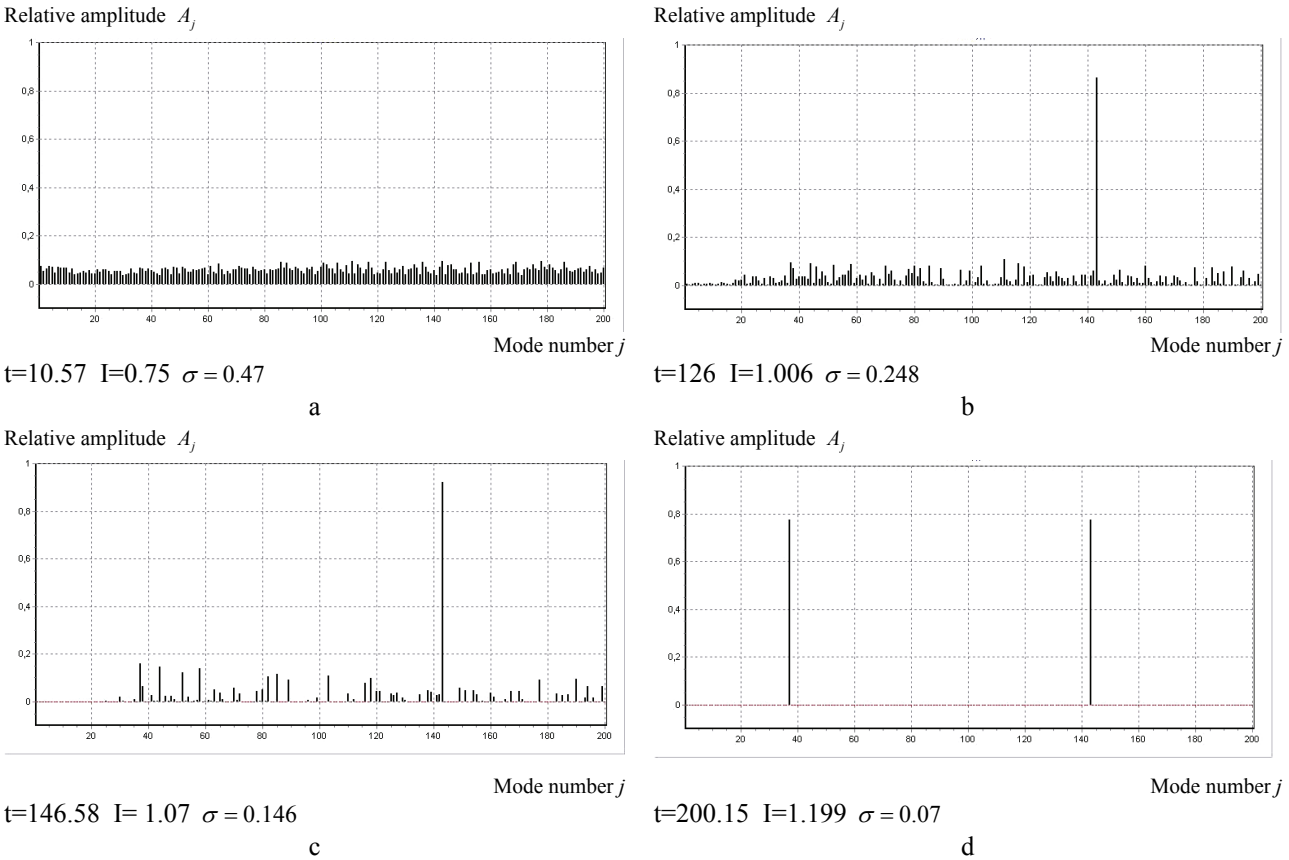

Fig. 7. Regimes of instability
a – the spectrum of the "amorphous" state, *b*,*c* – a short-lived intermediate state, *d* – stable state – convective cells.

If one of the modes gets the proper amount of energy, then the process of formation of a simplest convective structure – rolls begins. Note that in the nature, the thin clouds also can form the roll structure, as shown in Fig. 8

Fig. 8. A fragment of a thin cloud in the form of convective rolls. Circumurban Road, Kharkiv, 09.12.2012

The value of I in this case tends to unity ($I \to 1$). However, this state is not stable and then we can see the next structural transition: convective rolls are modulated along the axis of fluid rotation, and the typical size of this modulation phases down. In this transition state, the system stays for a sufficiently long time (which slightly increases within some limits with increase in the number of modes), and the value $I \approx 1.07$ remains constant during this time.

Further, the growth of side spectrum, rotated on 90^o relative to the fundamental mode (corresponding to the formation of the roll structure) results in rolls modulation (Fig. 9) and over the time there is the second structural-phase transition occurs leading to the formation of the metastable spatial structure with broken short-range order (Fig. 10) but possessing long-range order, that is a result of mode interference.

After a rather long time, ten times more than the inverse linear growth rate of the initial instability only the one mode "survives" from newly formed "side" spectrum, which amplitude is comparable with the amplitude of the primary leading mode. In the end, the stable convective structure –square cells is generated, and the quadratic form I reaches the value of $I = 1.2$.

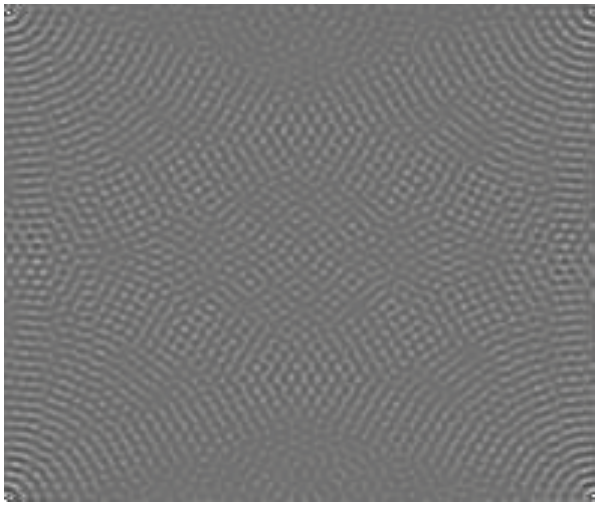

Fig. 9. Spatial short-lived convective structure with long-range order, but violations range order ($I = \sum_j a_j^2 = 15/14$).

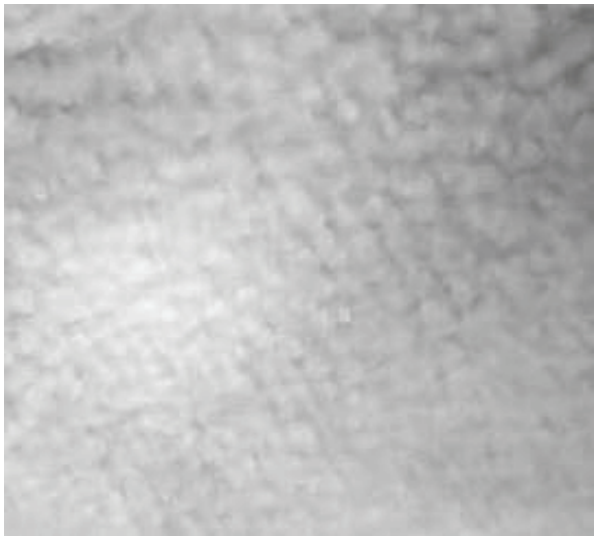

Fig. 10. A fragment of the spatial convection structure in a thin cloud layer. White Lake (Zmiyov), 06.10.2012

5.3. Structure imperfection

Let us consider in more detail the formation of square convective cells. Denote the amplitudes of the modes forming a spatial structure of square convective cells as a_1 and a_2. Consider the dynamics of "spectrum imperfection (defectiveness)" of the structure $D = \sum_{j \neq 1,2} a_j^2 / \sum_j a_j^2$. It is defined as the ratio of the sum of squared mode amplitudes which does not fit the system of square cells to the total sum of modes squares. In addition, let introduce so-called "visual imperfection (defectiveness)" $d = N_{def} / N$, where N_{def} is the number of defective spatial cells (the area of the structure occupied by irregular cells) and N is the number of cells in a perfect regular structure (the total area of the structure). The process of structure rearrangement is observed in the interval between the second and third burst of the derivative quadratic form (Fig. 2).

The criteria by which the cell was considered as regular and the method of calculation the number of these cells are following. The picture for the field is converted to 8-bit image. I.e. the maximum number of colors is reduced to 256. Thus, the formed structure becomes more evident and observable. Increasing this image, one can quite clearly distinguish which of the structural units is the proper cell, and which is not. The proper cell has the correct geometry with uniformly dark center and four lighter hills surrounding the center and of comparable size.

Despite on qualitative character of quantity description characterizing the spectral and visual defectiveness of structure we can note a similarity in its behavior (Fig. 11) near the completion of the structural transition.

Let place the grid mesh over the pattern obtained by simulation of Eq. (5.1) and count the number of picture elements (meshes) for each value of the temperature field Φ. The result can be considered as a field distribution function which characterizes the pattern (Fig. 12).

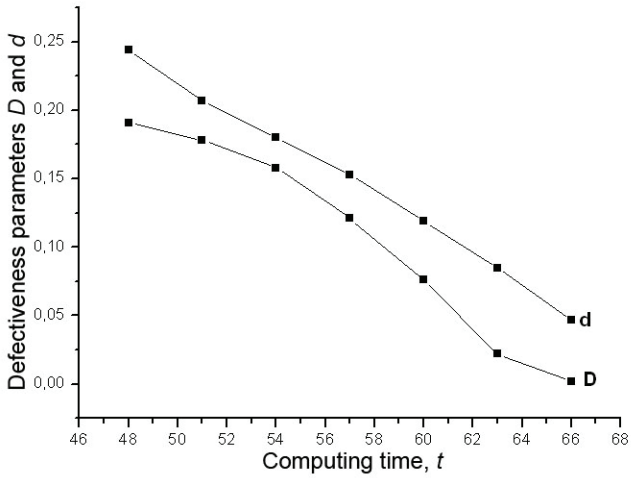

Fig. 11. Comparative analysis of the spectral D and visual defectiveness parameters d.
The number of modes is 50.

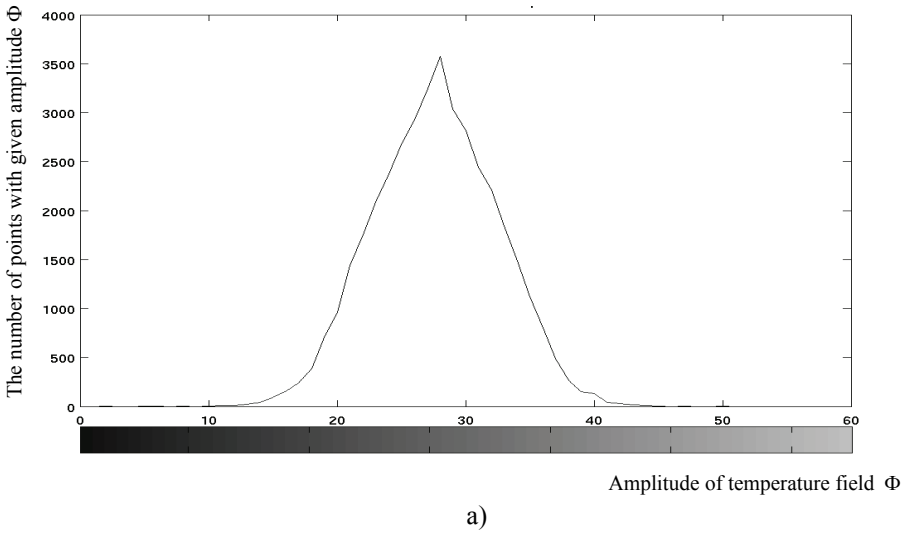

a)

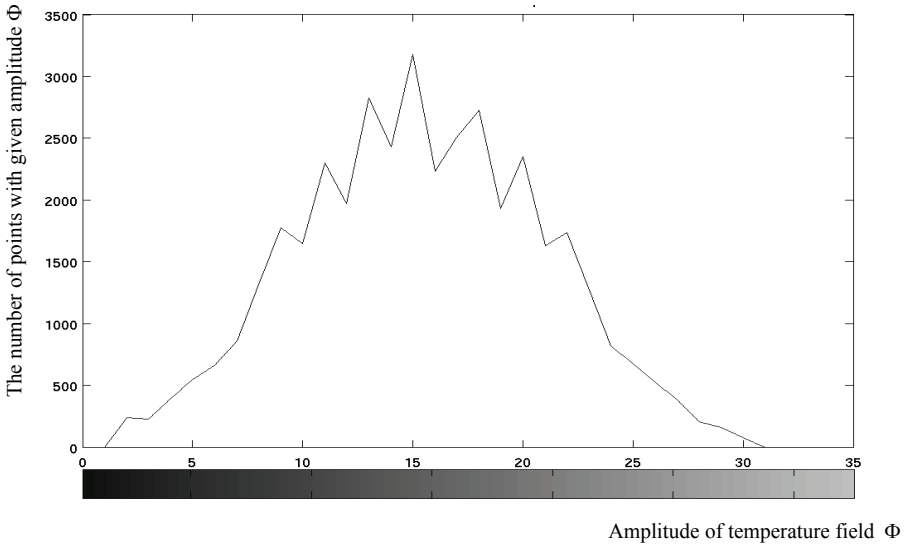

b)

Fig. 12. Distribution of the temperature field Φ
a - defective structure, *b* - regular structure

The analysis of this distribution (the presence of local maxima and minima of their position) gives ideas about the nature of the regular structure, the level of its imperfection, and helps to investigate it's topological features.

6. MODULATION INSTABILITY OF CONVECTIVE CELLS IN A THIN LAYER. EFFECT OF HYDRODYNAMIC DYNAMO

6.1. The Proctor-Sivashinsky-Pismen model

The first report about the possibility of the convective cells system modulation instability within framework of the extremely productive Proctor-Sivashinsky-Pismen model [65] was made in [66]. This modulation of the convective cells in a thin layer of liquid between poorly conducting heat horizontal surfaces (which origination was discussed earlier in this paper) is caused by generation of vortices of a different nature than those that form the convective structure. As a result of modulation instability the large flat vortices appear in the system of developed regular convective cells. In other words, this is the effect of hydrodynamic flow (vortex) dynamo [27, 66, 67] which in contrast to the well-known physical models constructed for media with a helical hydrodynamic turbulence (see review [25]) represents a regular process and there is no need in the presence of uncompensated helicity in the system for developing of this effect.

The Proctor-Sivashinsky model updated by author of [65] describes the convection with taking into account the toroidal component of the velocity $\vec{U}_{\text{tor}} = \text{rot}(\vec{e}_z \Psi)$,

$$\dot{\Phi} = \varepsilon^2 \Phi - \left(1 - \nabla^2\right)^2 \Phi + \frac{1}{3} \nabla \left(\nabla \Phi |\Phi|^2 \right) + \gamma \nabla \Phi \times \nabla \Psi , \tag{6.1}$$

$$\nabla^2 \Psi = \nabla \nabla^2 \Phi \times \nabla \Phi , \tag{6.2}$$

where γ is the inverse Prandtl number $\text{Pr}^{-1} = \kappa / \nu$, characterizing a non-equilibrium state of the fluid, ν is the kinematic viscosity and κ is the specific temperature conductivity, $\varepsilon << 1$.

Despite the fact that the model of Proctor-Sivashinsky-Pismen [65] was introduced for Prandtl numbers of unity order it remains applicable to description of evolution of developed convective cells structure for which, as shown above, $\Phi \propto \varepsilon$. Moreover, the modulation instability of the structure occurs only at low Prandtl numbers. [12].

It means that deriving Eq. (4.1) we assumed $\gamma \Psi \propto \gamma \Phi^2 \propto \varepsilon^2$, and $\gamma \propto 1$. The analysis of the modulation instability of the developed convective cells structure shows that non-vanishing values of $\Psi \propto \left(\frac{\Delta k}{k} \right) \Phi^2$, where in turn $\left(\frac{\Delta k}{k} \right) \propto \varepsilon$. Thus, the model [65] can be used to describe the modulation instability of the developed convective structure only when $\gamma \propto 1/\varepsilon$, because only in this case the condition $\gamma \Psi \propto \varepsilon^2$ is satisfied.

6.2. Secondary modulation instability of convective cells

The secondary instability threshold is determined by the setting the parameter $\varepsilon_2 = 27 b^2 \Gamma^2 / 20 - 1$ to zero, where $\Gamma = \varepsilon \gamma$, $b = \sqrt{5/3} A$ is the renormalized amplitude of perturbations in the primary instability discussed above. When the threshold is exceeded ($\varepsilon_2 > 0$) there are conditions for secondary instability with the maximum growth rate

$$\text{Im}\, \omega_{\max} = 1 - 6 b^2 / 5 + 27 \Gamma^2 b^4 / 200 + 2 / 27 \Gamma^2 , \tag{6.3}$$

located near the central modes of the primary structure ($k_x = \pm 1$, $k_y = 0$ and $k_x = 0$, $k_y = \pm 1$) and transversely spaced from these points at a range of $\Delta = (\sqrt{2} / b\Gamma) \, | \varepsilon_2 | << 1$.

When the gap between the modes of the secondary structure and the primary structure approaches zero, the growth rate of the modulation instability tends to zero too. The large-scale vortex perturbations, which arise due to the modulation instability, lead to occurrence of shear flows and deform the convective structure on a large scale.

The equation describing the evolution of the spectrum of instability is the following:

$$\dot{b}_j = b_j - \sum_j^N V_{ij} \, | b_i |^2 \, b_j + \sum_{i,n,m}^N W_{jinm} b_i b_n b_m , \tag{6.4}$$

where the coefficients are defined by the interaction $V_{jj} = 1$, ϑ is the angle between the vectors $\vec{k}_i$ and $\vec{k}_j$,

$$V_{ij} = (2/3) \left(1 - 2 \left(\vec{k}_i \vec{k}_j \right)^2 \right) = (2/3) \left(1 + 2 \cos^2 \vartheta \right) , \tag{6.5}$$

$$W_{jinm} = \left(\vec{k}_i \times \vec{k}_n \right) \left(\vec{k}_m \times \vec{k}_j \right) \left[\frac{k_i^2 - k_n^2}{\left(\vec{k}_i + \vec{k}_n \right)^2} + \frac{k_i^2 - k_m^2}{\left(\vec{k}_i + \vec{k}_m \right)^2} \right] \delta_{\vec{k}_j, \vec{k}_i + \vec{k}_n + \vec{k}_m} . \tag{6.6}$$

It can be shown that if we impose a condition of proper symmetry on the arising perturbations, the equations for the fundamental modes of convection cells (each of which has an amplitude equal to b) and for modes b_d having the fastest growing rate of the modulation instability (we suppose that the rest of the spectrum is suppressed due to action of above discussed competition mechanisms) have the form

$$\dot{b} = b\left(1 - b^2 - 4b_d^2\right), \tag{6.7}$$

$$\dot{b}_d = b_d\left(1 - b^2 - b_d^2\right) + \frac{2}{27\Gamma^2} b^2 b_d \theta\left(\varepsilon_2\right), \tag{6.8}$$

where the threshold of the modulation instability is introduced qualitatively by the theta-function $\theta(\varepsilon_2)$. When the modulation instability threshold is exceeded, the amplitudes of primary structure decreases from the values comparable with unity to values of $b_\infty{}^2 = 20/27\Gamma^2$, while the amplitude of the growing modes are reach the value of $b_{d\infty} = 1/2\,(1 - b_\infty^2)^{1/2}$. The intensity (i.e., the value $I = \sum |\, b_{k_i}\,|^2$) of the primary structure in the absence of modulation instability (at $\Gamma^2 < 20/27$ the primary structure is stable) and the intensity of the defective structure, which is a result of the development of this instability is found to be equal. The deficiency of the developed structures is equal to ε_2.

6.3. The effect of regular hydrodynamic dynamo

The interaction between the modes determining the modulation (modes of the distributed defect) and the modes of the primary structure is caused by the existence of large-scale vortices which streamlines in the configuration space can be represented as

$$\Psi \approx \varepsilon\varepsilon_2 b^2 \left[\cos(l_0\xi) - \cos(l_0\eta)\right], \tag{6.9}$$

where $l_0 = \varepsilon\Delta$, $\xi = \sqrt{\varepsilon}x$, $\eta = \sqrt{\varepsilon}y$ and the ratio of the characteristic linear size of the characteristic large-scale vortex L_V to the linear size of the convection cell L_C is equal to $L_V / L_C \approx \left(b\varepsilon\varepsilon_2\right)^{-1}$ (Fig. 13). The occurrence of such large-scale vortices is one of the possible realizations of the hydrodynamic dynamo effect [66, 67].

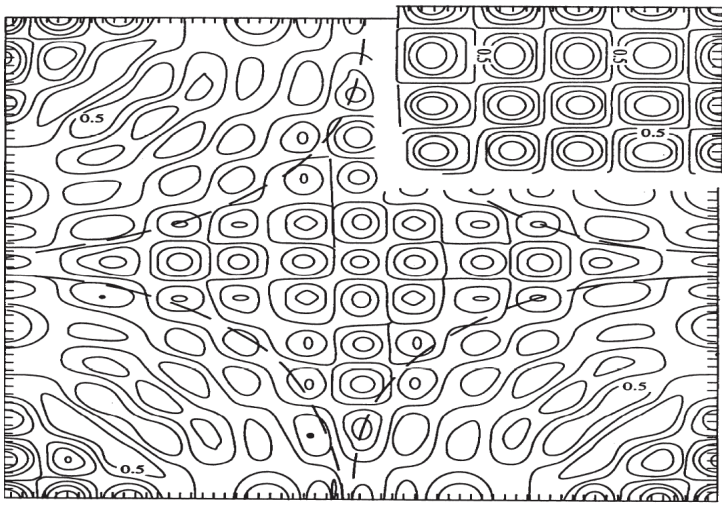

Fig. 13. Regular defect in the convective structure. The fragment of unperturbed primary structure is shown in the upper right corner. The dotted line shows the characteristic streamlines of large-scale vortices.

7. CONCLUSION

The special feature of the Proctor-Sivashinsky model is the existence of three possible metastable states. The times of structural transitions between these metastable states are much less than the time of their existence.

The characteristic size of the convective structures in the regime of advanced instability is of order $2\pi / k \propto 2\pi$ and the length of the wave vectors is of order unity (in conventional dimensionless units). The potential of interaction between spatial modes $V_{ij} = (2/3)\left(1 + 2\cos^2 \vartheta_{ij}\right)$ has a deep minimum for angles $\vartheta_{ij} = \vartheta_i - \vartheta_j = \pm\pi/2$ between vectors $\vec{k}_i$ and $\vec{k}_j$. Namely these minima are the reason of the instability of convective rolls [27, 28], because the existence of a minimum V_{ij} for modes with relatively low amplitudes allows them to continue growth, while suppressing the perturbations occurred before.

When approaching to the stable state, the spatial structure is getting rid of many defects. There is a correlation between the relative fraction of visually (geometrically) observed structural defects and the imperfection parameter, defined as the ratio of the squares of the spectrum mode amplitudes which does not fit the system of square cells to the total sum of squared modes.

The modulation instability of the developed convective cells results not only in appearing of the self-similar system – convective cells of different sizes [12] but also in formation of the large-scale poloidal vortices [66, 67]. This phenomenon, which was previously investigated for irregular models (see detailed review [25]), as was conjectured by S.S. Moiseev, can take place through the modulation instability of regular spatial convective structure of finite amplitude.

The model discussed above can be used after some small modification for purpose of simulation modeling of structures and second-order structural-phase transitions. With increase of the number of minima of the interaction potential $V_{ij}(\vartheta)$ (for example, three), the structures with another type of symmetry can arise (for example, hexagonal cells). Governing the spatial structure of the potential' local minima and their depth, one can form the structure of any specified symmetry type. It is possible in so doing to observe the formation of intermediate metastable states and all stages of structural transitions. This allows to use this model (appropriately modified if necessary) for a qualitative description of pattern formation in systems which possess the preferred spatial scale, particularly in condensed media.

REFERENCES

1. Busse F.H., Riahi N. Nonlinear convection in a layer with nearly insulating boundaries // J.Fluid Mech. – 1980. - Vol.96. - P.243.
2. Chandrasekhar S. Hydrodenamic and hydromagnetic stability. Third printing of the Clarendon Press. Oxford University Press edition, Dover Publication Inc.: New York, 1970. - 704 p.
3. Getling A.V. Structures in heat convection // Usp. Fiz. Nauk. – 1991. - Vol.11. – P.1-80.
4. Karpman V.I. Nonlinear waves in dispersive media. - M.: Nauka, 1973. – 175c.
5. Autowave processes in systems with diffusion / edited by M.T. Grekhov. - Gorky: IPF SA USSR, 1981. – 246s.
6. Engelbrecht J.K. Evolution equations and self-wave processes in the active medium // On nonlinear continuum mechanics. - Tallinn: Valgus, 1985. - P.119-131.
7. Kosevich A.M., Ivanov B.A., Kovalev A.S. Nonlinear waves of magnetization. – Kiev: Naukova Dumka, 1983. - 240s.
8. Schwartz L.W., Fenton J.D. Strongly nonlinear waves // Ann. Rev. Fluid. Mech. – 1982. - Vol.14. - P.39-60. Translation: Schwartz L., Fenton J. Strongly nonlinear waves. In Sat Nonlinear wave processes. Collection of articles. Series «Mechanics», № 42, Mir: 1987. - S.296.
9. Davydov A.S. Solitons in molecular systems. - Kyiv: Naukova Dumka, 1984. – 288s.
10. Yanovsky V.V. Lectures on nonlinear phenomena. Vol.2. - Kharkov: Institute for Single Crystals, 2007. - 448s.
11. Zaslavsky G.M., Sagdeev R.Z., Usikov D.A., Chernikov A.A. Weak chaos and quasi-regular structure. - Moscow: Nauka, 1991. – 320s.
12. Kuklin V.M. The role of absorption and dissipation of energy in the formation of spatial structures in nonlinear nonequilibrium media // Ukrainian Journal of Physics, Reviews. – 2004. – Vol.1, № 1. - P.49-81.
13. Dorodnitsyn V.A., Elenin G.G. Symmetry in solutions of equations of mathematical physics. - Knowledge, 1984. - 175s.
14. Ovsyannikov L.V. Group analysis of differential equations. – Moscow: Nauka, 1978. - 240s.
15. Ibragimov N.H. Transformation groups in mathematical physics. – Moscow: Nauka, 1983. - 240s.
16. Nikolis G., Prigogine I. Self-organization in nonequilibrium systems. - Academic Press, 1979. - 240s.
17. Haken H. Synergetics. - World: 1980. – 404p.
18. Tsytovich V.N. Nonlinear effects in plasma. - Moscow: Nauka, 1967. - 288s.
19. Zakharov V.E. Wave collapse in physics continuum / Problems of physical kinetics and solid state physics. Ed. Sitenko AG , Academy of Sciences of the USSR. ITP. - Kiev: Naukova Dumka, 1990. - 488s.
20. Petviashvili V.I., Pokhotelov O.A. Solitary waves in the plasma and the atmosphere. – Moscow: Energoatomizdat, 1989. - 200s.
21. Klimontovich L., Vilhelmson H., Yakimenko I.P. Statisticheskaya theory of plasma-molecular systems. - Moscow: Mosk. University Press, 1990. – 224s.
22. L'vov V.S. Wave Turbulence under Parametric Excitations. Applications to Magnetics. - Springer-Verlag, 1994; L'vov V.S. Nonlinear Spin Waves. – Moscow: Nauka, 1987. - 270s.
23. Kuklin V.M., Panchenko I.P., Khakimov F.H. Multiwave processes in plasma physics. – Dushanbe: Donish, 1989. - 175s.
24. Buts V.A., Lebedev A.N. Coherent emission of intense electron beams. - M. Ed. LPI RAS, 2006. - 333p.
25. Moiseev S.S., Hovhannisyan K., Rutkevich P.B., Tur A.V., Khomenko G.A., Yanovsky V.V. Vortex dynamos in helical turbulence / Integrability and kinetic equations for solitons. Ed. Bar'yakhtar V.G., Zakharov V.E, Chernousenko V.M. - Kiev: Naukova Dumka, 1990. – 472s.
26. Horsthemke B., Lefebvre R. Noise-Induced Transitions. Translated from English. - Academic Press, 1987. – 400p.
27. Kirichok A.V., Kuklin V.M. Allocated Imperfections of Developed Convective Structures // Physics and Chemistry of the Earth Part A. - 1999, № 6. - P.533-538.
28. Belkin E.V. Gushchin I.V., Kirichok A.V. Kuklin V.M. Structure transitions in the model Proctor-Sivashinsky // VANT, Ser. Plasma electronics and new methods of acceleration. - 2010, № 4(68). - S.296-298.
29. Kamyshanchenko N.V., Krasilnikov V.V., Neklyudov I.M., Parkhomenko A.A. Formation of spatial inhomogeneities in deformable irradiated materials // Condensed Matter and interphase boundaries. - 2001. - Vol.2, № 4. - P.339-341.
30. Krasil'nikov. V.V., Parkhomenko A.A., Savotchenko S.E. Internal-Stress distribution in deformed irradiated materials // Russian Metallurgy, Metally. – 2003. - №6. - P.559-565.
31. Bryk V.V., Krasilnikov V.V., Parkhomenko A., Savotchenko S. Self-organization mechanisms of radiation-induced defects in

complex alloys of zirconium // Izvestiya. Metals. – 2005. - № 4. - P.81-87.
32. Krasilnikov V.V, Klepikov V.F., Parkhomenko A.A. Savotcheoko S.E. Features self-dislocation and vacancy ensemble in irradiated deformable materials // VANT. Ser. FRP and PM. - 2005. - № 5. - P.26-32.
33. Landau L.D., Lifshitz E.M. Theoretical Physics. Vol.5. Statistical physics. Part 1. - Moscow: Francis, London, 2002.
34. Yuhnovsky I.R. Phase transitions of the second order: Collective variables method. – Singapore: World Scientific, 1987. - 327p.
35. Patashinskii A.Z., Pokrovskii V.L. Fluctuation theory of phase transitions. - 2nd ed., Rev. Moscow: Science - Home Edition physical and mathematical literature, 1982.
36. Hartri D. Calculations of atomic structures. - New York: Oxford, 1960. – 256s.
37. Sleter J. Methods of self-consistent field for molecules and solids. - Academic Press, 1978. - 664p.
38. Suhl H. Effective Nuclear Spin Interactions in Ferromagnets // Phys Rev. - 1958. - Vol.109, №2. - P.606.
39. Zaharov V.E., Lvov V.S. Starobinets S.S. Spin-wave turbulence beyond the threshold of parametric excitation // UFN. - 1974. – T.114, №4. - S.609-654.
40. Bogolyubov N.N., Shirkov D.V. Introduction to the theory of quantized fields. 4th ed. - Moscow: Nauka, 1984.
41. Abrikosov A.A., Gorkov L.P., Dzyaloshinskii I.E. Methods of quantum field theory in statistical physics. – M: Fizmatgiz, 1963.
42. Vasilev A.N. Quantum field renormalization group in the theory of critical behavior and stochastic dynamics. - St. Petersburg: Petersburg Nuclear Physics Institute, 1998.
43. Guld H., Tobochnik Ya. Computer Simulation in Physics. - Mir, 1990.
44. Lazarev N.P. Molecular dynamics simulation of phase transitions in liquids and solids // The Journal of Kharkiv National University, physical series "Nuclei, Particles, Fields". – 2007- №763. – Iss.1(33). - S.3-31.
45. Ziman J.M. Models of Disorder. - Cambridge: University Press, 1979.
46. White R.M., Geballe T.N .Long range order in solid. - New York: Academic Press, 1979, translation: Bumm P., Geball T. Long-range order in solids. - Academic Press, 1982.
47. Bonch-Bruevich V.D. et al. Electronic theory of disordered semiconductors. - Moscow: Nauka, 1981.
48. Efros A.L. Physics and geometry of the disorder. - Moscow: Nauka, 1982.
49. Rabinovich M.I., Fabrikant A.L., Tsimring L.S. A finite-dimensional disorder // Usp. Fiz. Nauk.. – 1992. - T.162, № 8. - S.1-42.
50. Senechal M., Quasicrystals and Geometry. - Cambridge: Cambridge Univ. Press, 1996.
51. Vekilov Y.F., Chernikov M.A. Quasicrystals // Usp. Fiz. Nauk. – 2010. - T.180, №6. - P.561-586.
52. Kuklin V.M. About interference nature of the formation of the fine structure of laser pulses and bursts of abnormal oscillation amplitude in the model Lighthill // VIII Khariton scientific reading. March 21-24, 2006, Sarov, Russia, Sat reports. - Sarov, 2006. - S.450-456; Effect of induced interference and the formation of spatial perturbation fine structure in nonequlibrium open-ended system // Problems of Atomic Science and Technology, Ser. Plasma electronics and new methods of acceleration. - 2006. - № 5(5). - S.63-68.
53. de Gennes P.G. The Physics of Uquid Crystals. - Oxford: Clarendon, 1974.
54. Eckmann J.-P., Procaccia I. The generation of spatio-temporal chaos in large aspect ratio hydrodynamics // Nonlinearity. – 1991. - Vol. 4, №2. - P.567-582.
55. Zaslavsky G.M., Sagdeev R.Z. Vvedenie in nonlinear physics: from the pendulum to turbulence and chaos, 1988. – 368s.
56. Landau, L.D. On the problem of turbulence // Doklady Akademii Nauk SSSR. – 1944. – T.44. - S.339-342.
57. Landau L.D., Lifshitz E.M. Theoretical physics. T.6. Hydrodynamics. - Moscow: Nauka, 1986. - 736s.
58. Hopf E. A mathematical example displaying features of turbulence // Comm. Pure and Appl. Math. - 1948. - Vol.1. - P. 303-322.
59. Swift J.V., Hohenberg P.C. Hydrodynamic fluctuations at the convective instability // Phys. Rev. A. – 1977. - Vol.15. - P.319.
60. Rabinovich M.I., Sushchik M.M. Regular and chaotic dynamics of structures in fluid flows // UFN. – 1990. - T.160, №1. - P.3-64.
61. Dimensions and Entropies in Chaotic Systems. / Ed. A Mayer-Kress. - Berlin: Springer-Verlag, 1986.
62. Chapman J., Proctor M.R.E. Nonlinear Rayleigh-Benard convection between poorly conducting boundaries // J. Fluid Mech. - 1980, №101. - P.759-765.
63. Gertsberg V., Sivashinsky G.E. Large cells in nonlinear Rayleigh-Benard convection // Prog. Theor. Phys. - 1981, №66. - P.1219-1229.
64. Malomed B.A., Nepomniachtchi A.A., Tribel'skii M.P. Two-dimensional quasi-periodic structures in nonequilibrium systems // Lett. – 1989. - Vol.96. - P.684-699.
65. Pismen, L., Inertial effects in long-scale thermal convection // Phys. Lett. A. – 1986. – Vol.116. – P.241-243.
66. Kirichok A.V. Kuklin V.M., Panchenko I.P., Moiseev S.S., Pismen L. Dynamics of large-scale vortices in the mode of convective instability / Inter. Conf. "Physics in Ukraine", Kiev, 22-27 June 1993. Proc. Contr. Pap. ITP, 1993. - P. 76-80.
67. Kirichok A.V. Kuklin V.M., Panchenko I.P. On the possibility of dynamo mechanism in non-equilibrium convective environment // Reports of the National Academy of Sciences. - 1997, № 4. - P.87-92.
68. Belkin E.V., Gushchin I.V. A mathematical model of convection of the liquid layer with a temperature gradient / Nauchno-tehnicheskaja konferencija s mezhdunarodnym uchastiem «Komp'juternoe modelirovanie v naukoemkih tehnologijah», Kharkov, 2010. - Vol.1. - P.39-40.
69. Busse F.G. Hydrodynamic instability and transition to turbulence / Ed. X. Sweeney, J. Gollaba. – M: Mir, 1984. – 124s.
70. Gershuni G.Z. Zhukovitsky E.M. Convective stability of incompressible fluid. - Moscow: Nauka, 1972. – 392s.
71. Whitehead J.A. Dislocations in convection and the onset of chaos // Phys. Fluids. – 1983. - Vol.26, №10. - P.2899.
72. Siggia E.D., Zippelius A. Dynamics of defects in Rayleigh Benard convection // Phys. Ref. A. – 1981. - Vol.24(2). - P.1036-1049.
73. Bodenschatz E., de Bruyn J.R., Ahlers G., Connell D. Experiments on three systems with non-variatinal aspects. - Preprint. - Santa Barbara, 1991.

Gushchin Ivan V. Lecturer of Department of Artificial Intelligence and Software, School (Faculty) of Computer Science, V.N. Karazin Kharkov National University.

Kirichok Aleksandr Vitalievich – Ass. Professor, PhD, Doctoral (D.Sc.) candidate of Department of Artificial Intelligence and Software, School (Faculty) of Computer Science, V.N. Karazin Kharkov National University. Research interests: nonlinear physics, plasma physics, hydrodynamics.

Kuklin Volodymyr Michailovich - Ph.D.; D.Sc.; Professor of Department of Reactor Material Science; Head of Department of Artificial Intelligence and Software, School (Faculty) of Computer Science, V.N. Karazin Kharkov National University.

UDC 533.95, 507.9.

HIGH CURRENT PLASMA ACCELERATORS: PHYSICS AND APPLICATIONS

I.E. Garkusha
** Institute of Plasma Physics of the National Science Center "Kharkov Institute of Physics and Technology*
Academicheskaya Street 1, Kharkov, 61108, Ukraine
E-mail: garkusha@ipp.kharkov.ua
Received 20 November 2012, accepted 24 January 2013

In this review paper, basic principles of high current plasma accelerators, history and recent state of their investigations in IPP NSC KIPT are briefly described. In such devices an internal magnetic field is created by high current up to several MA in the discharge and it is used for both plasma flow acceleration up to 1000 km/s. Particular attention is paid to the quasi-stationary plasma accelerators (QSPA), where discharge duration exceeds considerable the plasma flight time in acceleration channel. Application of QSPA for plasma-surface interaction studies relevant to thermonuclear reactors, like ITER and DEMO, is discussed. Results on surface modification and improvement of material properties by powerful pulsed plasma processing are described. Potential technological applications for materials treatment are emphasized.
KEY WORDS: plasma accelerator, high-energy streams of dense plasma, plasma-surface interaction, surface modification, extreme conditions of thermonuclear reactor ITER

СИЛЬНОТОЧНЫЕ УСКОРИТЕЛИ ПЛАЗМЫ: ФИЗИКА И ПРИМЕНЕНИЕ
И.Е. Гаркуша
Институт физики плазмы, Национальный научный Центр «Харьковский физико-технический институт»
Академическая, 1 61108, Харьков, Украина
В данной обзорной работе кратко описаны основные принципы сильноточных ускорителей плазмы, история и современное состояние их исследований в ИФП ННЦ ХФТИ. В таких устройствах собственное магнитное поле создается большим током до нескольких МА в разряде и оно используется для ускорения потока плазмы до скоростей порядка 1000 км/с. Особое внимание уделено квазистационарным плазменным ускорителям (КСПУ), в которых продолжительность разряда значительно превышает время полета плазмы в ускорительном канале. Описаны эксперименты по применению КСПУ для исследований взаимодействия плазмы с поверхностью в термоядерных реакторах, таких как ИТЭР и ДЕМО. Представлены результаты исследований по модификации поверхности и улучшению свойств материалов при обработке мощными импульсными потоками плазмы. Подчеркиваются потенциальные технологические приложения импульсной плазменной обработки.
КЛЮЧЕВЫЕ СЛОВА: плазменный ускоритель, высокоэнергетичные потоки плотной плазмы, взаимодействие плазмы с материалами, модификация поверхности, экстремальные условия термоядерного реактора ИТЭР

СИЛЬНОСТРУМОВІ ПРИСКОРЮВАЧІ ПЛАЗМИ: ФІЗИКА І ВИКОРИСТАННЯ
І.Є. Гаркуша
Інститут фізики плазми Національного Наукового Центру «Харківський фізики-технічний інститут»
Академічна, 1 61108, Харків, Україна
В даній оглядовій роботі коротко описані основні принципи сильнострумових прискорювачів плазми, історія та сучасний стан їх досліджень в ІФП ННЦ ХФТІ. У таких пристроях внутрішнє магнітне поле створюється великим струмом до декількох МА в розряді і воно використовується для прискорення потоку плазми до швидкостей порядку 1000 км/с. Особливу увагу приділено квазістаціонарним плазмовим прискорювачам (КСПП), у яких тривалість розряду значно перевищує час польоту плазми в прискорювальному каналі. Описано експерименти по застосуванню КСПП для досліджень взаємодії плазми з поверхнею в термоядерних реакторах, таких як ІТЕР і ДЕМО. Представлені результати досліджень по модифікації поверхні і поліпшення властивостей матеріалів при обробці потужними імпульсними потоками плазми. Підкреслюються потенційні технологічні застосування імпульсної плазмової обробки.
КЛЮЧОВІ СЛОВА: плазмовий прискорювач, високоенергетичні потоки щільної плазми, взаємодія плазми з матеріалами, модифікація поверхні, екстремальні умови термоядерного реактора ІТЕР

Plasma accelerators generating powerful dense plasma streams are able to be used for plasma injection into magnetic traps, investigations of plasma-surface interactions that can be occurred on the first wall or divertor plates during current disruption conditions and giant ELMs, for some technological applications related with modification and alloying of surface layers by plasma processing etc. In such devices an internal magnetic field is created by high current up to several MA in the discharge and it is used for both plasma flow acceleration up to 1000 km/s and also for dense magnetized plasma compression up to 10^{19}-10^{20} cm^{-3}. The plasma acceleration (compression) can be organized in pulsed or quasi-stationary regimes. In first case the pulse duration typically is comparable with the time-of-flight of plasma ions in the accelerating channel. The acceleration process can be described in the frame of electrodynamical approximation either within "snow plough" model or "current sheath", for instance. The detailed information can be found elsewhere [1,2], therefore the electrodynamical approach will not be discussed here. Due to the high efficiency of plasma bunches acceleration combined with relative simplicity and robust design the pulsed plasma accelerators (PPA) are especially attractive for different technological applications related with materials processing etc. In quasi-

stationary plasma accelerators (QSPA) the discharge duration exceeds considerable the plasma flight time t_f. Supersonic plasma flow is kept during hundreds and thousands t_f and, practically, it duration of plasma stream generation is limited only by parameters of the power supply system used (capacitor battery) [3].

The main aim of this review paper is to describe briefly the basic principles of high current plasma accelerators and recent state of their investigations in IPP NSC KIPT. Application of QSPA for plasma-surface interaction studies relevant to thermonuclear reactors, like ITER and DEMO, is underlined. Results on surface modification and improvement of material properties by powerful pulsed plasma processing are emphasized aiming at potential technological applications for materials treatment.

GENERAL PRINCIPLES OF QUASI-STATIONARY PLASMA FLOWS IN ACCELERATING CHANNELS

The general principles of quasi-stationary acceleration of high-power plasma streams have been formulated by Morozov [3,4] on the base magneto-hydrodynamics (MHD) approach, proposed by H. Alfven. In the frame of one-fluid MHD model the plasma flow acceleration due to the thermal and magnetic forces can be described by following system of equations:

$$\rho\left(\frac{\partial \vec{v}}{\partial t} + (\vec{v}\nabla)\vec{v}\right) = -\nabla p + \frac{1}{c}\left[\vec{j}, \vec{H}\right] \tag{1}$$

$$\frac{\partial \rho}{\partial t} + div\rho\vec{v} = 0 \tag{2}$$

$$j = \frac{c}{4\pi} rot\vec{H} \tag{3}$$

$$div\vec{H} = 0 \tag{4}$$

$$\frac{\partial \vec{H}}{\partial t} = rot\left[\vec{v}, \vec{H}\right] \tag{5}$$

$$p = p_0\left(\frac{\rho}{\rho_0}\right)^{\gamma} \tag{6}$$

Here ρ, p, and ν are density, pressure and velocity in plasma stream, index zero corresponds to entrance of the accelerating channel; J,H are electric current density and magnetic field.

In the case of stationary axial-symmetric flow: $\frac{\partial}{\partial t} = 0,\ H_r = H_z = 0,\ \upsilon_\theta = 0.$

The plasma flow is divided into narrow flux tubes with a width h=h(z). Under these assumptions three conservation lows (holding true for each flux tube) follow from the above system of equations:

$$\frac{\upsilon^2}{2} + \int \frac{dp}{\rho} + \frac{H^2}{4\pi\rho} = const \equiv U \tag{7}$$

Where, $i(\rho) \equiv \int \frac{dp}{\rho} = \frac{p_0}{\rho_0}\frac{\gamma}{\gamma - 1}\left(\frac{\rho}{\rho_0}\right)^{\gamma-1}$ is enthalpy,

$$\frac{H}{\rho} = const \equiv k \tag{8}$$

$$\rho v h = const \equiv \dot{m} \tag{9}$$

First one is well known Bernoulli equation that expresses the conservation of full energy in the flow. Second conservation low describes freezing-in azimuth magnetic flux into a plasma. And last one is mass conservation in the tube, resulting from continuity equation (2).

From (9) it is follows that the acceleration channel width $h = \frac{\dot{m}}{\rho v}$ for any chosen mass flow rate $\dot{m}$ tends to infinity at both input and output of the channel, where $\rho \to 0, v \to v_{\max}$ and $\rho \to \rho_0, v \to 0$ correspondingly. Therefore it should have a minimum in some so called "critical section", in analogy with profiled Laval nozzle.

In such MHD analog of Laval nozzle transition through the sound velocity occurs in critical section, and the sound's velocity role plays Alfven velocity $C_A = H/(4\pi\rho)^{1/2}$. Maximal plasma stream velocity at the output of acceleration channel is $v_{max} = (2)^{1/2} C_{A0} = H_0/(2\pi\rho)^{1/2}$, being fully defined by input parameters and giving potential possibility to achieve plasma streams with very large ion energies.

However, experimental realization of quasi-stationary plasma flows in discharges with solid (non-transparent)

electrodes showed severe restrictions related with the effect of "the discharge current crisis", strong erosion of electrodes, both anode due to the electric potential jump and cathode, due to the bombardment by ions [4]. Also instability of ionization zone led to the overloading the electrodes in insulator in the high current discharge.

An important step to solve these problems is related with the proposed physical concept of quasi-stationary plasma accelerator (QSPA) based on ion carried electric current in the acceleration channel and electrodes-transformers [4-7]. Briefly, QSPA concept proposed by A.I. Morozov in Kurchatov Institute, Moscow and experimentally realized in IPP NSC KIPT, Kharkov involves: 1) the transition to a two-stage scheme of acceleration in order to eliminate the influence of instability of the neutral gas ionization region; 2) the transition to the mode of operation, under which the electric discharge current in the main accelerating channel is carried by ions, thus providing for the best match of equipotential electrodes with electric and magnetic fields in the plasma stream; 3) magnetic screening of solid-state electrode components. The transition to the condition of discharge current transport by the ions significantly complicates the functions of electrodes, where the replacement of current carriers, namely, electrons in the accelerator's power supply circuit by ions in the plasma, should take place. Besides, the ions must be supplied to the accelerating channel on the anode side and be removed on the cathode side. So, the electrodes of a quasi-stationary high-current plasma accelerator would be magneto-plasma electrodes - transformers of a complicated design, which provide both the magnetic screening of their solid-state components and the conditions for accomplishing the regime of current transport by ions.

EXPERIMENTAL STANDS OF HIGH CURRENT PLASMA ACCELERATORS

Above described concept has been verified in QSPA of a simplified design with rod-like electrodes [4-7] and later on in full-block QSPA [8-10]. Those experiments have demonstrated the feasibility of the quasi-stationary mode of acceleration with quasi-radial current lines, that was lasting for about 20 to 30 μs (at a discharge length of ~300 μs for QSPA with passive transformers (QSPA P-50) and more than 200 μs for QSPA Kh-50. One can see such systems are prospective from the point of view of plasma generation with super high energy contentment in steady (quasi)-stationary operational regime. Up to now, when using full-block QSPA Kh-50, plasma streams with the mean proton energy ≤ 0.9 keV, plasma energy density up to 2 kJ/cm^2, mean plasma density (3-5)x10^{16} cm^{-3}), plasma stream diameter up to 50 cm, total energy of plasma stream ≤ 600 kJ, the time duration of quasi-stationary phase of acceleration ≥ 200 μs with total pulse length ≈ 300 μs are generated.

Plasma characteristics of three types of accelerators being in operation in IPP are shown in Table 1. The characteristics of the plasma flow in the accelerating channel as well as the parameters of the generated plasma streams were in strong dependence on the conditions on the electrodes.

Table 1.

Characteristics of the experimental devices

Installations	QSPA Kh-50	QSPA P-50	PPA
Parameters	Full-Block Quasi-Stationary Plasma Accelerator	Quasi-Stationary Plasma Accelerator with Passive Electrodes	Pulsed Plasma Accelerator
Mean ion energy, keV	≤ 0.9	≤ 0.2	≤ 5.0
Plasma stream density, cm^{-3}	≤ 5.10^{16} (Z=0.5 m) ≤ 2.10^{15} (Z=3.0 m)	≤ 2.10^{16} (Z=0.5 m) ≤ 10^{15} (Z=2.0 m)	≤ 10^{15} (Z=0.5 m)
Electron temperature, eV	≤ 4	≤ 4	≤ 50
Plasma stream energy, kJ	≤ 600	≤ 40	≤ 10
Plasma energy density, J/cm^2	2000 (Z=0.5 m) 200 (Z=3.0 m)	≤ 120 (Z=2.0 m)	≤ 40
Mean plasma diameter,cm	≤ 20 (Z=0.5 m) ≤ 100 (Z=3.0 m)	≤ 10 (Z=0.5 m) ≤ 40 (Z=2.0 m)	≤ 15
Plasma discharge duration,μs	300	300	5
Plasma stream generation duration, $\Delta\tau_p$, μs	≤ 150	≤ 40	≤ 3
Main discharge capacitor bank			
Capacity, C, μF	7200	5600	111
Voltage, U, kV	≤ 15	≤ 8	≤ 30

Schematic and general view of experimental stand of QSPA Kh-50, that is largest and most powerful device of this kind, is presented in Fig. 1. Electrodes configuration of QSPA P-50 and typical image of generated plasma stream are shown in Fig. 2. General view of upgraded PPA stand of pulsed plasma accelerator adjusted for technological tasks is shown in Fig. 3.

The full-block powerful quasi–steady–state plasma accelerator QSPA Kh–50 consists of two stages. The first one is used for plasma production and pre–acceleration. The second stage (main accelerating channel) is a coaxial system of shaped active electrodes–transformers with magnetically screened elements (those elements are current supplied either

from independent power sources or branching partly the discharge current in self–consistent regime of operation). The maximum total energy of capacitor banks supplying all active elements of the QSPA achieved 4 MJ. Design of accelerator is described in details in [8-11]. Plasma streams, generated by QSPA Kh-50 are injected into magnetic system of 1.6 m in length and 0.44 m in inner diameter consisting of 4 separate magnetic coils. The first magnetic coil is placed at the distance of Z_S = 1.2 m from accelerator output. The currents in each coil are specially selected to provide plasma streams propagation in slowly increasing magnetic field. The maximum value of magnetic field B_0=0.7 T was achieved in diagnostic chamber Z_S = 2.2-2.4 m from accelerator output.

The instrumentation for diagnostics of plasma flow in the accelerating channel and the parameters of the generated plasma streams includes a set of Rogowski coils, frequency-compensated voltage dividers, electric and magnetic probes, piezodetectors, bolometer, local movable calorimeters, high-speed cameras in different modifications, time-of-fly energy analyzer. The plasma stream density was determined from the Stark broadening of the H_β and self-absorption H_α spectral lines, or spectral lines of He, Ar, N [12], and also by using the autocollimation interferometer with view area of 200 mm in diameter. The velocity of different parts of the plasma stream was measured on the basis of time-dependent modulation of radiation using the slit scanning and registration by a high-speed camera, as well as by measuring the Doppler shift of spectral lines CII (λ=4267 Å) and self-absorption H_α (when working with hydrogen), or HeII (λ=4686 Å) and CII (λ=4267 Å) (for helium), or ArII (λ=6643 Å) and NII (λ=4630 Å) (when working with argon and nitrogen, respectively). Electron temperature was evaluated by the ratio of spectral lines intensities, or by the analysis of contours of self-absorption spectral line Hα.

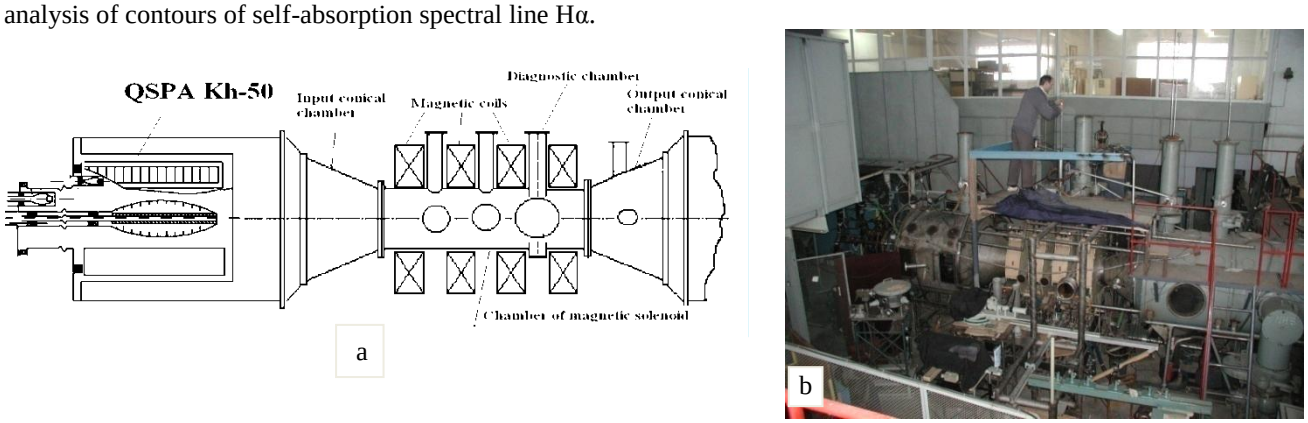

Fig.1. QSPA Kh-50 experimental stand

a – scheme, b - general view.

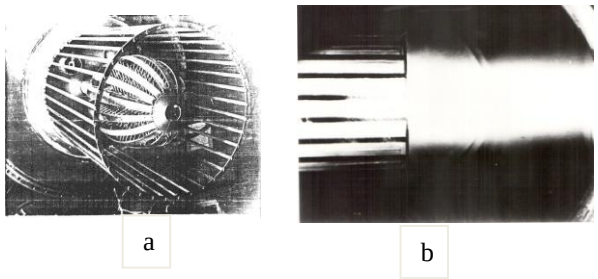

Fig.2. Electrodes of QSPA P-50 (a) and plasma stream photo (b).

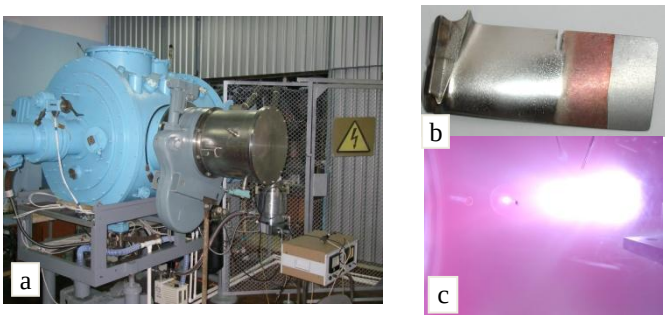

Fig.3. Upgraded PPA stand of pulsed plasma accelerator adjusted for technological tasks (a), plasma plume (c) and treated sample (b)

QSPA APPLICATION FOR SIMULATION OF TRANSIENT EVENTS IN ITER TOKAMAK-REACTOR

Experimental investigations of plasma-surface interaction (PSI) in conditions simulating transient events in fusion reactor ITER are of importance for the determination of erosion mechanisms of plasma facing materials, dynamics of erosion products, the impurities transport in the plasma, the vapor shield effects and its influence on plasma energy transfer to the material surface. In turn, the obtained results are used for validation of predictive models developed for ITER and DEMO, estimation of tolerable size of Type I ELMs and lifetime of divertor armour materials.

Energy range of ITER disruptions is Q_{disr} = (10-100) MJ/m^2, t = 1–10 ms. This is two orders of magnitude higher being far above of that in available tokamaks. Therefore, at present for experimental study of plasma-target interaction under the high heat loads the powerful plasma accelerators and other powerful simulators are be applied [13,14]. Quasi-stationary plasma accelerators (QSPA), which are characterized by essentially longer duration of plasma stream in comparison with pulsed plasma guns, are especially attractive for investigations of macroscopic erosion of tokamak armor materials under the loads expected at ITER off-normal events. In turn, the obtained experimental results are used for validation of the predictive numerical models. Therefore, largest in the word QSPA Kh-50, became unique and

practically most adequate simulator of plasma-surface interaction during ITER transient events, resulting in huge energy densities impacting to the divertor material surfaces.

Extrapolation of the ELMs erosion effects obtained at the present-day tokamaks to the transient peak loads of ITER remains uncertain. Experimental observations from different machines pointed out similarities and the open questions, which require further investigations are overviewed in [15,16]. The obtained power loads associated with the Type I ELMs generally do not affect the lifetime of divertor elements. However, the ITER ELMs may lead to unacceptable lifetime; their loads are estimated as Q_{ELM}= (1-3) MJ/m^2 at t = 0.1–1 ms and the repetition frequency of an order of 1 Hz (~ 400 ELMs during each ITER pulse. Special investigations on material behavior at the ELM relevant loads (both numerical and experimental) are thus very important.

In disruption and ELMs simulation experiments with QSPA Kh-50, the plasma stream parameters were varied by both changing the dynamics and quantity of gas filled the accelerator channel and changing the working voltage of capacitor battery of the main discharge. To achieve the working regimes for simulation both the disruptive and ELM-like plasma impacts, the main attention in these experiments was paid to possibility of effective variation of plasma stream energy density in wide range and determination of target heat load in dependence on plasma stream energy density.

Plasma parameters measured for 2 working regimes with plasma energy density of about 1 MJ/m^2 and 25-30 MJ/m^2 respectively, which were chosen for simulation experiments, are summarized in Table 2. Taking into account essentially longer duration of the thermal quench of ITER disruption, for disruption simulation regime special efforts were done to increase the plasma pressure in QSPA plasma stream up to 1.6-1.8 MPa. As it was shown in [17], this allowed to make clear the influence of plasma pressure gradient on melt motion even for QSPA plasma pulse duration and to approach the melt velocities to those expected for ITER disruptions.

Table 2.

Main parameters of QSPA Kh-50 plasma streams in different working regimes

	Disruption simulation regime	ELM simulation regime
Discharge duration [ms]	~0.3	0.28
Power pulse half-height width [ms]	0.1-0.14	0.1-0.12
Heat input [MJ/m^2]	25-30	0.9-1.5
Heat load on sample surface [MJ/m^2]	0.65-1.1	0.45-0.75
Maximal plasma stream pressure [MPa]	1.6-1.8	0.48
Average plasma density [10^{16} cm^{-3}]	4-8	1.5-2.5
Ions energy [keV]	~ 0.6	~ 0.2
Spot size of treated surface [cm]	10-12	12-14

Vapor shield effects

The key feature of plasma-surface interaction under disruption heat loads is vapor shield formation in front of material surface. Temporal and spatial distributions of plasma density in the shielding layer have been obtained with laser interferometry. Fig. 4. shows typical interferometric picture of high power plasma stream interaction with graphite surface and shielding layer in the vicinity of target surface. The plasma density in the shield is more than one order of magnitude higher in comparison with that in impacting plasma stream. Spatial distribution of electron density strongly depends on the energy density of the plasma stream and target size. The thickness of the shielding layer, formed close to the graphite target under normal irradiation of surface with plasma energy density of 25 MJ/m^2, which is expected for ITER disruptions, can be evaluated from Fig. 4. The figure shows that shielding layer thickness, being equal (1-2) cm for sample irradiation with no magnetic field, is exceeded 5 cm for B_{z0} = 0.72 T. The thickness of shielding layer grows with increasing magnetic field value and time of plasma interaction with a target.

Formation of dense plasma layer in front of the surface protects the material from the contact with impacting plasma. Thickness of the shielding layer essentially exceeds the particles free path. Shielding efficiency of carbon vapor is analyzed in [10,14], and, typically, only few percents of impacting plasma energy reaches the surface for disruption plasma loads. Dissipation of the plasma stream energy in the shielding layer results in shield expansion, heating and re-irradiated by the shield. Intense radiation from the shield may affect to the nearby surfaces of the ITER divertor, which are not contacted with plasma.

Measurements of radiation from the plasma shield in wavelength range of $\lambda \leq 3000$ Å have been performed with pyroelectric bolometer in regime of radiative calorimeter (Fig. 5). It is shown intensity of radiation from the shielding layer is in 7-10 times higher in comparison with free plasma stream (Fig. 6). Maximum of radiation is registered not from the near surface layer, but from thin region of ~ 5 mm corresponding to periphery zone of the shielding layer (2-3 cm from the surface) being contacting with impacting plasma stream.

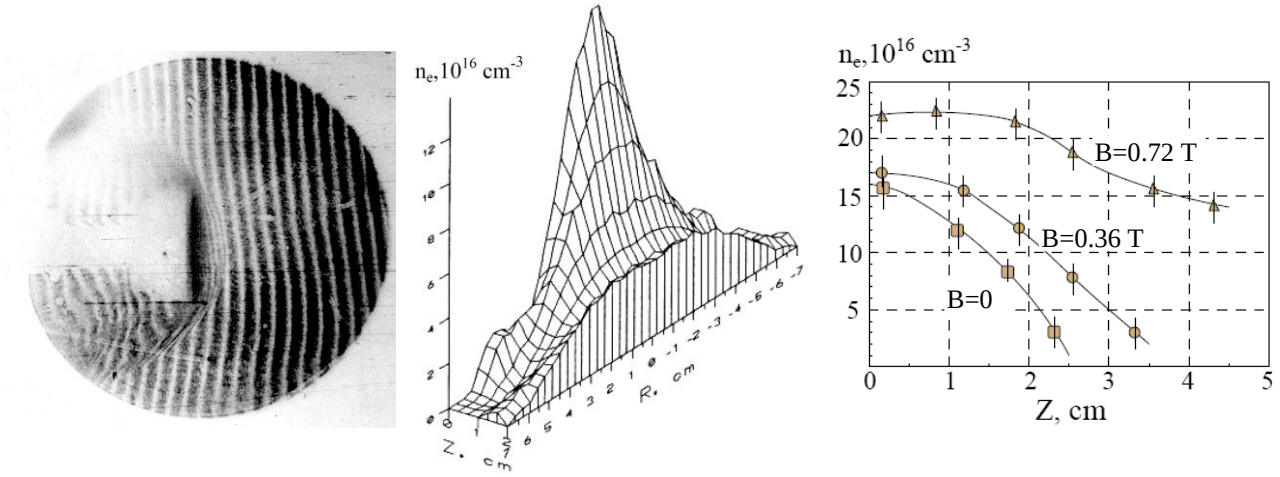

a b c

Fig. 4. Formation of vapor shield in front of the exposed surface
a - interferometric picture of plasma stream interaction with graphite target; b,c- electron density distributions in plasma shield. E=25 MJ/m^2, $\Delta\tau$=20 μs from the beginning of plasma interaction with the surface. Z=0 corresponds to the target surface

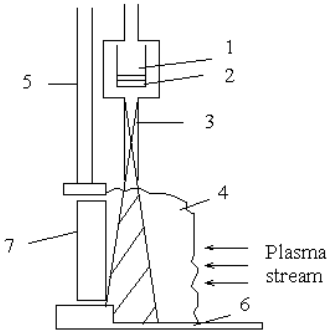

Fig. 5. Scheme of the bolometric measurements.1 - $LiNbO_3$ detector, 2 - LiF filter, 3-diaphragms, 4 - shielding layer, 5 - holder, 6 - restrictor, 7 - target

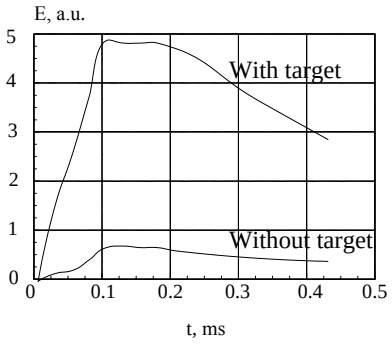

Fig.6. Intensity of radiation from the plasma stream and shielding layer in front of the target.

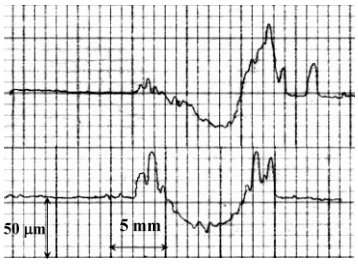

Fig. 7. Melt layer profiles on the exposed inclined surface in direction of inclination (upper) and in perpendicular direction (lower). Inclination angle $\alpha = 20^0$.

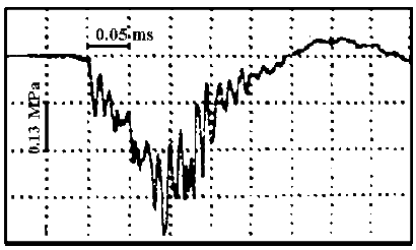

Fig. 8. Temporal behavior of plasma pressure in ELM simulation experiments. Z=2.3 m from accelerator output.

In spite of strong shielding, any metal surface will be subjected to strong melting during the disruption. The melt layer is subjected to external forces such as surface tension, gradients of both plasma pressure and recoil pressure of evaporating material, Lorentz force and others. The disruption simulation experiments with QSPA Kh-50 have shown that melt motion driven by external forces produces significant macroscopic erosion of materials. In particular, melt layer motion driven by plasma pressure results in erosion crater formation with rather large mountains of the resolidified material at the crater edge. Example of erosion crater appeared due to the melt motion on the metal surface exposed with inclined plasma stream impact is presented in Fig. 7.

Impacts of repetitive ELMs

Plasma pressure during ITER ELMs is anticipated to be essentially lower in comparison with disruptions. Therefore one possible to expected much smaller effects from the melt motion. In this case other macroscopic mechanisms such as brittle destruction and cracking may dominate the erosion, exceeding essentially contribution from microscopic mechanisms like sputtering or even evaporation.

ELM-simulation regimes in QSPA Kh-50 are characterized by experimentally chosen heat loads, which do not lead to the surface melting for tested tungsten samples, or result in melting initiation. Describing the plasma stream parameters for this regime it should be mentioned in addition to the data of Table 2, that triangular shape of plasma heat load has been realized. This simple shape is quite suitable for simulation of ITER ELM impacts. Temporal dependence of plasma pressure for this regime is presented in Fig. 8. Duration of plasma stream achieved 0.25 ms.

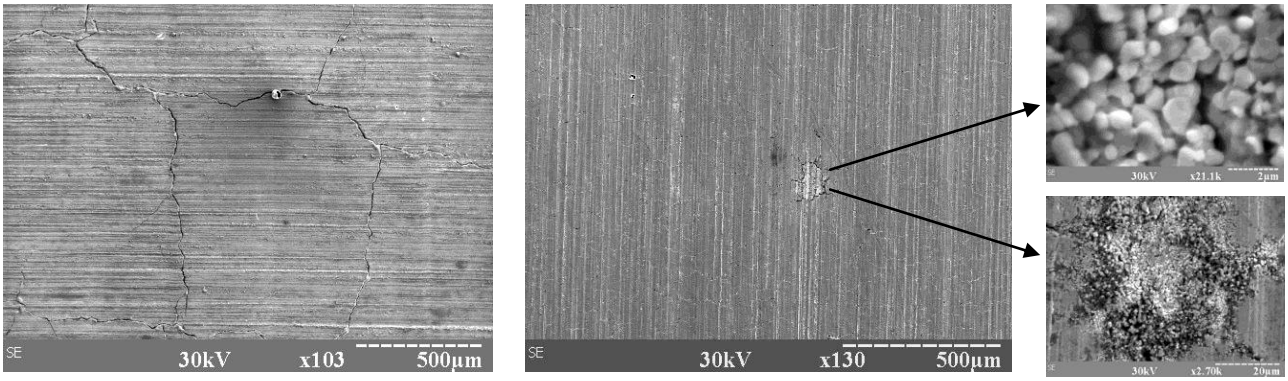

a) b)

Fig. 9. Tungsten surface after 210 plasma pulses of 0.45 MJ/m^2.
a) - RT target, b) - preheated target 650 C with enlarged images of the surface damage.

Examples of tungsten material damage below the melting threshold in ELM simulation experiments are presented in Fig. 9 for samples with different initial temperatures. Tungsten is primary choice for ITER divertor armour and even candidate for the DEMO first wall and divertor. It has highest melting temperature, low sputtering yield large sputtering threshold energy. Trinium retention in tungsten is also acceptable. However, main drawback is that tungsten is brittle material under moderate temperatures, the ductile-to-brittle transition temperature (DBTT) for some W grades may achieve 200-600 C. Brittleness of W gives rise to surface cracking. To minimize the brittle destruction erosion, the W-armor have to be kept above the DBTT. Analysis of effects of W temperature on material damage under ELMs impacts requires comprehensive experimental studies that now in progress in many fusion laboratories [18,19].

It is seen from Fig. 9, that for room temperature target the mesh of major cracks is developed on the surface, while for the material preheated to 650 C, the macro-cracks are absent. Nevertheless micro-cracks are registered on preheated surface. Thus, it is shown that tungsten cracking can not be completely mitigated by the preheating above the DBTT, but it can be essentially minimized, especially under the irradiation below the melting threshold. Tungsten preheating above DBTT allows suppressing the macrocracks formation on the surface. After first hundred of plasma pulses only microcracks were found and it can be classified as fatigue cracks resulting from repetitive stresses induced by numerous plasma impacts. Large number of pulses results also in surface modification (Fig 9,b) and formation of submicron structures. With further pulses such structures occupy all the surface and the tungsten, melting point decreases due to decreased heat conductivity in the modified layer. The surface became significantly damaged even after exposures with quite small energy loads.

Evolution of preheated tungsten surface as a result of plasma loads causing surface melting is demonstrated in Fig. 10. As follows from microscopy observation the surface is rather stable with increasing number of exposures up to 100-130 pulses. A blister-like structures and bubbles with the size of 100-300 μm are arisen on the surface after 100 pulses. The balls of nano size are registered inside the blister voids and in the crack volumes. Their size is varied within 10 nm - 1 μm. Surface modification with formation of cellular submicron structures is also occurs.

The most important changes in surface morphology are observed after increase of the exposition dose above 200 pulses, which results in qualitative evolution of the surface similar to that observed for exposures of RT targets in regimes with the same heat load of 0.75 MJ/m^2 and with the heat load of 1.1 MJ/m^2 (corresponds to the evaporation start) after similar number of pulses. The obtained results show that after the threshold number of exposures qualitative evolution of the surface is practically the same for all the cases mentioned above.

Due to the corrugations, the initially uniform melt layer tends to be transformed into “shagreen leather”. The width of the micro-cracks gradually increases with increasing the number of exposures, achieving 0.8-1.5 μm after 100 pulses and up to 20 μm after 200 pulses. Initially, the fine network of the cracks is remelted from pulse to pulse. With increasing width of the intergranular cracks, the surface became micro-brush-like, where surface areas of 20-50 μm are separated from each other. The following remelting with next pulses does not result furthermore in mixing because of the increased depth and width of the cracks and negligible melt motion during single pulse. Being separated, each cell

of the cracks network subjected to action of the surface tension directed to the minimization of cell area and under the large number of repetitive exposures the total contribution of plasma pulses results in progressive corrugation of the surface.

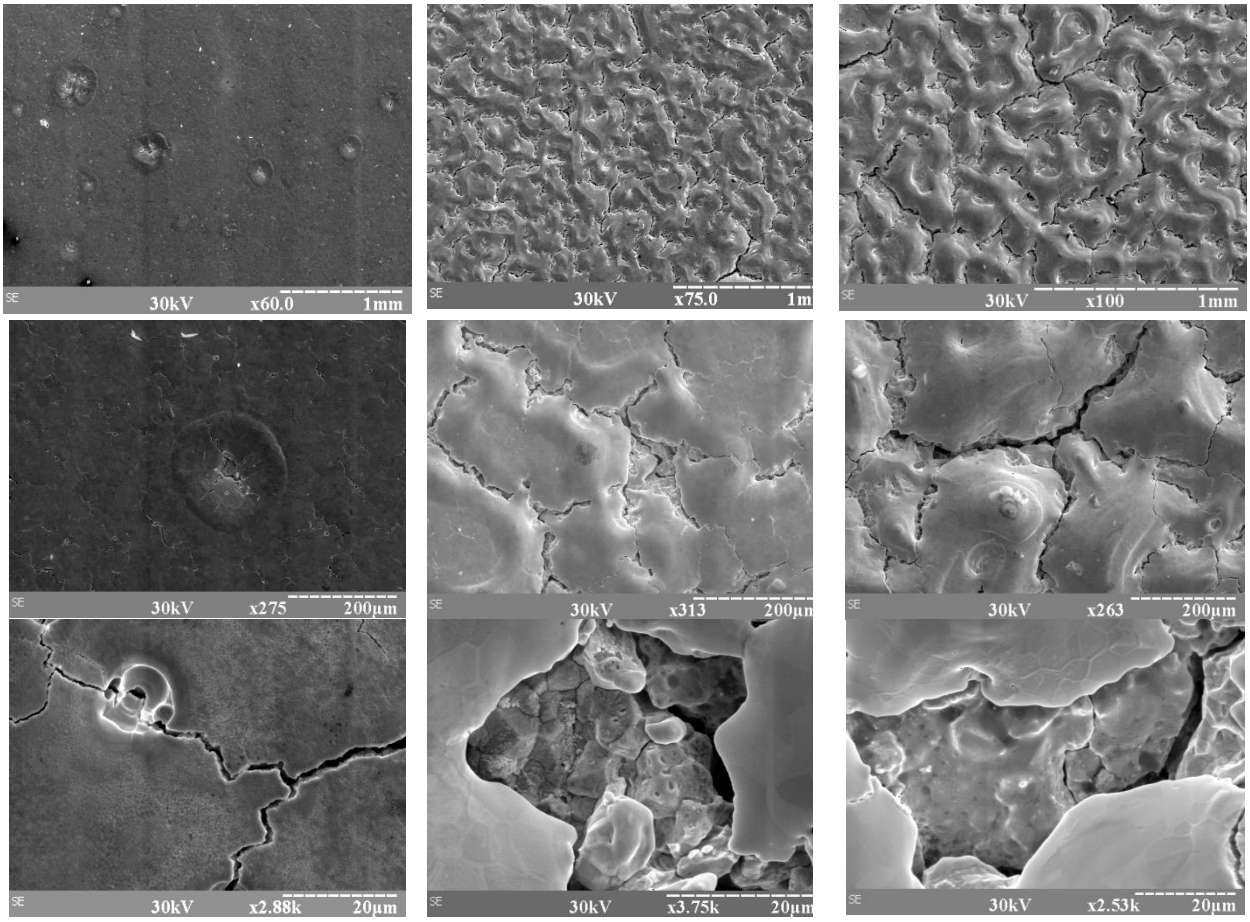

a b c

Fig. 10. SEM images of the tungsten surface
a – after 100, b – after 210, and c - after 350 pulses with different magnification

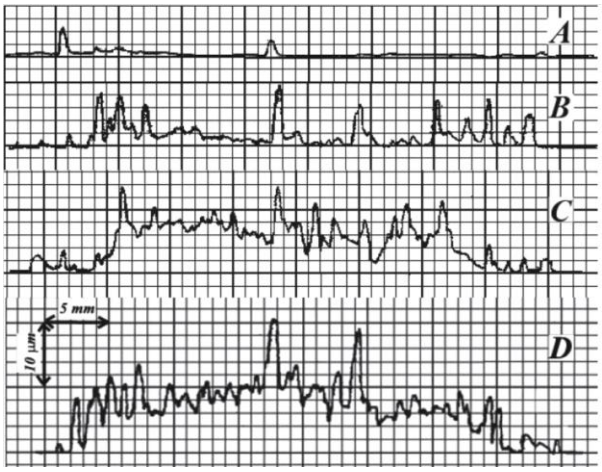

Fig. 11. Evolution of surface profiles of preheated tungsten in the course of plasma exposures.
A - 80 pulses, B - 150 pulses, C - 210 pulses, D - 350 pulses

Further evolution of the surface pattern is caused by loss of separated grains on exposed surface with increased number of impacts. It is seen that in result of 350 pulses (Fig.10,c) the surface became essentially destroyed by cracks. Thus, the damage, caused by cracking, became dominating after several hundreds of exposures, even for preheated target. The microscopy observations well correlate with profile measurements. The profile swelling, which is registered after 200 pulses, is caused by threshold changes in surface morphology (Fig.11).

Mechanisms of dust generation

Another important issue in ELM simulation experiments is generation of W dust in result of plasma impacts. The dust particles may penetrate in to the plasma core and thus to cool immediately the plasma. Also tritium retention due to developed surface area in dust layers has to be clarified. Performed studies of plasma-surface interaction in QSPA Kh-50 included measurements of plasma parameters in front of the exposed surfaces for normal and inclined plasma stream incidence, impurities dynamics in near-surface plasma and energy deposited to the material surface. Particular attention is paid to the material erosion due to particles ejection from the tungsten surfaces both in the form of droplets and solid dust.

The erosion products flying from the tungsten target have been registered using high-speed 10 bit CMOS digital

camera pco.1200 s from PCO AG with the exposure time 1μs…2ms, spectral range 290…1100 nm and space resolution of 1280×1024 pixels. Information from several camera frames with traces of particles flying from the tungsten surface after plasma shot (Fig. 12) allow calculation of the particles velocity and the time moment when it started from the target surface. Additionally the mass loss of the target was measured after several shots. Erosion products ejected in the form of droplets and solid dust were also collected and examined with microscopy.

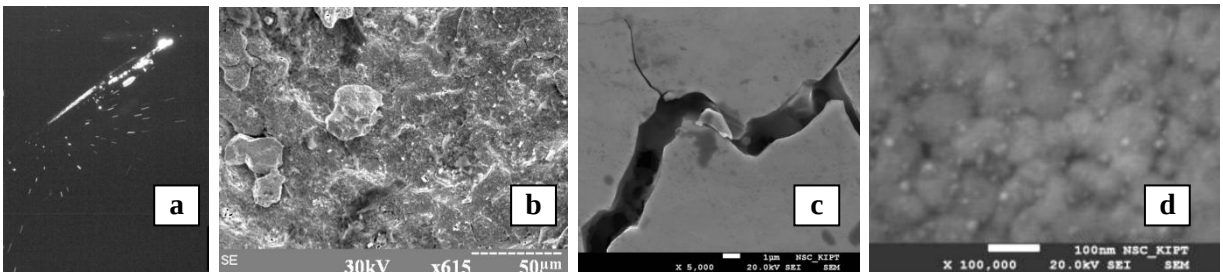

Fig. 12. Dust particles traces from inclined W target (a) and collected dust resulted from grain losses (b), cracking development (c) and W nano-powder due to the surface modification (d).

In recent studies with QSPA Kh-50 several mechanisms of dust generation under the transient energy loads to the tungsten surfaces have been recognized and identified basing on dust dynamics analysis, and particles characterization. Dust particles with sizes up to tens μm are ejected from the surface due to the cracking development and major cracks bifurcation. This mechanism would be dominating for first transient impacts when major crack mesh is formed. The energy loads in this case may not result in the melting, but it have to be above the cracking threshold. Taking into account that for many repetitive pulses the cracking threshold shifts to smaller energy loads, this mechanism can only be enfeebled by tungsten preheating above the ductile-to-brittle transition temperature. Fatigue cracks are still able to be developed after a large number of transient impacts to the preheated W surface [19]. This is a source of smaller dust. For plasma exposures with energy loads above the melting threshold both droplets splashing and solid dust ejection is observed. Melting of surface and development of fine meshes of cracks along the grain boundaries are accompanied by resolidified bridges formation through the fine cracks in the course of melt motion and capillary effects. With next impacts (even without melting) such bridges produce nm-size W dust. For this mechanism the mass taken away by any single particle is much smaller, but the number of dust particles is considerable.

Furthermore, even if mitigated cracking, the effects of surface modification of tungsten material after the repetitive plasma pulses with development of ordered submicron cellular structures [21] are able to contribute significantly to the nm-dust generation (Fig. 13). However the obtained experimental results show that majority of generated dust nano-particles, generated due to cells evolutions, are deposited back to the surface by a plasma pressure, in contrast to μm-size dust. This result is confirmed by spectroscopy measurements of W impurities in plasma in front of the surface. The results of QSPA plasma exposures are compared with short pulse PSI experiments (τ~ 0.1-5 μs) with pulsed plasma gun and dense plasma focus facilities [22], aiming at features of surface damage and tungsten impurities behaviour in near-surface plasma in front of the target.

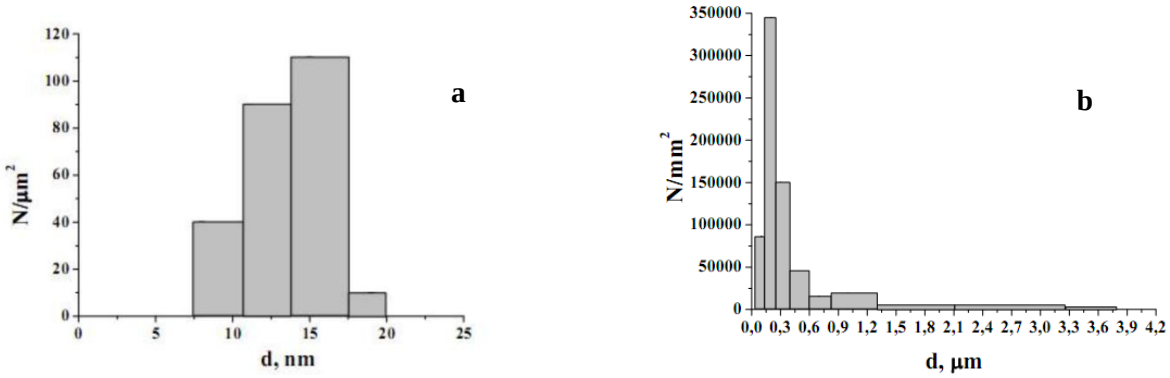

Fig. 13. Size distributions of W nano-particles (a) and collected W balls in crack voids (b)

MATERIALS MODIFICATION WITH POWERFUL PULSED PLASMA PROCESSING: FROM SURFACE DAMAGE TO THE MATERIAL IMPROVEMENT

Surface processing with pulsed plasma streams of different gases under moderate energy density range is found to be effective tool for modification of surface layers of various steel materials [23-26]. In particular, exposures with pulsed powerful plasma streams result in hardening their surfaces and increasing the wear resistance of industrial steels. In such “intelligent” regimes of plasma treatment the energy densities are adjusted to produce surface modification rather than erosion. Typically the heat load to the surface is above the melting threshold but essentially lower the

evaporation limit. Fast heating and melting of treated surface, considerable temperature gradients (~ 10^6 K/cm) arising in surface layer of material under the pulsed plasma impact contribute to high speed diffusion of plasma stream ions into the depth of the modified layer, during the liquid stage, phase changes in the surface layer, and formation of the fine-grained or quasi-amorphous structures under the following fast resolidification. The cooling speed of ~10^6-10^7 K/s is achieved in this case due to the contact of thin melt layer (h_{melt} ~ 10-50 μm) with massive bulk of the sample. Plasma can also be considered as a source of alloying elements to be introduced into modified layer structure. That is why nitrogen is preferentially used for pulsed plasma processing of different steels. Another possibility of alloying under the pulsed plasma processing is mixing of previously deposited thin (h_{coat}< h_{melt}) coatings of different predetermined composition with the substrate in result of powerful plasma impact.

Examples of modified surface layer structures for different materials are presented in Fig. 14. Analysis of samples cross-sections was performed for different materials processed with helium, oxygen and nitrogen plasma streams. Adjustment of plasma treatment regimes of processed materials was done to achieve optimal thickness of modified layer with simultaneously minimal value of surface roughness. Depth of aluminium modified layer under oxygen plasma treatment achieved 50 μm, microhardness in modified layer ~ 316 kg/ mm^2.

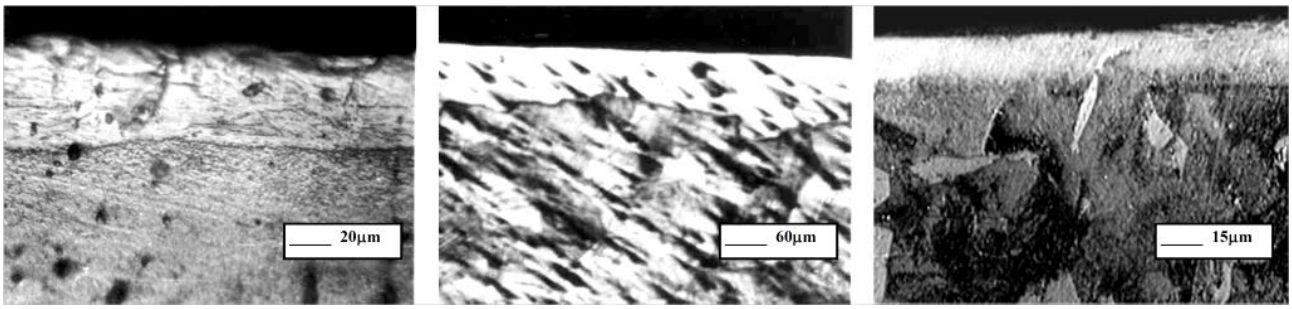

a b c

Fig. 14. Cross-sections of processed materials
a - Al processed with oxygen plasma, b - Ti-alloy VT22 processed with helium plasma, c - steel 40H processed with nitrogen plasma.

Using the light-weight gas for material treatment allowed to increase both pulse duration (up to 10-15μs) and energy density load to the sample surface (up to 50 J/cm^2). Therefore it was possible to increase the depth of modified layer for titanium alloy samples up to 100 μm under processing with He plasma streams. Modified layer of titanium alloy is not polarised and possibly consist on amorphous or β-Ti.

For different steels treatment with pulsed nitrogen plasma streams, it was formation of γ-Fe and nitrides as well as increase in the quantity of nitrides (mainly of ε-Fe2N) with increasing dose of the treatment. Stabilization of γ-Fe in modified layer was determined mainly by high temperature heating the surface under plasma processing and rapid cooling. However the quantity of nitrides is strongly depended on concentration of chromium, nickel and other alloying elements. The decrease of α-Fe lattice period and its increase for γ-Fe, decreasing the relative intensities of diffraction lines of phases α-Fe and γ-Fe, broadening of diffraction profiles can be considered as typical feature of processing by pulsed plasma streams. This can be attribute of surface amorphyzation.

More detailed studies of modified steels with CEMS spectroscopy revealed that modification of surface layer accompanied only partially by γ-Fe, but it is attributed mainly by formation of γ_N phase [27]. This phase has been named as oversaturated austenite, i.e austenite in which an Fe atom has an interstitial nitrogen atom in the nearest neighbor.

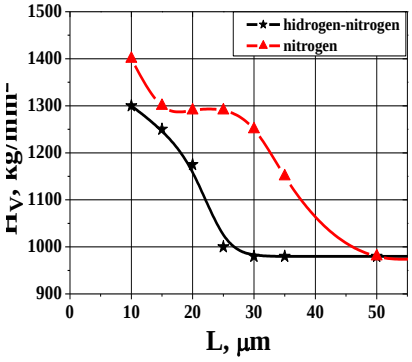

Fig. 15. Microhardness depth profiles of WC-20Co samples

Fig. 15 shows microhardness dependence on the depth of modified layer for the plasma treated WC-20Co samples. It should be noted that pulsed plasma processing with impacting particle dose of $5{\cdot}10^{18}$ ion/cm^2 leads to increasing microhardness from 1000 kg/mm^2 to 1400 kg/mm^2. Thickness of the layer with increased microhardness achieved 50 μm. Maximum value of Hv ≈1300 kg/mm^2 is observed WC-20Co surface in result of exposure with plasma stream which consists of the mixture of hydrogen and nitrogen in proportion of 1:1 and with the same dose of $5{\cdot}10^{18}cm^{-2}$. Similar increase has been observed after pure hydrogen plasma exposures. This means that in this case microhardness changes are probably caused by high-speed plasma quenching, i.e. predominantly thermal effects and only minor influence of nitrogening on the microhardness behaviour. Microhardness of the exposed surface is slightly decreased with further increase of the exposition dose. It can be caused by changes of phase composition of the modified layer in result of repetitive heating and cooling under pulsed plasma heat loads [28].

XRD showed that only WC phase is registered on the initial surface of WC-8Co. The high-temperature carbide phase W_2C with smaller content of carbon is appeared in the surface layer after nitrogen plasma impacts. Simultaneously, the content of WC is considerably decreased. Thus, primary removal of light component-carbon and saturation of surface layer by atoms of tungsten is observed. It can be caused by a selective sputtering of carbon under bombardment of WC-8Co by N^+ ions. In addition, halo is observed in diffraction patterns of irradiated target in the range of 25º-60º of 2Θ angles with maximum located at 40º. This is an indication of amorphous film development on the exposed surface, which may include both carbides and carbonitrides of tungsten and cobalt.

The virgin sample of WC-20Co is characterized by WC and α-Co phases. The phase structure of WC-20Co after irradiation with nitrogen plasma consists of the main carbide phase WC, α-Co and appeared small quantity of W_2C. An oxide phase CoO is not detected. In this case difractogramm has a wide halo area also, which is located in the same range of 2Θ angles.

Modification of thin (0.5-2 μm) PVD coatings of MoN, C+W, TiN, TiC, Cr, Cr+CrN and others with the pulsed plasma processing are analyzed also. It is shown that pulsed plasma treatment results in essential improvement of physical and mechanical properties of exposed materials. For example, microhardness of samples with Cr coating, after plasma treatment, increased in 2,5 times [29,30].

Experiments with different steels and cast iron reveal possibility for essential improvement of wear resistance in result of applied combination of coatings deposition with pulsed plasma processing. Alloying of surface layer in result of the coating-substrate mixing in liquid stage allows achievement of desirable chemical composition in surface layers being most loaded in all machine components. In particular, combined plasma processing is found to be prospective for modification of piston rings and other machine parts operating in conditions of bearing or dry friction.

CONCLUSION

Basic principles of high current plasma accelerators and recent state of their investigations in IPP NSC KIPT are briefly described. In such devices an internal magnetic field is created by high current up to several MA in the discharge and it is used for both plasma flow acceleration up to 10^3 km/s.

It is shown that quasi- stationary plasma accelerators (QSPA) are especially attractive systems from the point of view dense plasma generation with super high energy contentment that can be realized in long pulse operational regime, while short pulsed plasma guns have great potential for technological usage due to the high efficiency in combination with their robust design.

Results of simulation experiments relevant to plasma surface interactions in extreme conditions of thermonuclear reactor are discussed emphasizing key physical effects of plasma energy transfer under powerful plasma impacts to the material surface, erosion mechanisms and their contribution under various conditions, dynamics of erosion products as well as and resulting material damage.

Experimental studies of surface modification by pulsed plasma processing using pulsed plasma accelerator (PPA) operating with various working gases have revealed possibility of essential improvements of material properties, increase of microhardness and wear resistance in surface layers in result of plasma treatment, favorable structure changes in modified layers accompanied by material alloying from gas and metallic plasma, as well as due to the mixing process in liquid phase.

ACKNOWLEDGEMENTS

This paper reviews experimental results obtained in the Laboratory of Plasma Accelerators in IPP NSC KIPT during several years, and, partially, within international collaborations. The contribution of all team members participating in experiments is deeply appreciated.

REFERENCES

1. Encyclopedia of Low Temperature Plasma. – Vol. III / Ed. V.E. Fortov. – Moscow: Nauka, 2000.
2. Fizika i Primenenie Plazmennyh Uskoritelej. – Minsk: Nauka i Tekn, 1974. (in Russian).
3. Morozov A.I., Solov'yov L.S. Stationary plasma streams in a magnetic field // Voprosy Teorii Plazmy. – 1974. - Vol.8. - P.3-87. (in Russian).
4. Morozov A.I. Principles of quasistationary plasma accelerators (QSPA) // Sov. J. Plasma Phys. – 1990. - Vol.16 (2). - P. 48.
5. Tereshin V.I. et al. Investigation of powerful quasi-stationary coaxial plasma accelerators with rod electrodes. In book: Ionnye Inzhektory i Plasmennye Uskoriteli. – Moscow: Energoatomizdat, 1989. - P.106-123. (in Russian).
6. Voloshko A.Yu. et al. Study of two-stage quasistationary plasma accelerator (QSPA) with rod electrodes // Sov. J. Plasma Phys. – 1990. - Vol.16 (2). - P.85-91.
7. Voloshko A.Yu. et al. Investigation of the local parameters of plasma flow in a two-stage QSPA P-50 //Sov. J. Plasma Phys. - 1990. - Vol.16 (2). - P.91-95.
8. Kulik N.V. et al. Main characteristics of a high-power full scale quasi-stationary plasma accelerator QSPA Kh-50 and some results of preliminary experiments / 18th European Conference on Controlled Fusion and Plasma Phys. - 1991, Contributed papers, part III. - P.41-44.
9. Morozov A.I. et al. QSPA Kh-50 full scale high power quasistationary plasma accelerator // Plasma Devices and Operations. – 1992. - Vol.2. - P.155-165.

10. Tereshin V.I. Quasi-stationary plasma accelerators ant their applications // Plasma Phys. Contr. Fus. – 1995. - Vol.37. - P.A177-A190.
11. Tereshin V.I. et al. Powerful Quasi-Steady-State Plasma Accelerator for Fusion Experiments // Brazilian Journal of Physics. - 2002. - Vol.32, №1. - P.165-171.
12. Volkov Ya.F.et al. Investigation of plasma in cathode transformer of QSPA P-50 // Sov. J. Plasma Phys. - 1992. - Vol.18 (11). - P.718-723.
13. Arkhipov N.I. et al. Material erosion and erosion products in disruption simulation experiments at the MK-200 UG facility // Fus. Eng. and Design. – 2000. –Vol. 49-50. – P.151.
14. Chebotarev V.V., Garkusha I.E., Garkusha V.V. et.al. Characteristics of the transient plasma layers produced by irradiation of grap-hite targets by high power quasi-stationary plasma streams under the disruption modeling experiments // J. Nucl. Mater. - 1996. - Vol.233-237. - P.736-740.
15. Federici G. et al. Assessment of erosion of the ITER divertor targets during type I ELMs // Plasma Phys. Control. Fusion. – 2003. – Vol.45. – P. 1523.
16. Loarte A. et al. Characteristics of type I ELM energy and particle losses in existing devices and their extrapolation to ITER // Plasma Phys. Control. Fusion. – 2003. – Vol.45. – P.1549.
17. Tereshin V.I., Garkusha I.E., Bandura A.N. et.al. Influence of plasma pressure gradient on melt layer macroscopic erosion of metal targets in disruption simulation experiments // J. Nucl. Mater. - 2003. - Vol.313-316. - P.686-690.
18. Hirai T., et al. Cracking failure study of ITER-reference tungsten grade under single pulse thermal shock loads at elevated temperatures // Journ. Nucl. Mater. – 2009. - Vol. 390–391. - P. 751–754.
19. Garkusha I.E. et al. Latest Results from ELM-simulation Experiments in Plasma Accelerators // Physica Scripta. – 2009. - Vol.138. – P.014054.
20. Garkusha I.E. et al. Damage to Preheated Tungsten Targets after Multiple Plasma Impacts Simulating ITER ELMs // Journ. Nucl. Mater. – 2009. - Vol.386-388. - P.127-131.
21. Shoshin A.A. et al. Plasma-Surface Interaction During ITER Type 1 ELMs: Comparison of Simulation with QSPA KH-50 and the GOL-3 Facilities // Fusion Sci. and Techn. – 2011. - Vol.59, №1. - P.57-60.
22. Ladygina M.S. et al. Spectroscopy of Plasma Surface Interaction in Experiments Simulating ITER Transient Events // Fusion Sci. and Techn. – 2011. - Vol.60, №1T. - P.27-33.
23. Garkusha I.E., et. al. Properties of modified surface layers of industrial steels samples processed by pulsed plasma streams // Vacuum. – 2000. - Vol. 58. - P.195.
24. Tereshin V.I., et. al. Pulsed plasma accelerators of different gas ions for surface modification // Review of Scientific Instruments. – 2002. - Vol.73. - P. 831.
25. Uglov V.V., et. al. Formation of alloying layers in a carbon steel by compression plasma flows //Vacuum. – 2007. - Vol. 81. - P.1341.
26. Tereshin V.I., et.al. Coating deposition and surface modification under combined plasma processing // Vacuum. – 2004. - Vol.73. - P.555.
27. Langner J. et al. Surface modification of constructional steels by irradiation with high intensity pulsed nitrogen plasma beams // Surface and Coatings Technology. – 2000. – Vol.128-129. - P.105-111.
28. Makhlay V.A., et al. Features of materials alloying under exposures to pulsed plasma streams // European Physical Journal D. – 2009. – Vol.54. - P.185-188.
29. Byrka O.V., et al. Application of pulsed plasma streams for surface modification of constructional materials // Acta Technica. – 2011. - Vol.56. – P. T362-T372.
30. Bandura A.N., et al. Alloying and Modification of Structural Materials under Pulsed Plasma Treatment // International Journal of Plasma Environmental Science & Technology. – 2011. - Vol.5, №1. - P.2-6.

Garkusha Igor Evgenijovych, Dr. Sci, director of Institute of Plasma Physics of the NSC KIPT, professor in V.N. Karazin KhNU, Laureate of State Prize of Ukraine in the field of Science and Technology. Research activities include experimental plasma physics and controlled nuclear fusion, plasma dynamics and diagnostics, plasma-surface interaction and plasma technology (surface modification, coatings deposition, plasma processing in nanotechnology, plasma based EUV lithography), high voltage and vacuum techniques, surface analysis methods. Among the most important results: development and investigations of powerful quasi-steady-state and pulsed plasma accelerators, experimental simulation of ITER plasma loads and fusion materials damage in extreme conditions. He is co-author of "Encyclopedia of Low Temperature Plasma" book, 3 patents and more than 250 scientific publications.

UDC 539.165

STUDY OF NEUTRINO PROPERTIES AND WEAK INTERACTION IN DOUBLE BETA DECAY EXPERIMENTS

F.A. Danevich
Institute for Nuclear Research
prospekt Nauky 47 MSP 03680 Kyiv, Ukraine
e-mail: danevich@kinr.kiev.ua
Received 15 October 2012, accepted 15 January 2013

Investigation of the neutrinoless double beta decay is a unique way to probe physics beyond the Standard Model. The process is sensitive to the lepton number violation, the nature of neutrino (Majorana or Dirac particle), an absolute scale of neutrino mass and the neutrino mass hierarchy. Neutrinoless double beta decay is still not observed, only limits on its half-life were set in the most sensitive experiments. The searches for double beta decay are carried out by different methods, in particular with low-background scintillation and semiconductor detectors. To determine a neutrino mass hierarchy new generation experiment should be sensitive to the effective neutrino mass 0.02 – 0.05 eV, which corresponds to the half-lives $T_{1/2} \sim 10^{26} - 10^{27}$ years and requires ultra-low background detectors with a high energy resolution applying hundreds kilograms of the isotope of interest. Low temperature scintillating bolometers are the most promising technique for such experiments.
KEY WORDS: double beta decay, neutrino, weak interaction, low counting experiment

ИССЛЕДОВАНИЯ СВОЙСТВ НЕЙТРИНО И СЛАБОГО ВЗАИМОДЕЙСТВИЯ В ЭКСПЕРИМЕНТАХ ПО ПОИСКУ ДВОЙНОГО БЕТА-РАСПАДА АТОМНЫХ ЯДЕР

Ф.А. Даневич
Институт ядерных исследований НАН Украины
проспект Науки 47, МСП 03680 Киев, Украина

Исследования безнейтринного двойного бета-распада атомных ядер представляют собой уникальную возможность поиска новых физических эффектов за рамками стандартной модели элементарных частиц. Этот процесс чувствителен к нарушению закона сохранения лептонного числа, природе нейтрино (частица Дирака или Майораны), величине массы и схеме массовых состояний нейтрино. Безнейтринный двойной бета-распад все еще не обнаружен, во все более чувствительных экспериментах устанавливаются лишь пределы на его вероятность. Поиски двойного бета-распада ведутся разными методами, в частности с помощью низкофоновых сцинтилляционных и полупроводниковых детекторов. Для определения схемы массовых состояний нейтрино эксперимент должен иметь чувствительность к эффективной массе нейтрино на уровне 0.02 – 0.05 эВ, что соответствует периодам полураспада $T_{1/2} \sim 10^{26} - 10^{27}$ лет и требует создания сверхнизкофоновых детекторов с высоким энергетическим разрешением и массой исследуемого изотопа сотни килограммов. Низкотемпературные сцинтилляционные болометры представляют собой наиболее перспективную технику для осуществления таких опытов.
КЛЮЧЕВЫЕ СЛОВА: двойной бета-распад, нейтрино, слабое взаимодействие, низкофоновый эксперимент

ДОСЛІДЖЕННЯ ВЛАСТИВОСТЕЙ НЕЙТРИНО І СЛАБКОЇ ВЗАЄМОДІЇ В ЕКСПЕРИМЕНТАХ З ПОШУКУ ПОДВІЙНОГО БЕТА-РОЗПАДУ

Ф.А. Даневич
Інститут ядерних досліджень НАН України
проспект Науки 47, МСП 03680 Київ, Україна

Дослідження безнейтринного подвійного бета-розпаду атомних ядер являють собою унікальну можливість пошуку нових фізичних ефектів за рамками стандартної моделі елементарних частинок. Цей процес чутливий до порушення закону збереження лептонного числа, природи нейтрино (частинка Дірака чи Майорани), величини маси і схеми масових станів нейтрино. Безнейтринний подвійний бета-розпад все ще не виявлений, у все більш чутливих експериментах встановлюються лише межі на його вірогідність. Пошуки подвійного бета-розпаду ведуться різними методами, зокрема з допомогою низькофонових сцинтиляційних і напівпровідникових детекторів. Для визначення схеми масових станів нейтрино експеримент повинен мати чутливість до ефективної масі нейтрино на рівні 0.02 – 0.05 еВ, що відповідає періодам напіврозпаду $T_{1/2} \sim 10^{26} - 10^{27}$ років і вимагає створення наднизькофонових детекторів з високою енергетичною роздільною здатністю та масою досліджуваного ізотопу сотні кілограмів. Низькотемпературні сцинтиляційні болометри є найбільш перспективною технікою для здійснення таких дослідів.
КЛЮЧОВІ СЛОВА: подвійний бета-розпад, нейтрино, слабка взаємодія, низькофоновий експеримент

Properties of neutrino and weak interaction play a key role in particle physics, cosmology and astrophysics. Measurements of neutrino fluxes from the Sun, from cosmic rays in atmosphere, from reactors and accelerators give strong evidence of neutrino oscillations, an effect which cannot be explained in framework of the Standard Model of particles [1]. Search for neutrinoless double beta decay is considered now as an unique tool to study properties of neutrino. Study of this extremely rare nuclear decay with the help of nuclear spectrometry methods, without building of expensive accelerators, allows to investigate effects beyond the Standard Model: nature of neutrino (is neutrino Dirac or

Majorana particle), an absolute scale and the mass scheme of neutrino, to check the lepton number conservation, to probe existence of hypothetical Nambu-Goldstone bosons (majorons) and right-handed currents in weak interaction [2-9].

The half-life of 0ν2β decay rate depends on the effective Majorana mass of neutrino and admixtures of right handed currents in weak interaction:

$$\left(T_{1/2}^{0\nu 2\beta}\right)^{-1} = C_{mm}^{0\nu}\left(\frac{\langle m_\nu\rangle}{m_e}\right)^2 + C_{m\lambda}^{0\nu}\langle\lambda\rangle\left(\frac{\langle m_\nu\rangle}{m_e}\right) + C_{m\eta}^{0\nu}\langle\eta\rangle\left(\frac{\langle m_\nu\rangle}{m_e}\right) + C_{\lambda\lambda}^{0\nu}\langle\lambda\rangle^2 + C_{\eta\eta}^{0\nu}\langle\eta\rangle^2 + C_{\lambda\eta}^{0\nu}\langle\lambda\rangle\langle\eta\rangle,$$

where m_e is the electron mass, $\langle m_\nu\rangle$ is the effective Majorana neutrino mass, $\langle\lambda\rangle$ and $\langle\eta\rangle$ are the coupling strengths of the right-handed currents [10], coefficients $C_{ij}^{0\nu}$ can be defined through the nuclear matrix elements and phase space integrals of the 0ν2β decay. The effective Majorana mass of neutrino can be defined as following:

$$\langle m_\nu\rangle = \left|\sum U_{ej}^2 m_{\nu_i}\right|,$$

where m_{ν_i} are the mass eigenstates of neutrino, U_{ej} are the matrix elements of mixing between the mass eigenstates and flavor states of neutrino.

Investigations of double β decay are carrying out by different methods: geochemical, radiochemical, direct detection of the events by nuclear spectrometry. Taking into account an extremely low probability of the decay, the experimental facilities are placed deep underground in laboratories build in mines or tunnels. The two neutrino mode of the double β decay, being allowed in the Standard Model, is detected for 11 nuclei: ^{48}Ca, ^{76}Ge, ^{82}Se, ^{96}Zr, ^{100}Mo, ^{116}Cd, ^{128}Te, ^{130}Te, ^{136}Xe, ^{150}Nd and ^{238}U (see review [11] and references therein; for the recent observation of ^{136}Xe see [12,13]) with the half-lives in the range $T_{1/2} \sim 10^{19} - 10^{24}$ yr. In contrary, the neutrinoless decay is still not observed. Highest limits on the decay were set in direct experiments with several nuclei: $T_{1/2} \geq 10^{21}$ yr for ^{96}Zr [14], ^{114}Cd [15], ^{160}Gd [16], ^{150}Nd [17], ^{186}W [18]; $T_{1/2} \geq 10^{22}$ yr for ^{48}Ca [19], $T_{1/2} \geq 10^{23}$ yr for ^{82}Se [20,21], ^{100}Mo [22], ^{116}Cd [18], ^{128}Te [23], $T_{1/2} \geq 10^{24}$ yr for ^{130}Te [24] and $T_{1/2} \geq 10^{25}$ yr for ^{76}Ge [25,26] and ^{136}Xe [27,28]. These experiments restrict the effective Majorana neutrino mass $\langle m_\nu\rangle \leq (0.3 - 3)$ eV, the right-handed currents admixtures in the weak interaction ($\eta \leq 10^{-8}$, $\lambda \leq 10^{-8}$), the effective majoron-neutrino coupling constant ($g_M \leq 10^{-5}$). At the same time, HV Klapdor-Kleingrothaus with co-authors claims observation of 0ν2β decay of ^{76}Ge with the half-life $2.23^{+0.44}_{-0.31} \times 10^{25}$, which corresponds to the neutrino mass $\langle m_\nu\rangle = (0.32\pm0.03)$ eV [29]. Despite the skepticism of the scientific community, only new, more sensitive experiments could refute or confirm the claim.

Apart from the already running EXO and KamLand-Zen detectors [27,28], a few large-scale experiments are under construction or in R&D stage with the mass of isotopes of interest several tens – hundreds kg with the aim to achieve sensitivity to neutrinoless double β decay at the level of $T_{1/2} \sim 10^{26}$ yr, which corresponds to the neutrino mass $\langle m_\nu\rangle \sim 0.05$ eV. Taking into account the uncertainties of the theoretical calculations of the nuclear matrix elements, and the extremely low probability of the process, it is important to realize search for 0ν2β decay of different nuclei. Furthermore, to discard certainly an inverted hierarchy of the neutrino mass eigenstates one need to build experiments with the sensitivity to the neutrino mass on the level of 0.02 eV, which corresponds to the half-life $T_{1/2} \sim 10^{27}$ yr.

To achieve such a sensitivity a double β experiment should use about ton of isotope of interest, have an energy resolution of better than 1% and almost zero background. Cryogenic scintillating bolometers look only an option to realize such experiments with different nuclei [30] (in addition to germanium semiconductor detectors, which able to search by the calorimetric approach with high detection efficiency only ^{76}Ge). Currently, the most promising materials for cryogenic experiments are tellurium oxide crystals (assume simultaneous detection of Cerenkov light), zinc selenide, cadmium tungstate and zinc molybdate crystal scintillators.

Experimental investigations are concentrated mostly on $2\beta^-$ decays, processes featuring the emission of two electrons. Results for double positron decay ($2\beta^+$), electron capture with positron emission ($\varepsilon\beta^+$), and capture of two electrons from atomic shells (2ε) are much more modest. The most sensitive experiments give limits on the 2ε, $\varepsilon\beta^+$ and $2\beta^+$ processes on the level of $T_{1/2} \geq 10^{16} - 10^{21}$ yr. At the same time, studies of neutrinoless 2ε and $\varepsilon\beta^+$ decays could elaborate the mechanism of 0ν2β decay: is it due to the non-zero neutrino mass or to the right-handed admixtures in weak interactions [31,32]. Another important motivation to search for 0ν2ε decay appears from a possibility of a resonant process due to energy degeneracy between initial and final state of mother and daughter nuclei. Such a coincidence could give an enhancement of the 0ν2ε decay. The possibility of the resonant process was discussed in [33-36], where an increase of the decay rate by some orders of magnitude was predicted. Recent calculations show that the half-lives of some nuclei relatively to the neutrinoless electron capture can be comparable to the half-lives of the most promising 0ν2β decay candidates [37-39]. Several scintillation and HPGe experiments were performed to search for 2ε (including resonant processes on excited levels of daughter isotopes), $\varepsilon\beta^+$ and $2\beta^+$ decay in different nuclei.

In this paper, we review recent progress in the area of double beta decay experiments, in particular the results

obtained in the Institute for Nuclear Research (Kyiv, Ukraine) by using scintillation method and low-background HPGe gamma spectrometry. Development of cryogenic scintillating bolometers, which is extremely promising technique to go towards the inverted hierarchy of the neutrino mass, is briefly discussed.

SCINTILLATION EXPERIMENTS

Scintillators are successfully used in experiments to search for double β decay. It is worth to mention a pioneering work of der Mateosian and Goldhaber to search for neutrinoless 2β decay of ^{48}Ca by using enriched and depleted in ^{48}Ca ($^{48}CaF_2$(Eu) and $^{40}CaF_2$(Eu)) crystal scintillators [40]. Several 2β experiments were realized using crystal scintillators, which contain candidate nuclei (see Table I).

In the 2β experiment carried out in the Solotvina Underground Laboratory (Ukraine) with the help of enriched in ^{116}Cd cadmium tungstate crystal scintillators [18] a very low counting rate of 0.04 counts/(year keV kg) was reached in the energy window 2.5 – 3.2 MeV where a peak from the 0ν2β decay of ^{116}Cd was expected. The half-life limit on the neutrinoless 2β decay of ^{116}Cd was set as $T_{1/2} \geq 1.7 \times 10^{23}$ years at 90% confidence level, which corresponds to one of the strongest restriction on the effective Majorana neutrino mass $\langle m_\nu \rangle \leq 1.7$ eV.

Table 1.

The most sensitive double β experiments with crystal scintillators

2β transition	Scintillator	Main results: half-life (channels)	Years [References]
$^{40}Ca \rightarrow {}^{40}Ar$	CaF_2(Eu)	$\geq 5.9 \times 10^{21}$ yr (2ν2ε) $\geq 3.0 \times 10^{21}$ yr (0ν2ε)	1997 [41]
$^{48}Ca \rightarrow {}^{48}Ti$	CaF_2(Eu)	$\geq 1.4 \times 10^{22}$ yr (0ν2β) $\geq 5.8 \times 10^{22}$ yr (0ν2β)	2004 [42] 2008 [19]
$^{64}Zn \rightarrow {}^{64}Ni$	$ZnWO_4$	$\geq 6.2 \times 10^{18}$ yr (2ν2K) $\geq 1.1 \times 10^{19}$ yr (2ν2K) $\geq 9.4 \times 10^{20}$ yr (2νεβ$^+$)	2008 [43] 2011 [44] 2011 [44]
$^{70}Zn \rightarrow {}^{70}Ge$	$ZnWO_4$	$\geq 3.8 \times 10^{18}$ yr (2ν2β) $\geq 3.2 \times 10^{19}$ yr (0ν2β)	2011 [44]
$^{100}Mo \rightarrow {}^{100}Ru$	$^{40}Ca^{100}MoO_4$	$\geq 4.0 \times 10^{21}$ yr (0ν2β)	2011 [45]
$^{106}Cd \rightarrow {}^{106}Pd$	$CdWO_4$	$\geq 2.6 \times 10^{17}$ yr (2νεβ$^+$) $\geq 5.5 \times 10^{19}$ yr (0νεβ$^+$)	1996 [46]
	$^{116}CdWO_4$	$\geq 1.2 \times 10^{18}$ yr (2νεβ$^+$) $\geq 7.0 \times 10^{19}$ yr (0νεβ$^+$)	2003 [18]
	$^{106}CdWO_4$	$\geq 2.1 \times 10^{20}$ yr (2νεβ$^+$) $\geq 2.2 \times 10^{21}$ yr (0νεβ$^+$) $\geq 4.3 \times 10^{20}$ yr (2ν2β$^+$) $\geq 1.2 \times 10^{21}$ yr (0ν2β$^+$)	2012 [47]
$^{108}Cd \rightarrow {}^{108}Pd$	$CdWO_4$	$\geq 1.0 \times 10^{18}$ yr (0ν2ε)	2008 [15]
$^{114}Cd \rightarrow {}^{114}Sn$	$CdWO_4$	$\geq 1.3 \times 10^{18}$ yr (2ν2β) $\geq 1.1 \times 10^{21}$ yr (0ν2β)	2008 [15]
$^{116}Cd \rightarrow {}^{116}Sn$	$^{116}CdWO_4$	$\geq 1.7 \times 10^{23}$ yr (0ν2β) $= 2.9 \times 10^{19}$ yr (2ν2β)	2003 [18]
$^{130}Ba \rightarrow {}^{130}Xe$	BaF_2	$\geq 1.4 \times 10^{17}$ yr (0νεβ$^+$)	2004 [48]
$^{136}Ce \rightarrow {}^{136}Ba$	CeF_3 $CeCl_3$	$\geq 2.7 \times 10^{16}$ yr (2ν2K) $\geq 2.4 \times 10^{16}$ yr (2νεβ$^+$)	2003 [49] 2011 [50]
$^{138}Ce \rightarrow {}^{138}Ba$	CeF_3 $CeCl_3$	$\geq 3.7 \times 10^{16}$ yr (2ν2K) $\geq 4.4 \times 10^{16}$ yr (2ν2K)	2003 [49] 2011 [50]
$^{142}Ce \rightarrow {}^{142}Nd$	GSO(Ce) $CeCl_3$	$\geq 1.6 \times 10^{17}$ yr (2ν2β) $\geq 1.4 \times 10^{18}$ yr (2ν2β)	2003 [16] 2011 [50]
$^{160}Gd \rightarrow {}^{160}Dy$	GSO(Ce)	$\geq 1.3 \times 10^{21}$ yr (0ν2β) $\geq 1.9 \times 10^{19}$ yr (2ν2β)	2001 [16]
$^{180}W \rightarrow {}^{180}Hf$	$ZnWO_4$	$\geq 1.0 \times 10^{18}$ yr (2ν2K) $\geq 1.3 \times 10^{18}$ yr (0ν2ε)	2011 [44]
$^{186}W \rightarrow {}^{18O}Os$	$ZnWO_4$ $^{116}CdWO_4$	$\geq 2.3 \times 10^{19}$ yr (2ν2β) $\geq 1.1 \times 10^{21}$ yr (0ν2β)	2011 [44] 2003 [18]

High concentration of isotope of interest is one of the most important requirements to 2β detectors. This requirement can be satisfied by production of crystal scintillators from enriched isotopes [51]. High cost of enriched materials imposes a few specific requirements to the technology on all the stages of scintillators production: as low as possible loss of enriched materials, high output of crystals, prevention of radioactive contamination, recovery and purification of the isotopes and their return to the production cycle. The most important issue is to minimize as much as possible radioactive contamination of scintillators, especially by radium and thorium. Low-thermal-gradient Czochralski method provides a few advantages in comparison to the standard Czochralski technique: large output of crystals up to 90%, low losses of high cost enriched isotopes (less than 1%), higher optical quality. One could expect also higher radiopurity, which feature needs additional studies.

Recently high quality radiopure cadmium tungstate crystal scintillators were developed from enriched ^{106}Cd [52] and ^{116}Cd [53]. Excellent optical and scintillation properties of these scintillators were obtained thanks to the deep purification of raw materials and low-thermal-gradient Czochralski technique to grow the crystals. The experiments to search for double β decay of ^{106}Cd and ^{116}Cd are in progress in the Gran Sasso underground laboratory (Italy). Calcium molybdate crystal scintillators from enriched ^{100}Mo and depleted in ^{40}Ca were developed by AMoRE collaboration to search for 0ν2β decay of ^{100}Mo [54]. Development of enriched in ^{100}Mo zinc molybdate crystal scintillators is in progress [55].

A first stage experiment to search for double β processes in ^{106}Cd was realized at the Gran Sasso underground laboratory with the help of the $^{106}CdWO_4$ crystal scintillator [52]. After 6590 h of data taking, new improved half-life limits on the double β decay of ^{106}Cd were established at the level of 10^{19}–10^{21} yr. In particular, $T_{1/2}^{2\nu\varepsilon\beta+} \geq 2.1 \times 10^{20}$ yr, $T_{1/2}^{2\nu 2\beta+} \geq 4.3 \times 10^{20}$ yr, and $T_{1/2}^{0\nu 2\varepsilon} \geq 1.0 \times 10^{21}$ yr. The resonant neutrinoless double-electron captures to the 2718 keV, 2741 keV, and 2748 keV excited states of ^{106}Pd are restricted on the level of $T_{1/2} \sim 10^{20}$ yr. A new phase of the experiment with the enriched $^{106}CdWO_4$ crystal operating in coincidence with four HPGe detectors of 225 cm^3 volume each is in progress [47].

A low background experiment to search for double β decay of ^{116}Cd with the help of the enriched $^{116}CdWO_4$ crystal scintillators is in progress [56]. A sensitivity of a 5 yr experiment (depending on a level of background) can be estimated as $T_{1/2} \sim (0.5 - 1.5) \times 10^{24}$ yr. It corresponds, taking into account the recent calculations of matrix elements [57-58], to the effective neutrino mass $\langle m_\nu \rangle \sim 0.4 - 1.4$ eV. Very low segregation of K, Th and Ra was observed in the compound, which can be used to reduce the radioactive contamination of the crystals by recrystallization.

INVESTIGATION OF DOUBLE β PROCESSES BY γ SPECTROMETRY

Ultra-low background γ spectrometry is successfully used to search for double β processes accompanied by γ and X rays: $2\beta^-$ transitions to excited levels of daughter nuclei, double electron capture (2ε), electron capture with positron emission ($\varepsilon\beta^+$), double positron decay ($2\beta^+$).

Table. 2.

Half-life limits on resonant 0ν double electron capture in ^{96}Ru, ^{156}Dy, ^{158}Dy, ^{184}Os and ^{190}Pt.

Process of decay		Level of daughter nucleus (keV)	Experimental limit (yr) at 90% confidence level	Years References
$^{96}Ru \rightarrow {}^{96}Mo$	*KL*	2^+ 2700	5.8×10^{18}	2009 [59]
	2*L*	2713	1.3×10^{19}	
$^{156}Dy \rightarrow {}^{156}Gd$	2*K*	2^+ 1914.8	1.1×10^{16}	2011 [60]
	KL_1	1^- 1946.4	9.6×10^{15}	
	KL_1	0^- 1952.4	2.6×10^{16}	
	$2L_1$	0^+ 1988.5	1.9×10^{16}	
	$2L_3$	2^+ 2003.8	2.8×10^{14}	
$^{158}Dy \rightarrow {}^{158}Gd$	$2L_1$	4^+ 261.5	3.2×10^{16}	
$^{184}Os \rightarrow {}^{184}W$	2*K*	$(0)^+$ 1322.2	2.8×10^{16}	2012 [61]
	KL	2^+ 1386.3	6.7×10^{16}	
	2*L*	2^+ 1431.0	8.2×10^{16}	
$^{190}Pt \rightarrow {}^{158}Gd$	*MM, MN, NN*	$(0,1,2^+)$ 1382.4	2.9×10^{16}	2011 [62]

An experiment to measure 2β decay of ^{100}Mo to excited states of ^{100}Ru was realized deep underground in the Gran Sasso laboratory with the help of an ultra-low background semiconductor germanium detector. A 1.2 kg sample of molybdenum oxide enriched in ^{100}Mo to 99.5% was measured over 18120 h. Two γ quanta of 540 keV and of 591 keV

emitted in the de-excitation process after two neutrino double β decay of ^{100}Mo to the 0^+_1 excited level of ^{100}Ru with the energy 1131 keV were observed both in coincidence and in the sum spectra. The measured half-life of ^{100}Mo relatively to the transition is $T_{1/2} = 6.9^{+1.0}_{-0.8}$ (stat.) ± 0.7 (syst.) $\times 10^{20}$ yr [63], in agreement with results of previous experiments [64-66].

Possible resonant processes were studied in ^{96}Ru, ^{156}Dy, ^{158}Dy, ^{184}Os, and ^{192}Pt with the help of ultra-low background HPGe detectors at the Gran Sasso laboratory. For this purpose samples of ruthenium, dysprosium, platinum and osmium of high purity grade were measured a few thousand hours each. No peculiarities have been observed in the data which can be ascribed to the effects searched for. Half-life limits on resonant double electron capture in ruthenium, dysprosium, osmium and platinum isotopes established in the experiments are presented in Table 2.

LOW TEMPERATURE SCINTILLATING BOLOMETERS

According to Zdesenko [2] a sensitivity of a double β decay experiment (in terms of the lower half-life limit, lim $T_{1/2}$) can be expressed as following:

$$\lim T_{1/2} \sim \varepsilon \cdot \delta \sqrt{\frac{m \cdot t}{R \cdot BG}},$$

where ε is the detection efficiency, δ is the concentration of the isotope of interest, t is the measurement time, m, R and BG are the mass, energy resolution and background of the detector. Therefore, energy resolution is an important characteristic of a double β decay detector. Furthermore, as it was demonstrated in [67], the energy resolution plays a crucial role due to irremovable background coming from the two neutrino decay. It should be stressed that a few % energy resolution remains acceptable as far as the phenomenon is *not observed*: it still allows to suppress the background caused by two neutrino 2β decay events in the energy region of interest. However, the energy resolution becomes a crucial parameter in case if *an indication* of 0ν2β decay is obtained. Indeed, even in a case of high resolution HPGe detectors (with typical energy resolution over long time measurements FWHM ≈ 4 keV at $Q_{2\beta}$ of ^{76}Ge), one cannot exclude possibility to falsify the effect of the 0ν2β decay of ^{76}Ge (see e.g. [68]).

Apart from HPGe detectors (at present the most sensitive technique to search for 0ν2β decay of ^{76}Ge [25,69]), only cryogenic bolometers [30,70,71] are able to provide comparable energy resolution to realize large scale high sensitivity experiments to search for 0ν2β decay of different isotopes thanks to high energy resolution (a few keV) and detection efficiency (near 70% – 90% depending on crystal composition and size). Development, during the last decade, the technique of low temperature *scintillating* bolometers give a "second wind" for the scintillation method allowing to reach very high energy resolution, which are especially important feature for the next generation double β experiments. In addition to excellent energy resolution on the level of a few keV at energies 2 – 3 MeV, cryogenic scintillators allows almost complete particle discrimination ability. The technique also offers a very important possibility to use compounds with nuclei of interest. A few R&D projects are in progress to build double β decay experiments with aim to explore inverted hierarchy of neutrino mass by using $CaMoO_4$ [54], ZnSe [72], $CdWO_4$ [73], and $ZnMoO_4$ [55,74] crystal scintillators.

However, a disadvantage of cryogenic bolometers is a poor time resolution, typically a few ms. It can lead to background up to the energy of $2 \times Q_{2\beta}$ due to random coincidence of 2ν2β events. The random coincidence of 2ν2β events as a source of background in high-sensitivity 0ν2β cryogenic experiments was considered and discussed for the first time in [55]. The contribution of random coincidences of 2ν2β events to the counting rate in the energy region of the expected 0ν2β peak was estimated in [75]. It was shown that the pile-up effect can be substantially reduced by pulse-shape analysis and application of faster sensors in cryogenic scintillating bolometers.

CONCLUSIONS

Search for neutrinoless double β decay is one of the most promising ways to prove new physics beyond the Standard Model of particles. Despite almost seventy years of attempts the process still remains unobserved. Only half-life limits on the level of $T_{1/2} \sim 10^{22} - 10^{25}$ yr were set in the most sensitive experiments, which allow to restrict a Majorana neutrino mass on the level of 0.3 – 3 eV, set strong limits on admixture of right currents in weak interactions and on the decay with emission of majorons. Several experiments are in preparation or in R&D stage to explore the inverted hierarchy of the neutrino mass. In a case of non-observation of the decay on the level of sensitivity to the neutrino mass ≈ 0.02 eV one could conclude that a normal scheme of the neutrino mass eigenstates is realized.

Investigation of transitions to excited levels of daughter nuclei and search for "double beta plus processes" are carried out with the help of ultra-low background HPGe γ spectrometry. Investigation of neutrinoless 2ε and $\varepsilon\beta^+$ decays, as well as measurements of 0ν2β decay to 2^+ excited levels of daughter nuclei, could refine mechanism of 0ν2β decay if the process will be observed: is it due to the light neutrino mass mechanism or due to an admixture of right handed currents in weak interactions. Search for resonant neutrinoless double electron capture is considered as an alternative way to study properties of neutrino.

Scintillation detectors are widely used in the double β decay experiments. Using of crystal scintillators as scintillating bolometers with high energy resolution and low background is especially promising approach. A few high sensitivity experiments intending to apply this technique are under construction or in R&D stage to explore an inverted hierarchy of the neutrino mass.

REFERENCES

1. Mohapatra R.N. et al. Theory of neutrinos: a white paper // Rep. Prog. Phys. – 2007. – Vol.70. – P.1757–1867.
2. Zdesenko Yu.G. The future of double β decay research // Rev. Mod. Phys. – 2002. – Vol.74. – P.663–684.
3. Tretyak V.I., Zdesenko Y.G. Tables of double beta decay data — an update // At. Data Nucl. Data Tables – 2002. – Vol.80. – P.83–116.
4. Vergados J.D. The neutrinoless double beta decay from a modern perspective // Phys. Rept. – 2002. – Vol.361. – P.1–56
5. Avignone III F.T., Elliott S.R., Engel J. Double beta decay, Majorana neutrinos, and neutrino mass // Rev. Mod. Phys. – 2008. – Vol.80. – P.481–516.
6. Giuliani A. Searches for neutrinoless double beta decay // Acta Physica Polonica – 2010. – Vol.B41. – P.1447–1468.
7. Rodejohann W. Neutrino-less double beta decay and particle physics // Int. J Mod. Phys. – 2011. – Vol.E20. – P.1833–1930.
8. Elliott S.R. Recent progress in double beta decay // Mod. Phys. Lett. – 2012. Vol.A27. – P.1230009, 16 p.
9. Vergados J.D., Ejiri H. and Šimkovic F. Theory of neutrinoless double-beta decay // Rep. Prog. Phys. – 2012. – Vol.75. – P.106301, 52 p.
10. Doi M., Kotani T., and Takasugi E. Double Beta Decay and Majorana Neutrino // Prog. Theor. Phys. Suppl. – 1985. – Vol.83. – P.1–175.
11. Barabash A.S. Precise half-life values for two-neutrino double-β decay // Phys. Rev. – 2010. – Vol.C81. – P.035501, 7 p.
12. Ackerman N. et al. (EXO Collaboration). Observation of Two-Neutrino Double-Beta Decay in ^{136}Xe with the EXO-200 Detector // Phys. Rev. Lett. – 2011. – Vo.107. – P.212501, 5 p.
13. Gando A. et al. Measurement of the double-β decay half-life of ^{136}Xe with the KamLAND-Zen experiment // Phys. Rev. – 2012. – Vol.C85. – P.045504, 6 p.
14. Argyriades J. et al. Measurement of the two neutrino double beta decay half-life of Zr-96 with the NEMO-3 detector // Nucl. Phys. – 2010. – Vol.A847. – P.168–179.
15. Belli P. et al. Search for double-β decay processes in ^{108}Cd and ^{114}Cd with the help of the low background $CdWO_4$ crystal scintillator // Eur. Phys. J. – 2008. – Vol.A36. – P.167–170.
16. Danevich F.A. et al. Quest for double beta decay of ^{160}Gd and Ce isotopes // Nucl. Phys. – 2001. – Vol.A694. – P.375–391.
17. Argyriades J. et al. Measurement of the double-β decay half-life of ^{150}Nd and search for neutrinoless decay modes with the NEMO-3 detector // Phys. Rev. – 2009. – Vo.C80. – P.032501, 5 p.
18. Danevich F.A. et al. Search for 2β decay of cadmium and tungsten isotopes: Final results of the Solotvina experiment // Phys. Rev. – 2003. – Vol.C68. – P.035501, 12 p.
19. Umehara S. et al. Neutrino-less double-β decay of ^{48}Ca studied by CaF_2(Eu) scintillators // Phys. Rev. – 2008. – Vol.C78. – P.058501, 4 p.
20. Elliot S.R. et al. Double beta decay of ^{82}Se // Phys. Rev. – 1992. – Vol.C46. – P.1535–1537.
21. Arnold R. et al. First results of the search for neutrinoless double-beta decay with the NEMO 3 detector // Phys. Rev. Lett. – 2005. – Vol.95. – P.182302, 4 p.
22. Arnold R. et al. Measurement of double beta decay of ^{100}Mo to excited states in the NEMO 3 experiment // Nucl. Phys. – 2007. Vol.A781. – P.209–226.
23. Arnaboldi C. et al. A calorimetric search on double beta decay of ^{130}Te // Phys. Lett. – 2003. – Vol.B557. – P.167–175.
24. Arnaboldi C. et al. Results from the CIORICINO 0νββ-decay experiment // Phys. Rev. – 2008. – Vol.C78. – P.035502, 30 p.
25. Klapdor-Kleingrothaus H.V. et al. Latest results from the Heidelberg-Moscow double beta decay experiment // Eur. Phys. J. – 2001. – Vol.A12. – P.147–154.
26. Aalseth C.E. et al. The IGEX ^{76}Ge neutrinoless double-beta decay experiment: prospect for next generation experiments // Phys. Rev. – 2002. – Vol.D65. – P.092007, 6 p.
27. Auger M. et al. (EXO Collaboration). Search for Neutrinoless Double-Beta Decay in ^{136}Xe with EXO-200 // Phys. Rev. Lett. – 2012. – Vol.109. – P.032505, 6 p.
28. Gando A. et al. (KamLAND-Zen Collaboration). Measurement of the double-β decay half-life of ^{136}Xe with the KamLAND-Zen experiment // Phys. Rev. – 2012. – Vol.C85. – P.045504, 6 p.
29. Klapdor-Kleingrothaus H.V., Krivosheina I.V. The evidence for the observation of 0νββ decay: the identification of 0νββ events from the full spectra // Mod. Phys. Lett. – 2006. – Vol.A21. – P.1547–1556.
30. Giuliani A. Neutrino Physics with Low-Temperature Detectors // J Low Tem. Phys. – 2012. – Vol.167. – P.991–1003.
31. Hirsch M. et al. Nuclear structure calculation of $\beta^+\beta^+$, β^+/EC and EC/EC decay matrix elements // Z. Phys. – 1994. – Vol.A347. – P.151–161.
32. Klapdor-Kleingrothaus H.V. Lessons after the evidence for neutrinoless double beta decay – the next step // Int. J. Mod. Phys. – 2008. – Vol.E17. – P.505–517.
33. Winter R.G. Double K Capture and Single K Capture with Positron Emission // Phys. Rev. – 1955. – Vol.100. – P.142–144.
34. Voloshin M.B., Mitselmakher G.V., Eramzhyan R.A. Conversion of an atomic electron into a positron and double β^+ decay // JETP Lett. – 1982. – Vol.35. – P.656–659.
35. Bernabeu J., De Rujula A., Jarlskog C. Neutrinoless double electron capture as a tool to measure the electron neutrino mass // Nucl. Phys. – 1983. – Vol.B223. – P.15–28.

36. Sujkowski Z., Wycech S. Neutrinoless double electron capture: A tool to search for Majorana neutrinos // Phys. Rev. – 2004. – Vol.C70. – P.052501, 5 p.
37. Krivoruchenko M.I., Šimkovic F., Frekers D., Faessler A. Resonance enhancement of neutrinoless double electron capture // Nucl. Phys. – 2011. – Vol.A859. – P.140–171.
38. Šimkovic F., Krivoruchenko M.I. and Faessler A. Neutrinoless double-beta decay and double-electron capture // Prog. Part. Nucl. Phys. – 2011. – Vol.66. – P.446–451.
39. Suhonen J. Neutrinoless double beta decays of ^{106}Cd revisited // Phys. Lett. – 2011. – Vol.B701. – P.490–495.
40. der Mateosian E. and Goldhaber M. Limits for Lepton-Nonconserving Double Bea Decay of Ca^{48} // Phys. Rev. – 1966. – Vol.146. – P.810–815.
41. Bernabei R. et al. Improved limits on WIMP-^{19}F elastic scattering and first limit on the 2EC2ν ^{40}Ca decay by using a low radioactive CaF_2(Eu) scintillator // Astropart. Phys. – 1997. Vol.7. – P.73–76.
42. Ogawa I. et al. Search for neutrino-less double beta decay of ^{48}Ca by CaF_2 scintillator // Nucl. Phys. – 2004. – Vol.A730. – P.215–223.
43. Belli P. et al. Search for 2β processes in ^{64}Zn with the help of $ZnWO_4$ crystal scintillator // Phys. Lett. – 2008. – Vol.B658. – P.193–197.
44. Belli P. et al. Final results of an experiment to search for 2β processes in zinc and tungsten with the help of radiopure $ZnWO_4$ crystal scintillators // J. Phys. – 2011. – Vol.G38. – P.115107, 15 p.
45. So J.H. et al. Scintillation properties and internal background study of $^{40}Ca^{100}MoO_4$ crystal scintillators for neutrino-less double beta decay search // IEEE Trans. Nucl. Sci. – 2012. – Vol.59. – P.2214–2218.
46. Danevich F.A. et al. Investigation of $\beta^+\beta^+$ and β^+/EC decay of ^{106}Cd // Z. Phys. – 1996. – Vol.A355. – P.433–437.
47. Belli P. et al. Search for double β decay processes in ^{106}Cd with the help of $^{106}CdWO_4$ crystal scintillator // Phys. Rev. – 2012. – Vol.C85. – P.044610, 12 p.
48. Cerulli R. et al. Performances of a BaF_2 detector and its application to the search for ββ decay modes in ^{130}Ba // Nucl. Instr. Meth. – 2004. – Vol.A525. – P.535–543.
49. Belli P. et al. Performances of a CeF_3 crystal scintillator and its application to the search for rare processes // Nucl. Instr. Meth. – 2003. – Vol.A498. – P.352–361.
50. Belli P. et al. Search for 2β decay of cerium isotopes with $CeCl_3$ scintillator // J. Phys. – 2011. – Vol.G38. – P.015103, 15 p.
51. Danevich F.A. Development of Crystal Scintillators From Enriched Isotopes for Double Decay Experiments // IEEE Trans. Nucl. Sci. – 2012. – Vol.59. – P.2207–2213.
52. Belli P. et al. Development of enriched $^{106}CdWO_4$ crystal scintillators to search for double β decay processes in ^{106}Cd // Nucl. Instr. Meth. – 2010. – Vol.A615. – P.301–306.
53. Barabash A.S. et al. Low background detector with enriched $^{116}CdWO_4$ crystal scintillators to search for double β decay of ^{116}Cd // J. Instr. – 2011. – Vol.6. – P.P08011, 22 p.
54. Lee S.J. et al. The development of a cryogenic detector with $CaMoO_4$ crystals for neutrinoless double beta decay search // Astropart. Phys. – 2011. – Vol.34. – P.732–737.
55. Beeman J.W. et al. Potential of a next generation neutrinoless double beta decay experiment based on $ZnMoO_4$ scintillating bolometers // Phys. Lett. – 2012. – Vol.B710. – P.318–323.
56. Barabash A.S. et al. First results of the experiment to search for double beta decay of ^{116}Cd with the help of $^{116}CdWO_4$ crystal scintillators // to be published in Proceedings of the 4th International Conference "Current Problems in Nuclear Physics and Atomic Energy" (NPAE-2012), 03–07 September 2012, Kyiv, Ukraine.
57. Kortelainen M. and Suhonen J. Nuclear matrix elements of 0νββ decay with improved short-range correlations // Phys. Rev. – 2007. – Vol.C76. – P.024315, 6 p.
58. Šimkovic F. et al. Anatomy of the 0νββ nuclear matrix elements // Phys. Rev. – 2008. Vol.C77. – P.045503, 11 p.
59. Belli P. et al. Search for double-β decays of ^{96}Ru and ^{104}Ru by ultra-low background HPGe γ spectrometry // Eur. Phys. J – 2009. – Vol.A42. – P.171–177.
60. Belli P. et al. First search for double β decay of dysprosium // Nucl. Phys. – 2011. – Vol.A859. – P.126–139.
61. Belli P. et al. First search for double-β decay of ^{184}Os and ^{192}Os // submitted to Eur. Phys. J A.
62. Belli P. et al. First search for double-β decay of platinum by ultra-low background HP Ge γ spectrometry // Eur. Phys. J – 2011. – Vol.A47. – P.91, 8 p.
63. Belli P. et al. New observation of 2β2ν decay of ^{100}Mo to the 0_1^+ level of ^{100}Ru in the ARMONIA experiment // Nucl. Phys. – 2010. – Vol.A846. – P.143–156.
64. Barabash A.S. et al. Two neutrino double-beta decay of ^{100}Mo to the first excited 0^+ state in ^{100}Ru // Phys. Lett. – 1995. – Vol.B345. – P.408–413.
65. Arnold R. et al. Measurement of double beta decay of ^{100}Mo to excited states in the NEMO 3 experiment // Nucl. Phys. – 2007. – Vol.A781. – P.209–226.
66. Kidd M.F. et al. New results for double-beta decay of ^{100}Mo to excited final states of ^{100}Ru using the TUNL-ITEP apparatus // Nucl. Phys. – 2009. – Vol.A821. – P.251–261.
67. Zdesenko Yu.G., Danevich F.A., Tretyak V.I. Sensitivity and discovery potential of the future 2β decay experiments // J. Phys. – 2004. – Vol.G30. – P.971–981.
68. See footnote 15 in Zdesenko Yu.G. et al. Has neutrinoless double β decay of ^{76}Ge been really observed? // Phys. Lett. – 2002. – Vol.B546. – P.206–215.
69. Aalseth C.E. et al. The IGEX ^{76}Ge neutrinoless double-beta decay experiment: prospect for next generation experiments // Phys. Rev. – 2002. – Vol.D65. – P.092007, 6 p.

70. Twerenbold D. Cryogenic Particle Detectors // Rep. Prog. Phys – 1996. – Vol.59. – P.349–426.
71. Christian Enss (Editor) (2005), Cryogenic Particle Detection, Springer,Topics in applied physics, Vol. 99, 508 pages, ISBN 3-540-20113-0.
72. Arnaboldi C. et al. Characterization of ZnSe scintillating bolometers for Double Beta Decay // Astropart. Phys. – 2011. – Vol.34. – P.344–353.
73. Gironi L. et al. $CdWO_4$ bolometers for double beta decay search // Opt. Mater. – 2009. – Vol.31. – P.1388–1392.
74. Beeman J.W. et al. $ZnMoO_4$: A promising bolometer for neutrinoless double beta decays searches // Astropart. Phys. – 2012. – Vol.35. – P.813–820.
75. Chernyak D.M. et al. Random coincidence of 2ν2β decay events as a background source in bolometric 0ν2β decay experiments // Eur. Phys. J. – 2012. – Vol.C72. – P.1989, 6 p.

Fedor A Danevich - D.Sc. in physics and mathematics. Head of the Lepton Physics Department of the Institute for Nuclear Research (Kyiv, Ukraine). Research interest: search for double beta decay, dark matter, Solar axions, investigation of rare alpha and beta decays. Development of low radioactive technique, low background scintillation detectors. R&D of scintillators for astroparticle physics. The author and the co-author more than 390 scientific publications and one patent.

UDC 539.172

PRODUCTION OF CHARMONIUM AND JETS IN ULTRARELATIVISTIC PROTON–PROTON COLLISIONS

A.V. Dieiev*, V.V. Kotlyar, N.I. Maslov****
** V.N. Karazin Kharkov National University*
Svoboda Sq. 4, Kharkov 61022, Ukraine
*** National Science Center «Kharkov Institute of Physics and Technology»*
Akademichna 1, 61108 Kharkov, Ukraine
E-mail: kotlyarv@kipt.kharkov.ua
Received 10 December 2012, accepted 24 January 2013

Production of J/ψ–meson in association with jet in proton–proton collisions is studied at energy $s^{1/2}$ = 8 TeV. Jet pair production at $s^{1/2}$ = 7 TeV is considered briefly. Event generator Pythia 8 is employed in the simulations of the reactions. Distributions that depend on differences of transverse momenta, rapidities y_{mj}, and azimuthal angles φ_{mj} of the meson and jet are calculated. It is analyzed, how gluon radiation in initial and final states of the partonic processes along with multiple parton interactions influence the observables. Shapes of (y_{mj}, φ_{mj}, $y_{J/\psi}$)– and (y_{mj}, $p_{T\,J/\psi}$, $y_{J/\psi}$)–distributions, with $p_{T\,J/\psi}$ ($y_{J/\psi}$) being momentum (rapidity) of J/ψ, are shown to differ substantially for the mesons, emitted in the central and forward regions. The observables, measurements of which will help to impose severe constraints on used models, are discussed.
KEY WORDS: event generator Pythia, charmonium, jet production, proton–proton collisions, the LHC, experiments ALICE, ATLAS, CMS, LHCb

РОЖДЕНИЕ ЧАРМОНИЯ И СТРУЙ В СТОЛКНОВЕНИЯХ УЛЬТРАРЕЛЯТИВИСТСКИХ ПРОТОНОВ
А.В. Деев*, В.В. Котляр, Н.И. Маслов****
** Харьковский национальный университет им. В.Н. Каразина*
пл. Свободы, 4, г. Харьков, 61022, Украина
*** Национальный Научный Центр «Харьковский Физико-Технический Институт»*
ул. Академическая 1, г. Харьков, 61108, Украина
Рождение J/ψ мезона совместно со струёй в протон–протонных соударениях изучается при энергии $s^{1/2}$ = 8 ТэВ. Кратко рассматривается рождение пар струй при $s^{1/2}$ = 7 ТэВ. При моделировании реакций используется генератор событий Пифия 8. Рассчитаны распределения, которые зависят от разностей поперечных импульсов, быстрот y_{mj} и азимутальных углов φ_{mj} мезона и струи. Анализируется влияние на наблюдаемые излучения глюонов в начальном и конечных состояниях партонных процессов, а также многократного рассеяния партонов. Демонстрируется, что форма (y_{mj}, φ_{mj}, $y_{J/\psi}$)– и (y_{mj}, $p_{T\,J/\psi}$, $y_{J/\psi}$)–распределений, где $p_{T\,J/\psi}$ ($y_{J/\psi}$) есть поперечный импульс (быстрота) J/ψ, существенно различается для мезонов, рождающихся в центральной области и под малыми углами к оси пучков. Исследуются наблюдаемые, измерение которых может быть полезным для получения строгих ограничений на используемые модели.
КЛЮЧЕВЫЕ СЛОВА: генератор событий Пифия, чармоний, рождение струй, протон–протонные столкновения, Большой адронный коллайдер ЦЕРН, эксперименты ALICE, ATLAS, CMS, LHCb

НАРОДЖЕННЯ ЧАРМОНІЯ ТА СТРУМЕНІВ У ЗІТКНЕННЯХ УЛЬТРАРЕЛЯТИВІСТСЬКИХ ПРОТОНІВ
А.В. Дєєв*, В.В. Котляр, М.І. Маслов****
**Харківський національний університет ім. В.Н. Каразіна*
пл. Свободи 4, 61022, м. Харків, Україна
*** Національний Науковий Центр «Харківський Фізико-Технічний Інститут»*
вул. Академічна 1, м. Харків, 61108, Україна
Народження J/ψ мезону разом із струменем в протон–протонних зіткненнях вивчається при енергії $s^{1/2}$ = 8 ТеВ. Стисло розглядається народження пар струменів при $s^{1/2}$ = 7 ТеВ. При моделюванні реакцій використовується генератор подій Піфія 8. Розраховуються розподіли, що залежать від різниць поперечних імпульсів, бистрот y_{mj} та азимутальних кутів φ_{mj} мезона та струменю. Аналізується вплив на спостережувані випромінювання глюонів в початковому та кінцевому станах партонних процесів, а також багаторазового розсіяння партонів. Демонструється, що форма (y_{mj}, φ_{mj}, $y_{J/\psi}$)– та (y_{mj}, $p_{T\,J/\psi}$, $y_{J/\psi}$)–розподілів, де $p_{T\,J/\psi}$ ($y_{J/\psi}$) є поперечний імпульс (бистрота) J/ψ, істотно відрізняються для мезонів, що народжуються в центральній області та під малими кутами відносно осі пучків. Досліджуються спостережувані, вимірювання яких може бути корисним для отримання строгих обмежень на моделі, що використовуються.
КЛЮЧОВІ СЛОВА: генератор подій Піфія, чармоній, народження струменів, протон-протонні зіткнення, експерименти ALICE, ATLAS, CMS, LHCb, великий коллайдер адронів ЦЕРН

In recent years, production of charmonia, including $J/\psi(1S)$ –meson,

$$p + p \to J/\psi(1S) + X, \tag{1}$$

and of jets

$$p + p \to jet + X \tag{2}$$

is receiving much attention in experiments at the LHC.

Production of prompt J/ψ has been studied by ALICE [1], ATLAS [2], CMS [3,4], and LHCb [5] collaborations. ALICE has obtained the data for the differential cross section in the central region $|y_{J/\psi}|<0.9$ and $1.3\text{GeV/c} << p_{TJ/\psi}<10\text{GeV/c}$, where $y_{J/\psi}(p_{TJ/\psi})$ is J/ψ rapidity (transverse momentum). ATLAS has carried out measurements for four rapidity bins covering $|y_{J/\psi}|<2.4$ from $p_{TJ/\psi}=1\text{GeV/c}$ in $2<|y_{J/\psi}|<2.4$ and $p_{TJ/\psi}$ up to 70 GeV/c in $0.75<|y_{J/\psi}|<1.5$. CMS data are in five rapidity bins with $|y_{J/\psi}|<2.4$ for $p_{TJ/\psi}$ up to 70 GeV/c in central region $|y_{J/\psi}|<0.9$, and up to 30 GeV/c for $2.1<|y_{J/\psi}|<2.4$. Detailed measurements [5] in the forward region have been performed by LHCb for five rapidity slices 2, 2.5,… 4, 4.5 and $p_{TJ/\psi}$ up to 14 GeV/c…11 GeV/c.

Discussion of models, used in the calculations of the cross sections for (1), and of interpretation of the data can be found, e.g. in [6–8], and in the papers cited therein. Thus, it was shown in [8] that the computed cross sections depend noticeably on the renormalization and factorization scales. The variations due to these uncertainties in the calculations are substantial for $p_{TJ/\psi}<10\,GeV/c$, i.e. in the region of intensive experimental activity.

Jet production has been also studied in detail at the LHC. Here we mention results [9] of LHCb collaboration on jet pair production in the forward region, that are discussed below.

The obtained data for J/ψ and jet production allow to test theoretical predictions, based on perturbative QCD, computations of processes beyond the leading order, models that intend to treat non-perturbative effects and to describe fragmentation of partons.

The aim of this paper is to calculate observables in production of J/ψ in association with jet

$$p+p\to J/\psi(1S)+jet+X, \tag{3}$$

and of jet pairs $p+p\to jet_1+jet_2+X$ under conditions of the experiments at the LHC and to analyze mechanisms of the reactions in various kinematic regions.

FRAMEWORK FOR SIMULATION OF CHARMONIUM AND JET PRODUCTION

The present analysis of (2) and (3) is performed with the help of event generator Pythia 8.170 [10,11]. Within the used approach charmonia originate from $c\bar{c}$ – pairs, created in collisions of incoming partons. Color–singlet (a = 1) and color–octet (a = 8) intermediate $c\bar{c}$ – states that are included in the calculations are listed in Table 1. Orbital angular momentum, total spin, and total angular momentum are denoted by *L, S*, and *J*. For brevity these processes are referred below as “charmonium” group.

Table 1.

Partonic processes and quantum numbers of intermediate $c\bar{c}$ – states

process	$^{2S+1}L_J(a)$	
	a=1	a=8
$gg\to c\bar{c}\,[^{2S+1}L_J(a)]\,g$	$^3S_1$ and ^3P_J with $J=0,1,2$	$^3S_1,\ ^1S_0,\ ^3P_0$
$qg\to c\bar{c}\,[^{2S+1}L_J(a)]\,q$	^3P_J with $J=0,1,2$	
$q\bar{q}\to c\bar{c}\,[^{2S+1}L_J(a)]\,g,$		

Prompt J/ψ–mesons are produced directly in gluon–gluon scattering

$$g+g\to J/\psi(1S)+g \tag{4}$$

or in decays of color–singlet and color – octet $c\bar{c}$ –states, e.g. in $\chi_{cJ}\to\gamma+J/\psi$ and in $c\bar{c}\,[^{2S+1}L_J(8)]\to g+J/\psi$.

Integral cross sections of the partonic processes, obtained with Pythia 8 at total energy $\sqrt{s}=8$ TeV, are displayed in Fig. 1.

Set of parameters “4C” [11,12], parton distribution functions CTEQ6L1 [13] are used throughout this work. The minimum value of transverse momentum is chosen to be p_{Tmin} = 10 GeV/c. Values $c_R=c_F=1$ are accepted for scale parameters that determine renormalization and factorization scales.

The processes with integral cross section $\sigma_{\text{int}}(c\bar{c},\tau,p_T)>$ 50 nb are included in Fig. 1. In addition, cross section for (4) is shown for comparison. Contribution of this process turns out to be not essential in the current studies. Index τ labels partonic processes. The processes in Fig. 1 give more that 90% of cross section $\sigma_{\text{int}}(c\bar{c},p_T)=\sum_{\tau=1,\ldots,19}\sigma_{\text{int}}(c\bar{c},\tau,p_T)$, that is a sum for all contributions in correspondence with Table 1. Integral cross section for J/ψ production $\sigma_{\text{int}}(J/\psi,p_T)=840\,\text{nb}$ is visibly lower than $\sigma_{\text{int}}(c\bar{c},p_T)=1.314\,\mu\text{b}$, as far as the $c\bar{c}$ – states not always evolve into the meson.

J/ψ–mesons also come from decay of b–hadrons, especially from B–mesons. Such non–prompt J/ψ are disentangled from prompt ones in experiments [1-5] at the LHC. Essential mechanism of B–meson production, incorporated in Pythia, is string fragmentation. Since correlations of prompt J/ψ with jet in (3), where jet is generated by a parton in final states of “charmonium” processes, are intended to be studied below, the non–prompt J/ψ are not discussed in detail.

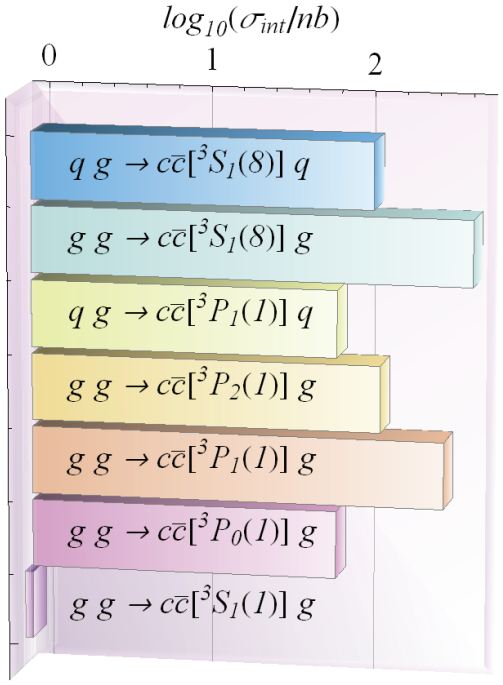

Fig. 1. Integral cross sections of some partonic processes, those result in creation of J/ψ meson.

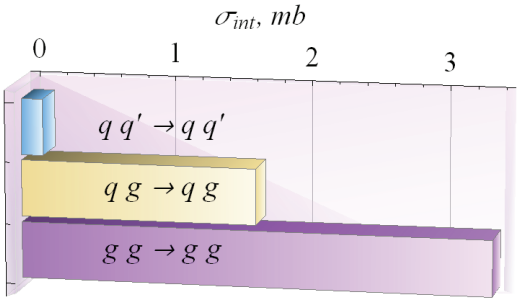

Fig. 2. Integral cross sections of some QCD processes, with that jet production is simulated.

As seen from Fig. 1, processes with two gluons in the initial states bring dominant contributions to $\sigma_{\text{int}}(c\bar{c}, p_T)$. The same holds for "hard QCD" processes [10,11], used in analysis of jet production (2). Some of them, which have the integral cross sections $\sigma_{\text{int}}(QCD, \tau, p_T) > 100$ μb, are shown in Fig. 2. These processes give more than 98% of the cross section $\sigma_{\text{int}}(QCD, p_T) =$ 5.36 mb, where $\sigma_{\text{int}}(QCD, p_T)$ involves all included "hard QCD" processes. Relatively large values of the cross sections for processes due to gluon scattering may provide for enhanced sensitivity of the observables to gluon distribution functions.

To find jets the generated events are analyzed with SlowJet program, being a component of Pythia 8. In searches of jets the anti-k_T algorithm is employed. The clusters with total transverse momenta, that do not exceed 10 GeV/c, are not considered as jets. The *r*–parameter, that determine jet–cone radius in rapidity–azimuthal angle space, is 0.7. Pseudorapidity region η>6 is excluded from jet searches. This pseudorapidity region corresponds to the polar angles $0 < \theta < 0.284°$. For a particle with energy E and 3–momentum $\vec{p} = (p_x, p_y, p_z)$ rapidity y and pseudorapidity η are defined as

$$y = \frac{1}{2}\ln\frac{E + p_z}{E - p_z}, \qquad \text{and} \qquad \eta = \frac{1}{2}\ln\frac{|\vec{p}| + p_z}{|\vec{p}| - p_z}.$$

The pseudorapidity and polar angle θ are related by $\eta = -\ln\tan(\theta/2)$.

Neutrinos and particles, that participate neither in strong nor in electromagnetic interactions, are left out.

MULTIPARTON INTERACTIONS, INITIAL–, AND FINAL–STATE RADIATION IN PRODUCTION OF J/ ψ–MESONS AND JETS

In this section we discuss influence of multiparton interactions (MPI), initial–state radiation (ISR), and final–state radiation (FSR) on observables in production of prompt J/ψ and jets. Throughout the paper simulation of proton–proton collisions is carried out under conditions of the LHC experiments at total energy $\sqrt{s} = 7$ TeV and 8 TeV.

As shown in Fig. 3, multiplicities of charged particles, obtained with "charmonium" and with "hard QCD" processes, change qualitatively when MPI, ISR, and FSR are switched on. Inclusion of these mechanisms results in substantial increase of event number in region $n_{ch} \geq 50$. In calculations with MPI, ISR, and FSR functions $1/N_{total}\ N(n_{ch})$ for "charmonium" and "hard QCD" groups of partonic processes do not differ more than about 10% for $n_{ch} \approx 30\ldots170$. Total number of generated events is denoted by N_{total}.

With inclusion of MPI, ISR, and FSR, jet multiplicities in (2) and (3) vary largely than charged particle multiplicities in (1) and (2), as it can be inferred from comparison of dash–dotted and solid curves in Figs. 4 and in Figs. 3. In simulations with "charmonium" (with "hard QCD") processes, when MPI, ISR, and FSR are not included, one (two) jet(s) are mainly produced in (3) (reaction (2)). Two (three) or more jets can be created in these reactions, when MPI, ISR, and FSR are taken into account. In Fig. 4 the multiplicities for (2) and (3), computed without ISR, FSR, and MPI, are multiplied by 0.6 and 0.5. For (2) $N_{events} = N_{total}$, while for (3) N_{events} is number of events, in which J/ψ is found.

Figs. 5 and 6 demonstrate that MPI, ISR, and FSR visibly manifest themselves in spectra for J/ψ in (1) and jets in (2) and (3). Reduction of the spectra of J/ψ in (1) and jets in (2) due to these mechanisms increases with J/ψ and jet transverse momenta $p_{T\,J/\psi}$ and $p_{T\,jet}$. Ratio of the distribution $dN/dp_{T\,J/\psi}$ ($dN/dp_{T\,jet}$), obtained without and with MPI,

ISR, and FSR, reaches ~6.3 (~7.1) at transverse momenta equal 100 GeV/c. At the same time, production of jets in (3) is enhanced by these mechanisms, as seen from Fig. 6. The corresponding ratio of the spectrum values is ~3.8 at $p_{T\,jet} = 100$ GeV/c. In region of the transverse momentum $p_T \approx 40\ldots100$ GeV/c, where distribution $dN/dp_{T\,jet}$ decreases more that in two orders of magnitude, ratio of jet spectra in (2) and (3), computed with MPI, ISR, and FSR, does not deviate considerably from 2, varying from ~1.9 up to ~2.2.

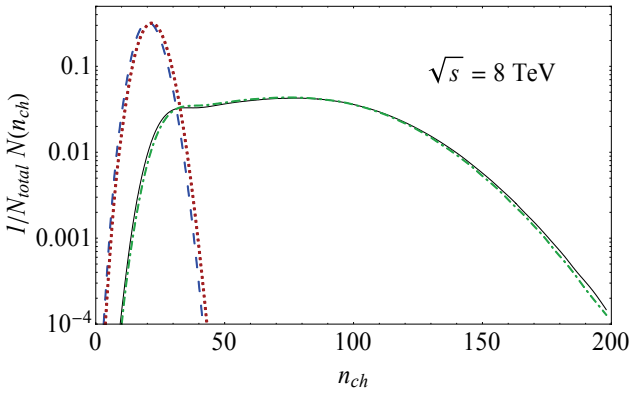

Fig. 3. Charge particle multiplicity for (1) (dashed and solid curves) and (2) (dotted and dash–dotted curves). Dashed and dotted (solid and dash–dotted) curves are obtained without (with) ISR, FSR, and MPI.

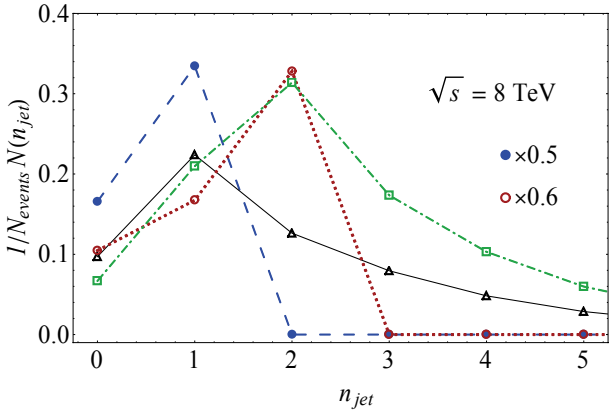

Fig. 4. Jet multiplicities in (2) and (3). Dotted and dash–dotted curves (○ and □) correspond to (2), dashed and solid curves (● and △) – to (3). Calculations without (with) ISR, FSR, and MPI are shown by dotted and dashed (dash–dotted and solid) curves.

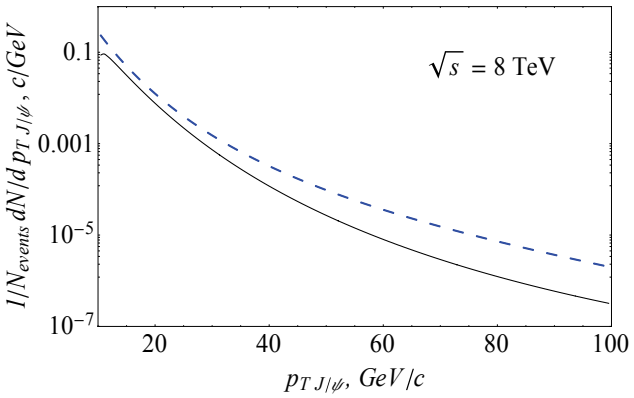

Fig. 5. Transverse momentum spectra of J/ψ in (1). Notation of the curves as in Fig 3.

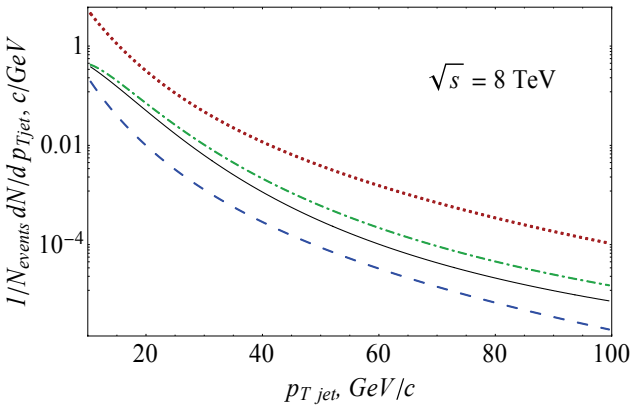

Fig. 6. Transverse momentum spectra of jets in (2) and (3). The curves are computed as in Fig 4.

To research into formation the transverse momentum spectra as well as distributions over $y_{mj} = y_{J/\psi} - y_{jet}$ and $\varphi_{mj} = \varphi_{J/\psi} - \varphi_{jet}$, where $y_{J/\psi}\,(\varphi_{J/\psi})$ and $y_{jet}\,(\varphi_{jet})$ are rapidities (azimuthal angles) of J/ψ and jet, we consider

$$dN(\xi,n)/d\xi = 1/\Delta y_n \int_{y_{n-1}}^{y_n} dy_{J/\psi}\, d^2N(\xi, y_{J/\psi})/d\xi dy_{J/\psi} \qquad (5)$$

with $\xi = p_{T\,mj}, y_{mj}$ or φ_{mj}. The difference of J/ψ and jet momenta is $p_{T\,mj} = p_{T\,J/\psi} - p_{T\,jet}$. Rapidity bins are numerated by n, $\Delta y_n = y_n - y_{n-1}$ is width of the bin. In Figs. 7, 8, and in 13,…16 below, curves with label n=1,3,4,…6 are obtained with y_n=n. Rapidity of J/ψ takes on values $y_{J/\psi} \in (n-1, n)$ in n*th* bin. Curves for $1 < y_{J/\psi} < 2$ lie in between ones with n=1, 3, which are not well separated. Therefore, curves with n=2 are not displayed. Polar angle $\theta_{J/\psi}$ of the meson, emitted with rapidity $y_{J/\psi}$ = 0,1,2,3,…,7 and transverse momentum $p_{TJ/\psi}$ = 10 GeV/c, is 90°, 39°, 15°, 5.5°, 2.0°, 0.74°, 0.27°, 0.10°, respectively. With increase of $p_{TJ/\psi}$ up to 100 GeV/c angle $\theta_{J/\psi}$ grows less than in 5%.

Jet spectra $dN(p_{Tmj})/dp_{Tmj}$ have maxima near p_{Tmj}= 0 in simulations of (3) with MPI, ISR, and FSR switched off. As demonstrated in Fig. 7, peaks in distributions slightly shift into negative area of p_{Tmj} with increase of J/ψ rapidity $y_{J/\psi}$. Fig. 8 shows that inclusion of these mechanisms enhances the shifting and leads to broadening of the peaks. However, one can conclude from the Figs. that J/ψ–mesons and jets are produced in (3) with the transverse momenta that are close to each other.

Figs. 9 and 10 indicate that the rapidity distributions $dN(y_{J/\psi})/dy_{J/\psi}$ of J/ψ in (1) and $dN(y_{jet})/dy_{jet}$ of jets in (2) and (3) rapidly decrease with growth of $y_{J/\psi}$ and y_{jet}, when $y_{J/\psi}$, $y_{jet} > 3\ldots4$. Rapidity distributions in (1) and (3),

shown by the dashed and solid curves, turn out to be almost insensitive to MPI, ISR, and FSR as opposed to ones in (2) and transverse momentum spectra in Figs. 5 and 6. Really, the distribution of J/ψ, created in (1), as functions of $y_{J/\psi}$, contains contributions of $p_{TJ/\psi}$ from a region adjacent to p_{Tmin}, since $dN(p_{TJ/\psi})/dp_{TJ/\psi}$ is a rapidly decreasing function. In this region the transverse–momentum spectrum is not affected strongly by the discussed mechanisms, as seen in Fig. 5. Transverse momenta of the jets and of the mesons in (3) do not duffer significantly, as demonstrated in Fig. 8.

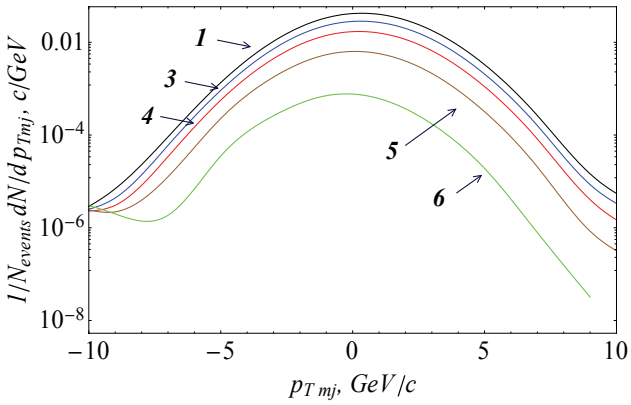

Fig. 7. Dependence of jet spectra $dN(p_{Tmj})/dp_{Tmj}$ in (3) on momentum p_{Tmj}.
Notation of the curves is explained in the text. Calculations are performed at $s^{1/2}$ = 8 TeV without ISR, FSR, and MPI.

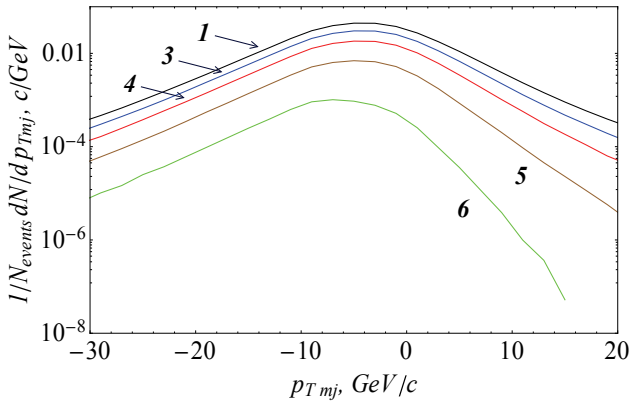

Fig. 8. The same as in Fig. 7.
The spectra are computed with inclusion of ISR, FSR, and MPI.

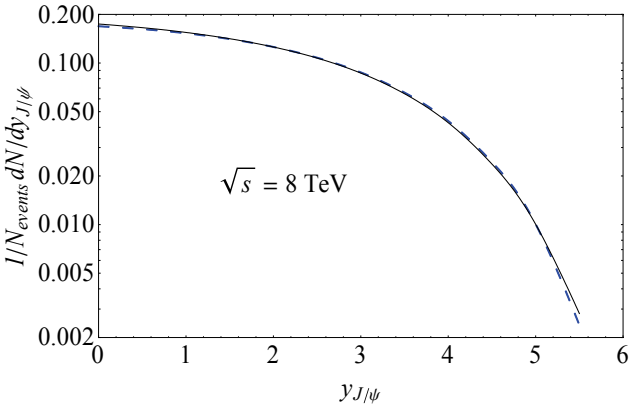

Fig. 9. Rapidity distributions of J/ψ in (1).
Notation of the curves as in Fig 3.

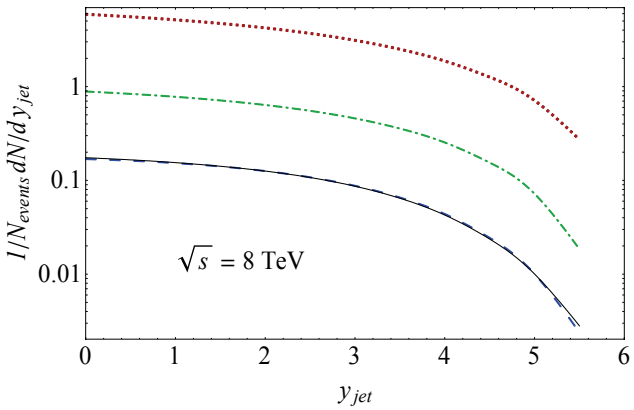

Fig. 10. Rapidity distributions of jets in (2) and (3).
Notation of the curves as in Fig 4.

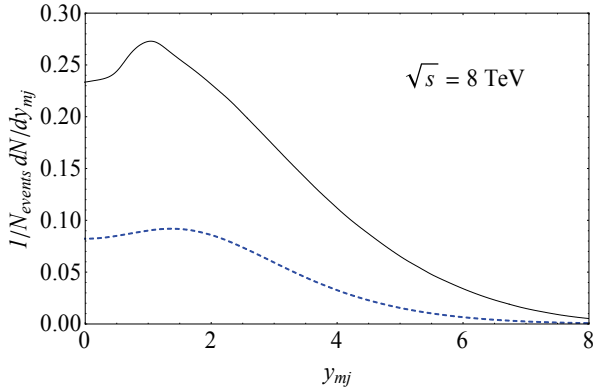

Fig. 11. Distributions $dN(y_{mj})/dy_{mj}$ for (3).
Solid (dashed) curve is obtained with (without) ISR, FSR, and MPI.

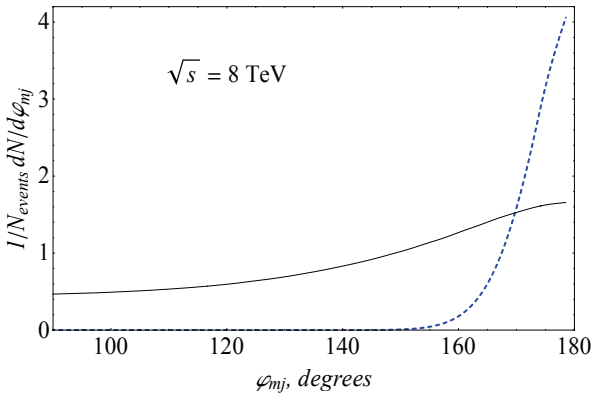

Fig. 12. Distributions $dN(\varphi_{mj})/d\varphi_{mj}$ for (3).
Curves are computed as in Fig 11.

Next we consider how J/ψ and jets, emitted in (3), are separated in rapidity and azimuthal angle. With this aim the distributions $N(y_{mj})$ and $N(\varphi_{mj})$ that depend on y_{mj} and φ_{mj} are calculated. The distributions $N(y_{mj})$ satisfy $N(y_{mj}) = N(-y_{mj})$. According to Fig. 11 functions $N(y_{mj})$ have maxima at $y_{mj} \neq 0$. As displayed in Fig. 12, $N(\varphi_{mj})$

peaks at $\varphi_{mj} \sim 180^\circ$. The transverse momentum vectors $\vec{p}_{T\,J/\psi}$ and $\vec{p}_{T\,jet}$ of J/ψ and jet, created in (3), are essentially oriented in opposite directions. Due to invariance with respect to rotations about the beam line and space inversion functions $N(\varphi_{mj})$ depend on $\vec{p}_{T\,J/\psi} \cdot \vec{p}_{T\,jet}$. The functions meet relations $N(\varphi_{mj}) = N(-\varphi_{mj})$, $N(\pi - \varphi_{mj}) = N(\pi + \varphi_{mj})$, etc. MPI, ISR, and FSR affect the distributions differently. Inclusion of these mechanisms results in $N(y_{mj})$ sharpening, but leads to broadening of $N(\varphi_{mj})$.

Character of y_{mj}–distributions depends on the rapidity $y_{J/\psi}$ of produced J/ψ–meson, as seen in Figs. 13 and 14. With increase of the meson rapidity $y_{J/\psi}$ distribution $dN(y_{mj}, y_{J/\psi})/dy_{mj}$ becomes broader and attains its maximum at larger values of y_{mj}. In the forward region, when $y_{J/\psi} \sim 5\ldots6$, minimum at $y_{mj} \sim 0$ is most pronounced. Nevertheless, the cross sections in this region are about 10^2 times smaller than in central region for $y_{J/\psi} \sim 1\ldots2$. Neither MPI, ISR, nor FSR alter significantly the shape of $N(y_{mj}, y_{J/\psi})$.

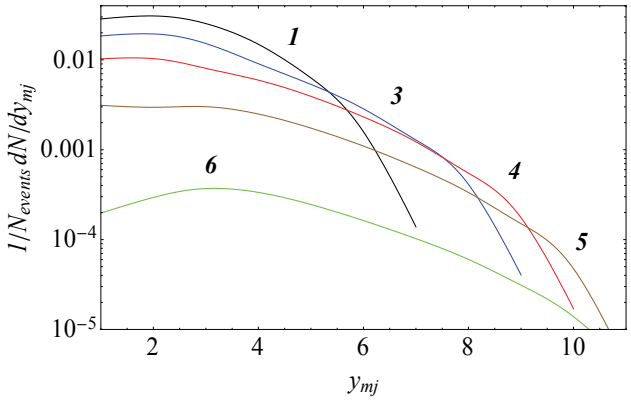

Fig. 13. Distributions $dN(y_{mj},n)/dy_{mj}$ for (3). Notation of the curves as in Fig 7.

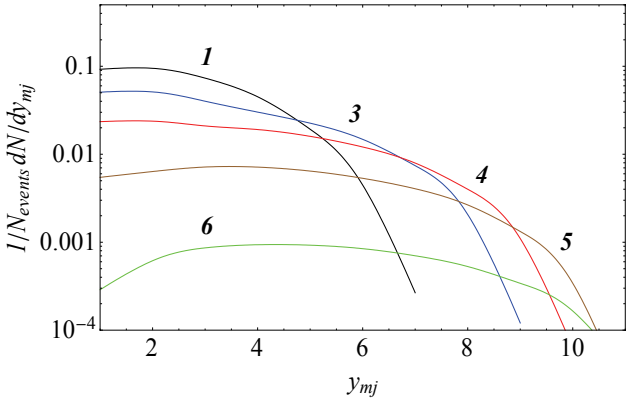

Fig. 14. The same as in Fig. 13. Curves are computed as in Fig 8.

The shape of distribution $dN(\varphi_{mj}, y_{J/\psi})/d\varphi_{mj}$ is not recast in the considered interval of rapidity $y_{J/\psi}$, as illustrated by Figs. 15 and 16. Note, the distributions are symmetrical with respect to transformation $n\pi - \varphi_{mj} \to \varphi_{mj} - n\pi$, where n is an integer. Being calculated without MPI, ISR, and FSR, the distributions exhibit a ridge at $\varphi_{mj} \sim 180^\circ$ and are localized at $\varphi_{mj} = 180^\circ \pm 40^\circ$. Within this approximation creation of more that one jet is strongly suppressed, as Fig. 4 shows, and single jet (if any) is ejected with the transverse momenta $\vec{p}_{T\,jet}$, directed in opposite direction to momentum $\vec{p}_{T\,J/\psi}$ of the meson. Such feature of the oversimplified picture in production of J/ψ–jet pairs does not survive in simulations with MPI, ISR, and FSR switched on. Fig. 16 demonstrates, that $dN(\varphi_{mj}, y_{J/\psi})/d\varphi_{mj}$ with $\varphi_{mj} = \pi \pm \varphi$ turns out to be a slowly decreasing function for $0 < \varphi < \pi/2$.

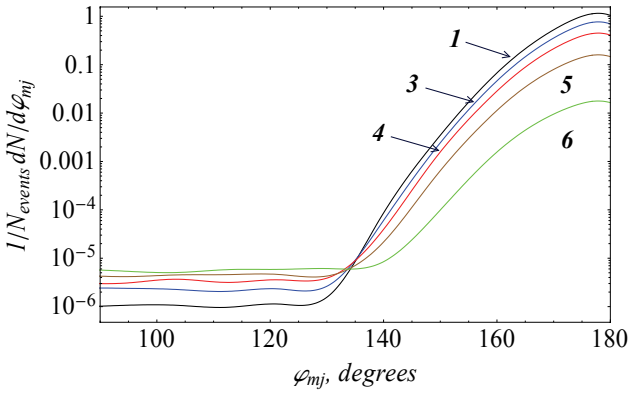

Fig. 15. Distributions $dN(\varphi_{mj},y_{J/\psi})/d\varphi_{mj}$ for (3). Notation of the curves as in Fig 7.

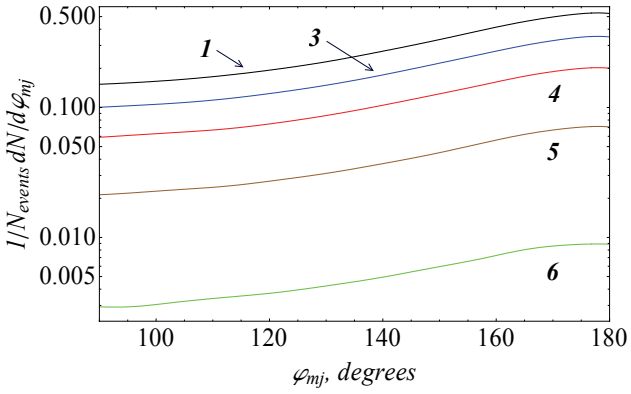

Fig. 16. The same as in Fig. 15. Curves are computed as in Fig 8.

Distance r for jet–pair production is about 2.5 both in (2) and (3), as one can see by comparing the dash–dotted and solid curves in Fig. 17. The quantity r is defined as $r = (\Delta y^2 + \Delta\varphi^2)^{1/2}$, where $\Delta y = y_i - y_k$, $\Delta\varphi = \varphi_i - \varphi_k$, with y_i and φ_i being the rapidity and the azimuthal angle of jet with number i. Since distances r between jets in J/ψ and jet

production take on close values, one can hope that the jet, created in association with the meson, can be disentangled from other jets. Dashed curve in Fig. 17 corresponds to very rare events, when more than one jet is produced in simulation of (3) without MPI, ISR, and FSR. Noticeable difference between solid and dashed curves stresses once more great significance of MPI, ISR, and FSR inclusion into calculations.

Our results for a spectrum in jet–pair production are compared with the recent LHCb data [9] in Fig. 18. In the LHCb experiment distribution of jet–pair invariant mass has been determined for jet pseudorapidities $2 \le \eta_1, \eta_2 \le 4.5$ and azimuthal angles $||\varphi_1 - \varphi_2| - \pi| < 0.7$. Transverse momenta of jets are restricted by $p_{T1}, p_{T2} \ge 20$ GeV/c. From Fig. 18 one can conclude that both LHCb and our simulations with Pythia 6.4 and 8.170, performed with the parton distribution functions CTEQ6L, reproduce the invariant mass dependence of the measured spectrum.

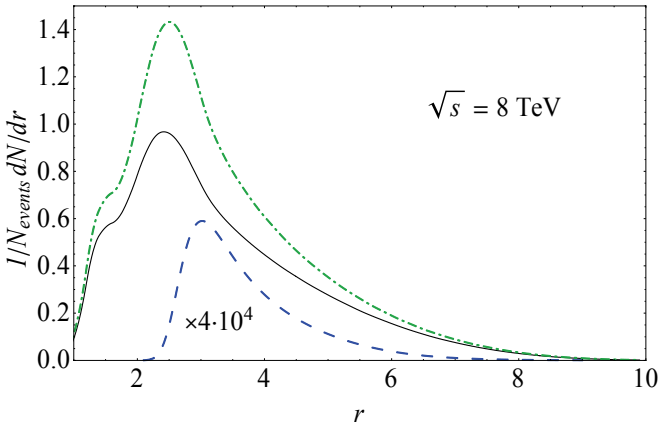

Fig. 17. Distance r between jets in (2) and (3). Curves are computed as in Fig 4.

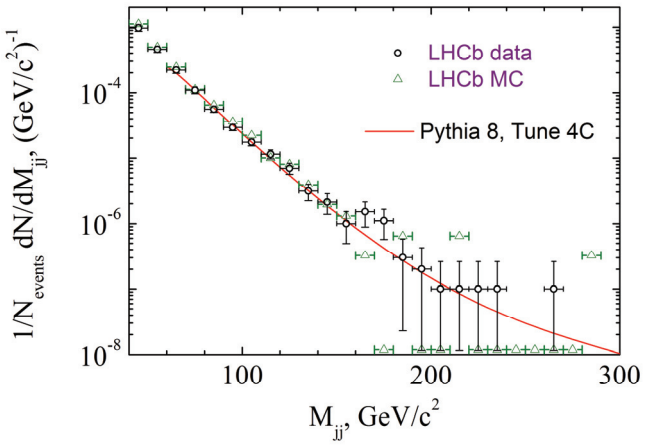

Fig. 18. Dijet spectrum as a function of dijet invariant mass. Circles (triangles) – results [9] of LHCb measurements (MC simulations) at $s^{1/2}$ = 7 GeV. The curve is computed in the present paper.

Spectra in (2) and in $p + p \to jet_1 + jet_2 + X$ under conditions of the LHCb experiment are sensitive to the gluon density in a region of Bjorken x, characterized by the dashed and solid curves in Fig. 19. For comparison dash–dotted curve, obtained in simulations of (1), is displayed as well. Values of x, at which the distribution of x attains its maximum, are shown in this figure. The smaller x from two values of x for 2 → 2 partonic processes is selected.

At rapidity $y_{J/\psi} \sim 2,...2.5$ the spectra in (1) depend on gluon distribution at $x \sim 10^{-3.3}...10^{-3.5}$. In the same region of pseudorapidities η_{jet} spectra for the jet production are determined by gluon distribution at larger values of x. In the forward region observables in processes with jets are affected by gluon density at much smaller x.

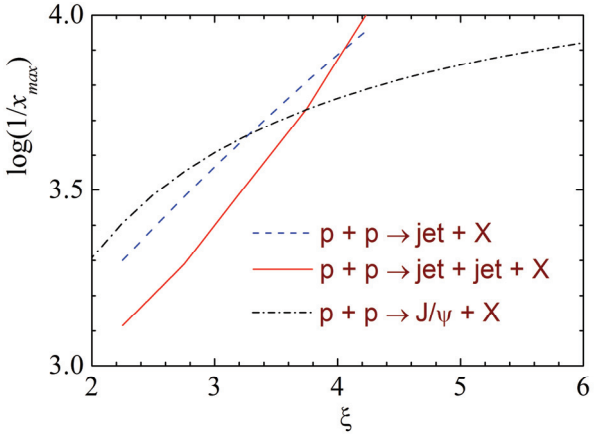

Fig. 19. Dependence of Bjorken $x_{Bj\,max}$ on values of ξ, where $\xi = \eta_{jet}$ or $y_{J/\psi}$ for jet or the meson production. Calculations are performed at $s^{1/2}$ = 7 (8) GeV for jet (charmonium) production.

PROPERTIES OF SPECTRA IN J/Ψ AND JET PRODUCTION IN SPECIFIC REGIONS OF THE PHASE SPACE

Above discussed distributions $N(p_{TJ/\psi})$, $N(y_{mj})$, $N(\varphi_{mj})$, $N(y_{mj}, y_{J/\psi})$, and $N(\varphi_{mj}, y_{J/\psi})$ vary quantitatively with inclusion of MPI, ISR, and FSR, but keep qualitative features of their forms unchangeable. In this section we discuss how shapes of distributions

$$d^2N(y_{mj}, \xi; n)/dy_{mj}\, d\xi = 1/\Delta y_n \int_{y_{n-1}}^{y_n} dy_{J/\psi}\; d^3N(y_{mj}, \xi, y_{J/\psi})/dy_{mj}\; d\xi\; dy_{J/\psi}, \qquad (6)$$

where $\xi = p_{TJ/\psi}$ and φ_{mj}, are affected by these mechanisms.

Fig. 20 gives in detail the (y_{mj}, φ_{mj}) area of interest. Taking into account the symmetry properties of the distribution, the region, shown in the Fig., is reduced to $y_{mj}>0$ and $\varphi_{mj}<\pi$. The curve with label n corresponds to φ_{mj} in bin $(\varphi_{n-1}, \varphi_n)$, where $\varphi_n = \pi n/20$ with n being an integer. For $\varphi_{mj} < \varphi_6$ and $2\pi - \varphi_6 < \varphi_{mj} < 2\pi + \varphi_6$ the curves have a

minima at $y_{mj}=0$ and maxima at $y_{mj}\sim\pm(1.5...1.6)$. With increase of φ_{mj} in interval $\varphi_6<\varphi_{mj}<2\pi-\varphi_6$ the minima are filled and the functions gain a peak at $y_{mj}=0$. Height of the peak goes up, when $\varphi_6\le\varphi_{mj}\le\varphi_8$, then falls in $\varphi_8\le\varphi_{mj}<\varphi_{10}$, and growths again in $\varphi_{10}\le\varphi_{mj}\le\pi$. The same structure also manifests itself, but less distinctively, in distribution $d^2N(y_{mj},\varphi_{mj})/dy_{mj}\,d\varphi_{mj}=\sum_n d^2N(y_{mj},\varphi_{mj};n)/dy_{mj}\,d\varphi_{mj}$, that collect contributions from all slices of J/ψ rapidity.

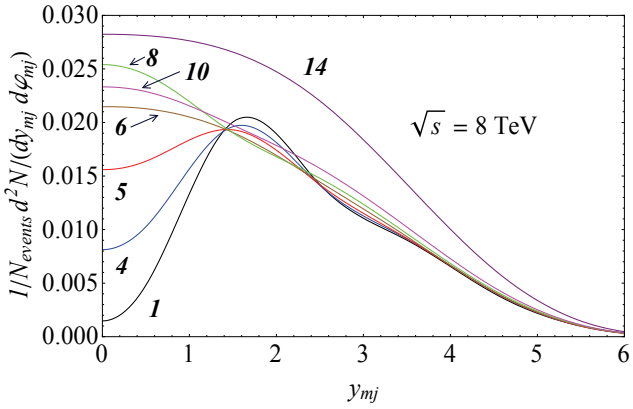

Fig. 20. Distribution $d^2N(y_{mj},\,\varphi_{mj},\,n)/(dy_{mj}d\varphi_{mj})$ for (3).
Labels on the curves are explained in the text.

Fig. 21 (a) and (b) show, that switching the mechanisms on fills in gap in vicinity of $y_{mj}\sim0$, $\varphi_{mj}\sim\pi$. These mechanisms smear the sharp peak, inherent to φ_{mj}–dependence in Fig. 21(a). The stretching is similar to that observed in Figs. 12, 15, and 16. Wings of the spreading peak acquire a structure visible in area of $|y_{mj}|\lesssim5$, $|\varphi_{mj}|\lesssim2\pi/3$. The behavior of distribution (6) as a function of y_{mj} with $\xi=\varphi_{mj}$ and rapidity of the meson in central region $y_{J/\psi}\in(-1,1)$ substantially depends on values of φ_{mj}.

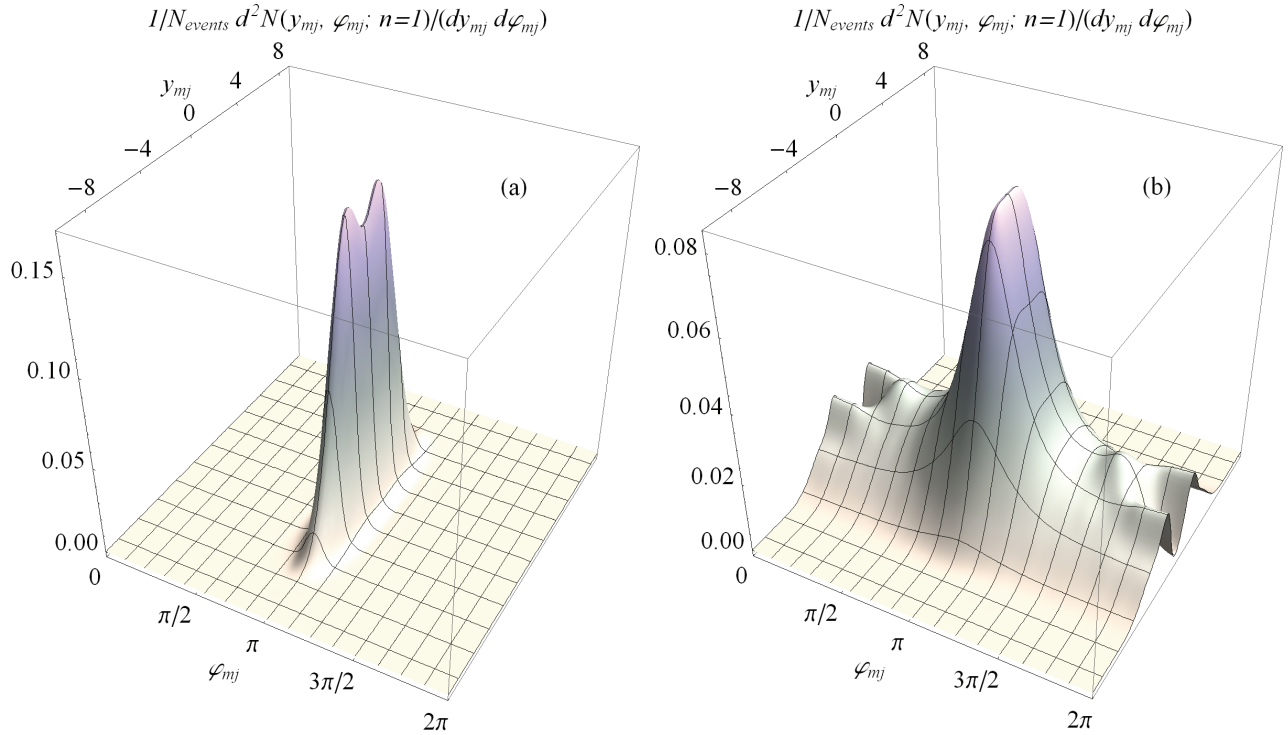

Fig. 21. Distribution $d^2N(y_{mj},\,\varphi_{mj},\,n)/(dy_{mj}d\varphi_{mj})$ for (3) with $y_{J/\psi}$ in interval (0,1) at $s^{1/2}=8$ GeV.
(a) – without MPI, ISR, and FSR, (b) – with inclusion of these processes.

As one can see from Fig. 21 (b) and Fig. 22 (a), (b), with growth of $y_{J/\psi}$ the distributions become wider in y_{mj}, peak at $y_{mj}\sim0$, $\varphi_{mj}\sim\pi$ splits and pronounced gap appears instead at the same place. The similar behavior is inherent to the distributions $dN(y_{mj};n)/dy_{mj}$, displayed in Fig. 14. Indistinct maxima at $\varphi_{max}\sim3\pi/8$ and 2π-φ_{max} in Fig. 21 (b) disappear in Fig. 22 (b).

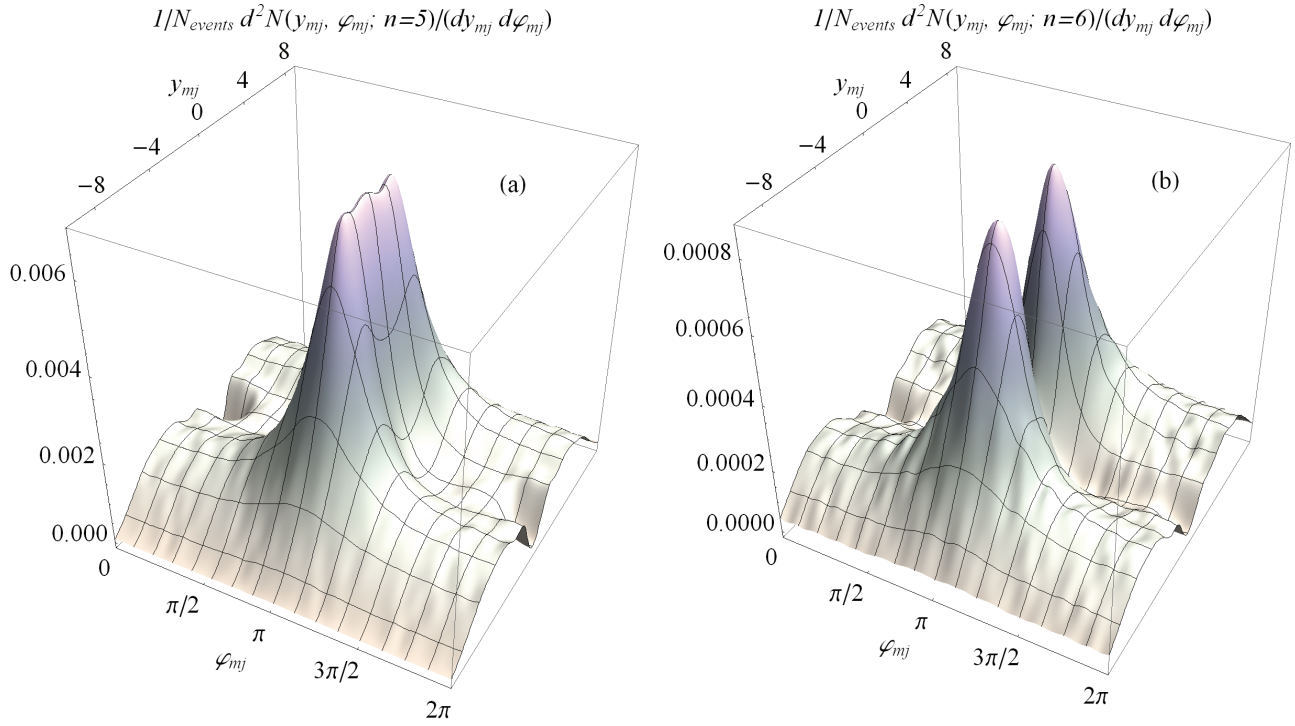

Fig. 22. The same as in Fig. 21 (b),
(a) – for $y_{J/\psi}$ in interval (4,5), (b) – (5,6).

The surface transformations with increase of the meson rapidity are followed by strong downfall of the distribution values that causes, inter alia, the short–range dithering outside of the peaks in Fig. 22. During simulation these areas receive smaller number of events, than regions in vicinity of maxima or in the central rapidity region.

In addition to scrutinizing the angular distributions, we examine properties of distributions (6) which depend on the transverse momentum $p_{TJ/\psi}$ of emitted J/ψ–meson. Transformations of the surface $N(y_{J/\psi}, y_{mj}, p_{TJ/\psi})$, when $y_{J/\psi}$ is running from the central into forward region, have much in common with those, observed in Figs. 20 and 21 for $N(y_{J/\psi}, y_{mj}, \varphi_{mj})$. The gap between two peaks in region $| y_{mj} | < 5$, $|p_{TJ/\psi} | < 5$ GeV/c deepens appreciably. The peaks, being partitioned to a small extent at $y_{J/\psi} \in (0,1)$, become well separated at $y_{J/\psi} \in (5,6)$.

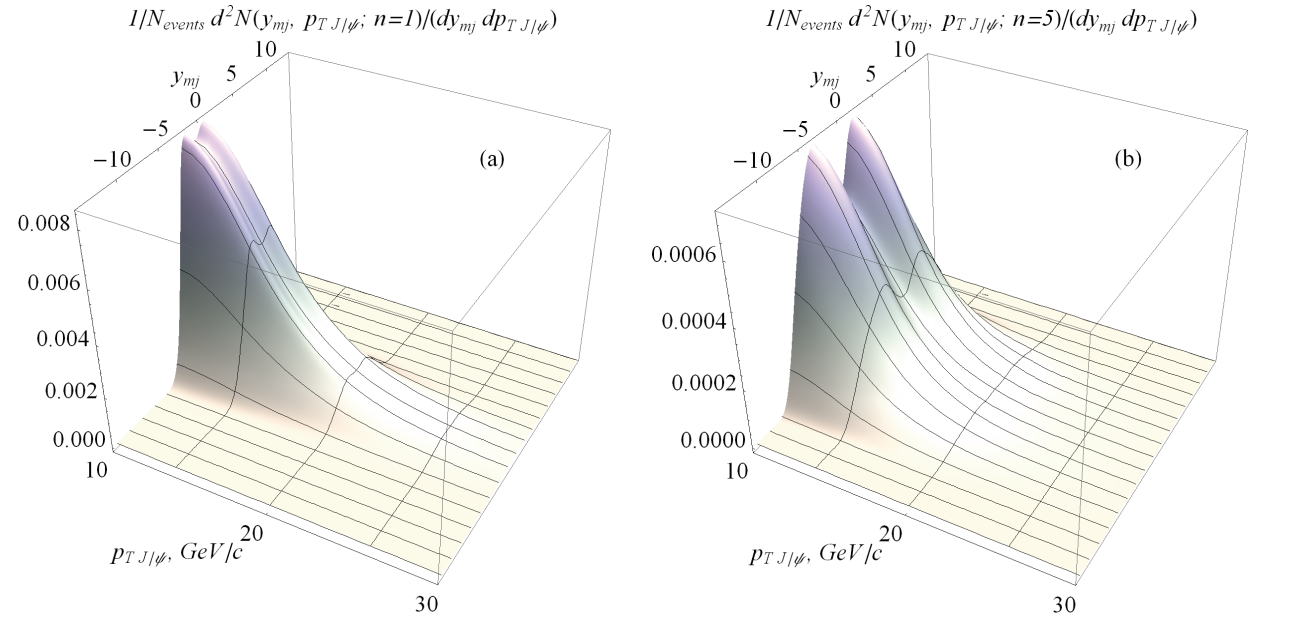

Fig. 23. Distribution $d^2N(y_{mj}, p_{TJ/\psi}, n)/(dy_{mj} d\, p_{TJ/\psi})$ for (3) at $s^{1/2}$ = 8 GeV, computed with MPI, ISR, and FSR.
(a) – for $y_{J/\psi}$ in interval (0,1), (b) – (4,5).

From comparison of the distributions in Figs. 23 and 24 (a) one can see that the spectra, as a functions of $p_{TJ/\psi}$, fall down more steeply with rapidity growth. The splitting of peaks is hardly noticeable in the distributions summarized over the rapidity slices. Figs. 23 (b) and 24 (b) indicate that the observable is considerably influenced by MPI, ISR, and FSR, changing the form of the surface at $y_{J/\psi} \sim 0$ in the forward rapidity region.

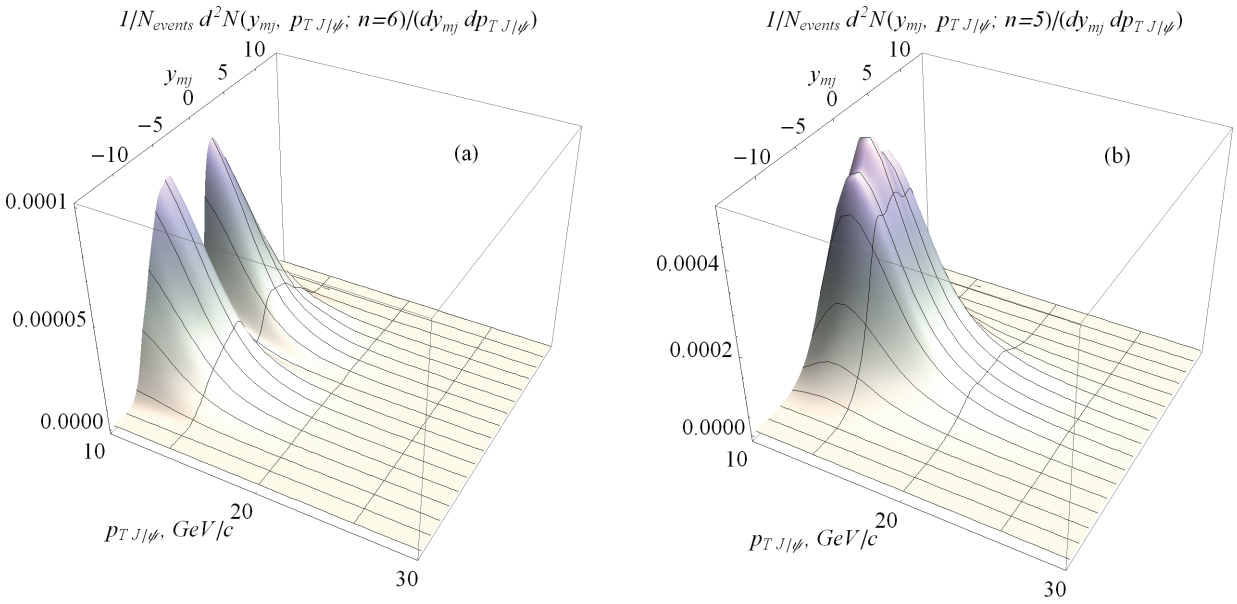

Fig. 24. The same as in Fig. 23,
(a) – with MPI, ISR, and FSR for $y_{J/\psi}$ in interval (5,6),
(b) – with these processes switched off for $y_{J/\psi}$ in interval (4,5).

CONCLUSIONS

Simulation of J/ψ production in proton–proton collisions is carried out with event generator Pythia 8.170. Events, in which the meson is created in association with at least one jet, are analyzed. The SlowJet program, included into Pythia 8 code, is employed for jet finding. Calculations are performed with set of parameter "4C" and parton distribution functions CTEQ6L1.

The observables, that are functions of J/ψ and jet transverse momenta, rapidities, and azimuthal angles, are calculated at $\sqrt{s} = 8$ TeV. Invariant mass spectrum in jet–pair production is computed at $\sqrt{s} = 7$ TeV. The results for the spectrum are in quite a good agreement with the LHCb data in the forward region.

It is shown that the observables in creation of J/ψ–jet pairs are strongly sensitive to initial– and final–state radiation of gluons, as well as to multiparton interactions. Qualitative features of these distributions are studied both in the central and forward regions of the meson emission. The distributions, those depend on differences of the J/ψ and jet rapidities y_{mj}, on differences of the azimuthal angles φ_{mj}, and on J/ψ rapidity $y_{J/\psi}$ or on y_{mj}, J/ψ transverse momentum $p_{TJ/\psi}$, and $y_{J/\psi}$, i.e. being functions of $y_{mj}, \varphi_{mj}, y_{J/\psi}$, and $y_{mj}, p_{TJ/\psi}, y_{J/\psi}$, vary substantially, when J/ψ rapidity passes from central into forward region. Surface shapes of the observables in the variables y_{mj}, φ_{mj} and $y_{mj}, p_{TJ/\psi}$ undergo fairly large changes.

Measurements of the correlation observables in J/ψ–jet pair production prove to be within the potentialities of the detectors at the LHC. New data may serve as a sensitive testing ground for predictions, based on perturbative QCD, and for the approaches, which simulation of initial–, final–state radiation of gluons, and multiparton interactions is based on. The data allow one to infer the validity of models that aim to elucidate mechanisms of heavy–quark pair production and to place severe constraints on them.

REFERENCES

1. Abelev B. (ALICE Collaboration) Measurement of prompt J/ ψ and beauty hadron production production cross sections at mid-rapidity in pp collisions at beauty hadron production $\sqrt{s}$ = 7 TeV // JHEP. – 2012. – Vol.1211. – Iss.11. – 065. – 31 p.
2. Aad G. (ATLAS Collaboration) Measurement of the differential cross-sections of inclusive, prompt and non-prompt J/ ψ production in proton-proton collisions at $\sqrt{s}$ =7 TeV // Nucl. Phys. B. – 2011. – Vol. 850. – P. 387-444.
3. Khachatryan V. (CMS Collaboration) Prompt and non-prompt J/psi production in pp collisions at $\sqrt{s}$ = 7 TeV // Eur. Phys. J. C. – 2011. – Vol.71. – 1575. – 26 p.
4. Chatrchyan S. (CMS Collaboration) J/ψ and ψ(2S) production in pp collisions at $\sqrt{s}$ = 7 TeV // JHEP. – 2012. – Vol.1202. – Iss.2. – 011. – 46 p.
5. Aaij R. (LHCb Collaboration) Measurement of J/ ψ production in pp collisions at $\sqrt{s}$ =7 TeV // Eur. Phys. J. C. – 2011. – Vol.71. – 1645. – 17 p.
6. Brodzicka J., Corradi M., Schienbein I. et al. Heavy Flavour Working Group Summary // arXiv:1208.3379. – 2012. – 16 p.

7. Bodwin G. Theory of Charmonium Production // arXiv:1208.5506. – 2012. – 25 p.
8. Kotlyar V.V., Krupina N.V. J/ψ, Y, and B meson production in proton-proton collisions at the LHC // Prob. Atomic Sci. Technol. – 2012. – Vol.77, Iss.1 – P.183-187.
9. Kucharczyk M. Jet measurements in LHCb and their relevance for PDF's // LHCb-TALK-2012-067. – 2012. – 15 p.
10. Sjoestrand T., Mrenna S., Skands P. PYTHIA 6.4 Physics and Manual // JHEP. – 2006. – Vol. 0605. – 026. – 576 p.
11. Sjoestrand T., Mrenna S., Skands P. A Brief Introduction to PYTHIA 8.1 // Comput. Phys. Commun. – 2008. – Vol.178.– P.852-867.
12. Buckley A., Butterworth J., Gieseke S. et al. General-purpose event generators for LHC physics // Phys. Rept. – 2011. – Vol.504. – P.145-233.
13. Pumplin J., Stump D.R., Huston J. et al. New generation of parton distributions with uncertainties from global QCD analysis // JHEP. – 2002. – Vol.0207. – Iss.7. – 012. – 44 p.

Dieiev Andrii V. is a student of Department of Physics and Technology at V.N. Karazin Kharkiv National University. He is involved in studies of silicon planar and microstrip detectors that are performed at “Physics of Radiation and Tracking Coordinate Detectors” Department at Institute of High–Energy Physics and Nuclear Physics in National Science Center Kharkov Institute of Physics and Technology.

Other area of his scientific interests belongs to phenomenology in high–energy physics. He participates in simulation of φ–, J/ψ–, Y–meson, Ξ–, Ω–baryon, and jet production in proton-proton scattering, investigation of reaction mechanisms, and analysis of correlation observables for the processes, in which pairs of φ, Ξ, Ω, jets, J/ψ–jet are created. Interpretation of results, obtained in the experiments at RHIC, Tevatron, and LHC, is essential direction of his work.

UDC 530.145; 530.1.19

HIGH-ENERGY WAVE PACKETS. 'HALF-BARE' ELECTRON

N.F. Shul'ga, S.V. Trofymenko
Akhiezer Institute for Theoretical Physics of NSC KIPT
1 Akademicheskaya Str., 61108 Kharkov, Ukraine
E-mail: strofymenko@gmail.com
Received 31 October 2012, accepted 14 January 2013

The evolution in space and time of localized high-energy electromagnetic wave packets, which take place in processes of radiation by ultra relativistic electrons is considered. It is shown that high energies make stabilizing influence on the motion of such packets and that the lengths, within which their dispersion and reconstruction into the packets of diverging waves occurs, can be macroscopic. The electromagnetic field evolution in the process of ultra relativistic electron emission from substance into vacuum is considered. It is demonstrated, that in this case the electron can be in 'half-bare' state with considerably suppressed low frequency Fourier-components of the field around it during long period of time after the emission. It is shown that such state of electron can manifest itself in significant dependence of further ionization energy losses of the electron in thin plate situated in the direction of the particle motion on the distance between the plate and the scattering point.
KEY WORDS: electromagnetic wave packets, ionization energy losses, transition radiation, density effect, 'half-bare' electron

ВЫСОКОЭНЕРГЕТИЧЕСКИЕ ВОЛНОВЫЕ ПАКЕТЫ. «ПОЛУГОЛЫЙ» ЭЛЕКТРОН

Н.Ф. Шульга, С.В. Трофименко
Институт теоретической физики им. А.И. Ахиезера ННЦ ХФТИ
ул. Академическая 1, Харьков, 61108, Украина

Рассмотрена пространственно-временная эволюция локализованных высокоэнергетических электромагнитных волновых пакетов, имеющих место в процессах излучения ультра релятивистскими электронами. Показано, что высокие энергии оказывают стабилизирующее влияние на движение таких пакетов и что длины, на которых происходит их расплывание и перестройка в пакеты расходящихся волн, могут иметь макроскопические размеры. Рассмотрена эволюция электромагнитного поля в пространстве при вылете ультра релятивистского электрона из вещества в вакуум. Показано, что в этом случае электрон в течение длительного промежутка времени после вылета из вещества может пребывать в «полуголом» состоянии с сильно подавленными низкочастотными компонентами Фурье в окружающем его поле. Также показано, что такое состояние электрона может проявляться в существенной зависимости его последующих ионизационных потерь энергии в тонкой пластинке, расположенной в направлении движения частицы, от расстояния между пластинкой и веществом.
КЛЮЧЕВЫЕ СЛОВА: электромагнитные волновые пакеты, ионизационные потери энергии, переходное излучение, эффект плотности, «полуголый» электрон

ВИСОКОЕНЕРГЕТИЧНІ ХВИЛЬОВІ ПАКЕТИ. «НАПІВГОЛИЙ» ЕЛЕКТРОН

М.Ф. Шульга, С.В. Трофименко
Інститут теоретичної фізики ім. О.І. Ахієзера ННЦ ХФТІ
вул. Академічна 1, Харків, 61108, Україна

Розглянуто просторово-часову еволюцію локалізованих високоенергетичних електромагнітних хвильових пакетів, що мають місце у процесах випромінювання ультра релятивістськими електронами. Показано, що високі енергії мають стабілізуючий вплив на рух таких пакетів і що довжини, на яких відбувається їх розпливання і перебудова у пакети розбіжних хвиль, можуть мати макроскопічні розміри. Розглянуто еволюцію електромагнітного поля в просторі при вильоті ультра релятивістського електрона з речовини у вакуум. Показано, що в цьому випадку електрон протягом тривалого проміжку часу після вильоту з речовини може перебувати в «напівголому» стані з сильно заглушеними низькочастотними компонентами Фур'є в оточуючому полі. Також показано, що такий стан електрона може виявлятися в істотній залежності його подальших іонізаційних втрат енергії в тонкій пластинці, розташованій у напрямку руху частинки, від відстані між пластинкою і речовиною.
КЛЮЧОВІ СЛОВА: електромагнітні хвильові пакети, іонізаційні втрати енергії, перехідне випромінювання, ефект густини, «напівголий» електрон

A lot of high-energy physical processes develop within large domains of space along the direction of particle motion (see, for example monographs [1-4] and references in them). In the case of electromagnetic processes the size of these domains can substantially exceed sometimes not only interatomic distances of substance but the size of experimental facility (detectors) as well [1, 2, 4-13]. Essential in this case is the fact that interaction of particles with atoms and experimental facility situated within such domains and outside them can substantially differ. Such situation arises, for example, when considering long-wave radiation in processes of bremsstrahlung and transition radiation by ultra relativistic electrons [14-16]. Therefore, it is necessary to know what happens within such regions and what the peculiarities of evolution of such processes in space and time are. In the present paper we consider the evolution of transition radiation process during relativistic electron emission from dielectric substance into vacuum and manifestation of transformation of electromagnetic field around the particle in this process during further interaction of

this electron with matter.

The considered problem is closely related to the problem of study of the behavior of localized high-energy wave packets. Therefore, firstly, we will consider some peculiarities of the behavior of such wave packets drawing special attention to the questions of their stability and reconstruction into the packets of diverging waves. Further we show that the discussed wave packets naturally arise in the process of relativistic electron emission from substance into vacuum.

The consideration is made on the basis of classical electrodynamics. In this case the moving electron is considered as a charge with its own Coulomb field moving together with it. During the electron traversal of the medium-vacuum interface the perturbation of this field occurs. This perturbation is treated here as appearance of a packet of free plane electromagnetic waves, which reconstructs then into a packet of diverging waves of transition radiation. For ultra relativistic particles, however, this does not happen at once. The distance from the interface, within which this process develops, has a name of the coherence length of the transition radiation process [1, 2]. It is $2\gamma^2$ times larger than the length λ of the considered radiated waves (γ is here the electron Lorentz-factor). We show that within this length the field around the electron in vacuum substantially differs from the Coulomb one and the particle exists in so called 'half-bare' state [17, 18] with suppressed low-frequency components of the field around it. It is possible to place thin dielectric plate within this distance from the substance in the direction of the electron motion and consider ionization energy losses of the particle in it. In the present paper it is shown that the electron energy losses in such plate significantly depend on the distance between the plate and the substance, from which the electron is emitted, and are defined by the magnitude of interference between the electron's own Coulomb field and the packet of free waves.

The aim of the paper is to investigate some peculiarities of space-time evolution of the field of high-energy electromagnetic wave packets and to consider the manifestation of such field evolution in the process of relativistic electron ionization energy losses.

HIGH-ENERGY WAVE PACKETS

The general solution of the wave equation can be presented in the form of a wave packet, which spatially disperses in course of time. In semiclassical approximation such packet does not disperse. It moves according to the laws of classical mechanics (see, for example [2, 19]). It is going beyond the semiclassical approximation that leads to the packet dispersion. The high-energy wave packets are of special interest because the speed of their dispersion decreases with the increase of their energy. Let us pay attention to some peculiarities of dispersion of such packets. Significant here is the fact that characteristic features of this dispersion are similar for all fields. Therefore it is sufficient to consider just scalar field.

The general solution of the wave equation

$$\left(\frac{\partial^2}{\partial t^2} - \nabla^2 + m^2\right)\varphi(\vec{r},t) = 0 \tag{1}$$

for a scalar particle with the mass m can be written in the following form of the expansion of the field $\varphi(\vec{r},t)$ over plane waves:

$$\varphi(\vec{r},t) = \int \frac{d^3\kappa}{(2\pi)^3} e^{i(\vec{\kappa}\vec{r} - \omega t)} C_{\vec{\kappa}}\,, \tag{2}$$

where $\omega = \sqrt{\vec{\kappa}^2 + m^2}$ and $C_{\vec{\kappa}}$ - are the expansion coefficients. Here and further we will use the system of units in which the speed of light c and the Plank constant $\hbar$ equal unit.

Let us consider the dispersion of the wave packet, which at the initial moment of time coincides with the Gaussian packet modulated by the plane wave with large value of the momentum $\vec{p}$ [2, 20]. Moreover we will assume that the initial widths of the packet $a_{\|}$ and $a_{\perp}$ parallel and perpendicular to the particle momentum $\vec{p}$ are different. For such packet at the initial moment of time the field $\varphi(\vec{r},t)$ has the following form:

$$\varphi(\vec{r},t) = \exp\left\{i\vec{p}\vec{r} - \frac{z^2}{2a_{\|}^2} - \frac{\vec{\rho}^2}{2a_{\perp}^2}\right\}, \tag{3}$$

where z and $\vec{\rho}$ are the coordinates parallel and orthogonal to $\vec{p}$. At the moment of time t this packet will be defined by the relation (2) with

$$C_{\vec{\kappa}} = (2\pi)^{3/2} a_{\|} a_{\perp}^2 \exp\left\{-\frac{(p-\kappa_z)^2 a_{\|}^2}{2} - \frac{\kappa_{\perp}^2 a_{\perp}^2}{2}\right\}. \tag{4}$$

We can write the obtained expression for the field $\varphi(\vec{r},t)$ in the form

$$\varphi(\vec{r},t) = Ae^{i(\vec{p}\vec{r}-\varepsilon\, t)} I(\vec{r},t)\,, \tag{5}$$

in which $A = a_{\|}a_{\perp}^2$, $\varepsilon = \sqrt{\vec{p}^2 + m^2}$ and

$$I(\vec{r},t) = (2\pi)^{-3/2} \int d^3\kappa \exp\left\{ i(\vec{\kappa} - \vec{p})\vec{r} - \frac{(p-\kappa_z)^2 a_{\|}^2}{2} - \frac{\kappa_{\perp}^2 a_{\perp}^2}{2} - i(\omega_k - \varepsilon)t \right\}. \tag{6}$$

Having made in this expression the variable substitution $\vec{\kappa} = \vec{p} + \vec{q}$ we find that

$$I(\vec{r},t) = (2\pi)^{-3/2} \int d^3q \exp\left\{ i\vec{q}\vec{r} - \frac{q_z^2 a_{\|}^2}{2} - \frac{q_{\perp}^2 a_{\perp}^2}{2} - i(\omega_{\vec{p}+\vec{q}} - \varepsilon)t \right\}. \tag{7}$$

In the case of large energies it is possible to make the expansion over $|\vec{q}|/p$ in the quantity $(\omega_{\vec{p}+\vec{q}} - \varepsilon)$ in (7). Having preserved the quadratic terms of expansion we obtain

$$\omega_{\vec{p}+\vec{q}} - \varepsilon \approx vq_z + \frac{q_z^2}{2\varepsilon\gamma^2} + \frac{q_{\perp}^2}{2\varepsilon}\,, \tag{8}$$

where $v = p/\varepsilon$ and $\gamma = (1-v^2)^{-1/2}$. Substituting this expression into (7) after simple calculations we obtain

$$I(\vec{r},t) = \frac{1}{\sqrt{a_{\|}^2 + i\dfrac{t}{\varepsilon\gamma^2}}} \;\; \frac{1}{a_{\perp}^2 + i\dfrac{t}{\varepsilon}} \;\; \exp\left\{ -\frac{(z-vt)^2}{2\left(a_{\|}^2 + i\dfrac{t}{\varepsilon\gamma^2}\right)} - \frac{\rho^2}{2\left(a_{\perp}^2 + i\dfrac{t}{\varepsilon}\right)} \right\}. \tag{9}$$

The formula (9) can be written in the following form as well:

$$I(\vec{r},t) = A(t) \exp\left\{ i\alpha(\vec{r},t) - \frac{(z-vt)^2}{2\Delta_{\|}^2(t)} - \frac{\rho^2}{2\Delta_{\perp}^2(t)} \right\}, \tag{10}$$

in which $A(t)$ is a slowly changing quantity

$$A(t) = \frac{1}{\left(a_{\perp}^2 + i\dfrac{t}{\varepsilon}\right)\sqrt{a_{\|}^2 + i\dfrac{t}{\varepsilon\gamma^2}}}\,, \tag{11}$$

$\alpha(\vec{r},t)$ is the real phase

$$\alpha(\vec{r},t) = \frac{(z-vt)^2}{2} \frac{t/\varepsilon\gamma^2}{a_{\|}^4 + \left(t/\varepsilon\gamma^2\right)^2} + \frac{\rho^2}{2} \frac{t/\varepsilon}{a_{\perp}^4 + \left(t/\varepsilon\right)^2}\,, \tag{12}$$

$\Delta_{\|}(t)$ and $\Delta_{\perp}(t)$ are the longitudinal and transverse widths of the packet at the moment of time t

$$\Delta_{\|}^2(t) = a_{\|}^2 + \left(\frac{t}{a_{\|}\varepsilon\gamma^2}\right)^2, \qquad \Delta_{\perp}^2(t) = a_{\perp}^2 + \left(\frac{t}{a_{\perp}\varepsilon}\right)^2. \tag{13}$$

In the case of $a_{\|} = a_{\perp}$ the obtained above formulae coincide with the corresponding result of the paper [20].

The formulae (13) show that in longitudinal and transverse directions the squares of the widths of the packet $\Delta_{\|}^2(t)$ and $\Delta_{\perp}^2(t)$ grow with time proportionally to t^2m^4/ε^6 and t^2/ε^2. In nonrelativistic case these quantities do not depend on the particle energy ($t^2/\varepsilon^2 = t^2/m^2$). In relativistic case the quantities t^2m^4/ε^6 and t^2/ε^2 are substantially smaller

than the corresponding values for nonreativistic particles. Let us note that the additional factor m^4/ε^4 exists for longitudinal direction in $\Delta_{\|}^2(t)$. It leads to the substantial decrease of the speed of the packet dispersion in this direction compared to the speed of the packet dispersion in transverse direction. Thus the relativistic effects do the stabilizing influence upon the wave packets.

Now let us consider high energy packets of free electromagnetic waves. Scalar and vector potentials of such packets are the solutions of the wave equation (1) with $m=0$. Therefore in order to analyze the peculiarities of dispersion of such packets we can use the previous formulae assuming that all the terms in them containing the Lorentz-factor γ equal zero. In this case for scalar potential we find that

$$\varphi(\vec{r},t) = Ae^{i(\vec{k}\vec{r}-\omega t)} I(\vec{r},t)\,, \tag{14}$$

where $\vec{k}$ and ω are the wave vector and the frequency of the electromagnetic wave and

$$I(\vec{r},t) = A(t)\exp\left\{ i\alpha_k(\vec{r},t) - \frac{(z-t)^2}{2\Delta_{\|}^2} - \frac{\rho^2}{2\Delta_{\perp}^2} \right\}. \tag{15}$$

Here

$$A(t) = \frac{1}{a_{\|}\left(a_{\perp}^2 + it/\omega\right)}, \qquad \alpha(\vec{r},t) = \frac{\rho^2}{2}\frac{t/\omega}{a_{\perp}^4 + \left(t/\omega\right)^2}\,, \tag{16}$$

and

$$\Delta_{\|}^2(t) = a_{\|}^2\,, \qquad \Delta_{\perp}^2(t) = a_{\perp}^2 + \left(t/a_{\perp}\omega\right)^2.$$

The obtained formulae show that the initially Gaussian packet does not disperse in the direction parallel to the $\vec{k}$ vector. In transverse direction the square of the packet widths grows proportionally to $(t/\omega)^2$. Thus the speed of the packet dispersion decreases with the increase of the wave frequency ω.

When considering a process of radiation by relativistic electrons it is often necessary to deal with packets, which are constructed of plane waves with wave vectors, which directions are close to the direction of a given vector $\vec{k}$. Such wave packets differ somehow from the ones considered above. Let us consider some peculiarities of dispersion of such packets assuming for simplicity that at the initial moment of tome $t=0$ the distribution of the waves over the wave vectors is Gaussian relative to the given vector $\vec{k}$ [21]. For such distribution in the initial moment of time the scalar potential $\varphi_k(\vec{r},0)$ has the following form:

$$\varphi_k(\vec{r},0) = \frac{1}{\pi\bar{\Delta}_{\vartheta}^2}\int d^2\vartheta e^{-\vartheta^2/\bar{\Delta}_{\vartheta}^2} e^{i\vec{k}\vec{r}}\,, \tag{17}$$

where ϑ is the angle between the packet wave vector and the wave vector $\vec{k}$, $\bar{\Delta}_{\vartheta}^2$ is the average value of the square of the angle ϑ, $\bar{\Delta}_{\vartheta}^2 << 1$.

The coefficients $C_{\vec{q}}$ of the Fourier expansion (2) for such initial packet have the following form

$$C_{\vec{q}} = (2\pi)^3 \int \frac{d^2\vartheta}{\pi\bar{\Delta}_{\vartheta}^2} e^{-\vartheta^2/\bar{\Delta}_{\vartheta}^2} \delta(\vec{k}-\vec{q})\,, \tag{18}$$

in which $\delta(\vec{k}-\vec{q})$ is the delta-function. As a result we come to the following expression for the scalar potential

$$\varphi_k(\vec{r},t) = \frac{1}{1+ikz\bar{\Delta}_{\vartheta}^2/2} e^{ik(z-t) - \frac{(k\rho/2)^2\bar{\Delta}_{\vartheta}^2}{1+ikz\bar{\Delta}_{\vartheta}^2/2}}\,, \tag{19}$$

where z and $\vec{\rho}$ are the coordinates parallel and orthogonal to $\vec{k}$.

The given expression for the wave packet has the same structure as the corresponding expression for the packet (14). If the substitutions $(t/a_{\perp}^2\varepsilon) \to (\omega\, z\bar{\Delta}_{\vartheta}^2/2)$ and $a_{\|}^2 \to \infty$ are made in the latter expression the both formulae for the wave packet will become identical.

The formula (19) shows that for $\omega\, z\bar{\Delta}_{\vartheta}^2/2 << 1$

$$\langle \varphi_k(\vec{r},t)\rangle \approx \exp\left\{ i\omega(z-t) - \left(\frac{\omega\rho}{2}\right)^2 \bar{\Delta}_\vartheta^2 \right\}, \tag{20}$$

and for $\omega\ z\bar{\Delta}_\vartheta^2/2 >> 1$

$$\langle \varphi_k(\vec{r},t)\rangle \approx -\frac{2i}{\omega\ z\bar{\Delta}_\vartheta^2} \exp\left\{ i\omega(z-t) + i\omega\frac{\rho^2}{2z} - \frac{\rho^2}{z^2\bar{\Delta}_\vartheta^2} \right\}. \tag{21}$$

For $z >> \rho$ the latter formula can be written in the form of a diverging wave

$$\langle \varphi_k(\vec{r},t)\rangle \approx -\frac{2i}{\omega\ r\bar{\Delta}_\vartheta^2} \exp\left\{ i\omega(r-t) - \frac{\rho^2}{z^2\bar{\Delta}_\vartheta^2} \right\}, \tag{22}$$

where $r = \sqrt{z^2+\rho^2} \approx z + \rho^2/2z$. Thus on distances z from the center of the initial packet, which satisfy the condition

$$\omega\ z\bar{\Delta}_\vartheta^2/2 << 1 \tag{23}$$

the form of the packet (19) coincides with the form of the packet at $t = 0$. Only on the distances, which satisfy the condition

$$\omega\ z\bar{\Delta}_\vartheta^2/2 >> 1 \tag{24}$$

the transformation of the packet (19) to the packet of spherical diverging waves occurs.

Let us note that in the theory of radiation of electromagnetic waves by a moving electron the spatial region in which the formation of spherical diverging waves occurs has a name of the wave zone (see for example [22]). In particular, for nonrelativistic charged particles the wave zone begins on distances from the radiation region, which exceed the length of the radiated wave λ . However, the condition (24) shows that for $\bar{\Delta}_\vartheta^2 << 1$ the wave zone formation occurs not on distances $z >> \lambda$ as in the case of a nonrelativistic particle but on distances

$$z >> 2\lambda/\bar{\Delta}_\vartheta^2, \tag{25}$$

which are much larger than the wave length $\lambda = 1/\omega$. For sufficiently small values of $\bar{\Delta}_\vartheta^2$ the length $z = 2\lambda/\bar{\Delta}_\vartheta^2$ can reach macroscopic size.

ELECTROMAGNETIC FIELD OF ELECTRON AFTER ITS EMISSION FROM SUBSTANCE

The electromagnetic wave packets similar to the ones considered above arise, for example, in the process of ultra relativistic electron traversal of boundary between two substances. In particular, let us consider some peculiarities of evolution of such packets during the electron emission from dielectric substance into vacuum.

During the motion of a charged particle in substance with dielectric permittivity ε_ω the screening of its own Coulomb field on large distances from the particle takes place. It happens due to polarization of the substance by the particle's field. In transverse direction with respect to the particle motion such screening occurs on distances $\rho \geq 1/\omega_p$, where ω_p is the plasma frequency. After the particle emission from the substance into vacuum the field around it is defined from the solution of Maxwell equations with corresponding boundary conditions for electric field and induction on the dielectric-vacuum interface. Taking into account these boundary conditions the electric field around the electron in vacuum can be presented as superposition of the electron's own Coulomb field in vacuum $\vec{E}^c(\vec{r},t)$ and the field of packet of free waves $\vec{E}^f(\vec{r},t)$: $\vec{E}(\vec{r},t) = \vec{E}^c(\vec{r},t) + \vec{E}^f(\vec{r},t)$. Significant here is the fact that considerable interference between these fields takes place, as a result of which on small distances from the interface the total field $\vec{E}(\vec{r},t)$ around the electron significantly differs from the Coulomb one. With the increase of distance between the particle and the interface such interference decreases and it is possible to consider the fields $\vec{E}^c$ and $\vec{E}^f$ as independent electron's own field and the field of radiation. For the Fourier-components of these fields with different frequencies such separation, however, occurs independently and on different distances. Therefore further we will consider the evolution of a single-frequency Fourier-component of the surrounding electron field.

In the considered ultra relativistic case the field around the electron can be considered as transversal to the direction of the particle motion (which is chosen to coincide with positive direction of z - axis), having just ρ - component. Taking into account the mentioned above boundary conditions, the Fourier-harmonic of frequency ω of the transversal component of the total field around the electron in vacuum can be presented in the next form (watch for example [1]):

$$E_\omega(\vec{\rho},z)=-\frac{ie}{\pi v}\frac{\vec{\rho}}{\rho}\int_0^\infty d^2q\vec{q}e^{i\vec{q}\vec{\rho}}\left\{\ Q_f(q)e^{iz\sqrt{\omega^2-q^2}}+Q_c(q)e^{i\omega\ z/v}\right\},\tag{26}$$

where

$$Q_f(q)=\frac{\sqrt{\omega^2-q^2}}{\sqrt{\omega^2\varepsilon-q^2}+\varepsilon\sqrt{\omega^2-q^2}}\left[\frac{1+\frac{v}{\omega}\sqrt{\omega^2\varepsilon-q^2}}{q^2+\frac{\omega^2}{v^2\gamma^2}-(\varepsilon-1)\omega^2}-\frac{\varepsilon+\frac{v}{\omega}\sqrt{\omega^2\varepsilon-q^2}}{q^2+\frac{\omega^2}{v^2\gamma^2}}\right],$$

$$Q_c(q)=\frac{1}{q^2+\frac{\omega^2}{v^2\gamma^2}}$$

and $\vec{q}$ is the orthogonal to z - axis component of the wave vector $\vec{k}$. The first term in (26) defines the packet of free waves in vacuum, which appears during the particle traversal of the substance-vacuum interface and gradually transforms into the field of transition radiation. It is a packet of plane waves with different directions of wave vector $\vec{k}$ ($\left|\vec{k}\right|=\omega$) of the similar type as the packet (19) (here we do not include the time-dependent factor $e^{-i\omega\ t}$ to the expression for E_ω). The second term in (26) defines the electron's own Coulomb field uniformly moving in vacuum.

After integration over the angle between $\vec{q}$ and $\vec{\rho}$ in (26) we receive:

$$E_\omega(\rho,z)=\frac{2e}{v}\int_0^\infty dqq^2J_1(q\rho)\left\{\ Q_f(q)e^{iz\sqrt{\omega^2-q^2}}+Q_c(q)e^{i\omega\ z/v}\right\},\tag{27}$$

where $J_1(x)$ is the Bessel function.

Let us note, that in the region $q>\omega$ the term in (27), which contains the quantity Q_f, exponentially decreases with the increase of z. Therefore it is possible to neglect the contribution of the region $q>\omega$ to the integral over q in this term.

In ultra relativistic case the frequencies ω, which make the main contribution to transition radiation spectrum, significantly exceed the plasma frequency of the substance ω_p. In this case we can use the following expression for dielectric permittivity of the substance, from which the electron is emitted:

$$\varepsilon(\omega)\approx 1-\omega_p^2/\omega^2.\tag{28}$$

In the terms containing Q_f in (27) the main contribution to the integral over q is made by values $q\le\omega_p<<\omega$ and the square roots in (27) can be expanded in parameter q^2/ω^2. At the same time due to convergence of the integral over q the integration in terms containing Q_f can be extended to infinity. As a result for the Fourier-component of the total field we obtain the expression

$$E_\omega(\rho,z)=\frac{2e}{v}e^{i\omega\ z}\int_0^\infty dqq^2J_1(q\rho)\left\{\ \widetilde{Q}_f(q)\exp\left(-i\frac{\omega\ z}{2v^2\gamma^2}-i\frac{q^2z}{2\omega}\right)+Q_c(q)\right\},\tag{29}$$

with

$$\widetilde{Q}_f=-\frac{\omega_p^2}{\left(q^2+\omega_p^2+\frac{\omega^2}{v^2\gamma^2}\right)\left(q^2+\frac{\omega^2}{v^2\gamma^2}\right)}.$$

On very small distances from the interface between the substance and the vacuum ($z\to 0$) the harmonic (29) of the total field around the electron nearly coincides with the harmonic of the particle's Coulomb field in the substance screened by polarization:

$$E_\omega(\rho,z)=\frac{2e}{v}\sqrt{\frac{\omega^2}{v^2\gamma^2}+\omega_p^2}\,K_1\left(\rho\sqrt{\frac{\omega^2}{v^2\gamma^2}+\omega_p^2}\right)e^{i\omega\ z}. \qquad (30)$$

From (30) we can see that after the electron emission from substance the Fourier-components of frequencies $\omega \le \gamma\omega_p$ are suppressed in the field around the electron comparing to the corresponding Fourier components of electron's Coulomb field in vacuum, which are defined by the expression (30) with $\omega_p = 0$. The electron with such field is known as 'half-bare' electron [17, 18]. Such state of the particle also appears in the process of ultra relativistic electron scattering to a large angle and can manifest itself, for example, during further collisions of such electron with atoms of substance causing different effects of bremsstrahlung suppression (Landau-Pomeranchuk-Migdal effect [23, 24], the effect of radiation suppression in thin layer of substance (TSF-effect [25, 26]), etc.). The 'half-bare' state of the scattered electron should also manifest itself in the process of further transition radiation by such electron [14-16].

With the increase of distance between the electron and the substance the interference between the particle's own field and the packet of free waves decreases and the half-bare electron 'dresses' with its proper Coulomb field in vacuum. The distance z from the substance, on which the 'dressing' of the particle and reconstruction of the wave packet into the field of transition radiation occur is the coherence length of the radiation process. It is defined by the relation $l_c \approx 2\gamma^2/\omega$ and significantly exceeds the wavelength of the considered Fourier-component $\lambda = 2\pi/\omega$. In the considered case of ultra relativistic electron the transition radiation is mainly concentrated in the range of small angles ϑ between the radiation direction and the electron velocity [27]. For such angles in the region of distances from the substance $z \ge l_c$ the integral over q in the first item in (29) can be calculated with the use of stationary phase method. In this case the Fourier-harmonic of the total field naturally divides into the harmonic of electron's Coulomb field in vacuum and spherical diverging wave of transition radiation:

$$E_\omega(\rho,z)=\frac{2e}{v}\left\{\frac{\omega}{v\gamma}K_1\left(\frac{\omega\rho}{v\gamma}\right)e^{i\omega\ z/v}+\frac{e^{i\omega\ r}}{r}F(\vartheta)\right\}, \qquad (31)$$

where

$$F(\vartheta)=\frac{\omega_p^2}{\omega^2}\frac{\vartheta}{(\vartheta^2+\omega_p^2/\omega^2+1/v^2\gamma^2)(\vartheta^2+1/v^2\gamma^2)},$$

$\vartheta = \rho/z << 1$ and $r=\sqrt{\rho^2+z^2} \approx z+\rho^2/2z$.

The spectral-angular density of transition radiation, associated with the second item in (31) is given by the formula

$$\frac{d\mathcal{E}}{d\omega do}=\frac{r^2}{4\pi^2}\left|E_\omega^f(\vec{r})\right|^2=\frac{e^2}{\pi^2}F^2(\vartheta)$$

and coincides with the well-known expression of transition radiation theory [27].

IONIZATION ENERGY LOSSES OF 'HALF-BARE' ELECTRON IN THIN PLATE

Let us now consider how the reconstruction of the field around the electron after its emission from substance can influence on further interaction of the electron with matter. In particular, let us consider how the 'half-bare' state of the electron manifests itself in the particle ionization energy losses in thin dielectric plate situated close to the substance from which the electron is emitted.

A fast charged particle in substance loses its energy on excitation and ionization of the atoms of the substance. In the case of not very fast particles the value of such energy losses is defined by Bethe-Bloch formula [28, 29]. With the increase of the particle energy Fermi density effect [30] becomes essential, which leads to the decrease of energy losses in comparison with the correspondent result of Bethe and Bloch. This effect is caused by polarization of the atoms of the medium by the field of the particle which moves in substance. During the particle traversal of the border between two media due to reconstruction of the particle's field its ionization energy losses in the boundary region can significantly differ from the energy losses on large distances from the border. The possibility of such effect was indicated in the paper of G.M. Garibian [31], in which it was shown that in the case of passage of ultra relativistic electrons through sufficiently thin layer of substance (a layer of thickness less than $\delta = I/\omega_p^2$, where I is mean ionization potential of the atoms of substance and ω_p is the plasma frequency) Fermi density effect is absent and ionization energy losses are defined by Bethe-Bloch formula even in the case of very large particle energies. Experimentally such effect was observed in the works [32,33]. Let us note that some deviation from Fermi density effect was observed in the work [34] for ionization energy losses of ultra high energy electrons in relatively thick plates

of substance as well.

Significant role in the process of ionization of the atoms of substance is played by Fourier-components of the particle's field with the frequencies close to the own frequencies of the atoms of substance. At the same time the characteristic distances from the boundary between two media, on which the reconstruction of the field around the electron occurs, are defined by the lengths of absorption of these Fourier-components in substance. By the order of the magnitude these lengths correspond to thicknesses of the targets, for which the Garibian effect in ionization energy losses takes place.

Let us consider now the ionization energy losses of the electron in thin dielectric plate, situated on distance z from the point of the electron emission from substance (see Fig.). The peculiarity of the considered process is in the fact that the reconstruction of the field around the electron after its emission occurs in vacuum in the absence of any absorption. Hence in this process the effects associated with reconstruction of the field around the electron can be observed in the particle ionization energy losses on large distances between the plate and substance, which significantly exceed the distances, on which the effect of Garibian takes place.

The consideration of the given process is carried out on the basis of Bohr's method [35, 36] of description of fast particle ionization energy losses in substance associated with separate consideration of the process in the region of small and large values of impact parameters. We draw the special attention in this case to the processes associated with large impact parameters. In this case the particle interaction with electron subsystem of the plate is considered in Fermi model of atoms of the medium [37], in which the bound atomic electrons are represented by a set of harmonic oscillators. In the region of large values of impact parameters the excitation of the atoms of the plate by incident electron is caused mostly by the Fourier-harmonics of transversal component of the electromagnetic field around the electron inside the plate, with frequencies ω of the order of characteristic frequencies of electron vibration in atoms ω_0. At the same time if the plate thickness is less than the absorption length of electromagnetic waves with frequency $\omega \approx \omega_0$ in substance, the energy transmitted to the electron subsystem of the plate will be defined by the Fourier-component (27) with the frequency $\omega \approx \omega_0$ of the field falling on the plate. In the simplest model of atoms of the medium, in which the own frequencies of electron oscillators ω_0 are taken to equal mean value of atomic ionization potential of the substance, the energy transfer to each atomic electron is defined by the relation [38]:

$$\Delta\mathcal{E} = \frac{e^2}{2m}\left|E_{\omega_0}\right|^2,$$

where e and m are charge and mass of the electron and E_{ω_0} – Fourier-component of the field around the incident electron transverse to the direction of the particle motion. Let us note that the electric field E_{ω_0} includes both electron's own Coulomb field in vacuum and the packet of free waves, which appeared as a result of electron emission from substance.

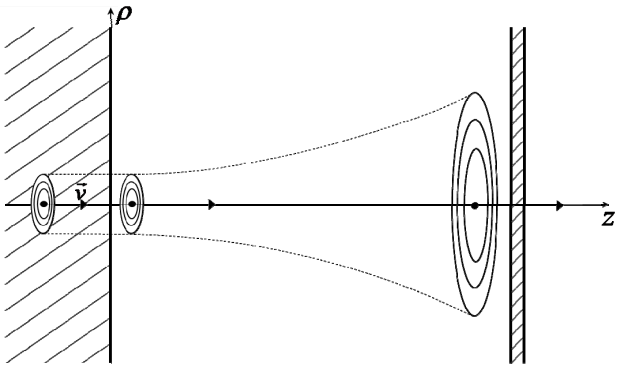

Fig. Traversal of thin plate by an electron after its emission from substance

The energy transmitted to the electron subsystem of the plate per unit path of the incident electron inside the plate is defined then by the following expression:

$$\frac{d\mathcal{E}}{dz} = \frac{\pi e^2 n}{m}\int_0^\infty d\rho\rho\left|E_{\omega_0}(\rho, z)\right|^2, \qquad (32)$$

where n is the electron density in the plate. If the condition $\omega_0 >> \omega_p$ is fulfilled, for calculation of the energy losses it is possible to use the expression (28) for dielectric permittivity of the substance, from which the electron is emitted. In this case the considered Fourier-harmonic of the field around the electron is defined by the expression (29) with $\omega = \omega_0$. Substituting it into (32) we obtain the following expression for the energy losses

$$\frac{d\mathcal{E}}{dz} = \frac{4\pi e^4 n}{mv^2}\int_0^\infty dqq^3\left\{\left|\widetilde{Q}_f\right|^2 + 2Q_c\,\mathrm{Re}\,\widetilde{Q}_f\exp\left\{-i\frac{\omega_0 z}{2v^2\gamma^2} - i\frac{q^2 z}{2\omega_0}\right\} + Q_c^2\right\}. \qquad (33)$$

The term in (33) containing Q_c^2, defines the contribution to the energy losses associated with Coulomb interaction of the moving particle with the electron subsystem of the plate. On the upper limit in this term the integral over q

diverges and it should be restricted by some maximum value q_0 defined from the condition of applicability of the used here model of the atomic electron subsystem as a set of harmonic oscillators. The latter is still valid if $R^{-1} \geq q_0 > \omega_0$, where R is the radius of screening of the atomic potential. As a result we come to the following formula for restricted energy losses, for which $q < q_0$:

$$\frac{d\mathcal{E}}{dz} = \frac{4\pi e^4 n}{mv^2}\left\{\int_0^{q_0} dqq^3 Q_c^2 + \int_0^{\infty} dqq^3\left[\tilde{Q}_f^2 + 2\tilde{Q}_f Q_c \cos\left(\frac{\omega_0 z}{2v^2\gamma^2} + \frac{q^2 z}{2\omega_0}\right)\right]\right\}. \qquad (34)$$

Let us consider several limiting cases of the formula (34). For $z \to 0$, as can be easily verified,

$$\frac{d\mathcal{E}}{dz} = \frac{4\pi e^4 n}{mv^2}\left(\ln\frac{q_0}{\omega_p} - \frac{1}{2}\right).$$

This formula shows that the energy losses in the plate situated close to the border of the substance, from which the electron emerges, are defined by Fermi density effect like in substance, in which the particle moved before the collision with the plate.

In the region of distances z, which satisfy the conditions $\omega_0/\omega_p^2 << z << \gamma^2/\omega_0$, the energy losses in the plate are defined by the formula

$$\frac{d\mathcal{E}}{dz} = \frac{4\pi e^4 n}{mv^2}\left(\ln\frac{q_0\omega_p z}{2\omega_0} - \frac{1}{2} + G\right),$$

where $G = 0.577$ is the Euler's constant. Let us note that in the considered range of distances the logarithmic increase of the energy losses with the increase of z takes place. This effect is caused by the reconstruction of the field around the electron after its emergence from substance.

On sufficiently large distances from the point of the particle emission from substance $z > 2\gamma^2/\omega_0$, according to (34),

$$\frac{d\mathcal{E}}{dz} = \frac{4\pi e^4 n}{mv^2}\left\{\left(\ln\frac{q_0 v\gamma}{\omega_0} - \frac{1}{2}\right) + \left(\ln\frac{\omega_p v\gamma}{\omega_0} - 1\right)\right\}. \qquad (35)$$

The energy losses in this case do not depend on z. The first term in (35) corresponds to ionization produced by the particle's own Coulomb field and coincides with the corresponding result of Bethe and Bloch for contribution to energy losses associated with large impact parameters. Fermi density effect is not presented in ionization energy losses in the considered case of thin plate. The second term in (35) defines the contribution to ionization by the packet of free (radiated) waves. In the considered logarithmic approximation in (35) the interference term does not contribute to energy losses.

Let us draw attention to the fact that in the present paper we considered the energy transmission to bound electrons in the atoms of medium, for which $\omega_0 >> \omega_p$. The used here method is not applicable for description of energy transmission to free particles ($\omega_0 \to 0$), to which the paper [39] is devoted.

Thus with the increase of the distance in vacuum between the point of electron emission from substance and the plate there occurs the logarithmic increase of ionization energy losses per unit path from the value defined by Fermi density effect to the value defined by corresponding result of Bethe and Bloch complimented by contribution to ionization of radiation field. The distances z, within which such reconstruction of energy losses takes place, by the order of magnitude are defined by relation

$$z \approx 2\gamma^2/\omega_0 .$$

In the case of ultra high energy particles these distances can reach macroscopic size. In particular, for electrons with the energy of the order of 100 Gev the length $z \approx 2\gamma^2/\omega_0$ can reach several tens of meters and consequently the predicted effect of reconstruction of ionization energy losses can be observed at energies achievable on CERN accelerators.

CONCLUSION

The behavior of localized high-energy electromagnetic wave packets, which take place in processes of radiation by ultra relativistic electrons has been considered. It is shown that with the increase of the energy the stabilization of characteristics of motion of such packets takes place, which consists in substantial decrease of the speed of their dispersion. Essential here is the fact that at high energies the lengths on which the reconstruction of the form of such

packets into packets of diverging waves takes place can reach macroscopic size, which can exceed the size of experimental facility.

Such situation takes place, for example, after ultra relativistic electron emission from substance into vacuum. It is shown that as a result of such emission a localized packet of free electromagnetic waves appears and transforms into a packet of diverging waves of transition radiation on large distance from the emission point. The transformation of a certain Fourier-harmonic of the packet field takes place within the coherence length of the radiation process, which substantially exceeds the length of the considered wave of radiation and can be macroscopic. On small distances from substance-vacuum interface the interference between the considered packet and the electron's own Coulomb field leads to suppression of low frequency Fourier-components in the field around the electron in the same way as inside the substance from which the electron was emitted. The electron with such field is known as 'half-bare' electron. It is shown that such state of electron should manifest itself, for example, in the particle ionization energy losses during further interaction of the electron with a plate situated in the direction of the electron motion on distances from the substance less than $2\gamma^2 / I$. In this case the effects in ionization energy losses associated with reconstruction of the field around the electron may be observed on distances, which considerably exceed the distances, on which the effect of Garibian takes place. It is shown that for small distance between the plate and the point of the electron emission from substance the particle ionization energy losses in the plate are defined by the formula, which takes into account the Fermi density effect. Then with the increase of this distance the ionization energy losses in the plate logarithmically increase, reaching the maximum value on distances, on which the separation of the Fourier-components of the particle's own field and the field of radiated waves takes place. In the case of ultra high energies of the particle these distances may be macroscopic, which opens new possibilities for investigation of manifestation of the electron in 'half-bare' state with suppressed low-frequency components of the surrounding field.

REFERENCES

1. Ter-Mikaelyan M.L. High-Energy Electromagnetic Processes in media. – Yerevan: Publ. of Acad. of Sc. of Arm. SSR, 1969. – 457 p.
2. Akhiezer A.I., Shul'ga N.F. High Energy Electrodynamics in Matter. – Moscow: Nauka, 1993. – 344 p.
3. Dokshitzer Yu. L., Khoze V.A., Mueller A.H. and Troyan S.I. Basics of Perturbative QCD. – Gif sur Yvette Cedex: Editions Frontiers, 1991. – 274p.
4. Garibyan G.M., Shi Y. X-Ray transition radiation. – Yerevan: Publ. of Acad. of Sc. of Arm. SSR, 1983. – 320p.
5. Ginzburg V.L., Tsytovich V.N. Transition Radiation and Transition Scattering. – Moscow: Nauka, 1984, 360 p.
6. Rullhusen P., Artru X., Dhez P. Novel radiation sources using relativistic electrons. – Singapore: World Scientific Publ., 1998. – 202p.
7. Shibata Y., Hasebe S., Ishiki K., et al. Observation of coherent diffraction radiation from bunched electrons passing through a circular aperture in the millimeter- and submillimeter- wave length regions // Phys. Rev. E. – 1995. – Vol. 52. – P. 6737.
8. Dobrovolsky S.N., Shul'ga N.F. Transversal spatial distribution of transition radiation by relativistic electron in formation zone by the dotted detector // Nucl. Instrum. Methods B. – 2003. – Vol. 201. – P. 123-132.
9. Gorham P. et al. Radio-frequency measurements of coherent transition and Cherenkov radiation: implication for high energy neutrino detection // Phys. Rev. E. – 2000. – Vol. 62. – P. 8590-8605.
10. Verzilov V. A. Transition radiation in the pre-wave zone // Phys. Lett. A. – 2000. – Vol. 273. – P. 135-140.
11. Akhiezer A.I., Shul'ga N.F., Fomin S.P. Landau-Pomeranchuk-Migdal Effect . – Physics Reviews. – 2005. – Vol. 22. – P. 1-215 (Edited by I. M. Khalatnikov), Cambridge Sci. Publ., Printed in UK.
12. Potylitsyn A.P. Electromagnetic Radiation of Electrons in Periodic Structures. – Berlin: Springer, 2011. – 213 p.
13. Naumenko G.N., Potylitsyn A.P., Sukhih L. G. et. al. Macroscopic effect of shadow of electromagnetic field of relativistic electrons // Pis'ma v Zh. Eksp. Teor. Fiz. – 2009. – Vol. 90, Iss. 2. – P. 105-110.
14. Shul'ga N.F., Trofymenko S.V., Syshchenko V.V. On transition radiation and bremsstrahlung by relativistic electron with nonequilibrium field // Pis'ma v Zh. Eksp. Teor. Fiz. – 2011. – Vol. 93, Iss. 1. – P. 3-7.
15. Shul'ga N.F., Trofymenko S.V., Syshchenko V.V. The Space-Time Evolution of the Process of Transition Radiation by Relativistic Electron // Visnyk of Kharkiv National University. – 2010. – № 916, phys. series "Nuclei, Particles, Fields" Iss. 3(47). – P. 23-41.
16. Shul'ga N.F., Trofymenko S.V., Syshchenko V.V. The prewave zone effect in transition radiation and bremsstrahlung by relativistic electron // Problems of atomic science and technology. – 2012. – №1 series: Nuclear Physics Investigations. Vol. 57. – P. 134-138.
17. Feinberg E.L. Consecutive interaction at high energies // Zh. Eksp. Teor. Fiz. – 1966. – Vol. 50. – P. 202.
18. Akhiezer A.I., Shul'ga N.F. Radiation by relativistic particles in single crystals // UFN. – 1982. – Vol. 137. – P. 561-604.
19. Miller W. Classical Limit Quantum Mechanics and the Theory of Molecular Collisions. – New York: Wiley, 1974. – P. 69-177.
20. Blokhintsev D.I. In the book: High-Energy Physics and Elementary Particles Theory. – Kiev: Nauk. Dumka, 1967. – P. 778.
21. Shul'ga N.F., Syshchenko V.V., Shul'ga S.N. On the motion of high-energy wave packets and transition radiation by 'half-bare' electron // Phys. Lett. A. – 2009. – Vol. 374. – P. 331-334.
22. Landau L.D., Lifshitz E.M. The Classical Theory of Fields. – Moscow: Nauka, 1967. – 460 p.
23. Landau L.D., Pomeranchuk I.Ya. Electron-cascade processes at ultra-high energies // Dokl. Acad. Nauk. SSSR. – 1953. – Vol. 92. – P. 735.
24. Migdal A.B. Bremsstrahlung and pair production in condensed media at high energies // Phys. Rev. – 1956. – Vol. 103. – P. 1811.

25. Ternovsky F.F. On the theory of radiative processes in piece wise homogeneous media // Zh. Eksp. Teor. Fiz. – 1960. – Vol. 39. – P. 171.
26. Shul'ga N.F., Fomin S.P. Suppression of radiation in an amorphous medium and a crystal // Pis'ma v Zh. Eksp. Teor. Fiz. – 1978. – Vol. 27. – P. 126.
27. Landau L.D., Lifshitz E.M. Electrodynamics of Continuous Media. – Moscow: Nauka, 1982. – 621 p.
28. Bethe H.A. Theory of the passage of rapid corpuscular rays through matter // Ann. de Phys. – 1930. – Vol. 5. – P. 325.
29. Bloch F. Bremsvermögen von Atomen mit mehreren Electronen // Zs. Phys. – 1933. – Vol. 81. – P. 363.
30. Fermi E. The ionization loss of energy in gases and in condensed materials // Phys. Rev. – 1940. – Vol. 57. – P. 485-493.
31. Garibian G.M. On the theory of transition radiation and ionization energy losses of a particle // Zh. Eksp. Teor. Fiz. – 1959. – Vol. 37. – P. 527-533.
32. Alikhanian A.I., Garibian G.M., Lorikian M.P., Walter A.K., Grishaiev I.A., Petrenko V.A., Fursov G.L. Ionization energy losses of fast electrons in thin films // Zh. Eksp. Teor. Fiz. – 1963. – Vol. 44. – P. 1122-1124.
33. Alikhanian A.I., Garibian G.M., Lorikian M.P. et al. Ionization energy losses of fast electrons in thin layers of polystyrene // Zh. Eksp. Teor. Fiz. – 1964. – Vol. 46. – P. 1212-1215.
34. Andersen K.K., Esberg J., Hansen K.R. et. al. Restricted energy loss of ultrarelativistic particles in thin targets – a search for deviations from constancy // Nucl. Instrum. Methods B. – 2010. – Vol. 268. – P. 1412-1415.
35. Bohr N. On the theory of the decrease of velocity of moving electrified particles on passing through matter // Phil. Mag. – 1913. – Vol. 25. – P. 10.
36. Bohr N. On the decrease of velocity of swiftly moving electrified particles in passing through matter // Phil. Mag. – 1915. – Vol. 30. – P. 581.
37. Fermi E. Nuclear Physics. – Moskow: Publ. of foreign lit., transl. from English, 1950. – 346 p.
38. Jackson J. D., Classical Electrodynamics. – Moscow: Mir, first ed., 1965. – 702 p.
39. Shul'ga N.F., Syshchenko V.V. On ionization energy losses of relativistic particles created in matter // Nucl. Instrum. Methods B. – 2000. – Vol. 164-165. – P. 180-185.

Shul'ga Nikolai Fyodorovich – D. Sc. in physics and mathematics, academician of the National Academy of Sciences of Ukraine. Currently working as a Director of Akhiezer Institute for Theoretical Physics of National Science Center 'Kharkov Institute of Physics and Technology' and as a Deputy Director of this Center. His research interests are in quantum electrodynamics and physics of interaction of high-energy particles with crystalline and amorphous media. He is the author of more than 250 scientific publications.

Trofymenko Sergii Valeriyovich – Currently working as junior research worker at Akhiezer Institute for Theoretical Physics of National Science Center 'Kharkov Institute of Physics and Technology' and is a post-graduate student in this Institute. His research interests are in electromagnetic radiation and ionization energy losses of relativistic particles.

UDC 539

STRANGE QUARK MATTER IN A STRONG MAGNETIC FIELD

A.A. Isayev
Kharkov Institute of Physics and Technology
Academicheskaya Street 1, Kharkov, 61108, Ukraine
Kharkov National University
Svobody Sq., 4, Kharkov, 61022, Ukraine
E-mail: isayev@kipt.kharkov.ua
Received 12 October 2012, accepted 14 January 2013

Thermodynamic properties of strange quark matter are considered in strong magnetic fields up to 10^{20} G. It is shown that the appearance of the longitudinal (along the magnetic field) instability beyond some critical magnetic field precludes the formation of fully polarized quark states in strange quark matter as well as prevents a significant drop of strangeness which, otherwise, could happen in such ultrastrong magnetic fields.
KEY WORDS: strange quark matter, strong magnetic field, pressure anisotropy, longitudinal instability

ДИВНА КВАРКОВА МАТЕРІЯ В СИЛЬНОМУ МАГНІТНОМУ ПОЛІ

О.О. Ісаєв
Харківський фізико-технічний інститут
вул. Академічна, 1, Харків, 61108, Україна
Харківський національний університет
пл. Свободи, 4, Харків, 61022, Україна

Розглядаються термодинамічні властивості дивної кваркової матерії в сильних магнітних полях до 10^{20} Гс. Показане, що поява повздовжньої (вздовж магнітного поля) нестійкості в полях більш за критичного перешкоджає виникненню повністю поляризованих кваркових станів у дивної кваркової матерії, а також запобігає значному зменшенню дивини, які, інакше, могли б відбутися за такими сильними магнітними полями.
КЛЮЧОВІ СЛОВА: дивна кваркова матерія, сильне магнітне поле, анізотропія тиску, повздовжня нестійкість

СТРАННАЯ КВАРКОВАЯ МАТЕРИЯ В СИЛЬНОМ МАГНИТНОМ ПОЛЕ

А.А. Исаев
Харьковский физико-технический институт
ул. Академическая, 1, Харьков, 61108, Украина
Харьковский национальный университет
пл. Свободы, 4, Харьков, 61022, Украина

Рассматриваются термодинамические свойства странной кварковой материи в сильных магнитных полях до 10^{20} Гс. Показано, что появление продольной (вдоль магнитного поля) неустойчивости в полях больше критического препятствует возникновению полностью поляризованных кварковых состояний в странной кварковой материи, а также предотвращает значительное уменьшение странности, которые, иначе, могли бы произойти в таких сильных магнитных полях.
КЛЮЧЕВЫЕ СЛОВА: странная кварковая материя, сильное магнитное поле, анизотропия давления, продольная неустойчивость

The study of Quantum Chromodynamics (QCD) phase diagram under extreme conditions of temperature and/or density is currently a hot research topic. In particular, when the baryon density is essentially larger than the nuclear saturation density (equal approximately to 0.16 fm^{-3}), quarks are expected to be liberated from the nucleon bags. It was suggested [1-3] that strange quark matter (SQM), composed of deconfined u, d and s quarks, can be the true ground state of matter. If this conjecture will be confirmed, it would have important astrophysical implications. In particular, SQM can form strange quark stars self-bound by strong interactions [4]. Also, if SQM is metastable at zero pressure, it can appear in the high-density core of a neutron star as a result of the deconfinement phase transition. In this case, the stability of SQM is provided by the gravitational pressure from the outer hadronic layers. Then a relevant astrophysical object is a hybrid star having a quark core and the crust of hadronic matter.

Another important aspect related to the physics of compact stars is that they are endowed with the magnetic field. For magnetars, the field strength at the surface can reach the values of about 10^{14} - 10^{15} G. In the interior of a magnetar the magnetic field strength can reach even larger values of about 10^{20} G [5]. In such ultrastrong magnetic fields, the effects of the $O(3)$ rotational symmetry breaking by the magnetic field become important [5-8]. In particular, the longitudinal (along the magnetic field) pressure is less than the transverse pressure resulting in the appearance of the longitudinal instability of the star's matter if the magnetic field exceeds some critical value. The effects of the pressure anisotropy should be accounted for in the consistent investigation of structural and polarization properties of a strongly magnetized stellar object. The aim of this research is to study the effects of the pressure anisotropy in SQM under the presence of a strong magnetic field within the framework of the Massachusetts Institute of Technology (MIT) bag model.

BASIC EQUATIONS

In the simplest version of the MIT bag model, quarks are considered as free fermions moving inside a finite region of space called a "bag". The effects of the confinement are accomplished by endowing the finite region with a constant energy per unit volume, the bag constant B. The energy spectrum of free relativistic fermions (u, d, s quarks and electrons) in an external magnetic field has the form

$$\varepsilon_\nu^i = \sqrt{k_z^2 + m_i^2 + 2\nu\,|\,q_i\,|\,H}, \quad \nu = n + \frac{1}{2} - \frac{s}{2}\mathrm{sgn}(q_i), \quad i = u,d,s,e,$$

where $\nu = 0,1,2...$ enumerates the Landau levels, n is the principal quantum number, $s = +1$ corresponds to a fermion with spin up, and $s = -1$ to a fermion with spin down. The lowest Landau level with $\nu = 0$ is single degenerate and other levels with $\nu > 0$ are double degenerate.

Further we will consider magnetized SQM at zero temperature. In the zero temperature case, the thermodynamic potential for an ideal gas of relativistic fermions of i th species in the external magnetic field reads [9]

$$\Omega_i = -\frac{|\,q_i\,|\,g_i H}{4\pi^2}\sum_{\nu=0}^{\nu_{\max}^i}(2-\delta_{\nu,0})\left\{\mu_i k_{F,\nu}^i - \bar{m}_{i,\nu}^2 \ln\left|\frac{k_{F,\nu}^i + \mu_i}{\bar{m}_{i,\nu}}\right|\right\}, \tag{1}$$

where the factor $(2-\delta_{\nu,0})$ takes into account the spin degeneracy of Landau levels, g_i is the remaining degeneracy factor [$g_f = 3$ for quarks (number of colors), and $g_e = 1$ for electrons], μ_i is the chemical potential, and

$$\bar{m}_{i,\nu} = \sqrt{m_i^2 + 2\nu\,|\,q_i\,|\,H}, \quad k_{F,\nu}^i = \sqrt{\mu_i^2 - \bar{m}_{i,\nu}^2}\,.$$

In Eq. (1), summation runs up to $\nu_{\max}^i = I\left[\dfrac{\mu_i^2 - m_i^2}{2\,|\,q_i\,|\,H}\right]$, I[...] being an integer part of the value in the brackets. The number density $\varrho_i = -\left(\dfrac{\partial\Omega_i}{\partial\mu_i}\right)_T$ of fermions of i th species is given by

$$\rho_i = \frac{|\,q_i\,|\,g_i H}{2\pi^2}\sum_{\nu=0}^{\nu_{\max}^i}(2-\delta_{\nu,0})k_{F,\nu}^i\,. \tag{2}$$

The sum in Eq. (2) can be split into two parts representing the fermion number densities with spin up and spin down. As explained earlier, the only difference between the two sums is in the term with $\nu = 0$, corresponding to spin-up fermions if they are positively charged, and to spin-down fermions, if they are negatively charged. Then the zero temperature expression for the spin polarization parameter of the i th species subsystem reads:

$$\Pi_i \equiv \frac{\varrho_i^\uparrow - \varrho_i^\downarrow}{\varrho_i} = \frac{q_i g_i H}{2\pi^2 \varrho_i}\sqrt{\mu_i^2 - m_i^2}\,. \tag{3}$$

In a strong enough magnetic field, when only a lowest Landau level is occupied by fermions of i th species, a full polarization occurs with $|\,\Pi_i\,| = 1$.

In order to find the chemical potentials of all fermion species, we will use the following constraints:

$$\frac{1}{3}(\rho_u + \rho_d + \rho_s) = \rho_B\,, \tag{4}$$

$$2\rho_u - \rho_d - \rho_s - 3\rho_{e^-} = 0\,, \tag{5}$$

$$\mu_d = \mu_u + \mu_{e^-}\,, \tag{6}$$

$$\mu_d = \mu_s\,, \tag{7}$$

being the conditions of the total baryon number conservation, Eq. (4) (ϱ_B is the total baryon number density), charge neutrality, Eq. (5), and chemical equilibrium, Eqs. (6), (7), with respect to the weak processes

$$d \to u + e^- + \bar{\nu}_e, \quad u + e^- \to d + \nu_e, \tag{8}$$

$$s \to u + e^- + \bar{\nu}_e, \quad u + e^- \to s + \nu_e, \tag{9}$$

$$s + u \leftrightarrow d + u\,, \tag{10}$$

occurring in the quark core of a neutron star [4].

At zero temperature, the energy density $E_i = \Omega_i + \mu_i \varrho_i$ for fermions of i th species reads

$$E_i = \frac{|q_i| g_i H}{4\pi^2} \sum_{\nu=0}^{\nu_{\max}^i} (2 - \delta_{\nu,0}) \left\{ \mu_i k_{F,\nu}^i + \bar{m}_{i,\nu}^2 \ln \left| \frac{k_{F,\nu}^i + \mu_i}{\bar{m}_{i,\nu}} \right| \right\}. \tag{11}$$

In the MIT bag model, the total energy density E, longitudinal p_l and transverse p_t pressures in quark matter are given by [5]

$$E = \sum_i E_i + \frac{H^2}{8\pi} + B, \tag{12}$$

$$p_l = -\sum_i \Omega_i - \frac{H^2}{8\pi} - B, \quad p_t = -\sum_i \Omega_i - HM + \frac{H^2}{8\pi} - B, \tag{13}$$

where B is the bag constant, and $M = \sum_i M_i = -\sum_i \left(\frac{\partial \Omega_i}{\partial H} \right)_{\mu_i}$ is the total magnetization. It is seen that the magnetic field strength enters differently to the longitudinal and transverse pressures that reflects the breaking of the $O(3)$ rotational symmetry in a magnetic field. In a strong enough magnetic field, the quadratic on the magnetic field strength term (the Maxwell term) will be dominating, leading to increasing the transverse pressure and to decreasing the longitudinal pressure. Hence, there exists a critical magnetic field H_c, at which the longitudinal pressure vanishes, resulting in the longitudinal instability of SQM. In the astrophysical context, this means that in the magnetic fields $H \geqslant H_c$ a neutron star with the quark core will be subject to the gravitational collapse along the magnetic field.

NUMERICAL RESULTS AND CONCLUSIONS

As was mentioned in Introduction, SQM can be in absolutely stable state (strange quark stars), or in metastable state, which can be stabilized by high enough external pressure (hybrid stars). Note that the analysis of the absolute stability window in the parameter space for magnetized superconducting color-flavor-locked strange matter [10] shows that the maximum allowed bag pressure decreases with the magnetic field strength (see Eq. (32) of that work). The same holds true for magnetized nonsuperconducting SQM because the arguments of Ref. [10] can be reiterated in the given case with the only change that in Eq. (32) of Ref. [10] one should use the potential $\Omega = \sum_i \Omega_i$ with Ω_i given by Eq. (1) of the present study. In numerical calculations, we adopt two values of the bag constant, $B = 100$ MeV/fm^3 and $B = 120$ MeV/fm^3, which are slightly larger than the upper bound $B \simeq 90$ MeV/fm^3 from the absolute stability window at zero magnetic field strength [3]. The core densities corresponding to these bag pressures are chosen equal to $\varrho_B = 3\varrho_0$ and $\varrho_B = 4\varrho_0$, respectively, which are, in principle, sufficient to produce deconfinement ($\varrho_0 = 0.16$ fm^{-3} being the nuclear saturation density). Therefore, in the astrophysical context, we assume a scenario in which SQM can be formed in the core of a strongly magnetized neutron star. For the quark masses, we use the values $m_u = m_d = 5$ MeV, and $m_s = 150$ MeV [9]. The value of the strange quark mass m_s is an important issue because it substantially affects the SQM equation of state [11]. Here we do not study the impact of varying strange quark mass m_s on the critical magnetic field H_c. This can be done analogously to that in Ref. [3] where such an impact on the energy per baryon of nonmagnetized SQM was investigated.

Fig. 1 shows the chemical potentials of all fermion species as functions of the magnetic field strength. It is seen that the chemical potentials of fermions, first, stay practically constant under increasing the magnetic field, with d and s quark chemical potentials being somewhat larger (on the value of $\mu_{e^-} \sim 14 - 16$ MeV) than the u quark chemical potential. The apparent Landau oscillations of the chemical potentials appear beginning from $H \sim 3 \cdot 10^{18} - 4 \cdot 10^{18}$ G, depending on the total baryon number density. At $H \gtrsim 4 \cdot 10^{19}$ G, the quark chemical potentials decrease with the magnetic field. An interesting peculiarity occurs in a narrow interval near $H \sim 2 \cdot 10^{19}$ G, marked by the vertical dotted

lines. Namely, for magnetic field strengths from that interval the u quark chemical potential is larger than the d and s quark chemical potentials, $\mu_u > \mu_d = \mu_s$.

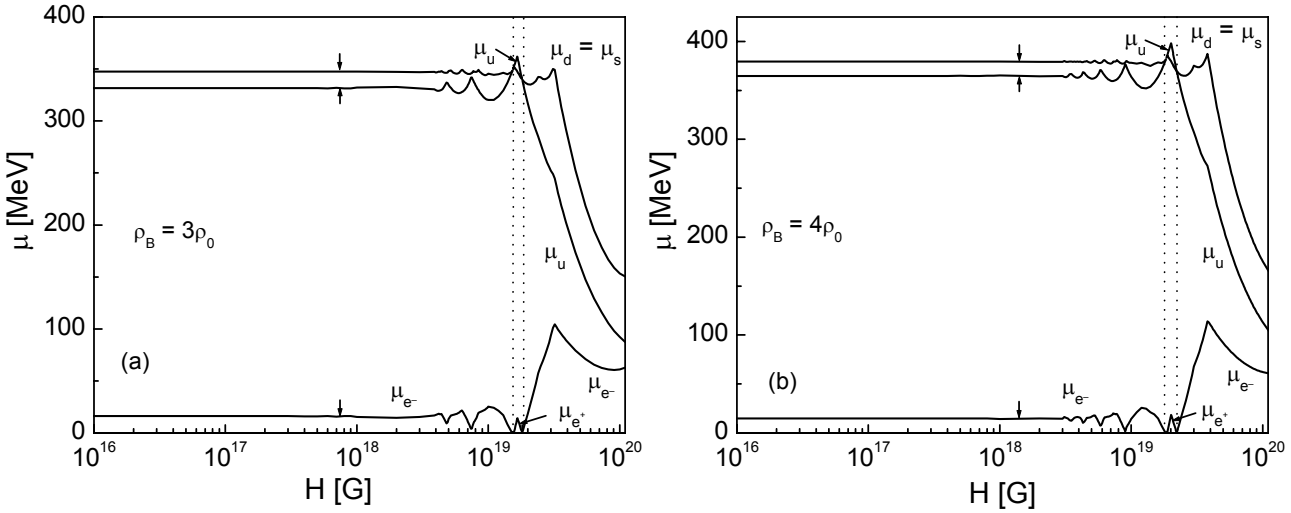

a) b)

Fig. 1. Various fermion species chemical potentials as functions of the magnetic field strength at zero temperature for the total baryon number density a) $\varrho_B = 3\varrho_0$ and b) $\varrho_B = 4\varrho_0$.

The chemical potentials of quarks and positrons are shown by the curves between the vertical dotted lines. The vertical arrows indicate the points corresponding to the critical field H_c; see further details in the text.

Hence, for such magnetic fields, according to Eq. (6), the electron chemical potential would be negative, $\mu_{e^-} < 0$. If to recall the finite temperature expression for the electron number density [9]:

$$\varrho_{e^-} = \frac{|q_e|H}{2\pi^2}\sum_{\nu=0}^{\infty}(2-\delta_{\nu,0})\int_0^{\infty} dk_z \left(\frac{1}{e^{\beta(\varepsilon_\nu^e-\mu_{e^-})}+1} - \frac{1}{e^{\beta(\varepsilon_\nu^e+\mu_{e^-})}+1}\right),$$

its zero temperature limit at $\mu_{e^-} < 0$ is, formally, negative, contrary to the constraint $\varrho_{e^-} \geqslant 0$. In fact, this means that in this interval on H electrons are missing and, hence, the weak β^- processes (8), (9) are impossible. However, for such magnetic fields, the following weak β^+ processes become allowable

$$u \to d + e^+ + \nu_e, \quad d + e^+ \to u + \bar{\nu}_e,$$
$$u \to s + e^+ + \nu_e, \quad s + e^+ \to u + \bar{\nu}_e.$$

Hence, for this specific range of the magnetic field strengths, the charge neutrality and chemical equilibrium conditions should read

$$2\varrho_u - \varrho_d - \varrho_s + 3\varrho_{e^+} = 0, \tag{14}$$

$$\mu_u = \mu_d + \mu_{e^+}, \quad \mu_d = \mu_s, \tag{15}$$

which should be solved jointly with the condition of the total baryon number conservation, Eq. (4). The quark and positron chemical potentials obtained as solutions of these equations are shown graphically in Fig. 1 as the corresponding curves between the vertical dotted lines. With increasing the core density, the width of the interval on H, where positrons appear, increases slightly as well (cf. the ranges $1.56{\cdot}10^{19}$ G-$1.80{\cdot}10^{19}$ G at $\varrho_B = 3\varrho_0$ and $1.86{\cdot}10^{19}$ - $2.21{\cdot}10^{19}$ G at $\varrho_B = 4\varrho_0$). Thus, as a matter of principle, in strongly magnetized strange quark matter at zero temperature, subject to the total baryon number conservation, charge neutrality and chemical equilibrium conditions, positrons can appear in a certain narrow interval of the magnetic field strengths, replacing electrons. In this case, strange quark matter will have negative hadronic electric charge.

Note that, according to Ref. [3], the contact of stable strange quark matter, having negative hadronic electric charge, with the ordinary matter would have the disastrous consequences for the latter, because positively charged nuclei would be attracted to strange quark matter and absorbed. However, the contact of metastable strange quark matter, having negative hadronic electric charge, with hadronic matter in the interior of a neutron star is possible, because the outer hadronic layer provides the necessary external pressure to stabilize strange quark matter in the core and cannot be completely depleted. Nevertheless, we should calculate the critical field H_c for the appearance of the

longitudinal instability, which could prevent the occurrence of positrons in a certain range of magnetic field strengths with $H \gtrsim 10^{19}$ G. The meaning of the vertical arrows in Fig. 1 will be discussed later in the text.

Fig. 2 shows the abundances of various fermion species as functions of the magnetic field strength. The number densities of u and d quarks are quite close to each other for all magnetic fields under consideration. The electron number density begins quite rapidly to increase at $H \approx 2.2 \cdot 10^{16}$ G for $\varrho_B = 3\varrho_0$ and at $H \approx 1.9 \cdot 10^{16}$ G for $\varrho_B = 4\varrho_0$. As noted earlier, in the narrow interval near $H \sim 2 \cdot 10^{19}$ G electrons are replaced by positrons, and beyond this interval electrons appear again with the number density increasing with H. The s quark content of strange quark matter stays practically constant till the field strength $H \approx 4.1 \cdot 10^{18}$ G at $\varrho_B = 3\varrho_0$ and $H \approx 3.8 \cdot 10^{18}$ G at $\varrho_B = 4\varrho_0$, beyond which the s quark number density experiences visible Landau oscillations. Then, beginning from the field strength $H \approx 3.2 \cdot 10^{19}$ G at $\varrho_B = 3\varrho_0$ and $H \approx 3.9 \cdot 10^{19}$ G at $\varrho_B = 4\varrho_0$, the s quark content rapidly decreases. Strange quark matter loses its strangeness and turns into two-flavor quark matter in the magnetic fields slightly larger than 10^{20} G. Again, we should determine the critical field H_c in order to check whether this significant drop of strangeness could happen in a strong magnetic field.

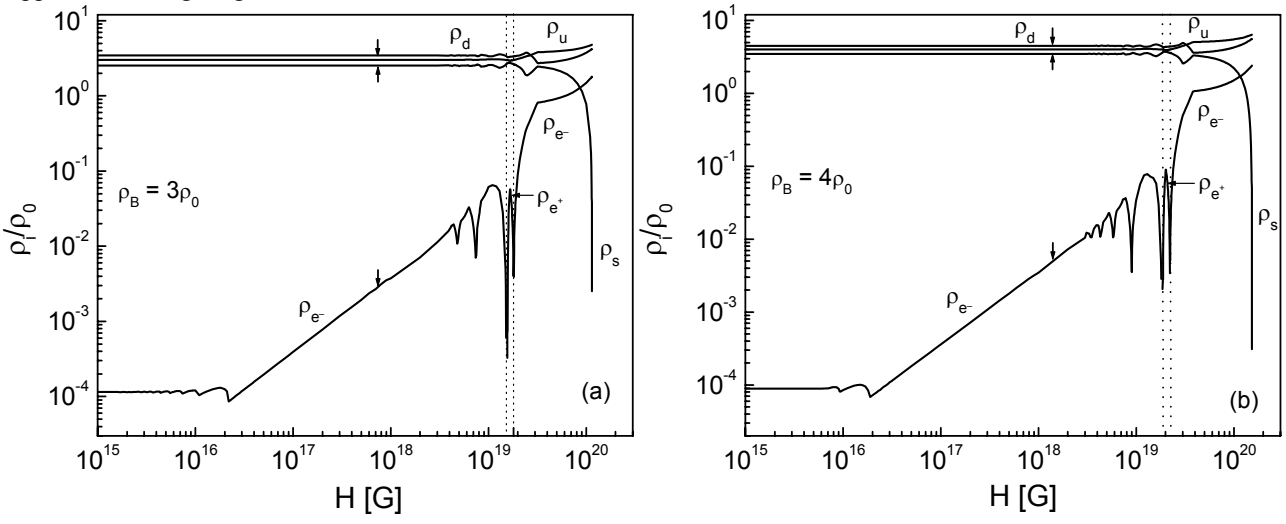

a) b)

Fig. 2. Same as in Fig. 1 but for the particle number densities ϱ_i / ϱ_0 of various fermion species.
a) $\varrho_B = 3\varrho_0$ and b) $\varrho_B = 4\varrho_0$.

Fig. 3 shows the spin polarization parameter Π_i for various fermion species, determined according to Eq. (3), as a function of the magnetic field strength. Spin polarization of u quarks is positive while for d, s quarks and electrons it is negative. The magnitude of the spin polarization parameter Π_i increases with H till it is saturated at the respective saturation field H_s^i. At $H = H_s^i$, the corresponding ith fermion species becomes fully spin polarized. The respective values of the saturation field are: $H_s^e \approx 2.2 \cdot 10^{16}$ G for electrons, $H_s^u \approx 1.7 \cdot 10^{19}$ G for u quarks, $H_s^s \approx 2.5 \cdot 10^{19}$ G for s quarks and $H_s^d \approx 3.2 \cdot 10^{19}$ G for d quarks at $\varrho_B = 3\varrho_0$, and $H_s^e \approx 1.9 \cdot 10^{16}$ G for electrons, $H_s^u \approx 2.0 \cdot 10^{19}$ G for u quarks, $H_s^s \approx 3.1 \cdot 10^{19}$ G for s quarks and $H_s^d \approx 3.9 \cdot 10^{19}$ G for d quarks at $\varrho_B = 4\varrho_0$. Note that quite a rapid increase of the electron number density with the magnetic field (cf. Fig. 2) begins just at the saturation field H_s^e, and, hence, this increase occurs when electrons become completely spin polarized. Further oscillations in the electron number density are, in fact, caused by the Landau oscillations of the quark number densities, which influence the electron population through the charge neutrality condition. Although the s-quark current mass is larger than that for d quark, $m_s > m_d$, s quarks become fully polarized at a smaller saturation field because their particle density is smaller than for d quarks, $\varrho_s < \varrho_d$. The spin polarization parameter of various fermion species in the magnetic field range, where positrons appear, is shown by the respective curves between the vertical dotted lines. It is seen that positrons occur already fully polarized, and u quarks become totally polarized just in this range of the magnetic field strengths. Nevertheless, as mentioned before, only after determining the critical field H_c for the appearance of the longitudinal instability, it would be possible to determine the degree of spin polarization which could be reached for each of the fermion species.

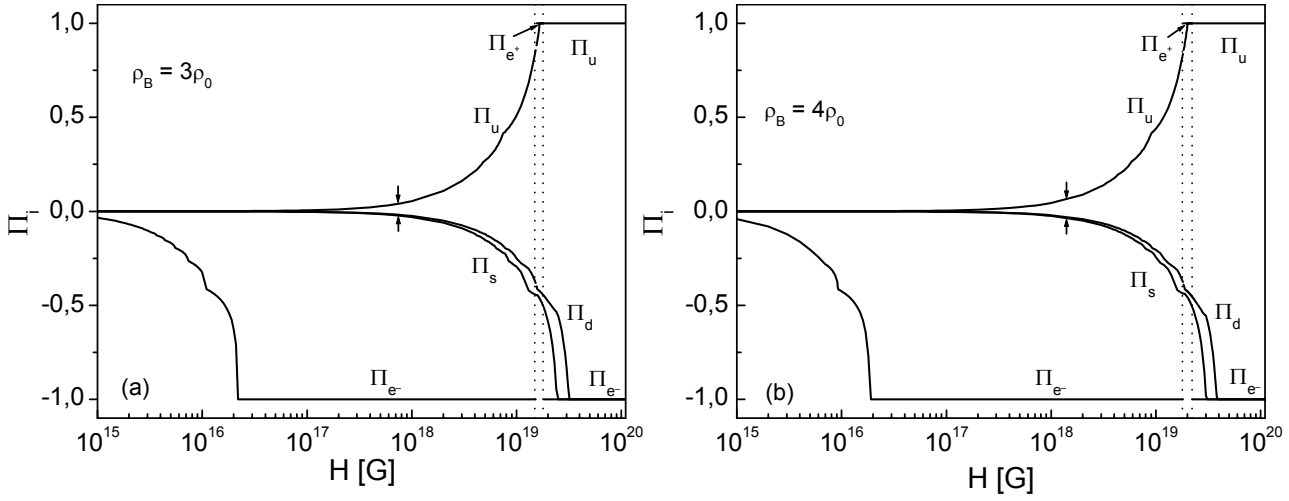

a) b)

Fig. 3. Same as in Fig. 1 but for the spin polarization parameter of various fermion species. a) $\varrho_B = 3\varrho_0$ and b) $\varrho_B = 4\varrho_0$.

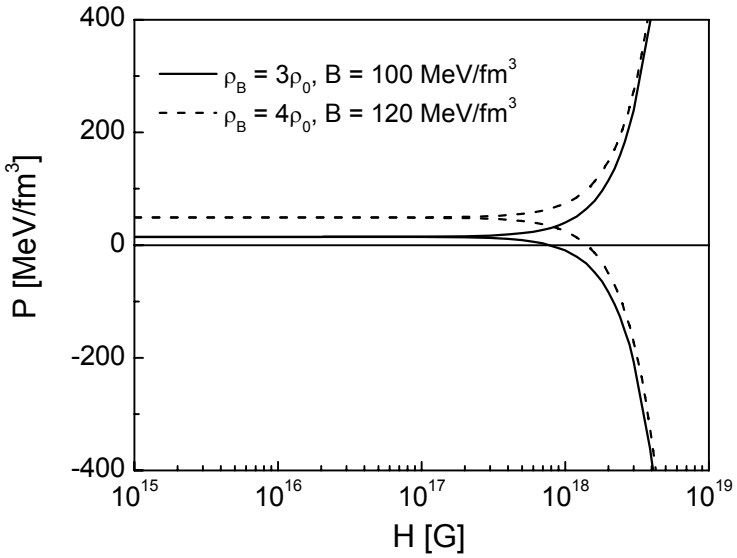

Fig. 4. Transverse (ascending branches) and longitudinal (descending branches) pressures in magnetized SQM at zero temperature as functions of the magnetic field strength for $\varrho_B = 3\varrho_0, B = 100$ MeV/fm^3 (solid lines) and $\varrho_B = 4\varrho_0, B = 120$ MeV/fm^3 (dashed lines).

Now we present the results of calculations of the longitudinal p_l and transverse p_t pressures. Fig. 4 shows the longitudinal p_l and transverse p_t pressures at zero temperature as functions of the magnetic field strength. It is seen that, first, the transverse and longitudinal pressures stay practically constant and indistinguishable from each other. This behavior of the pressures p_t and p_l corresponds to the isotropic regime. Beyond some threshold magnetic field H_{th}, the transverse pressure p_t increases with H while the longitudinal pressure p_l decreases with it, clearly reflecting the anisotropic nature of the total pressure in SQM in such strong magnetic fields (anisotropic regime). In the critical magnetic field H_c, the longitudinal pressure p_l vanishes. This happens at $H_c \approx 7.4 \cdot 10^{17}$ G for $\varrho_B = 3\varrho_0, B = 100$ MeV/fm^3, and at $H_c \approx 1.4 \cdot 10^{18}$ G for $\varrho_B = 4\varrho_0, B = 120$ MeV/fm^3. Above the critical magnetic field, the longitudinal pressure is negative leading to the longitudinal instability of SQM. Therefore, the thermodynamic properties of SQM should be considered in the magnetic fields $H < H_c$.

Now, in order to see, which of the discussed already features of strange quark matter at zero temperature in a strong magnetic field are preserved before the appearance of the longitudinal instability, we show in Figs. 1-3 by the vertical arrows the respective values of the physical quantities corresponding to the critical field H_c. Let us begin with Fig. 1 for the chemical potentials of various fermion species. It is seen that the chemical potentials of quarks and

electrons stay practically unchanged before the appearance of the longitudinal instability. The significant changes in the chemical potentials occur only in the fields $H > H_c$. In particular, the longitudinal instability precludes the appearance of positrons for which the fields $H \gtrsim 10^{19}$ G are necessary.

Let us turn to Fig. 2 for the abundances of various fermion species. Till the critical field H_c, the content of quark species stays practically constant while the electron fraction remains quite small, $\varrho_{e^-} / \varrho_0 \lesssim 10^{-2}$. Also, there is no room for the significant drop of the strange quark content in a strong magnetic field which occurs in the fields $H \sim 10^{20}$ G. In fact, despite the presence of strong magnetic fields $H \sim 10^{18}$ G, strange quark matter has the same fraction of s quarks as in the field-free case.

Let us now consider Fig. 3 for spin polarizations of various fermion species. It is seen that the full polarization in a strong magnetic field can be achieved only for electrons. For various quark species, the spin polarization remains quite moderate up to the critical magnetic field H_c. E.g., at $\varrho_B = 4\varrho_0, H = H_c$ we have $\Pi_u \approx 0.06$, $\Pi_d \approx -0.03$, $\Pi_s \approx -0.04$; at $\varrho_B = 3\varrho_0, H = H_c$, the quark spin polarizations are similar to these values with the maximum magnitude of the spin polarization parameter for u quarks, $\Pi_u \approx 0.04$. Therefore, the occurrence of a field-induced fully polarized state in strange quark matter is prevented by the appearance of the longitudinal instability in the critical magnetic field.

In summary, we have considered the impact of strong magnetic fields up to 10^{20} G on the thermodynamic properties of strange quark matter at zero temperature under additional constraints of total baryon number conservation, charge neutrality and chemical equilibrium with respect to various weak processes occurring in the system. The study has been done within the framework of the MIT bag model with the finite current quark masses $m_u = m_d \neq m_s$. In the numerical calculations, we have adopted two sets of the total baryon number density and bag pressure, $\varrho_B = 3\varrho_0, B = 100$ MeV/fm^3 and $\varrho_B = 4\varrho_0, B = 120$ MeV/fm^3. It has been found that in strong magnetic fields up to 10^{20} G some interesting features in the chemical composition and spin structure of strange quark matter could occur:

(1) The content of strange quarks rapidly decreases in the fields somewhat larger than 10^{19} G and becomes negligible in the fields slightly exceeding 10^{20} G;

(2) For the magnetic field strengths in the quite narrow interval near $H \sim 2 \cdot 10^{19}$ G the constraints of total baryon number conservation, charge neutrality and chemical equilibrium can be satisfied only if positrons appear in various weak processes in that range of the field strengths (instead of electrons);

(3) Electrons occupy only the lowest Landau level and, hence, become completely spin polarized in the magnetic fields somewhat larger than 10^{16} G; u, s and d quarks become fully polarized in the fields somewhat larger than 10^{19} G (the recitation of the quark species is in the order in which they appear fully polarized under increasing H).

Nevertheless, under such strong magnetic fields, the total pressure containing also the magnetic field contribution, becomes anisotropic, and the effects of the pressure anisotropy change most of the above conclusions. Namely, the longitudinal (along the magnetic field) pressure decreases with the magnetic field (contrary to the transverse pressure increasing with H) and vanishes in the critical field H_c resulting in the longitudinal instability of strange quark matter. The value of the critical field H_c depends on the total baryon number density of strange quark matter and the bag pressure B, and it turns out to be somewhat less or larger than 10^{18} G for the two sets of the parameters, considered in the given study. Therefore, the appearance of the longitudinal instability in strong magnetic fields beyond the critical one precludes the features (1), (2) in the chemical composition of strongly magnetized strange quark matter. Concerning the conclusion (3), only electrons can reach the state of full polarization, that is not true for quarks of all flavors, whose polarization remains mild even for magnetic fields near H_c.

The obtained results can be important in the studies of structural and polarization properties of strongly magnetized neutron stars with quark cores. In particular, it is worth noting that, since the equation of state (EoS) of strange quark matter becomes highly anisotropic in an ultrastrong magnetic field, the usual scheme for finding the mass-radius relationship based on the Tolman-Oppenheimer-Volkoff (TOV) equations [12] for a spherically symmetric and static stellar object should be revised. Instead, the corresponding relationship should be found by the self-consistent treatment of the anisotropic EoS and axisymmetric TOV equations substituting the conventional TOV equations in the case of an axisymmetric neutron star with the quark core. The masses and radii of neutron stars are measurable quantities, and, hence, the relevance of the effects of the pressure anisotropy in a strong magnetic field can be directly tested for strongly magnetized compact stars.

The author would like to thank the Organizing Committee of the International Conference “Problems of Modern Physics”, held in occasion of the 50th anniversary of the Physics and Technology Faculty at Kharkov National University, for kind invitation and possibility to present the results of this study at the meeting.

REFERENCES

1. Bodmer A. Collapsed Nuclei // Phys. Rev. D – 1971. – Vol. 4. – P. 1601 – 1606.
2. Witten E. Cosmic separation of phases // Phys. Rev. D – 1984. – Vol. 30. – P. 272 – 285.
3. Farhi E., Jaffe R. L. Strange matter // Phys. Rev. D – 1984. – Vol. 30. – P. 2379 – 2390.
4. Alcock C., Farhi E., Olinto A.V. Strange stars // Astrophys. J. – 1986. – Vol. 310.- P. 261 – 272.
5. Ferrer E.J., de la Incera V., Keith J.P., et al. Equation of state of a dense and magnetized fermion system // Phys. Rev. C – 2010. – Vol. 82. – 065802.
6. Khalilov V.R. Macroscopic effects in cold magnetized nucleons and electrons with anomalous magnetic moments // Phys. Rev. D – 2002. – Vol. 65. – 056001.
7. Isayev A.A., Yang J. Anisotropic pressure in dense neutron matter under the presence of a strong magnetic field // Phys. Lett. B – 2012. – Vol. 707. – P. 163-168.
8. Isayev A.A., Yang J. Finite temperature effects on anisotropic pressure and equation of state of dense neutron matter in an ultrastrong magnetic field // Phys. Rev. C – 2011. – Vol. 84. – 065802.
9. Chakrabarty S. Quark matter in a strong magnetic field // Phys. Rev. D – 1996. – Vol. 54. – P. 1306-1316.
10. Paulucci L., Ferrer E. J., de la Incera V., Horvath J. E. Equation of state for the magnetic-color-flavor-locked phase and its implications for compact star models // Phys. Rev. D – 2011. – Vol. 83. - 043009.
11. Kurkela A., Romatschke P., Vuorinen A. Cold quark matter // Phys. Rev. D – 2010. – Vol. 81. - 105021.
12. Tolman R.C. Static Solutions of Einstein's Field Equations for Spheres of Fluid // Phys. Rev. – 1939. – Vol. 55. – P. 364-373; Oppenheimer J.R., Volkoff G.M. On Massive Neutron Cores // Phys. Rev. – 1939. – Vol. 55. – P. 374-381.

Isayev Alexander Alexeyevich – D.Sc. in physics and mathematics. Currently working as a Leading Research Associate of Akhiezer Institute for Theoretical Physics at National Science Center "Kharkov Institute of Physics & Technology". He is the author of more than 100 scientific publications.
Research interests: Superfluidity/superconductivity, Bose-Einstein condensation, BCS-BEC crossover, equation of state of strongly interacting systems, neutron star physics, physical phenomena in strong magnetic fields.

UDC 621.384.6.

BEAM DYNAMICS IN OUTPUT CHANNELS FROM RECIRCULATOR SALO

I.S. Guk, S.G. Kononenko, F.A. Peev, A.S. Tarasenko
National Science Centre "Kharkov Institute of Physics and Technology"
Academicheskaja str. 1, Kharkov, Ukraine, 61108
E-mail: guk@kipt.kharkov.ua
Received 26 November 2012, accepted 24 January 2013

Optimization of recirculator SALO magnetic structure allowed to refine essentially parameters of electron beams in input points of output channels in the basic observational halls. Parameters of a beam along a trajectory of a motion and on an exit of the basic channels are given. Calculations are spent taking into account non-linear fields of dipole and quadrupole recirculator magnets.
KEY WORDS: electron, recirculator, dipole magnet, quadrupole lens, SALO.

ДИНАМИКА ПУЧКА В КАНАЛАХ ВЫВОДА ИЗ РЕЦИРКУЛЯТОРА SALO
И.С. Гук, С.Г. Кононенко, Ф.А. Пеев, А.С. Тарасенко
Национальный научный центр «Харьковский физико-технический институт»
ул. Академическая 1, 61108, Харьков, Украина
Оптимизация магнитной структуры рециркулятора SALO позволила существенно улучшить параметры пучка электронов в точках выпуска частиц в основные экспериментальные залы. В работе приведены параметры пучка вдоль траектории движения и на выходе основных каналов вывода пучка из рециркулятора. Расчёты проведены с учетом нелинейных составляющих полей дипольных и квадрупольных магнитов рециркулятора.
КЛЮЧЕВЫЕ СЛОВА: электрон, рециркулятор, дипольный магнит, квадруполь, SALO.

ДИНАМІКА ПУЧКА В КАНАЛАХ ВИВОДУ З РЕЦИРКУЛЯТОРА SALO
І.С. Гук, С.Г. Кононенко, Ф.А. Пеєв, О.С. Тарасенко
ННЦ "Харківський фізико-технічний інститут" НАН України
вул. Академічна 1, 61108, м. Харків, Україна
Оптимізація магнітооптичної структури рециркулятора SALO дозволила суттєво поліпшити параметри пучка електронів в точках виводу часток в основні експериментальні зали. В роботі приведені параметри пучка вздовж траєкторії руху і на виході основних каналів виводу пучка з рециркулятора. Разрахунки проведені з урахуванням впливу нелінійних компонентів магнітного поля дипольних і квадрупольних магнітів рециркулятора.
КЛЮЧОВІ СЛОВА: електрон, рециркулятор, дипольний магніт, квадруполь, SALO.

Project recirculator SALO, developed in KIPT, provides the withdrawal of the electron beam in several experimental areas [1, 2]. Of greatest interest is the consideration of the motion of particles in the channels intended for nuclear physics research [2, 3], as the requirements for the beam on these channels, the strongest. Characteristic of the beams on these channels will be fairly frequent change of the electron energy, which in turn may require adjustment of the position and size of the beam on the target. Prediction of the behaviour of beams in the channels is also important for the development of the equipment needed for physical research [4]. The work main task is research of the electron beams movement along the basic channels and research possibilities of management by these beams on an exit of channels.

As shown in [5, 6], the parameters of the beam in the recirculator can have a significant impact nonlinear components of dipole and quadrupole magnets. Beam transport channels contain a sufficiently large number of dipoles and quadrupoles. Therefore the characteristics of the beam can be changed on these channels under the influence of the same factors. Study of the motion of the particles was performed using the program MAD X [7], by tracking particles through a magnetic system of channels. The structure of the magnetic systems of beam channels [3, 8] is the dipole magnets of the first recycling ring and the dipole magnets and quadrupoles of the second recirculator ring [2, 6]. The values of sextupole field component of the dipole magnets of the first ring recycling were taken from [9]. In this publication, they were measured on the prototype magnets to be used in the recirculator SALO. Dipole magnets of the second ring recycling and transportation channels are not produced. Because they are like armor, naturally assume that sextupole field component of these magnets will not exceed the values measured for the magnets to the first ring. [9] Octupole component value of the quadrupole lenses was calculated based on data from the literature [10]. These data have been used in numerical simulations of particle dynamics in the channels. Sextupole component is taken into account in the description of the dipole. Octupole component were simulated thin lens on the entrance and exit of the quadrupole. The drawings are in the distribution used in the simulation of motion 3000 particles through magnetic channel structure.

Magneto-optical systems all considered channels are consistent with achromatic requirement. Parameters for all of the magnetic elements have been optimized to meet the specified requirements.

CHANNELS A, B, C

In the channels A, B and C can be derived a beam with an energy of 60 to 750 MeV [1-3, 6]. For beam forming on channels A and B (see Fig. 1) is used first recycling ring dipole magnet 12M1, four quadrupoles A2Л1-A2Л4 and four dipole magnets A3M1-A3M3, B3M1. Beam passes into the channel C when dipole A3M2 is off. Beam can be directed into the channel A (using a magnet A3M3) or channel B (using a magnet B3M1) when you turn on the magnet. In the area between the dipole magnets A2M1 and A3M2 beam moves in the concrete protection thickness of 6 meters, between the target hall where you want to place a recirculator, and Hall SP-103 spectrometer, where the supposed location of the main units using a maximum energy of 730 MeV.

Beam with an energy of 270 MeV (a single passage of the accelerating structure) can be displayed in these rooms with the magnetic system of the injection tract and magnets that are part of the magnetic system of channels [6]. To produce a beam with an energy of up to 490 MeV is necessary to use a magnetic system of the first ring of recycling. For maximum energy used magnetic system of the second ring of recycling. The beam will be three times the accelerating structure. Dynamics of changes in the cross section of the beam from the entrance to the transport channel (before magnet 12M1) to magnet A2M3 in the channel A at the maximum energy of 730 MeV is shown in Fig. 2. The distance is measured from the entrance to the magnet 12M1.

In Fig. 3 in Figure 4 shows the distribution of particles in phase space x, x 'and y, y' at the output of channel A on the target at a distance of 23.175 m from the output for the same energy.

Distribution of the particle density at the target at the same point in Fig. 5.

Density distribution of the particles on targets located on channels B and C, will be similar to those described for channel A.

Ports A, B and C are designed for experiments with beams of polarized and non-polarized electrons. Installing a free electron laser is available on the channel C [1, 2].

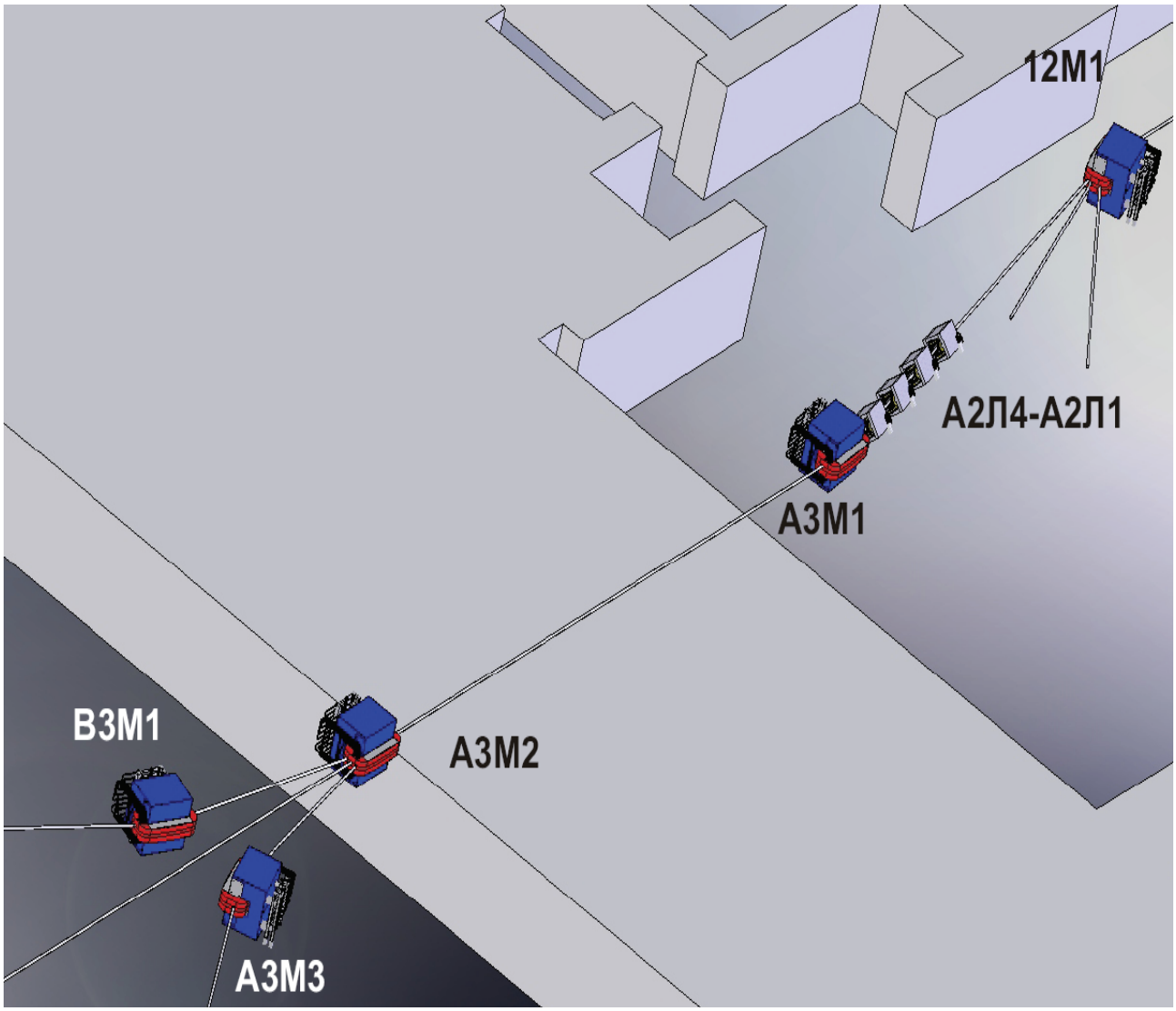

Fig. 1. Arrangement of magnets and quadrupoles on channels A, B, C

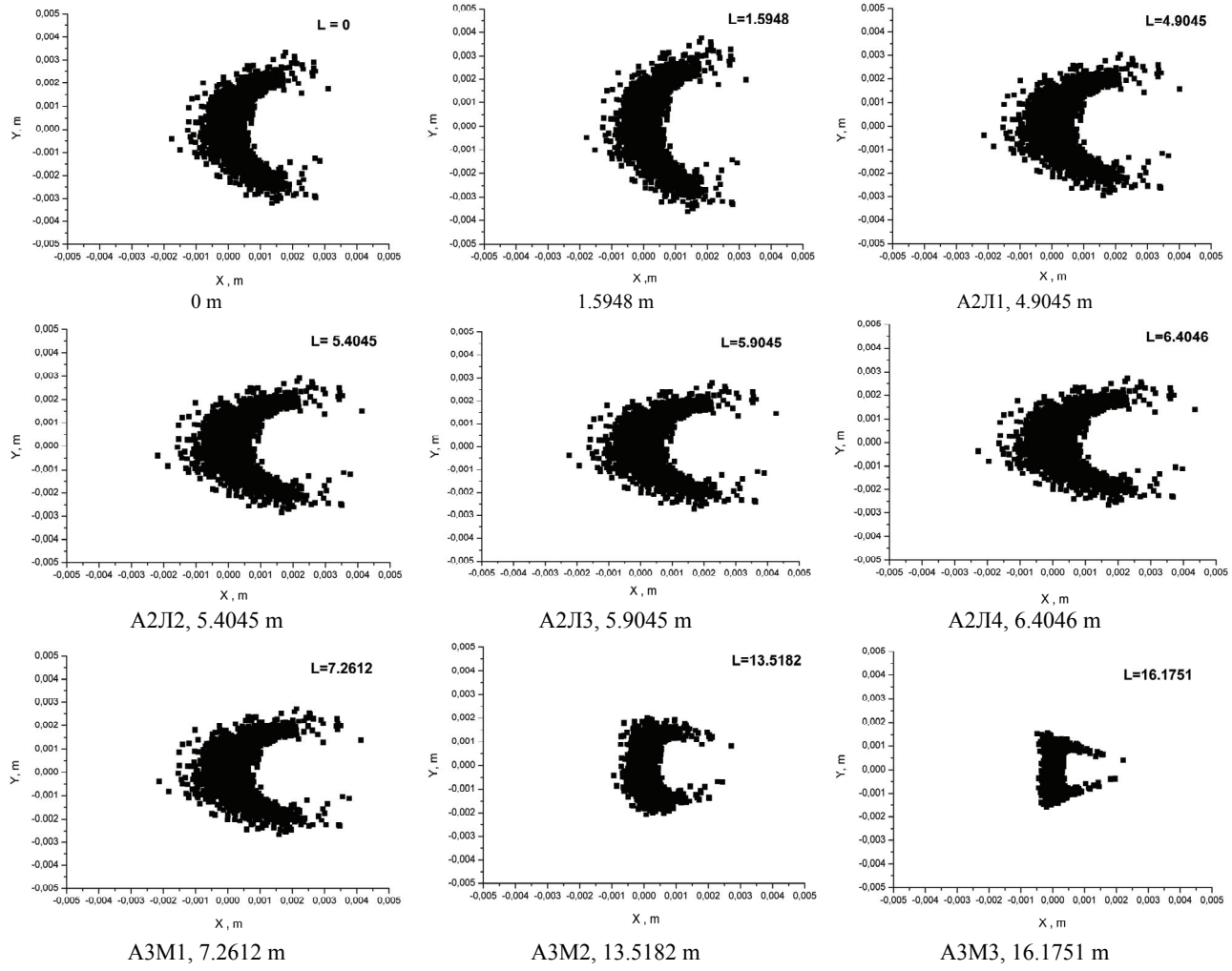

Fig. 2. Electron density distribution in the beam cross section along the trajectory of the channel A

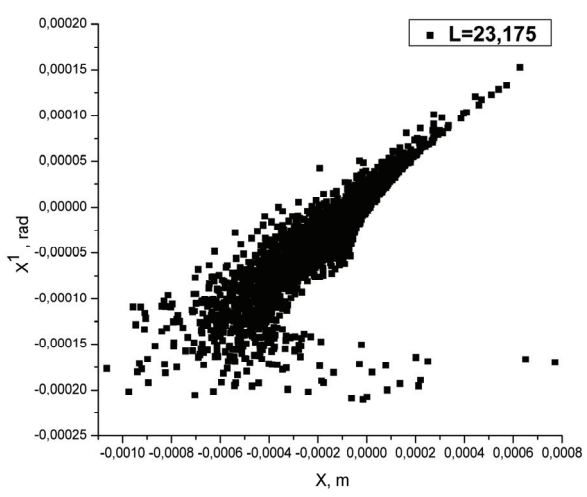

Fig.3. The distribution of particles in the phase space x, x' on target for channel A

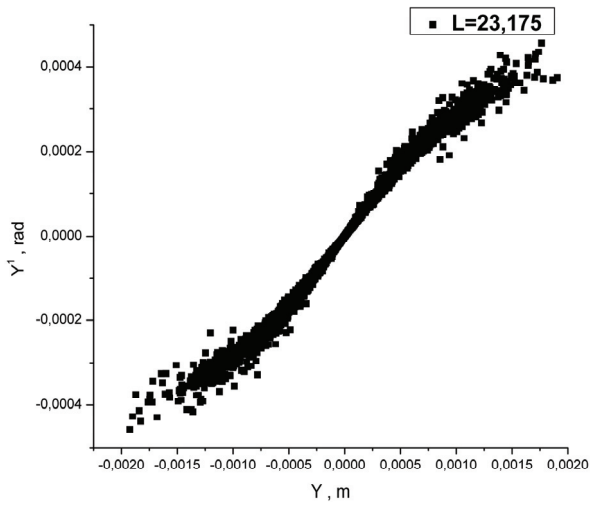

Fig.4. The distribution of particles in the phase space y, y' on target for channel A

The density distribution of the particles in Fig. 5 was obtained by taking into account all the nonlinearities of the magnetic elements channel A, on Fig. 5b off octupole components of quadrupoles, and on Fig. 5c off sextupole components of the dipole magnets. We see that only they affect the distribution of electrons in the beam in this channel.

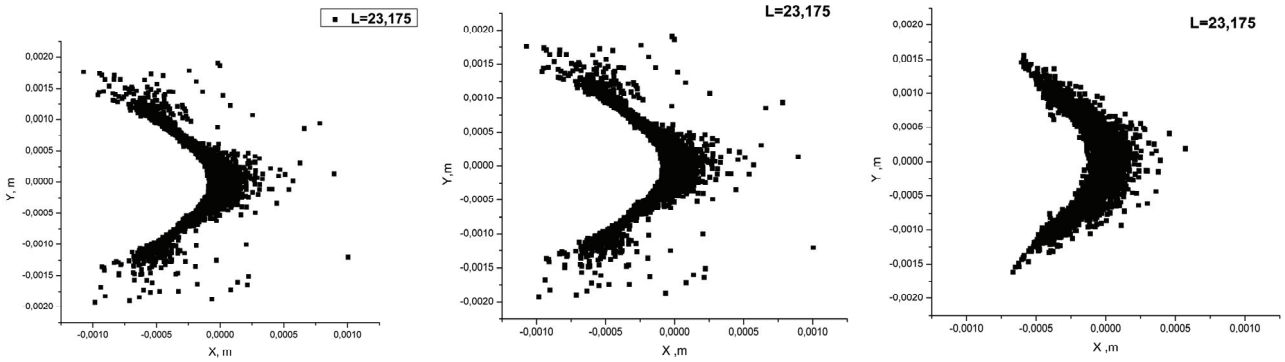

a b c

Fig. 5. The distribution of the particle density at the target output channel A
a - all nonlinearities are include, b - octupole components are switched off, c - all nonlinearities are switched off

CHANNEL D

Electrons with a maximum beam energy of 260 MeV can be output in the D-channel after a single passage through the recirculator accelerating structure. At double the maximum of the beam energy can be increased up to 500 MeV [6]. The dipole magnet of the first recycling ring 12M6, five quadrupole lenses of the second recycling ring - 22Л9-22Л12 and 23Л13, two dipole magnets 23M1D and 23M2D and five quadrupole lenses 23Л1D-23Л5D (Fig. 6) can be used for output and beam formation at the target on the channel. The design of the 23M1D and 23M2D magnets similar construction of the second recycling ring magnets, and used on the channel quadrupole lenses are similar to the first and second recycling rings lens [2,3,6,8]. Modes of all elements of the magnetooptical channel system selected so as to achieve the system achromatism on output channel MD target at a distance of 59.82 m from the entrance of the magnet 12M6.

D channel to be used for work on the beams of electrons and photons.

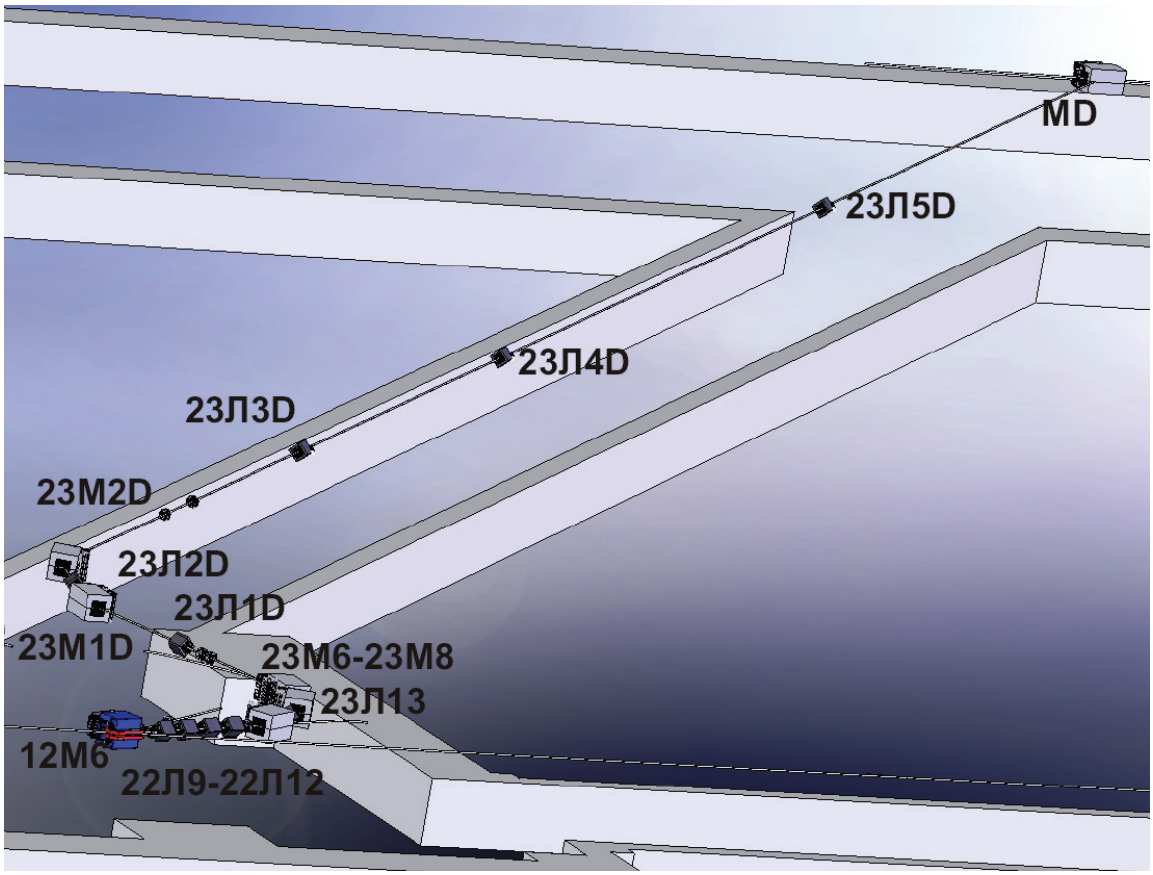

Fig. 6. Arrangement of magnets and quadrupoles on channel D

The dynamics of electron density distribution in the cross section of the beam and the beam size along the transport channel are shown in Fig. 7.

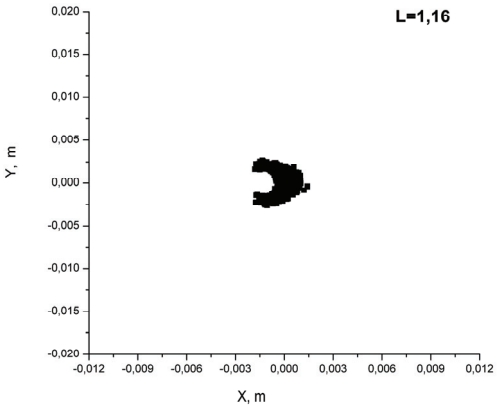

22ЛІ9, 1.16 m

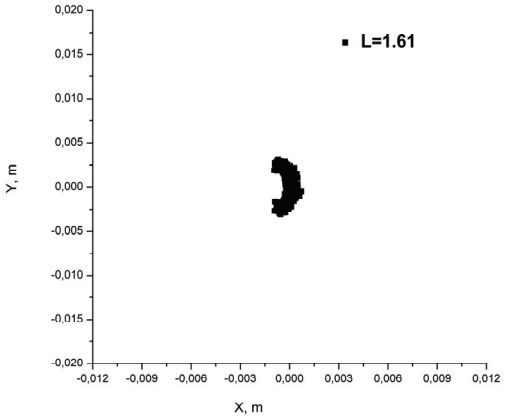

22ЛІ10, 1.61 m

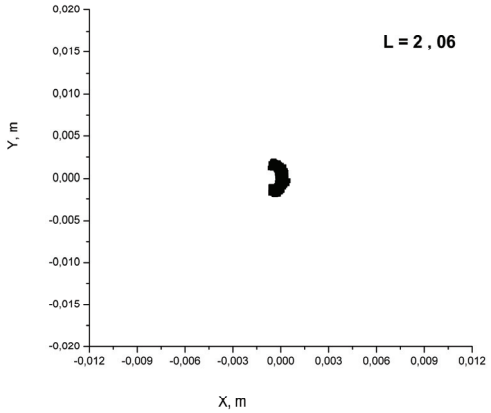

22ЛІ11, 2.06 m

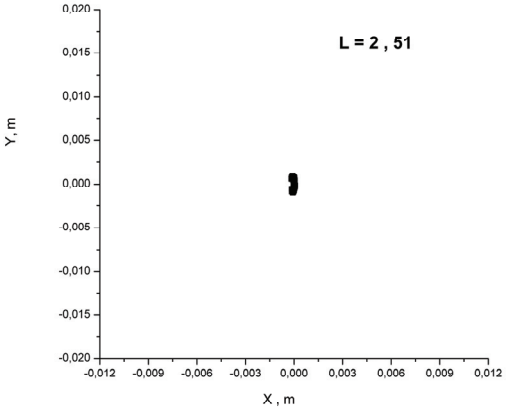

22ЛІ12, 2.51 m

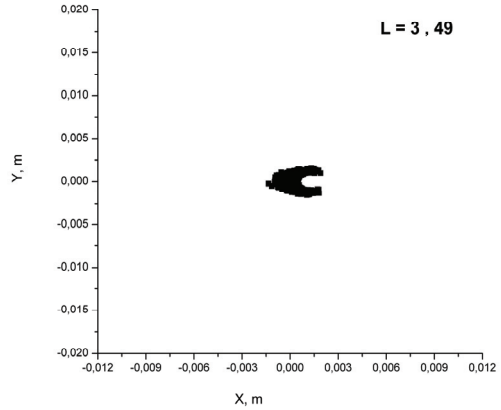

23M6, 3.49 m

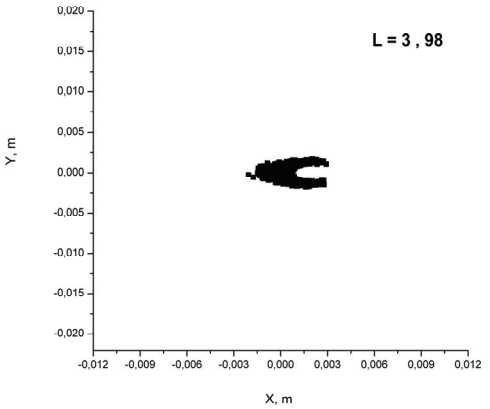

23ЛІ13, 3.98 m

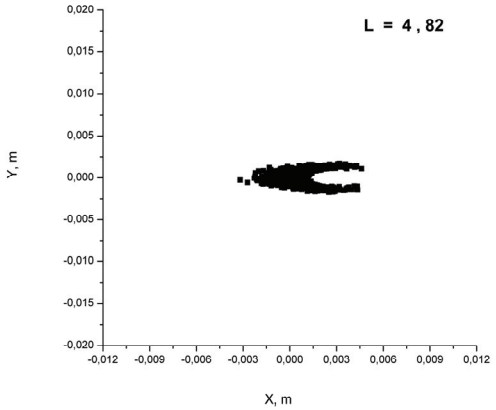

23M7, 4.82 m

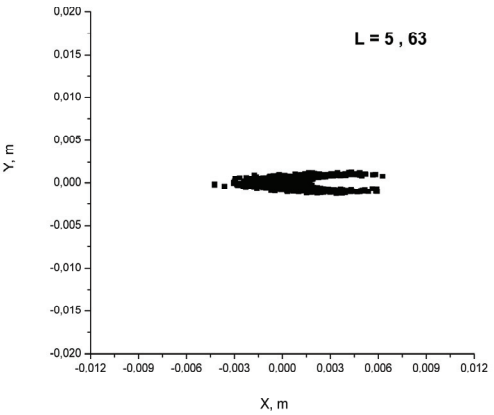

23M8, 5.63 m

Fig. 7. Electron density distribution in the beam cross section along the trajectory of the channel D

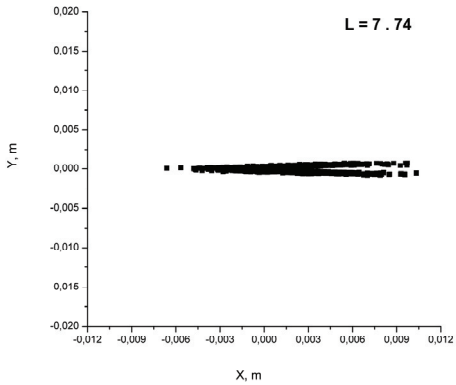

23JI1D, 7.74 m

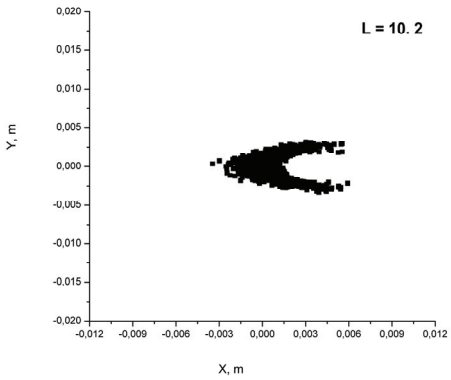

23M1D, 10.20 m

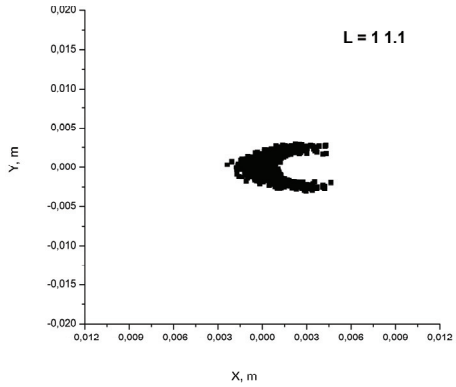

23JI2D, 11.1 m

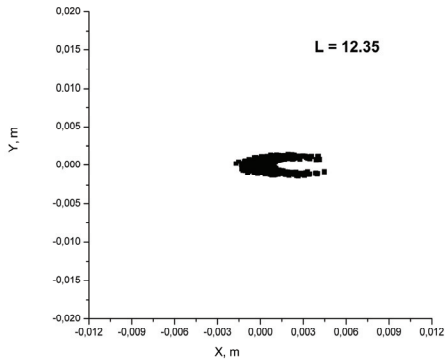

23 M2D, 12.35 m

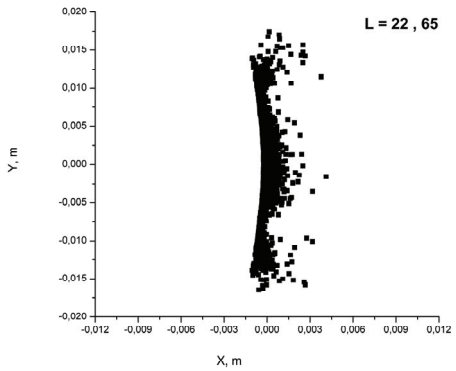

23JI3D, 22.65 m

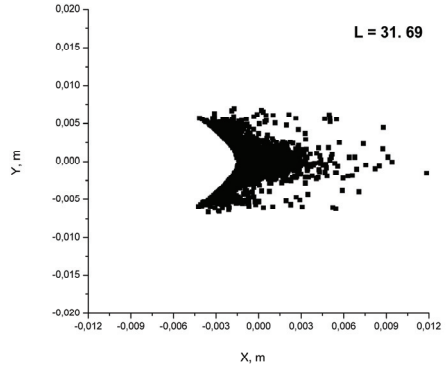

23JI4D, 31.69 m

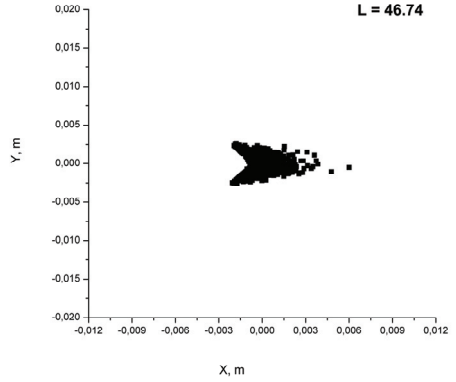

23JI5D, 46.74 m

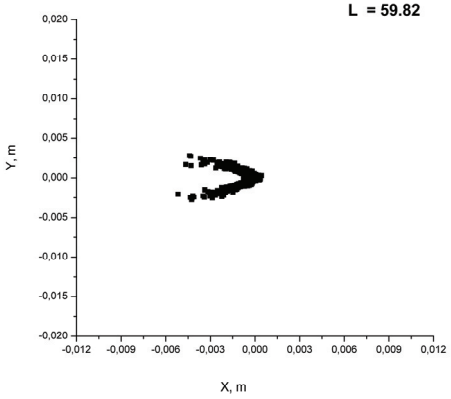

MD, 59.82 m

Fig. 7(Continued). Electron density distribution in the beam cross section along the trajectory of the channel D

Shown in Fig. 7 distribution was obtained by optimizing the structure of the magnetooptical recirculator system. The density distribution of the beam in phase space x, x 'and y, y' at the entrance to the dipole magnet 12M6 shown in Fig. 8 and Fig. 9. Modeling the movement was carried out for the energy 493 MeV. The density distribution of the particles in the beam cross section at this point is shown in Fig. 10.

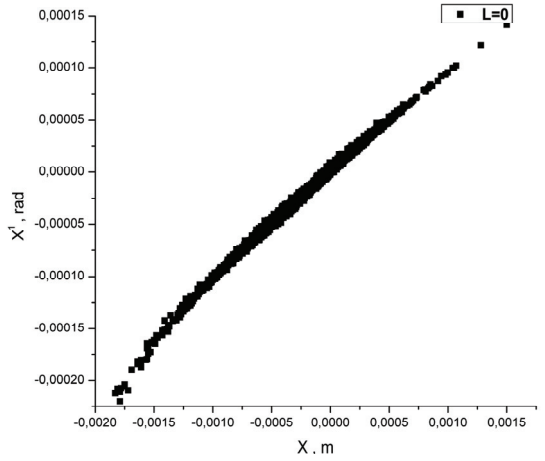

Fig. 8. The distribution of particles in the phase space x, x' at the entrance to the magnet 12M6

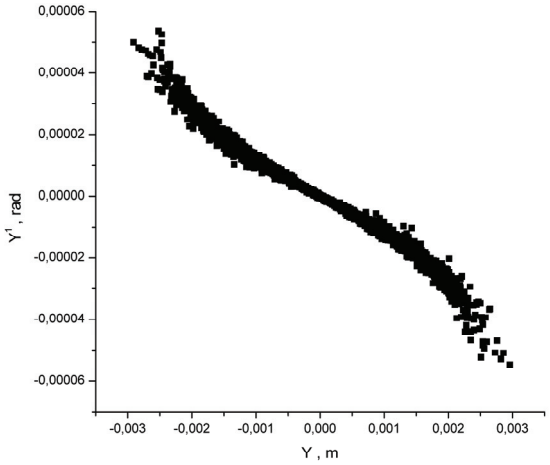

Fig. 9. The distribution of particles in the phase space y, y' at the entrance to the magnet 12M6

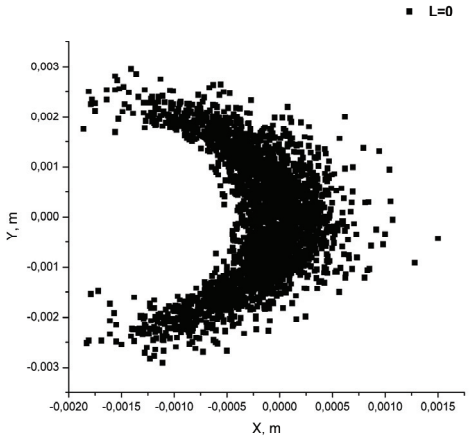

Fig. 10. The density distribution of the electron beam at the entrance to the magnet 12M6

The cross-sections shown in Fig. 7 in the sequence performed at the same scale charts, which gives the opportunity to observe the evolution of the beam, and come to the conclusion that at the selected vertical and horizontal aperture of the magnetic elements of the channel: dipoles, quadrupoles, correctors, beam losses along the path will be negligible.

Influence of nonlinear field components of the dipoles and quadrupoles on channel D on the transverse dimensions of the beam and the density of electrons in the beam at the output of the channel shows Fig. 11. In Fig. 11a shows the results of the tracking of particles with non-linear components of the field, in Fig. 11b octupole components quadrupoles are zero. In Fig. 11c additional sextupole field components of the dipoles are zero also.

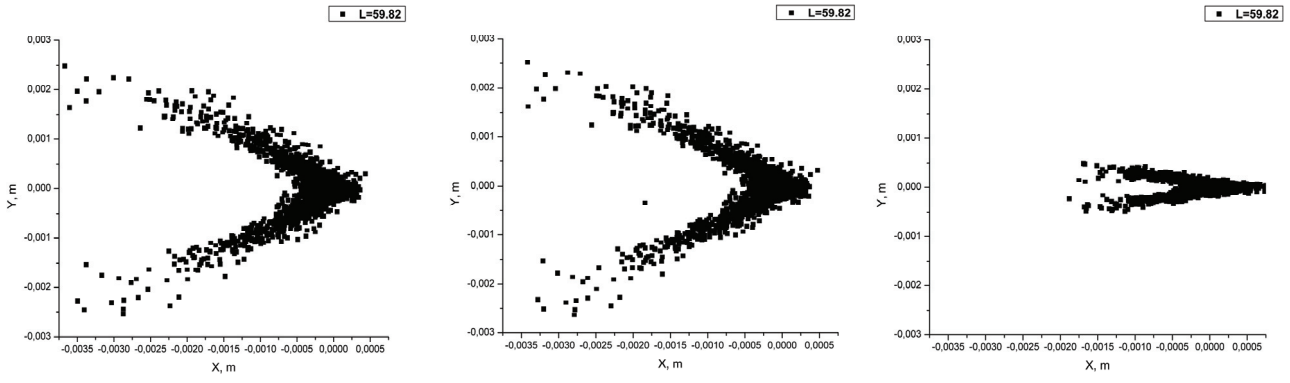

Рис. 11. The distribution of the particle density on the target of the D channel output
a - all nonlinearities are include, b - octupole components are switched off, c - all nonlinearities are switched off

Apparently, octupole components of quadrupoles to make minor changes in the density distribution of the beam, while the sextupole components dipoles fivefold increase vertical size and twice the horizontal size.

Dimensions of the beam at the output can be changed by the lens, located at the end of the channel. Since the density distribution of the beam, resulting in tuning achromatic channel mode (see Fig. 12) is transformed into the distribution shown in Fig. 13 when the field gradient in the 23JI5D lens alter from -0.0723 to 0.09 T m. Using a larger

number of lenses allows for more fine-tuning the parameters of the beam on the target.

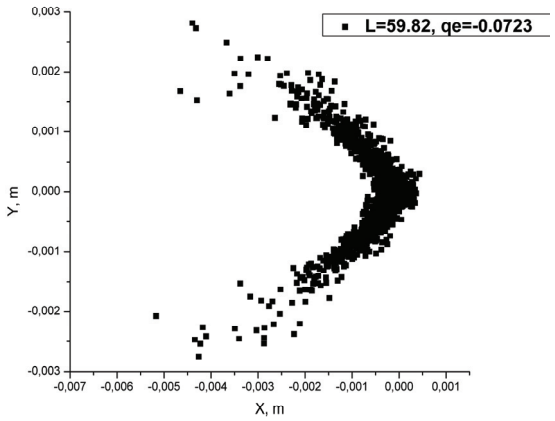

Fig. 12. The density distribution of the electron beam at the output of the channel D
the field gradient in the 23Л5D lens is -0.0723 T m

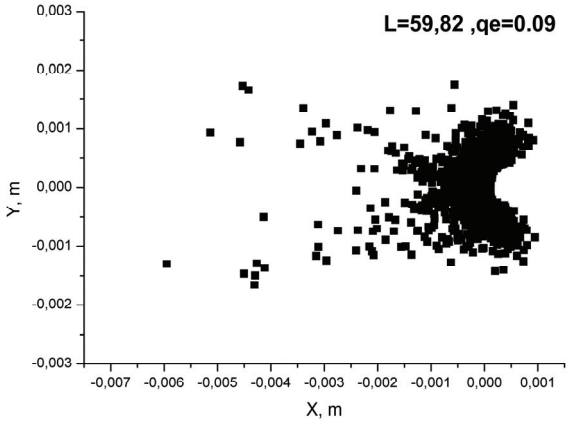

Fig. 13. The density distribution of the electron beam at the output of the channel D
the field gradient in the 23Л5D lens is equal 0.09 T m

CHANNEL EFEL

EFEL channel suppose to use to work with beams of electrons and photons up to an energy of 500 MeV. General view of the magnetic system EFEL channel is shown in Fig. 14. In a channel beam with an energy of 240 MeV can be derived using the first five magnets of the first recycling ring and magnets are turned off in the second semi-ring [6]. To focus and adjust the position of the beam is necessary to use quadrupoles and correctors, located on the first arch of the first ring - 22Л5 – 22Л8 and 2К3, 2К4 [6]. Beam with a maximum energy of up to 490 MeV is displayed in the channel when turned off magnets second arch of the second ring of recycling. Beam in this channel can be formed by four quadrupoles 22Л9 – 22Л12 belonging to the second recycling ring, and four quadrupoles Л1Е – Л4Е on the channel, and two dipole magnets 23М1Е 23М2Е set on the channel (the second ring magnet 23М6 off). Correction of the beam can be achieved correctors following the magnet 12М6 and 22Л12 lens. To output beam transmitted accelerating structure only once, with energies up to 240 MeV, the magneto-optical elements can also be used to form the beam after the magnet 12М6. The transverse distribution of particles for energy 493 MeV at the entrance to the canal in front of the magnet 12М6 similar to that shown in Figures 7, 8 and 9.

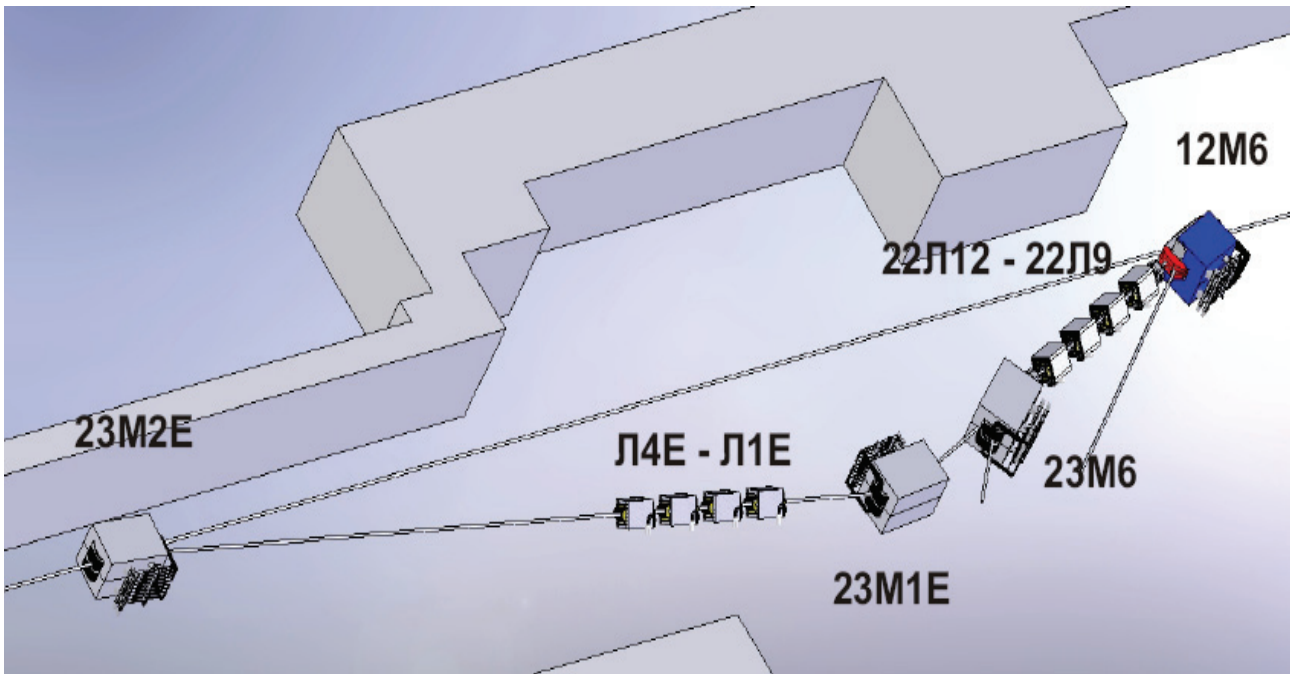

Fig. 14. Arrangement of magnets and quadrupoles on channel EFEL

In Fig. 15a shows the distribution of the particle density at the target MD, calculated on the basis of non-linear components of the dipole and quadrupole magnets. In Fig. 15b and Fig. 15c - when you turn off octupole field components quadrupoles and sextupole components of the dipole magnets, respectively.

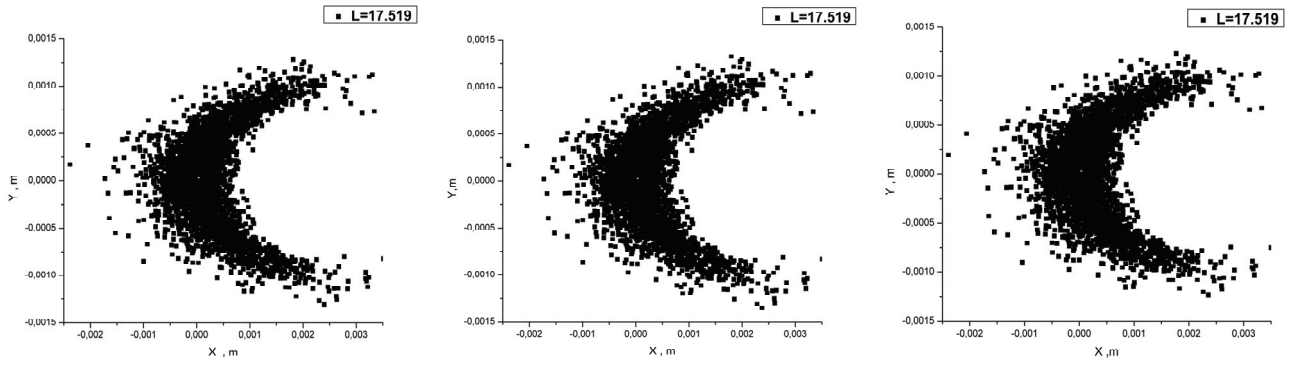

a b c

Fig. 15. The distribution of the particle density on the target of the EFEL channel output
a - all nonlinearities are include, b - octupole components are switched off, c - all nonlinearities are switched off

It can be seen that, as the channel D, the main influence on the size of the beam on the target MD, located at a distance of 17.519 meters from the entrance to the magnet 12M6, has sextupole component of the dipole magnets used for beam forming in the channel, however, in contrast to the D, changing the size of the beam is small.

The cross section of the beam along the channel for the energy 493 MeV is shown in Fig. 16.

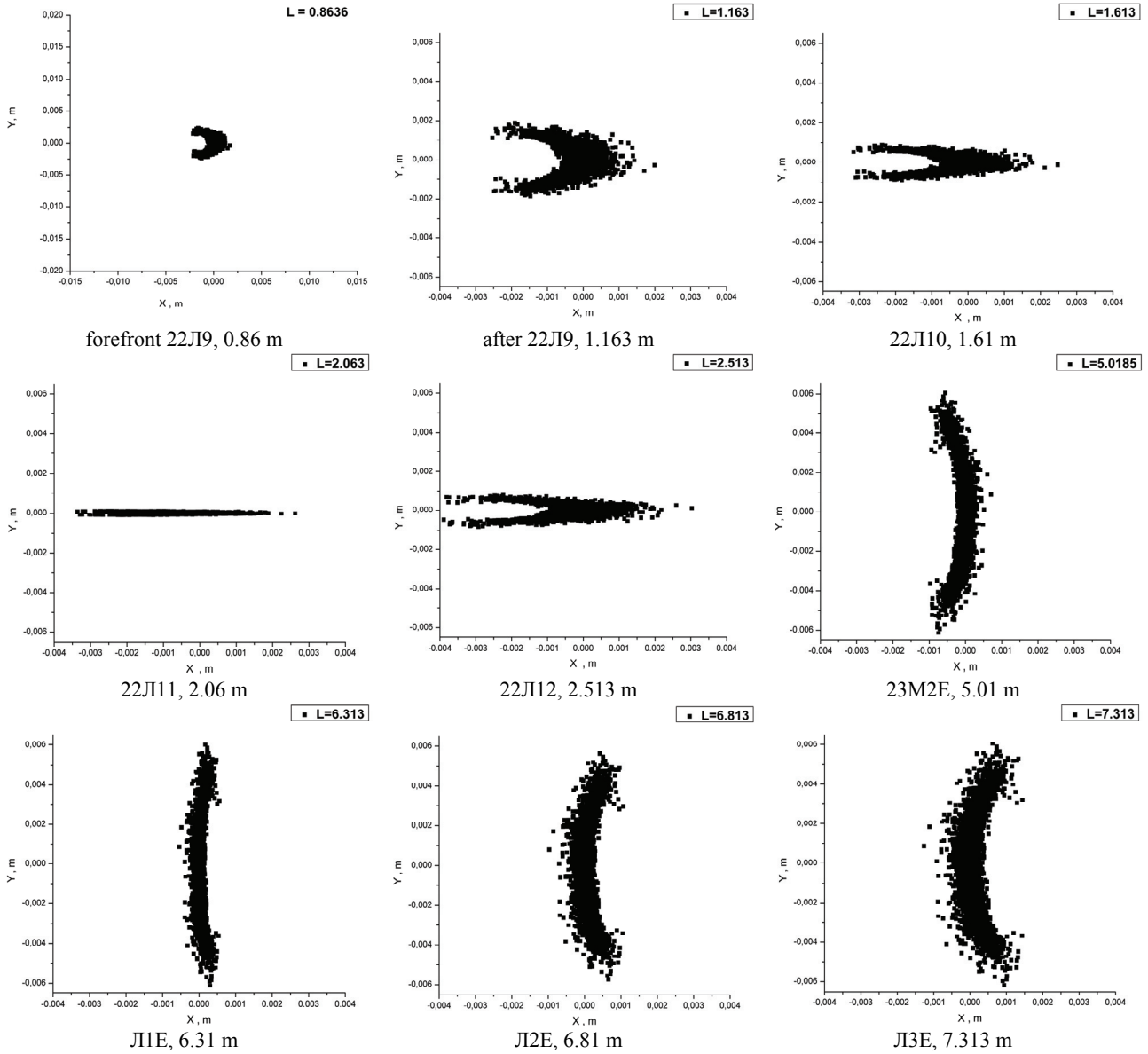

forefront 22Л9, 0.86 m after 22Л9, 1.163 m 22Л10, 1.61 m

22Л11, 2.06 m 22Л12, 2.513 m 23M2E, 5.01 m

Л1E, 6.31 m Л2E, 6.81 m Л3E, 7.313 m

Fig. 16. Electron density distribution in the beam cross section along the trajectory of the EFEL channel

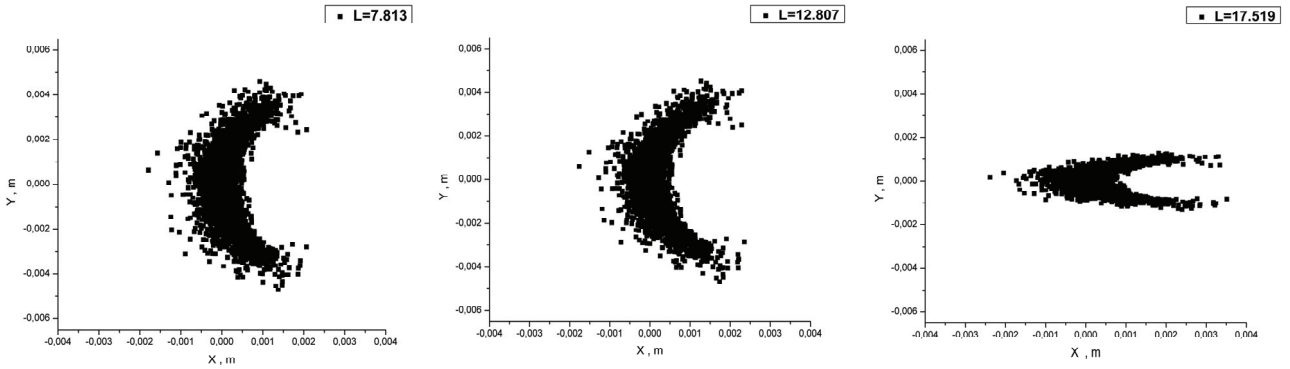

JI4E, 7.813 m 23M2E, 12.807 m MD, 17.519 m

Fig. 16(Continued). Electron density distribution in the beam cross section along the trajectory of the EFEL channel

Shown in Fig. 16 in the same scale cross sections make it easy to trace the horizontal and vertical beam sizes are small enough in magnetic elements and will not result in a substantial loss in transit through the channel.

CONCLUSION

Output channels of electrons in the main experimental facilities differ both in length and structure magnetooptical system. This is primarily due to the placement of recirculator in the current targets hall linear accelerator LU 2000 [1-3]. Selected options in the beam transport channels provide minimal loss of electrons along the trajectory and the required size on the target. Common to all channels is a small effect of octupole components of the quadrupole lenses on the density distribution of the particles, the main contribution to the increase in size and density changes make sextupole components of the dipole magnets. Available on channels quadrupole lenses let you change the size of the beam on the target in a wide range and provide a change in the parameters of the beam when alter the experimental conditions and recirculator tuning.

REFERENCES

1. Arkatov Yu.M., Dovbnya A.N., Glamazdin A.V., Guk I.S., Kononenko S.G., van der Weil M., Botman J.I.M., Peev F.A., Tarasenko A.S. “SALO” project. – National Science Center Kharkov Institute of Physics Technology, Kharkiv, 2005. – 104 p.
2. Dovbnya A. N., Guk I. S., Kononenko S. G., Peev F. A., Tarasenko A. S., Botman J. I. M.. Accelerating complex for basic researches in the nuclear physics. // Proceedings of the 2-nd International Conference “Current Problems in Nuclear Physics and Atomic Energy”, June 9 to June 15, 2008, Kyiv, Ukraine, Kyiv, 2009. – P. 790-795.
3. Dovbnja A.N., Ganenko V.B., Guk I.S., Kononenko S.G., Tarasenko A.S. The electron beam lines from SALO recirculator to physical installation // The Journal of Kharkov National Univesity, №784, physical series “Nuclei, Particles, Fields”, Issue 4/36/. – 2007. - P. 74 - 78.
4. Khvastunov V.M., Denyak V.V. High-resolution spectrometer for "SALO"-project // Problems of atomic science and technology. Series “Nuclear Physics Investigations”. 2001. - № 3 (55). – 2011. - P. 83-86.
5. Guk I.S., Kononenko S.G., Tapasenko A.S. Investigation of the effect of non-linear parameters of dipole and quadrupole magnets on the beam parameters in recirculator SALO // Problems of atomic science and technology. Series “Nuclear Physics Investigations” No 3 (79). – 2012. - P. 137-141.
6. Guk I.S., Kononenko S.G., Tapasenko A.S., Peev F.A. The basic summaries of working out of recirculator SALO magnetooptical system. // The Journal of Kharkov National University physical series “Nuclei, Particles, Fields”. – 2012, №1017. - Issue 3/55/. - P. 107-116.
7. http://mad.home.cern.ch/mad/
8. Dovbnya A.N., Guk I.S., Kononenko S.G., Koval’ev G.G., Mytsykov A.Y., Peev F.A. Draft design of recirculator SALO magnetic system // The Journal of Kharkov National Univesity, physical series “Nuclei, Particles, Fields”. – 2007, №784. - Issue 4/36/. – P.3 – 14.
9. Boling Xi, Botman J.I.M., Timmermans C.J., Hagedoorn H.L.. Design study of storage ring EUTERPE // Nucl. Instr. and Meth. – 1992. – Vol.B68. - P. 101.
10. Guk I.S., Dovbnya A.N., Kononenko S.G., Peev F.A., Tarasenko A.S. Aberrations of Magnetooptical System of SALO Recirculator // Physics of Particles and Nuclei Letters. – 2010. - Vol. 7, №7. –P. 1–4.

Guk Ivan Semenovich, Ph.D., senior scientific researcher NSC KIPT
Scientific interests: framing of large accelerating complexes, beam dynamics in accelerators, synchrotron radiation, powerful sources of neutrons and electrons. The author and the co-author more than 120 papers and 2 books

Kononenko Stanislav Grigor'evich, senior scientific researcher NSC KIPT
Scientific interests: beam dynamics in accelerators, powerful sources of neutrons and electrons
The author and the co-author more than 110 papers and 2 books

Peev Fedor Andreevich, scientific researcher NSC KIPT
Scientific interests: framing of large accelerating complexes, powerful sources of neutrons and electrons
The author and the co-author more than 90 papers and 2 books

Tarasenko Alexander Sergeevich, senior scientific researcher NSC KIPT
Scientific interests: beam dynamics in accelerators, synchrotron radiation, powerful sources of neutrons and electrons
The author and the co-author more than 110 papers and 2 books

ПРАВИЛА ДЛЯ АВТОРІВ

“Вісник Харківського національного університету” (серія: фізична «Ядра, частинки, поля») є збірником наукових робіт з фізики елементарних частинок, ядерної фізики, фізики плазми та плазмових технологій, фізики твердого тіла та радіаційної фізики. Журнал публікує наукові статті, короткі повідомлення, оглядові статті та рецензії на книги. До публікації у збірнику приймаються статті, які підготовлені у відповідності до правил для авторів і які отримали дві позитивні рецензії. Рукописи, які не відповідають правилам не розглядаються.

Для редагування тексту у MS Office Word можна застосовувати шаблон з готовими стилями, який розміщений на сайті журналу:

http://www-nuclear.univer.kharkov.ua.

Об'єм статті, мова, супровідні документи. До редакції подається рукопис об'ємом не менше 3-х сторінок українською, російською або англійською мовами в двох екземплярах з направленням закладу і актом експертизи, а також повний електронний варіант статті у форматі MS Office Word, а також ОКРЕМО електронні варіанти усіх рисунків у форматах "bmp", "tiff" або "jpg". Безпосередня вставка рисунків з інших програм не допускається. Якість рисунків повинна бути достатньою для відтворення тонких ліній, градацій відтінків та кольорів при чорно-білому друці. Редакція залишає за собою право вимагати поліпшення якості малюнків для отримання задовільної якості чорно-білого друку.

Папір, формат, поля. Текст друкується на білих листах формату А4 через один інтервал. Рекомендується використовувати редактор MS Word, шрифт Times New Roman (Cyr), редактор формул MathType версія 5.0 і вище. Поля справа, зліва і знизу по 2 см, зверху - 3 см.

Нумерація сторінок. Сторінки нумеруються послідовно на зворотному боці листа олівцем.

Підписи авторів. Один екземпляр рукопису повинен бути підписаним на зворотному боці листа усіма авторами.

ПОСЛІДОВНІСТЬ РОЗМІЩЕННЯ МАТЕРІАЛУ

Індекс класифікації. На першій сторінці зверху пропускаються два рядка; у третьому рядку у лівому верхньому куті друкується УДК *(курсив*, 9 pt.) і/або PACS і значення індексу.

Назва статті, список авторів статті. Нижче індексу класифікації після пропуску одного рядка розміщується назва статті (прямий напівжирний шрифт, 12 pt., усі букви прописні, вирівнювання по центру). Нижче назви статті після пропуску одного рядка друкуються ініціали і прізвища авторів (прямий напівжирний шрифт, 12 pt., вирівнювання по центру).

Назва і адреса організацій, що представляють автори. Нижче списку авторів у наступному рядку друкуються повні назви і адреси організацій, які представляють автори (шрифт *курсив*, 9 pt., вирівнювання по центру), у наступному рядку - адреса електронної пошти для переписки. Якщо організацій декілька, то для вказівки відповідності авторів і організацій слід застосовувати виноски зірочкою або цифрами.

Дата представлення статті в редакцію. Нижче адреси електронної пошти друкується дата представлення статті в редакцію: число - цифрами, місяць - прописом, рік - цифрами (шрифт прямий, 9 pt., вирівнювання по центру).

Реферати, ключові слова іншими мовами*. Після пропуску одного рядка друкується реферат мовою статті об’ємом не менше ніж 500 знаків без відступів, з коротким викладом постановки задачі, методів, що були використані та основних результатів (шрифт прямий 9 pt., вирівнювання по ширині). Слово "реферат" не друкується. У наступному рядку після слів (мовою статті) **"КЛЮЧОВІ СЛОВА:"** (прописом, шрифт прямий напівжирний, 9 pt., без відступу) мовою статті розміщуються ключові слова (5-8 слів, шрифт прямий 9 pt., вирівнювання по ширині). Далі після пропуску одного рядка двома іншими мовами друкується назва статті (шрифт прямий напівжирний 9 pt., вирівнювання по центру), список авторів (шрифт прямий напівжирний 9 pt., вирівнювання по центру), список організацій, що представляють автори (шрифт курсив 9 pt., вирівнювання по центру), текст реферату та ключові слова.

Основний текст статті, абзацний відступ. Нижче реферату після пропуску одного рядка друкується основний текст статті (шрифт прямий 10 pt.). Абзацний відступ 0,75 см.

Розбиття статті на розділи. Рекомендується розбиття статті на такі розділи: вступ (назва цього розділу не друкується) **МАТЕРІАЛИ І МЕТОДИ** (обов'язково для експериментальних робіт), **РЕЗУЛЬТАТИ І ОБГОВОРЕННЯ, ВИСНОВКИ.**

Для теоретичних робіт допускається більш вільний розподіл матеріалу на розділи, наприклад, замість розділу **МАТЕРІАЛИ І МЕТОДИ** рекомендуються розділи **ПОСТАНОВКА ЗАВДАННЯ, МОДЕЛЬ** і тому подібне. Розділи не нумеруються, в назвах розділів усі букви прописні і виділяються напівжирним шрифтом, вирівнювання по центру. При необхідності розділи діляться на підрозділи. Назви підрозділів друкуються з великої літери і виділяються напівжирним шрифтом, вирівнювання по центру. Після кожного розділу чи підрозділу залишається один пустий рядок.

Фонди, гранти. Наприкінці тексту статті після пропуску одного рядка, якщо потрібно, вказується назва фонду, який фінансував роботу, і номер гранту.

Формули, таблиці, малюнки, підписи, нумерація. Математичні і хімічні символи, рівняння і формули друкуються в тексті статті за допомогою програми Math Type. Рисунки вставляються в текст статті у форматах: «bmp», «tiff» або «jpg». Всі надписи на рисунках і осях друкуються шрифтом не менше 8 pt. Підписи під рисунками друкуються шрифтом 9 pt. Формули, таблиці і рисунки послідовно нумеруються арабськими цифрами, наприклад: (1); Табл. 1; Рис. 1. Назва таблиць і рисунків є обов'язковими.

Посилання і список літератури. Використані у рукопису літературні джерела нумеруються в порядку цитування в тексті, номер посилання друкується в квадратних дужках. Список літератури (шрифт прямий 9 pt.) розміщується відразу за основним текстом статті і виділяється як розділ **СПИСОК ЛІТЕРАТУРИ** (шрифт прямий напівжирний 9 pt.). Не допускаються посилання на неопубліковані роботи.

* For foreign authors is sufficient to provide abstracts in Russian and English.
Для зарубежных авторов достаточно рефератов на русском и английском.